(NASA-CR-135389) DESIGN, FABRICATION, AND
TEST OF A COMPOSITE MATERIAL WIND TURBINE
ROTOR BLADE Final Report (United
Technologies Corp.) 185 p HC A09/MF A01
CSCL 10A G3/44

N79-10525

Unclas
33934

DESIGN, FABRICATION, AND TEST OF A COMPOSITE MATERIAL WIND TURBINE ROTOR BLADE

D. G. Griffee, Jr., R. E. Gustafson,
and E. R. More
Hamilton Standard Division
United Technologies Corporation

November 1977

DESIGN, FABRICATION, AND TEST
OF A COMPOSITE MATERIAL
WIND TURBINE ROTOR BLADE

D. G. Griffee, Jr., R. E. Gustafson,
and E. R. More
Hamilton Standard Division
United Technologies Corporation
Windsor Locks, Connecticutt 06096

November 1977

TABLE OF CONTENTS

LIST OF FIGURES (Continued)

LIST OF FIGURES (Continued)

LIST OF FIGURES (Continued)

LIST OF TABLES

SUMMARY

This report describes the aerodynamic design, structural design,
fabrication, and structural testing of a 60-foot (18.3-meter)-long
filament wound, fiberglass/epoxy resin matrix, wind turbine rotor
blade for a 125-foot (38.1M) diameter, 100 kW wind energy conversion
system. One blade was fabricated which met all aerodynamic shape
requirements and was structurally capable of operating under all
specified design conditions. The feasibility of filament winding
large rotor blades was demonstrated.

INTRODUCTION

NASA Lewis Research Center awarded Contract NAS3-19773 to Hamilton
Standard Division of United Technologies Corporation on February 11, 1976.
The contract covered the design, fabrication, and test of a composite
material wind turbine rotor blade which would be compatible with an
existing 125-foot (38.1 M) diameter, 100 kW,wind generator system at the
Plum Brook Station of Lewis Research Center, near Sandusky, Ohio.

Studies conducted by Hamilton Standard as part of the General Electric
Company team under NASA Contract NAS3-19403 showed that light weight
filament wound composite material wind turbine rotor blades would best
meet the performance, structure, and cost objectives for a viable wind
energy conversion system.

The purpose of the work performed under this contract was to demonstrate
the structural capability, ease of fabrication, and economic benefit of
a filament wound fiberglass/epoxy matrix wind turbine rotor blade for a
cost effective wind energy conversion system.

DISCUSSION AND CONCLUSIONS

A filament wound, fiberglass epoxy composite is an attractive material for fabrication of large wind turbine blades because of the potential for a highly automated method of production with a resulting low cost i.e., the labor associated with accurately positioning and carefully bonding together many blade sections or panels to form a single structural unit, is not required. The fabrication of a blade by filament winding also has the obvious advantage of reducing the extent to which the structural integrity of the blade relies on bonded joints and reduces the amount of inspection required during manufacture and when the blade is in service. The blade described in this report was the first large blade to be filament wound and as is normal in development programs of this sort, several unanticipated fabrication problems were encountered. These problems included filament bridging on spar and shell, filament winding machine drive shaft weld fractures, shell winding offset fixture weld fractures, machine misindexing due to a revolution counter malfunction, and difficulty in shell mandrel removal. However, in spite of these problems and the necessity to meet a specific schedule milestone, the blade was successfully wound and demonstrated structural characteristics which were satisfactory for all of the specified load conditions.

One consideration in selecting the NACA23018 airfoil for the blade was that the face side contour is convex and could be generated by using proven filament winding techniques.

Design work and manufacturing studies conducted since the airfoil designation was fixed have indicated that the filament winding process can generate other types of airfoils, such as the Whitecomb GA (W)-2, thereby providing performance benefits on the order of 1% to 2%. Airfoils which require a face side concavity can be manufactured by winding most of the shell width and attaching a small, non-structural, preformed trailing edge incorporating the concave portion of the airfoil. Normally this preformed section would be approximately 10% of the width of the airfoil and would only be required on the outer 50% of the blade.

Based on the design, fabrication and test work completed during this program, the following conclusions can be drawn:

1. Filament winding is a viable process for fabricating large wind turbine blades.

2. The manufacturing prototype blade has satisfactory structural properties for the Plum Brook installation.

3. A successful filament wound fiberglass blade can be fabricated for the Plum Brook installation without the use of an internal spar support. This blade is discussed in Appendix A.

4. Filament wound fiberglass structure can be easily, effectively and economically inspected on a production basis.

5. Design techniques can closely predict the response characteristics of the blade.

DESCRIPTION

DESIGN STUDY

AERODYNAMIC ANALYSIS

The aerodynamic analysis was carried out using aerodynamic methodology for wind turbines derived from the propeller vortex theory as developed and used by Hamilton Standard over the past 37 years.

Wind generator site wind data was employed to aerodynamically optimize the wind turbine blade in terms of annual energy conversion within the constraints of the power output requirements, specified operating conditions, and overall geometric characteristics of the wind generator system. Figure 1 shows the optimized aerodynamic blade design with a NACA 23018 airfoil in terms of chord width to diameter ratio (B/D), thickness to chord width ratio (T/B), and twist distribution (Θ) all versus blade radius ratio (r/R).

Performance analysis of this blade using NACA roughness airfoil data showed that a rated power of 139 kW at the rotor was available at 18 mph (28.96 km/hr) rated wind speed and 40 rpm rotor synchronous speed. This exceeded the contract power rating requirement of 133 kW. Since it was appreciated that airfoil roughness has an effect on both performance and air loads, both smooth and NACA rough airfoils were analyzed. Figure 2 shows the calculated performance comparison of the blade with smooth airfoils and with NACA rough airfoils and a performance plot in terms of power ratio (P.R. = power output/$(1/2 \, \rho \, (\pi D^2/4) \, V^3)$ where D = rotor diameter and V is wind speed) versus velocity ratio (V.R. = Tip speed/V). These calculations indicated that the rated power of the blade with smooth airfoils was 158 kW or an increase of 13.7 percent over the blade with NACA rough airfoils. Based on a 9 mph (14.48 km/hr) mean wind velocity curve for the wind generator site, the blade with NACA rough airfoils produces 236,000 kWh per year and the blade with smooth airfoils produces 272,000 kWh per year. Figure 3 shows airfoil aerodynamic characteristics for smooth and NACA rough NACA 23018 airfoils. Smooth airfoils produce increased lift coefficients and lift to drag ratios with the result that air loads for smooth airfoils during gust conditions are increased substantially. Since the surface finish resulting from filament winding was estimated to be closer to smooth than NACA rough and to provide conservatism to the design, the blade was sized to meet rated performance conditions using rough airfoils and structurally sized using smooth airfoils.
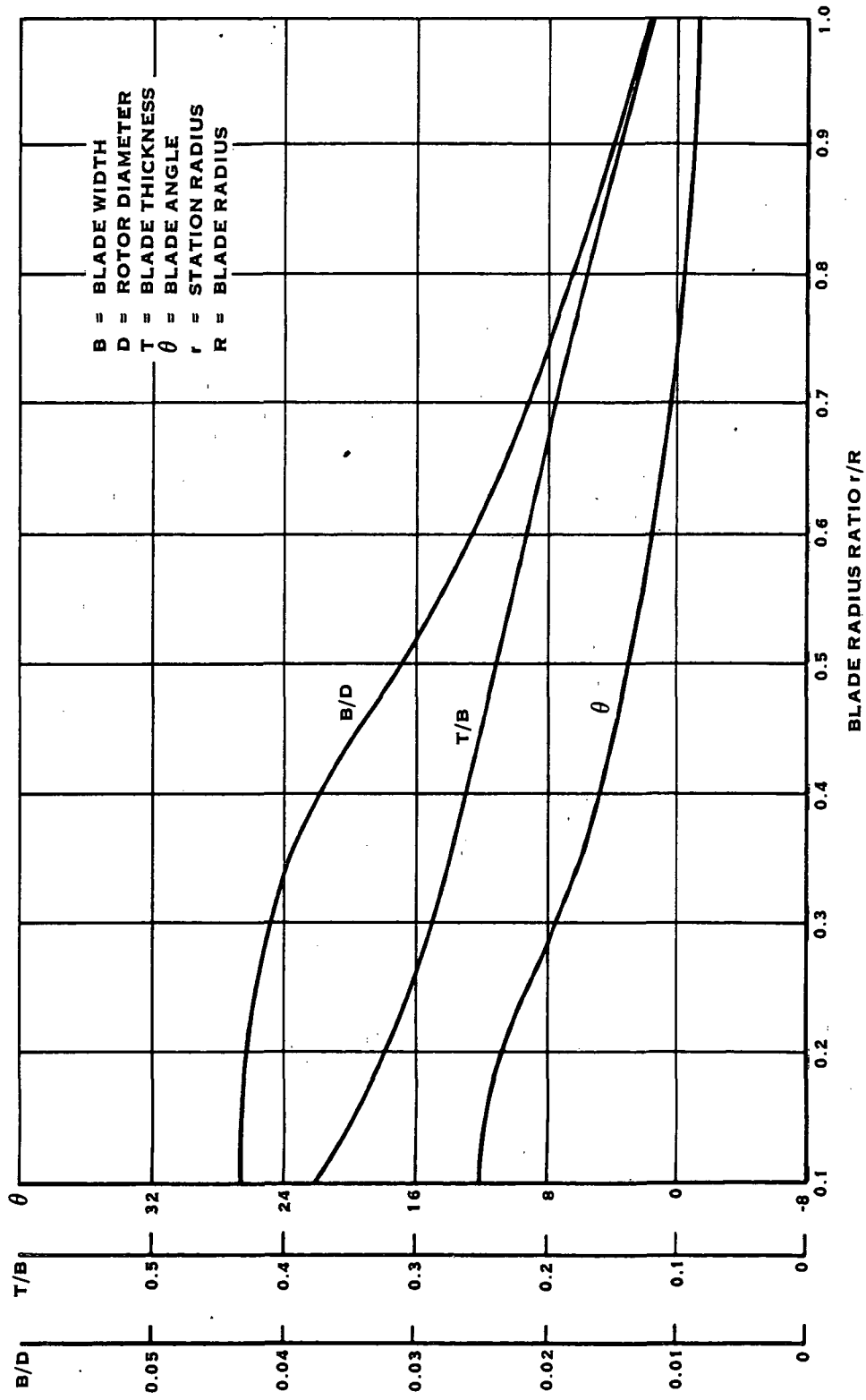
FIGURE 1. PRELIMINARY AERODYNAMIC DESIGN

	NACA ROUGH	SMOOTH
RATED POWER RATIO	0.383	0.435
RATED POWER (KW)	139	158
ANNUAL POWER (KWH)	236,000	272,000
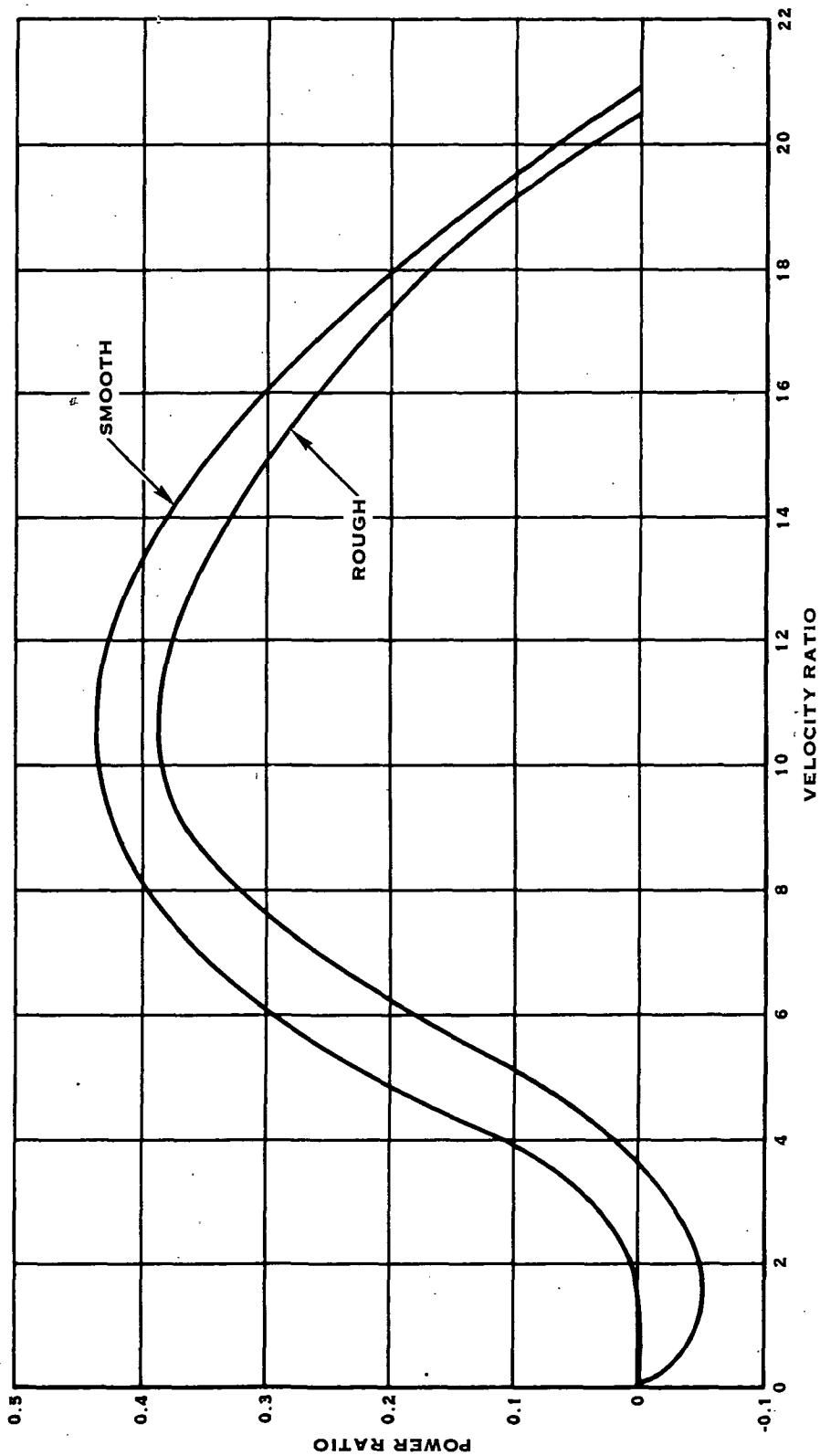
FIGURE 2. PERFORMANCE COMPARISON OF SMOOTH AND ROUGH AIRFOILS

7
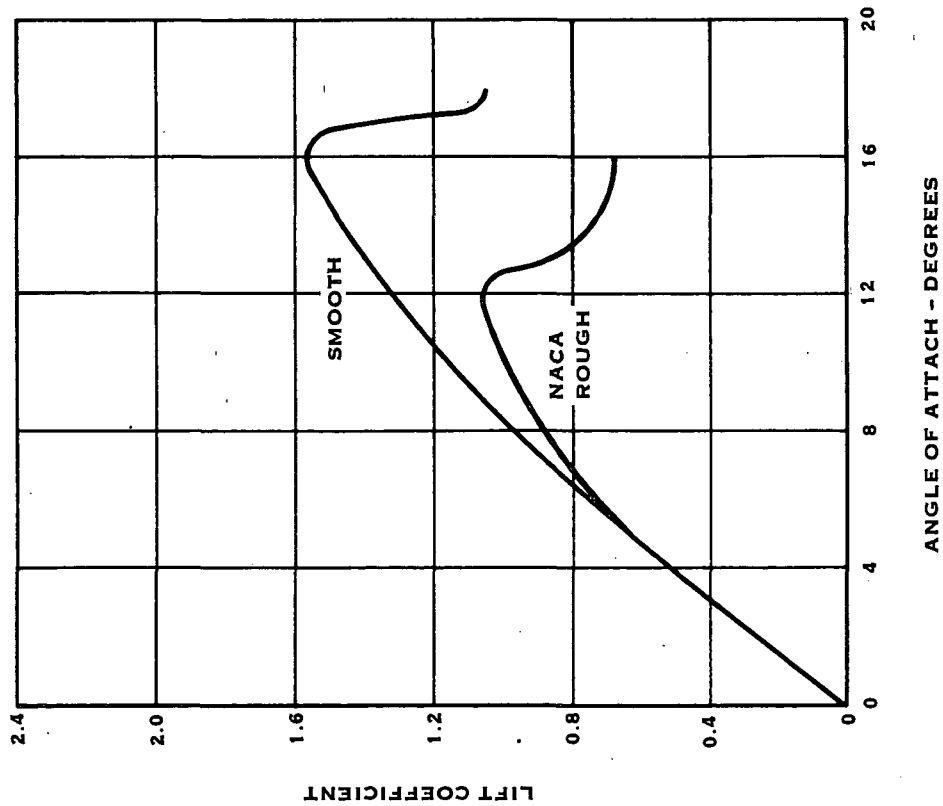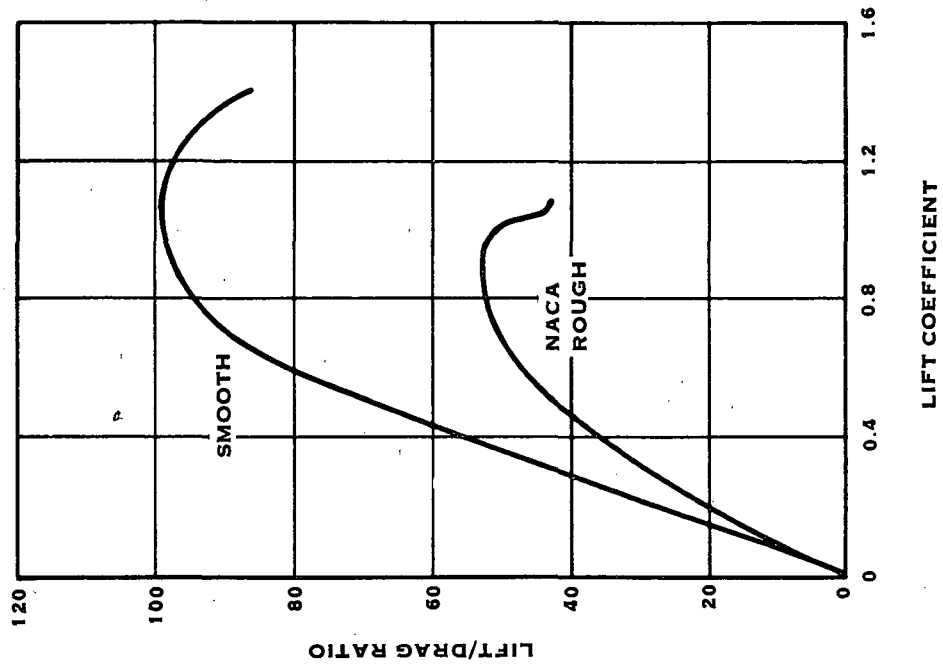
FIGURE 3. NACA 23018 AIRFOIL AERODYNAMIC CHARACTERISTICS

8

STRUCTURAL ANALYSIS

While blade aerodynamic design optimization for annual energy conversion was in process the aerodynamic design characteristics of the wind turbine blade originally designed for operation on the wind generator were used to mathematically model a spar/shell and a monocoque blade for structural analysis. The initial aerodynamic loading studies provided the basis for the decision to use rough airfoil data for aerodynamic performance analysis and smooth airfoil data for structural analysis in order to be conservative in each area. Figures 4 and 5 show the effect of roughness for a steady 18 mph (28.96 km/hr) wind and for an 18 mph (28.96 km/hr) to 36 mph (57.92 km/hr) gust condition, respectively. For the steady 18 mph (28.96 km/hr) wind case the rough airfoil produces a slightly higher load because of increased drag. However, in the gust case the rough airfoil stalls and the load drops off whereas the smooth airfoil remains unstalled and produces approximately 100% more load.

The Design Study loads were composed of the following conditions: (1) those selected as the sizing loads from those specified in NASA-LeRC Contract Number NAS3-19773 Exhibit B, paragraph B.4 and (2) those added by Hamilton Standard. These are:

Case 1: The rated performance condition of 18 mph wind velocity with NASA supplied wind shear and 100% tower shadow as a vibratory moment. Since this condition resulted in a relatively low load, the current installation measured vibratory moment of ± 720,000 in-lb (81360 N-M) was used for the study. The total shank moment was 150,000 ± 720,000 in-lb (16950 ± 81360 N-M).

Case 2: Wind gusting instantaneously from 18 mph (28.9 km/hr) to 36 mph (57.92 km/hr) and rotor speed increasing from 40 rpm to 56 rpm. The total shank moment was 1,352,000 ± 720,000 in-lb (152776 ± 81360 N-M).

Case 4: Wind decreasing instantaneously from 18 mph (28.96 km/hr) to zero. The total shank moment was 90,000 ± 676,000 in-lb (10170 ± 76388 N-M).

Case 2b: This case was added by Hamilton Standard for this study as it appeared to result in higher loads, in the mid-blade region, than those cases defined in the specification. With wind gusting from 18 mph (28,96 km/hr) to 36 mph (57.92 km/hr), with rotor speed constant at 40 rpm, and with no increase in blade centrifugal restoring moment; the mid-blade moments were increased over those in Case 4.
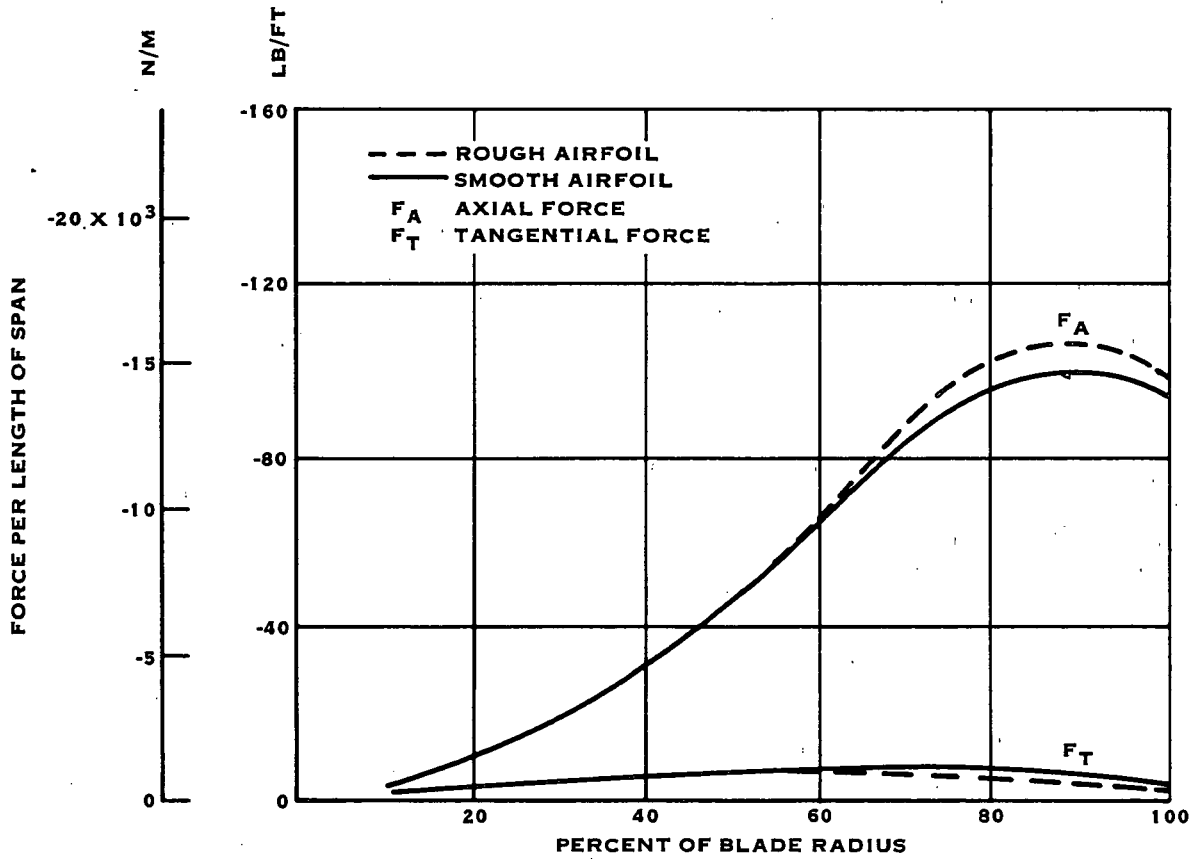
FIGURE 4. EFFECT OF ROUGHNESS ON AIRLOADS – STEADY WIND
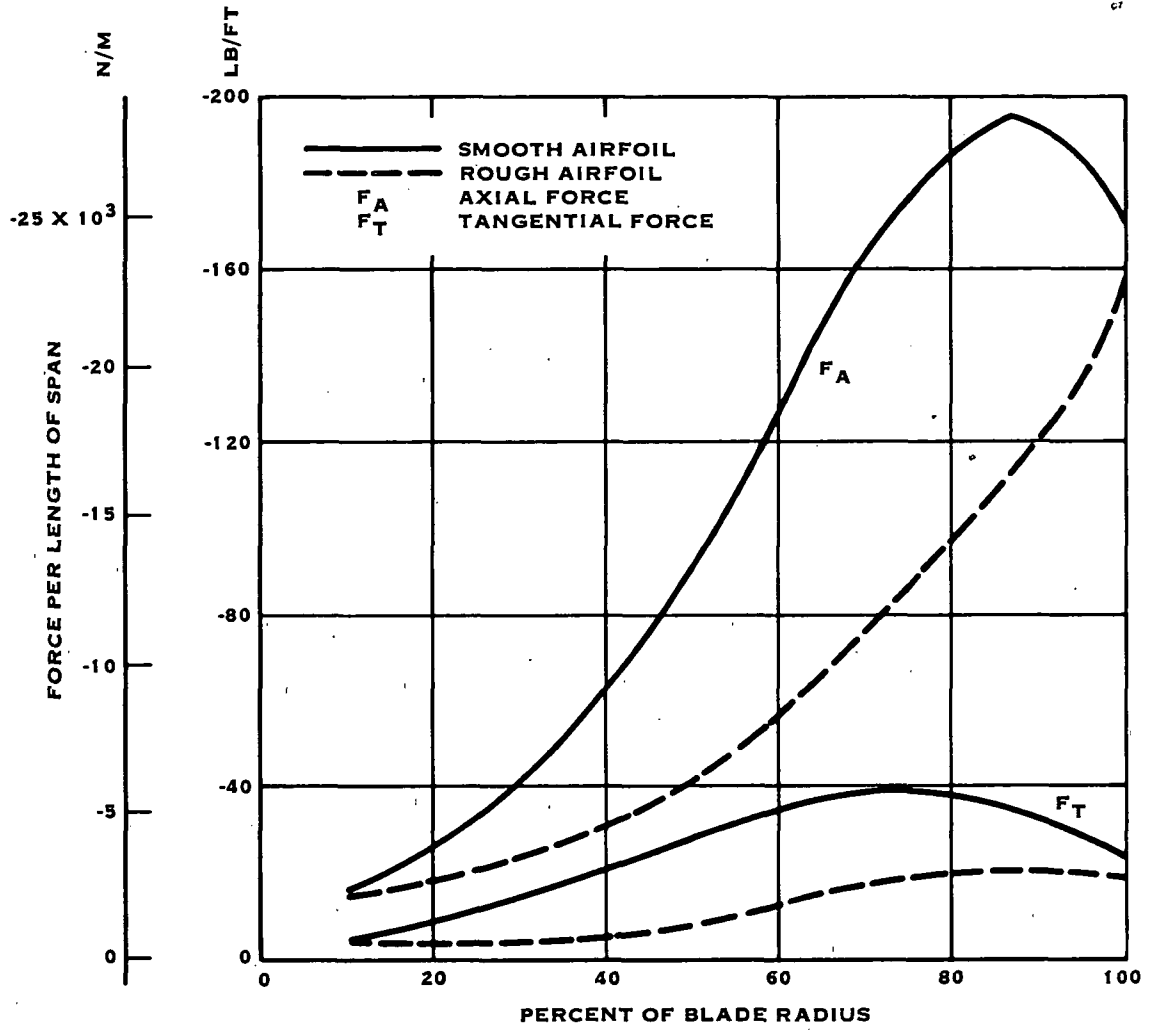
FIGURE 5. EFFECT OF ROUGHNESS ON AIRLOADS – GUST CONDITION

Case 1 is an infinite life (10^8 cycles) case and Cases 2, 4, and 2b occur frequently (5 x 10^4 cycles) during operation at 40 rpm.

Blade stressing, frequency, and stability were selected as the parameters for the spar/shell vs. monocoque design comparison. Figure 6 is a Goodman diagram for the blade material and shows that from a stress standpoint, both spar/shell and monocoque blade designs are acceptable for infinite life for the load conditions imposed.

Table I shows, in terms of natural frequency to operating frequency order ratio (ω_N/Ω), that both blade designs meet the contract requirements that (1) the first flatwise natural frequency be at least 20% above the first order line and (2) the first edgewise natural frequency be at least 20% above the third order line, both at a rotor operating speed of 40 rpm. To determine that the placement of these frequencies would not be adversely affected by retention stiffness, a sensitivity search was conducted for a range of retention stiffnesses. Figure 7 is a plot of the 1st flatwise and 1st edgewise frequency vs. retention stiffness and shows that the retention stiffness has little effect on frequency placement in the region of estimated retention stiffness. The estimated blade stiffness was based on NASA supplied structural data for the blade mounting shaft (12.3 x 10^2 in-lb/rad) (1.39 x 10^8 N-M/rad) and included the steel blade-to-hub adapter spring rate.

The final area of comparison was the determination of blade stability under various stipulated loading conditions. Figures 8 and 9 are the results of these studies and show that, without structural damping, the monocoque blade design, with its construction dictating a center of gravity location at approximately 50% of chord width, displays negative damping in all cases. The spar/shell blade design, with the center of gravity located 35% of the chord width from the leading edge, is positively damped for all conditions. This indicates that stability is more easily achieved with the spar/shell design. It was estimated that an additional 600 pounds (272 kg) of structure would be necessary to meet the combined objective of positive damping (without structural damping) and specified frequency placement for the monocoque design blade.

Transition to the NASA hub shaft was common for both designs. It was made through integrally bonded double shear sleeves with a reverse locking taper and redundant shear bolts installed through the sleeves and blade and a conical blade-to-hub adapter bolted to the outer sleeve and the hub shaft as shown in Figure 10. The conical adapter facilitated mandrel removal after winding by providing a large removal hole. The conical adapter was selected after a straight cylindrical adapter was studied and found undesireable due to excessive bolt loading at the flange interface with the NASA hub shaft.

12
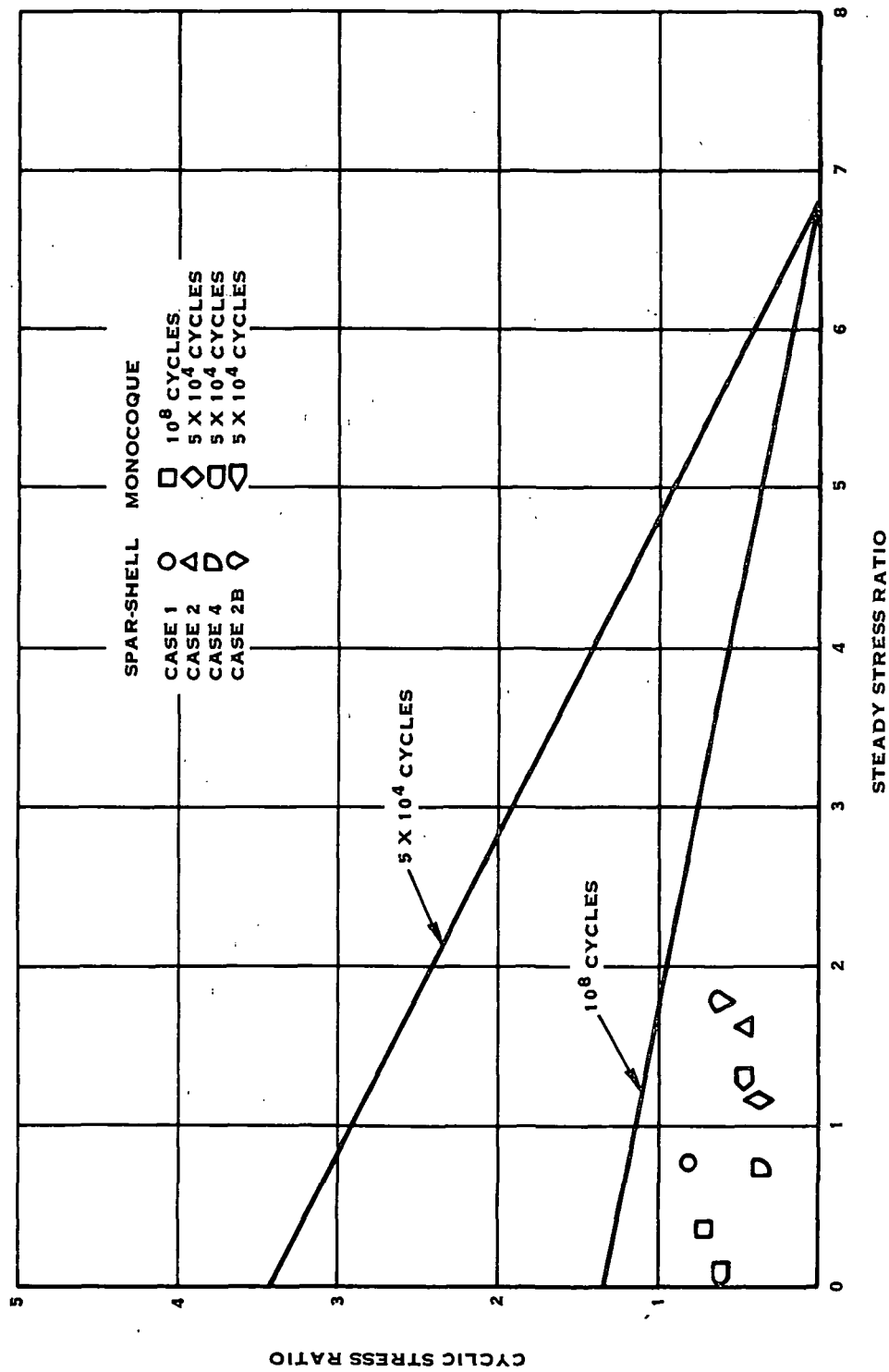
FIGURE 6. BLADE DESIGN STRESS COMPARISON

TABLE I

UNCOUPLED BLADE FREQUENCIES

$$\frac{\omega N}{\Omega}$$

	Retention Stiffness 7×10^8 in-lb/radian		$(7.91 \times 10^7$ N-m/radian)
Mode	Spar-shell	Monocoque	Minimum Contract Requirement
1st Flatwise	2.25	2.25	2.2
1st Edgewise	4.38	4.43	3.2
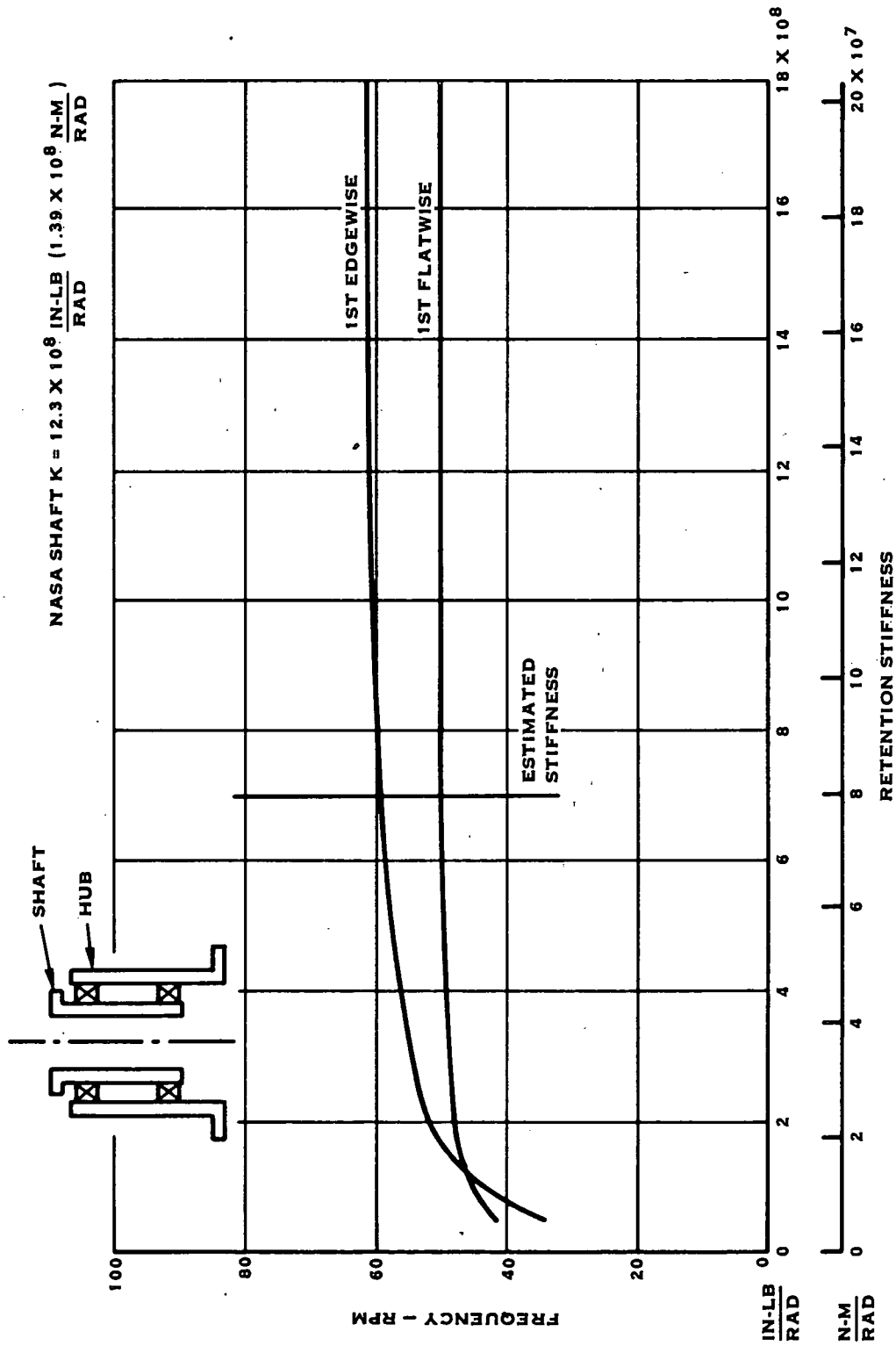
FIGURE 7. RETENTION STIFFNESS SENSITIVITY
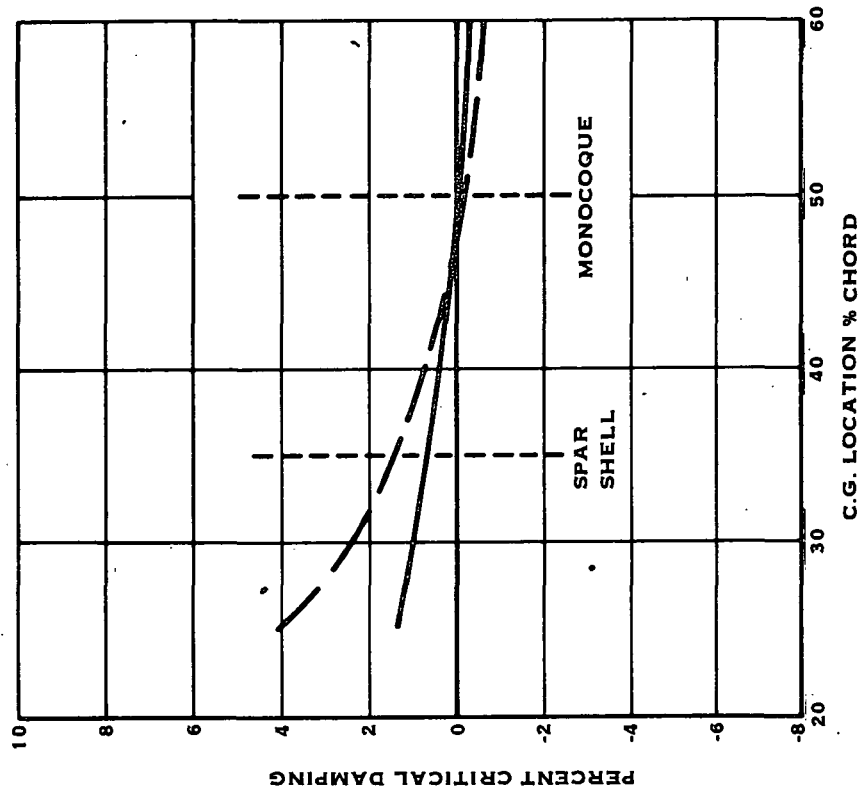
A. 18 MPH (28.96 KM/HR) WIND-RATED CONDITION
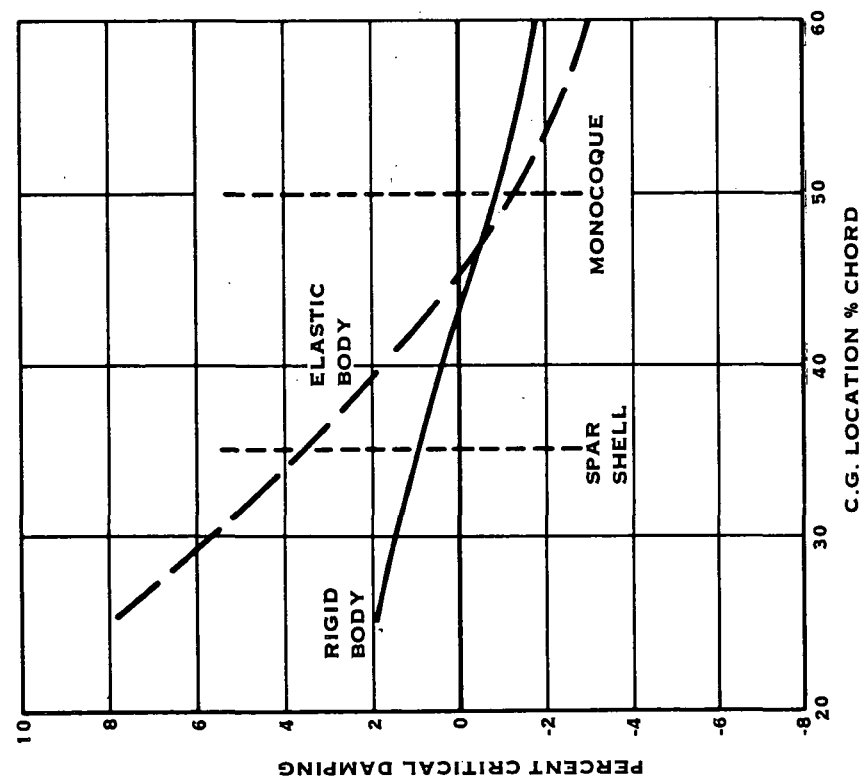
B. 80 MPH (128.72 KM/HR) WIND-FEATHERED BLADE

FIGURE 8. BLADE DAMPING CHARACTERISTICS

16
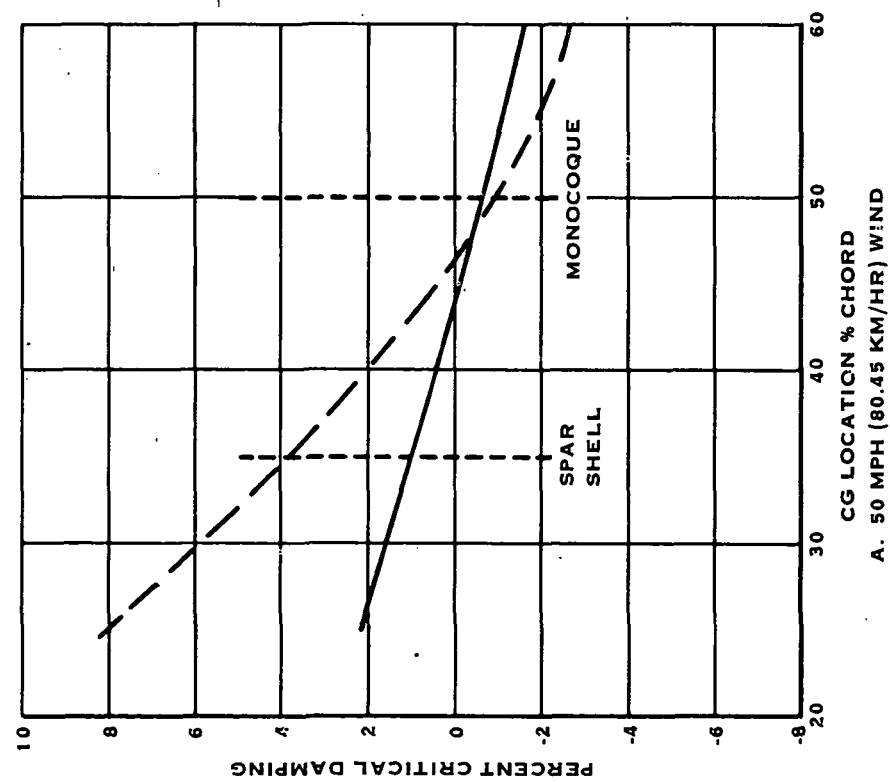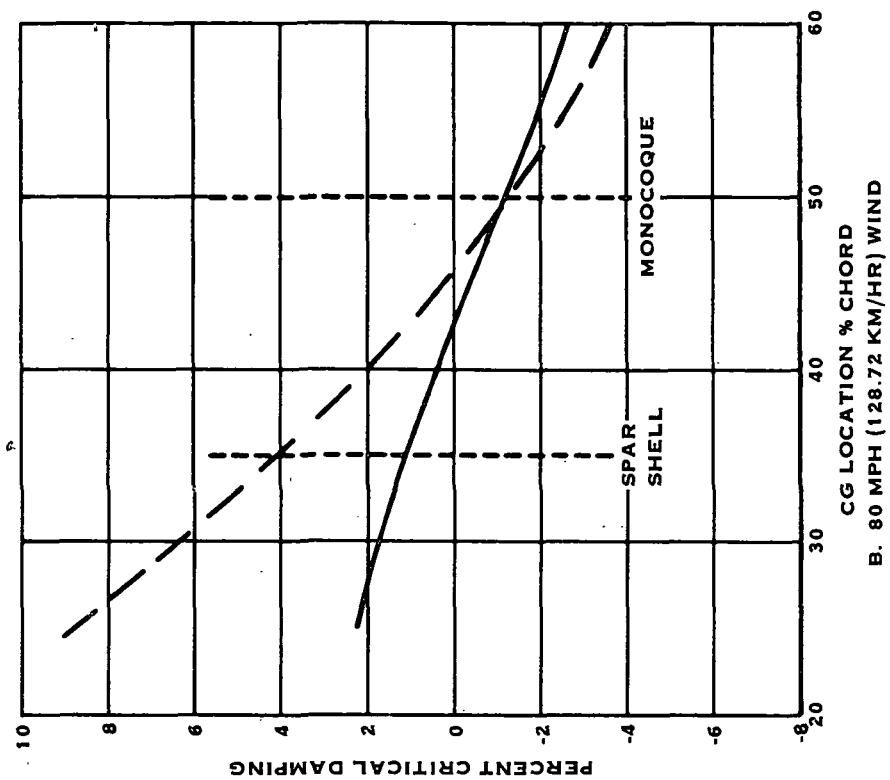
FIGURE 9. BLADE DAMPING CHARACTERISTICS
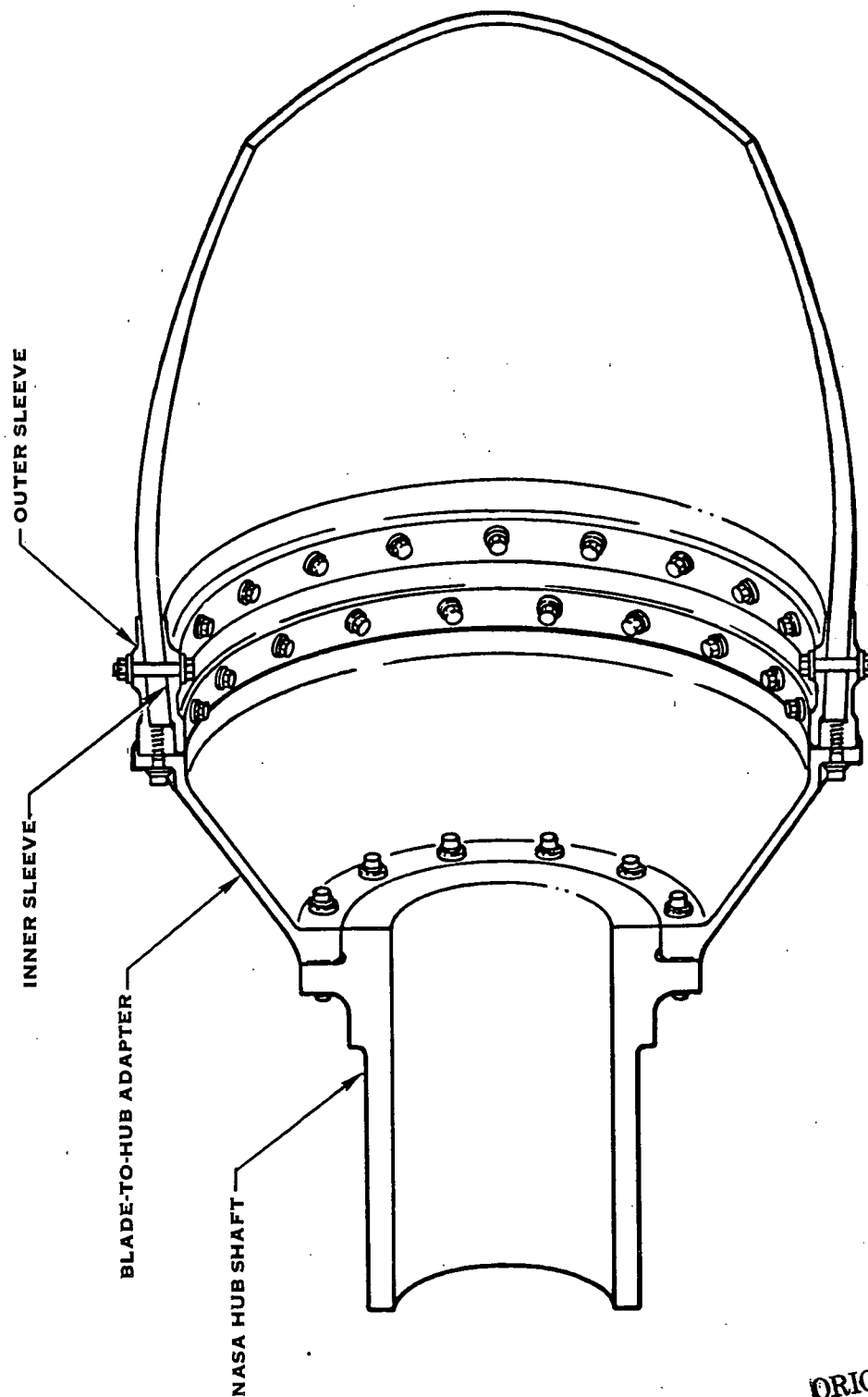
FIGURE 10.   BLADE RETENTION

OUTER SLEEVE

INNER SLEEVE

BLADE-TO-HUB ADAPTER

NASA HUB SHAFT

18

FABRICATION CONSIDERATIONS

Concurrent with the structural analysis a study of the spar/shell and monocoque blade filament winding fabrication processes was conducted with the aid of Hercules, Inc., Allegany Ballistics Laboratory. The spar/shell blade requires a multi piece spar mandrel and a multi piece shell former. The monocoque blade requires a multi piece mandrel, an inboard shell former, and a trail edge cover former. The spar/shell blade is fabricated by winding the thick walled structural spar, assembling the shell formers, winding the relatively thin shell and curing the entire structure to create the aerodynamic contour with no subsequent operations. The monocoque blade is wound as a single aerodynamic structure with constant wall thickness across the chord at each cross section. Separate precured trailing edge caps and inboard shells are bonded to the main structure to provide the desired aerodynamic shape.

Machining for and installation of the retention hardware is common to both blade designs.

SELECTION FOR DETAILED DESIGN

At the completion of the design study the spar/shell blade was selected for detailed design. Table II presents items contributing to the selection of the spar/shell design. As can be seen, the structural capacity, blade twisting moment, and actuator capacity per blade are equal. Selection was based on positive damping and lower weight for the spar/shell blade. The selected design and rationale for the selection were formally presented to NASA on April 14, 1976 and approval to proceed with the detailed design of the spar/shell blade was provided by NASA on April 20, 1976.

DETAILED DESIGN

The design philosophy established for the detailed design phase was to design a maximum capacity blade within the imposed weight and schedule limitations. This resulted in the blade design shown in Appendix B, which had the following characteristics:

1. Structural capacity for all specified load conditions.

2. Unlimited life up to 30 mph (48.27 km/hr) wind velocity.

3. Critical speed requirements met.

4. Large stability margin.

5. Weight of 2277 pounds (1032.8 kg).

6. Compatible with filament winding method of fabrication.

19

Table III shows the blade weight breakdown for the preliminary design and final design spar-shell blades.

TABLE II
DESIGN STUDY BLADE COMPARISON

	Spar-Shell	Monocoque
Total Weight	2083 lb	2240 lb (1016.1 kg)
Adapter & Misc.	680 lb (308.4 kg)	680 lb (308.4 kg)
Structural Capacity	120,000 ft-lb (162720N-m)	120,000 ft-lb (162720N-m)
Blade Twisting Moment	60,000 in-lb (678N-m)	60,000 in.-lb (6780N-m)
Actuator Capacity/Blade	171,600 in-lb (19391N-m)	171,600 in.-lb (19391N-m)
Stability	Positive damping	Negative damping
C.G. Location	35% of chord	50% of chord

TABLE III
SPAR-SHELL BLADE DESIGN WEIGHT BREAKDOWN

	Preliminary	Final
Spar and Shell	1470 lb (666.8 kg)	1470 lb (666.8 kg)
Retention Rings	260 lb (117.9 kg)	260 lb (117.9 kg)
Adapter and Bolts	236 lb (107.1 kg)	236 lb (107.1 kg)
Balance Weights	45 lb (20.4 kg)	45 lb (20.4 kg)
Spar Support	- -	194 lb (88.0 kg)
Paint	36 lb (16.3 kg)	36 lb (16.3 kg)
Tip and Root Closures	11 lb (5.0 kg)	11 lb (5.0 kg)
Lighting Protection	25 lb (11.3 kg)	25 lb (113. kg)
	2083 lb (944.8 kg)	2277 lb (1032.8 kg)

AERODYNAMIC ANALYSIS

Only minor changes were made to the aerodynamic shape generated during the design study. They were to decrease the thickness ratio and increase the width ratio in the inboard 25% of the blade. This was done to simplify the inboard spar transition tooling and to facilitate both spar and shell mandrel removal. Figure 11 shows the final blade geometry in terms of chord width to diameter ratio, thickness to chord width ratio and twist distribution. These changes did not effect the performance of the blade and the rated power available at the rotor with an 18 mph (28.96 km/hr) wind speed remained at 139 kW.

BLADE GEOMETRY

The blade construction consisted of four major elements: spar, shell, spar support, and blade-to-hub adapter as shown in Figure 10.

Spar

The spar was the main load carrying element of the blade design. This spar was basically "D" shaped, fabricated from filament wound fiberglass, hollow with tapered wall thickness and cross section and was constructed with no joints. The use of the filament winding process allowed for varying the spar and shell wall thicknesses and fiber orientation as shown in Figures 12 and 13. This flexibility provided a means of optimizing the blade section properties of strength and stiffness along the blade. This approach provided a superior balance of material properties in all directions with good interlaminar and translaminar shear characteristics and provided the capability of taking predicted and unanticipated loads. The shank of the blade included steel inner and outer adapter sleeves. The spar was wound over the inner sleeve and the outer sleeve was bonded to the spar. Shear bolts were bonded around the rings at two radial locations to provide redundancy. The blade loads were transferred from the spar to the steel rings by either shear across the adhesive joints or through the shear bolts.

Shell

The blade aerodynamic shape was formed by filament winding fiberglass directly over the spar forming a monolithic structure, effectively eliminating any structural joints. This approach transfers aerodynamic loads to the spar continuously along its entire length. The shell properties were not a significant contributor to establishing the overall blade properties for frequency placement. The shell ending was cut off at a 45° angle to allow the shell loading to spread as it was transferred to the spar. The closure was comprised of two foam bulkheads and a fiberglass cover.
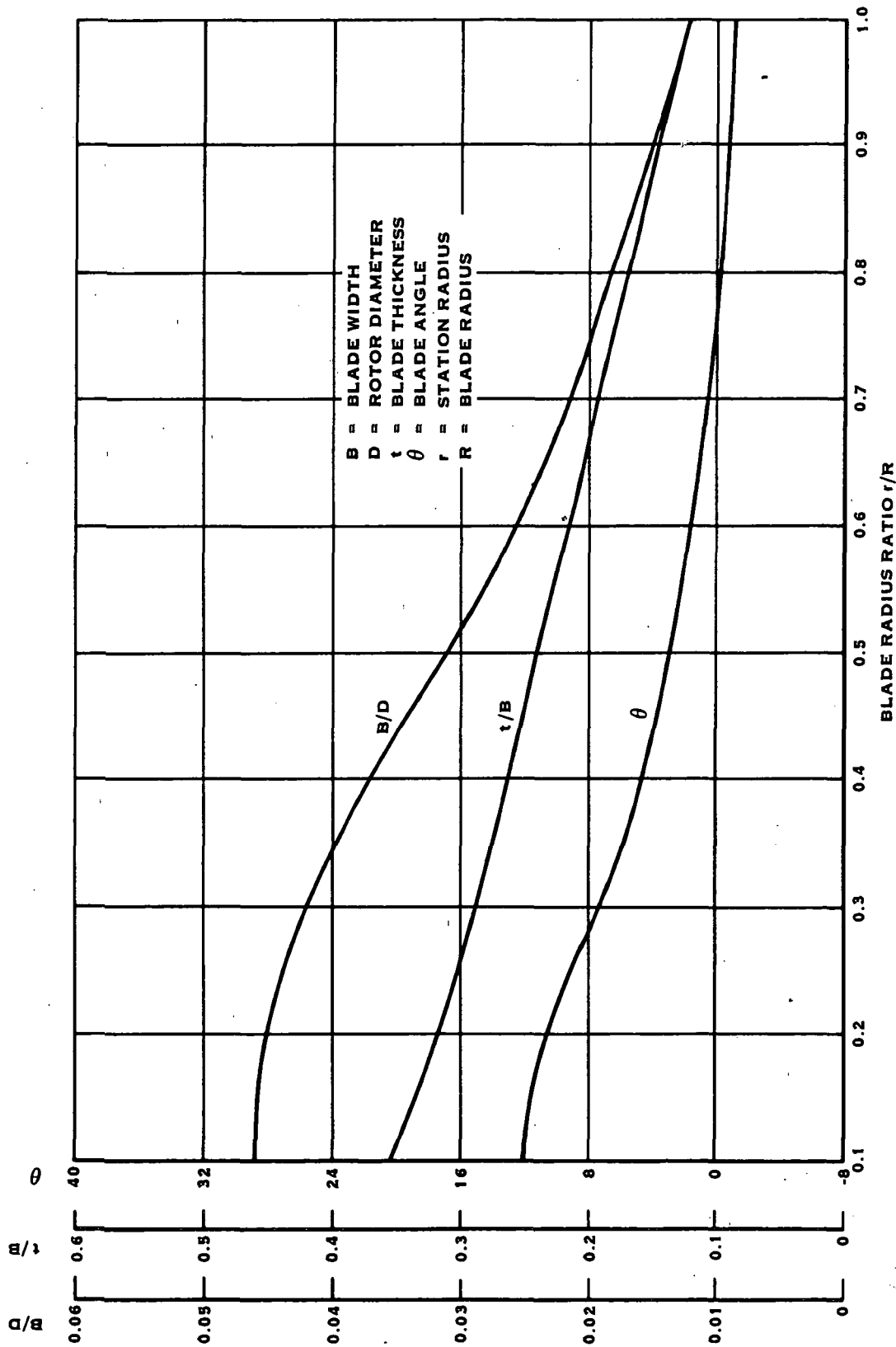
FIGURE 11. FINAL AERODYNAMIC DESIGN

22
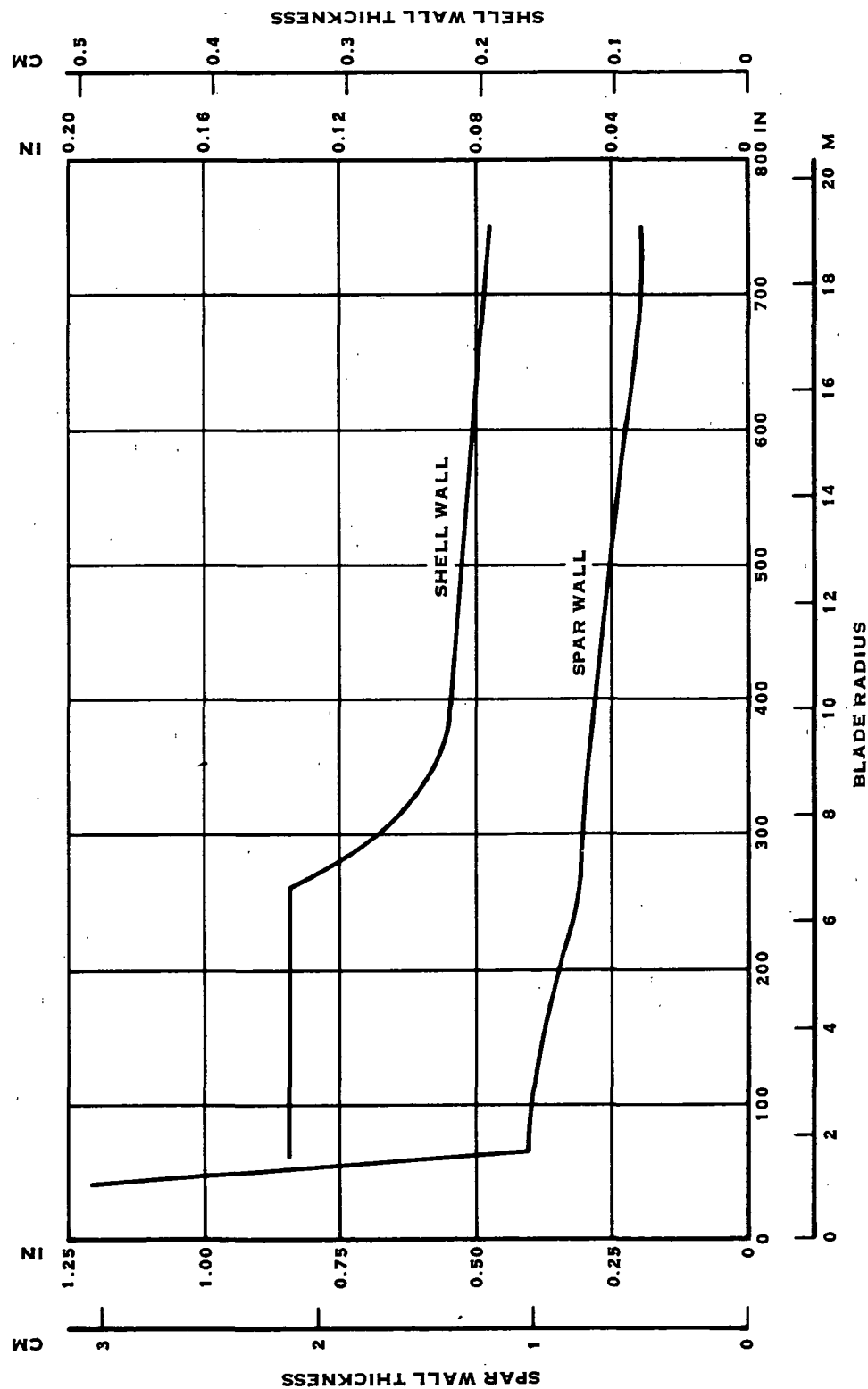
FIGURE 12. BLADE WALL THICKNESSES
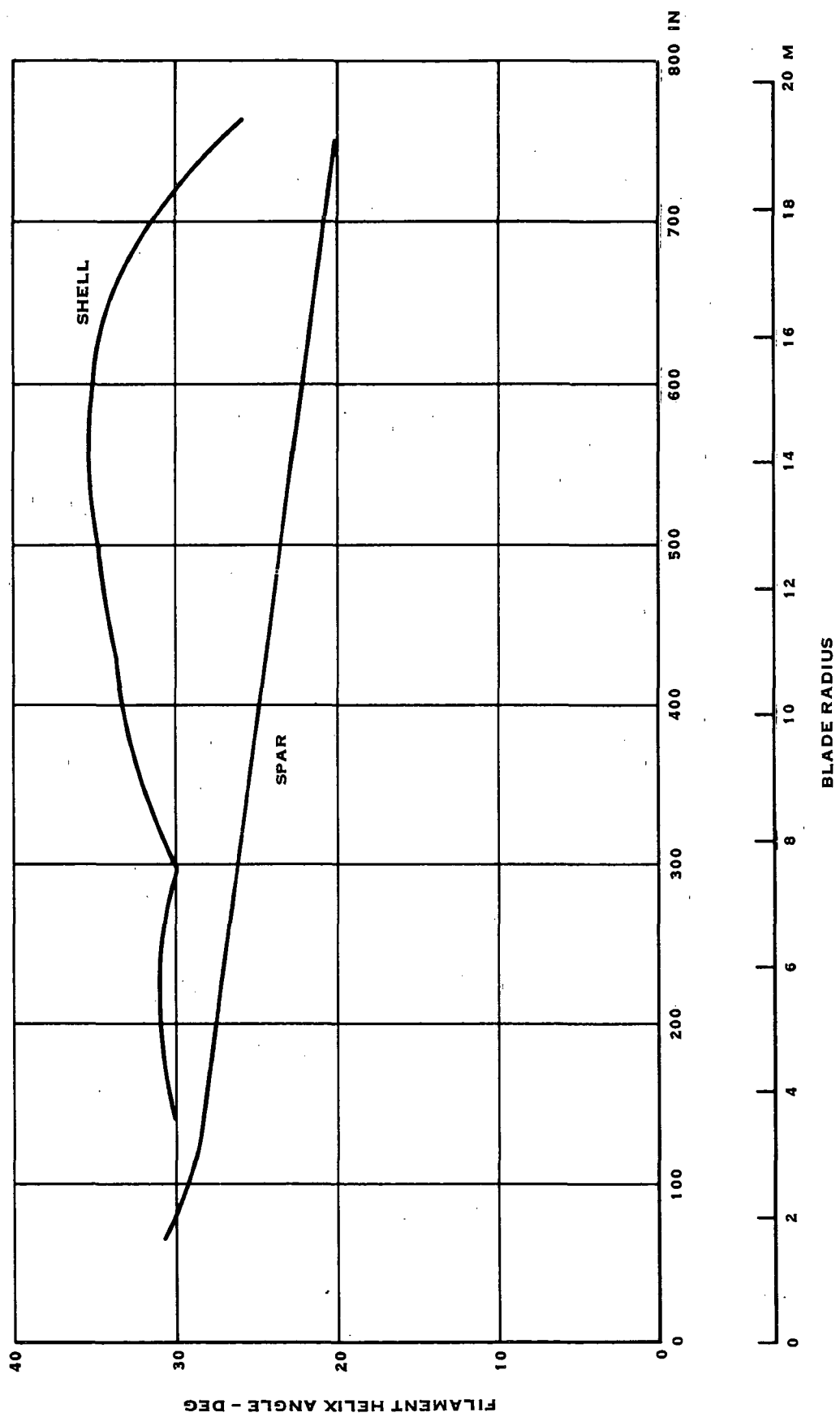
FIGURE 13. BLADE FILAMENT ORIENTATION

Spar Support

The spar supports were composite beams composed of foam and fiberglass panels. Typical bulkhead cross-sections at three stations are shown in Figure 14. The fiberglass panels raised the blade buckling capacity to a level above the highest buckling load the blade was expected to experience in service. The foam panels provided the necessary buckling capacity for the fiberglass panels. This support concept produced a blade with maximum buckling capacity for minimum weight increase.

Blade-to-Hub Adapter

The steel conical blade-to-hub adapter provided the connection between the blade adapter sleeves and the existing rotor hub hardware. Production rotor hardware could be designed to eliminate need for this part.

STRUCTURAL ANALYSIS

The structural design criteria used for the detailed design were (1) smooth airfoil loadings as discussed in the Design Study portion of this report, (2) 100% tower shadow over an 18° azimuthal arc, and (3) two percent (2%) structural damping.

The blade was analyzed for the load cases shown in Table IV using Hamilton Standard computer program G400. G400 is a single blade helicopter program which has been modified for wind turbine analysis (i.e. gravity vector altered for horizontal shaft machine). The principal characteristics of the program are as follows:

1. Constant rotor RPM.

2. Rigid shaft or prescribed hub motion.

3. Blade modeled as an elastic coupled beam.

4. Section center of gravity and aerodynamic center noncoincident with twist axis - values are independent and variable with spar.

5. Modal analysis with a maximum of four (4) flatwise, three (3) edgewise and three (3) torsion uncoupled blade modes.

6. Dynamic stall data.

7. Multiharmonic and/or Glauert momentum inflow - variable spanwise.

STA-525.00 (13.33M)

STA-345.00 (8.76M)

FIBERGLASS

FOAM

SPAR SUPPORT

SPAR

SHELL

STA-75.00 (1.90M)
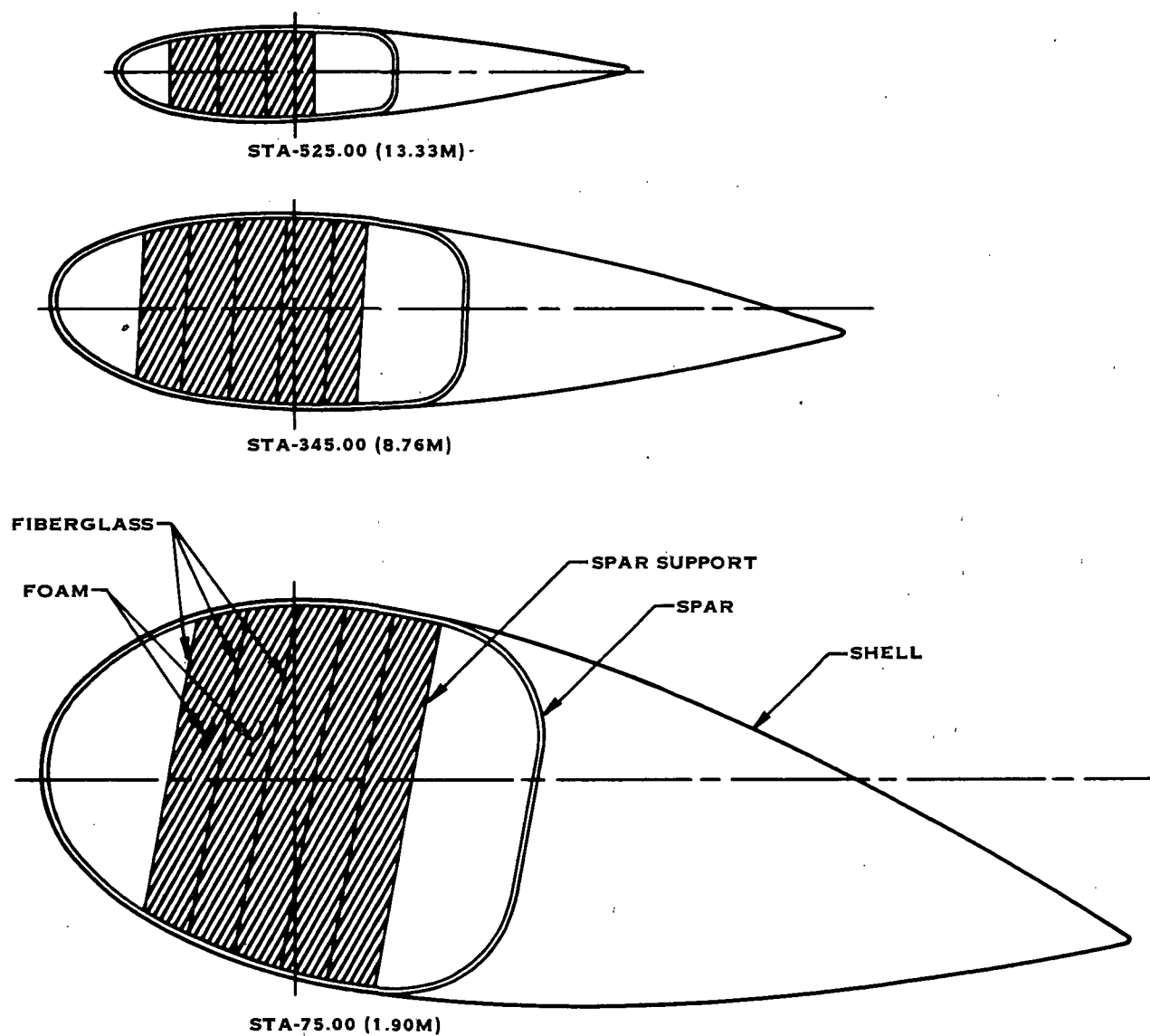
FIGURE 14. SPAR SUPPORT CROSS SECTIONS

26

TABLE IV
BLADE DETAILED DESIGN CONDITIONS

Case 1:   A wind velocity of 18 mph (28.96 kn/hr) occurs 100 ft (30.48M) above ground level. The rotor produces 133 kW of power (no losses) at 40 rpm. The rotor blades shall be capable of operating for 10,000 hours minimum for this design condition.

Case 2:   With the rotor blades set to operate for Case 1, the wind velocity increases to 36 mph (57.92 km/hr) in 0.25 sec. No change in blade pitch angle occurs. The rotor speed increases to 56 rpm.

Case 2a: With the rotor blade pitch angle set to produce 133 kW of power (no losses), the wind velocity is at 45 mph (72.40 kn/hr) and the rotor speed at 40 rpm, the wind velocity increases to 90 mph (144.21 kn/hr) in 0.25 sec and the rotor speed increases to 44 rpm.

Case 3:   With the rotor blade pitch angle set to operate for Case 1, the wind velocity is at 18 mph (28.96 km/hr) and the rotor speed at 44 rpm, the blade pitch angle is changed to the feathered position in 1.0 sec.

Case 4:   With the rotor blade rpm and pitch angle set to operate for Case 1, the wind velocity decreases from 18 mph (28.96 kn/hr) to 0 mph in 0.25 sec.

Case 4a: With the rotor blade pitch angle set to produce 133 kW of power (no losses), the wind velocity is at 45 mph (72.40 km/hr) and the rotor speed at 40 rpm, the wind velocity decreases to 0 rpm in 0.25 sec.

Case 5:   With the blades set and locked in a horizontal feathered position at 100 ft (30.48 M) above ground level a maximum wind velocity of 150 mph occurs. The wind direction at 150 mph may occur in any direction while the blade yaw angle remains fixed.

Case 6:   Same as Case 1 except trailing edge shell only half effective

Cases 1 and 6 are infinite life cases (10^8 cycles)

Cases 2 and 4 occur frequently during operation at 40 rpm (5×10^4 cycles)

Cases 2a, 3, 4a, and 5 are infrequent loading conditions

The basic analytical capabilities of the program are:

1. Eigensolutions: calculations of coupled frequencies and mode shapes, and of simple flutter and/or aeromechanical instabilities.

2. Time-History Solutions: calculations of transient and harmonic stresses and loads, and of nonlinear or otherwise complex flutter and/or aeromechanical instability phenomena.

3. Transient Spectral Stability Analysis: qualification of stability characteristics of transient time-history solutions using Fourier techniques.

A complete description of the analysis technique is reported in NASA Report CR2638.

The resulting shank and midblade moments and stresses for selected load cases are shown in Figures 15 through 26. Shank moments and stresses are taken at 61.5 inch (1.56 m) station and midblade moments and stresses are taken at the 350 inch (8.89 m) station. The mid blade stresses shown are the maximum radial stress across the blade chord at the 350 inch (8.89m) station.

Figures 15 and 16 show the shank and mid blade flatwise moments vs. azimuthal blade position for Case 1 steady state running with the initial position vertical upward. These curves show that the maximum and minimum moments occur at 30° and 200° azimuthal positions respectively. Figures 17 and 18 show the shank and mid blade flatwise and edgewise stresses vs. azimuthal position for Case 1 steady state running. The stresses were obtained from the moment of Figures 15 and 16 and the blade cross section properties at the shank and mid blade stations. Figure 19 shows the maximum and minimum flatwise moment vs. blade radius for Case 1. Figure 20 shows the maximum and minimum flatwise stress vs. blade radius for Case 1. Figures 21 and 22 show the shank and mid blade flatwise and edgewise stresses vs. blade azimuthal position for the 18 to 36 mph (28.96 km/hr to 57.92 km/hr) instantaneous gust without blade angle change. The figures contain one revolution of the blade preceeding the gust and the first revolution of the blade after the gust is imposed. These curves show that the maximum flatwise stress occurs at the 50° azimuthal position after the gust and the minimum flatwise stress occurs at the 200° azimuthal position before the gust. Figures 23 and 24 show the maximum and minimum flatwise moments and stresses vs. blade radius for Case 2.

Figure 25 shows the shank flatwise moment vs. blade angle for Case 3.

Figure 26 shows the shank flatwise stress vs. blade azimuthal position for Case 4 as a Case 1 steady state condition for one revolution preceeding the wind velocity decrease from 18 mph (28.96 km/hr) to 0 mph.

Figure 27 shows the flatwise and edgewise bending moments vs. blade radius for Case 2a.

28
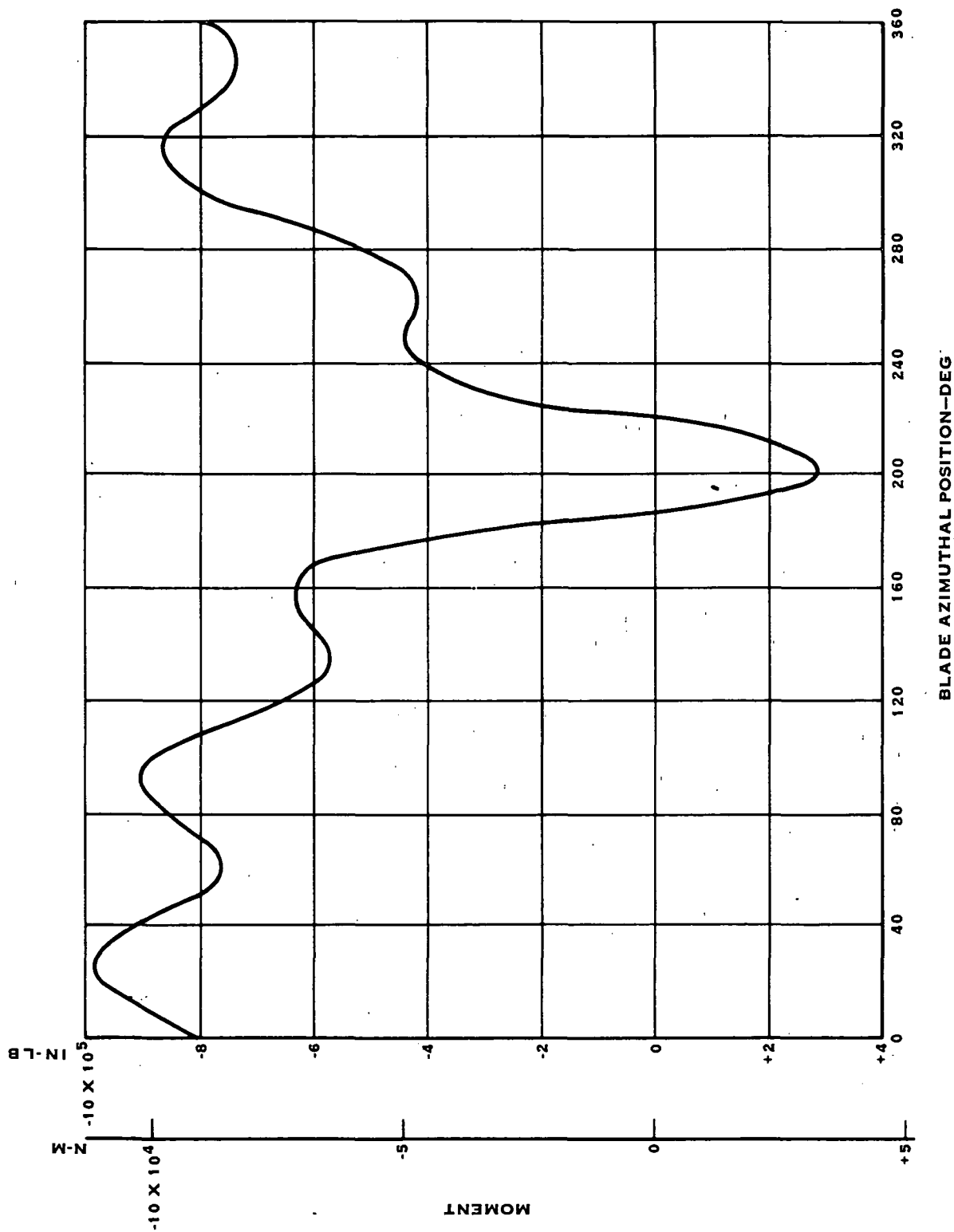
FIGURE 15. SHANK FLATWISE MOMENT – CASE 1
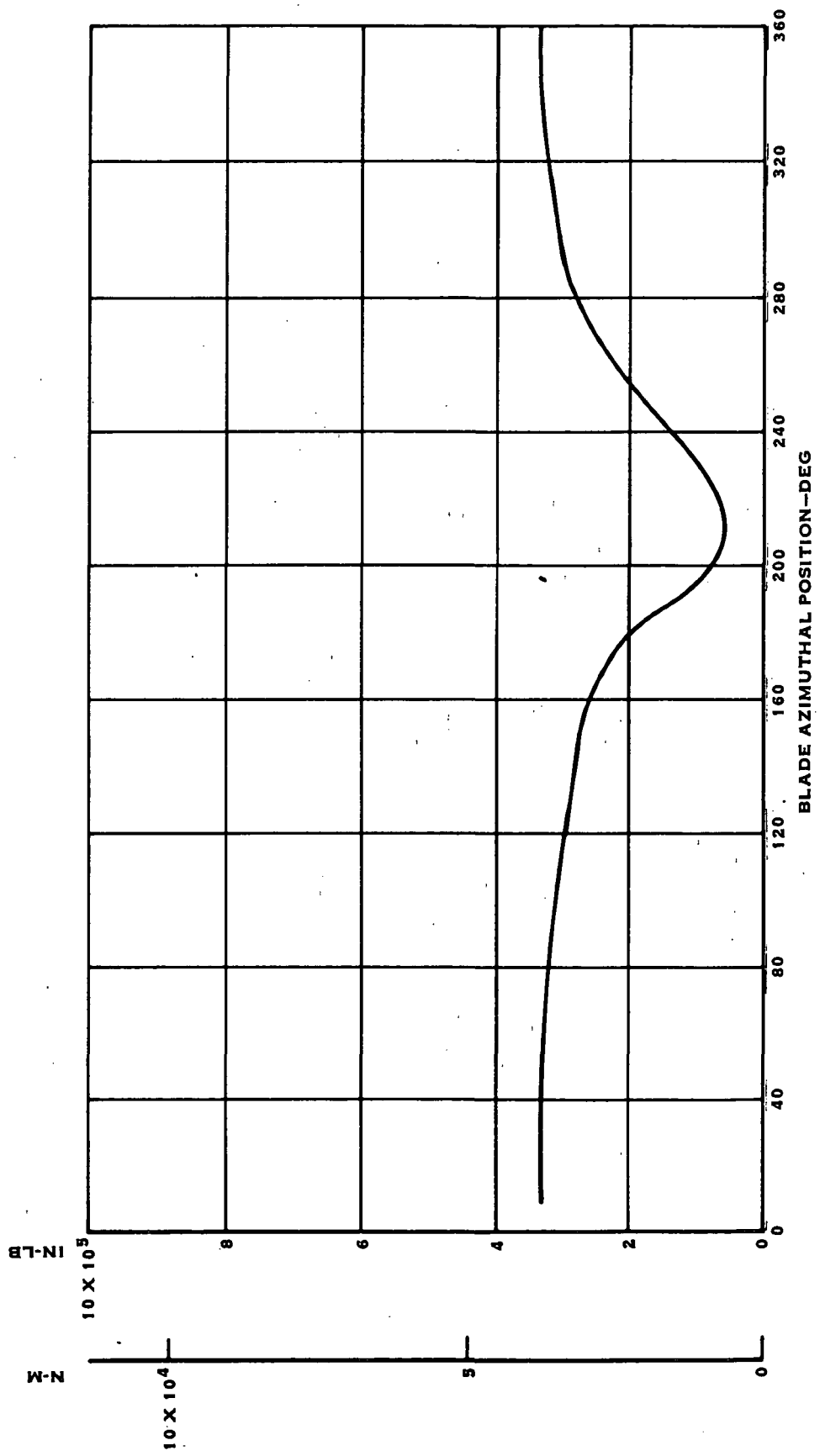
FIGURE 16. MID BLADE FLATWISE MOMENT – CASE 1
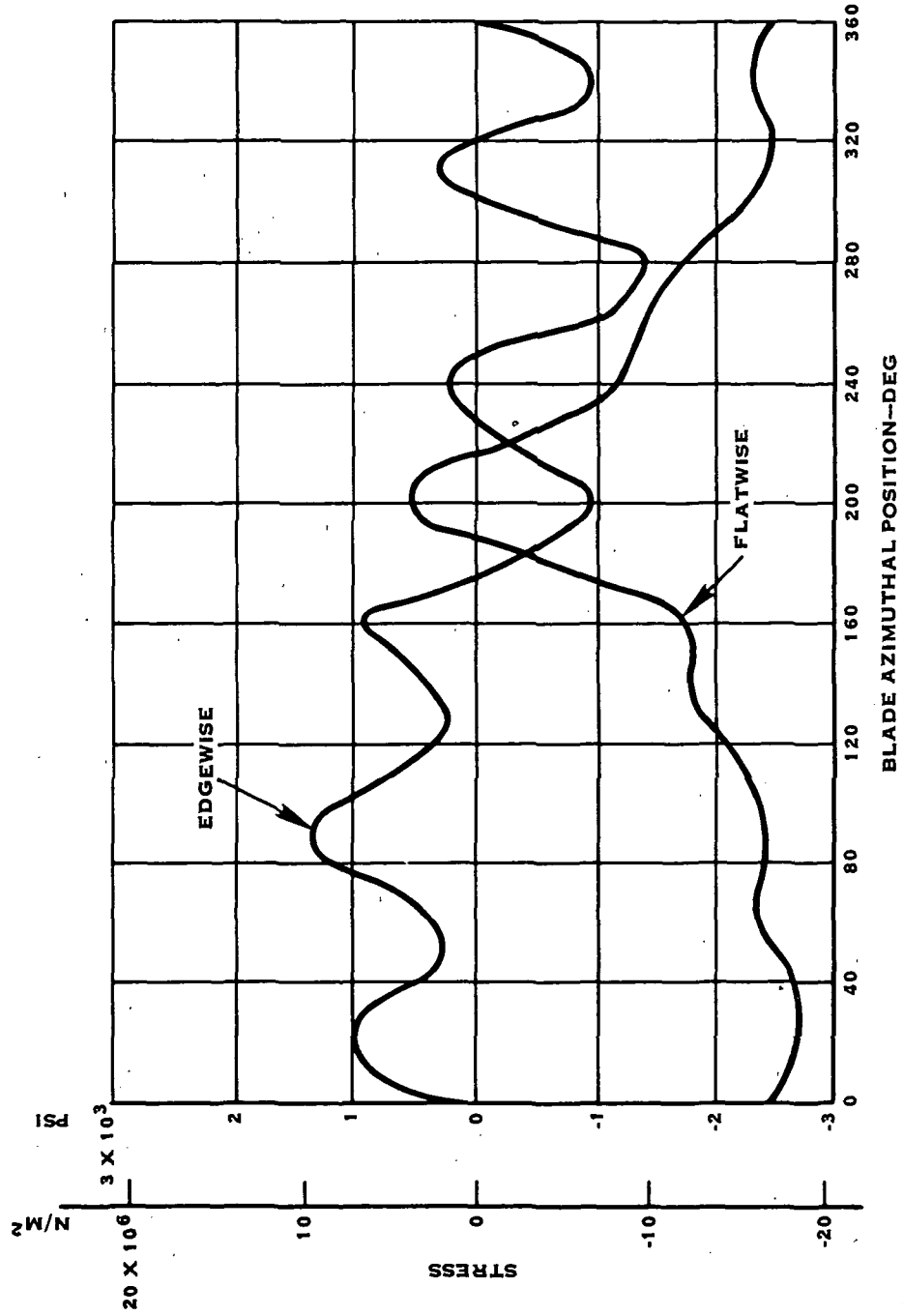
FIGURE 17. SHANK STRESSES – CASE 1
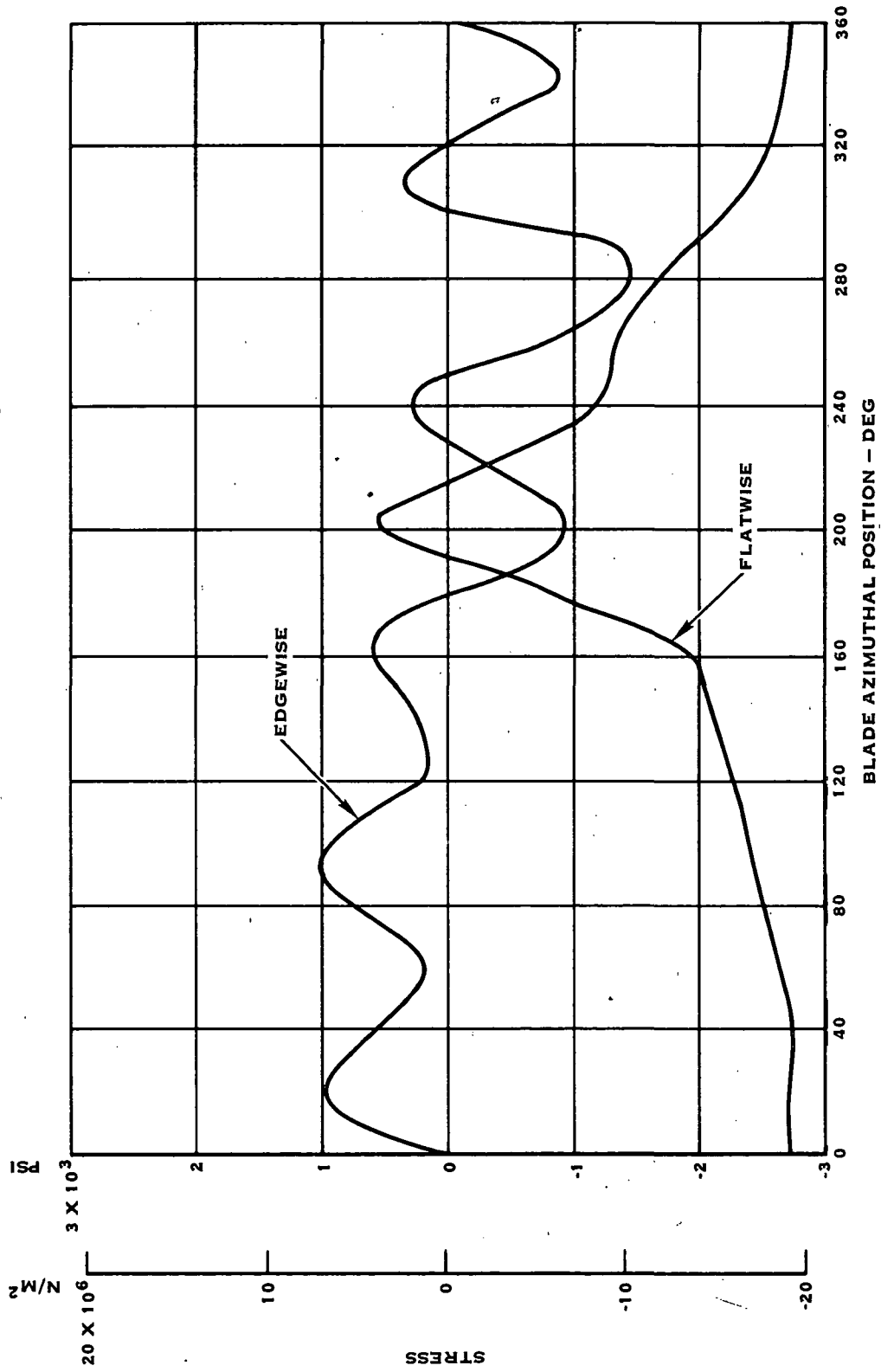
FIGURE 18. MID BLADE STRESSES — CASE 1
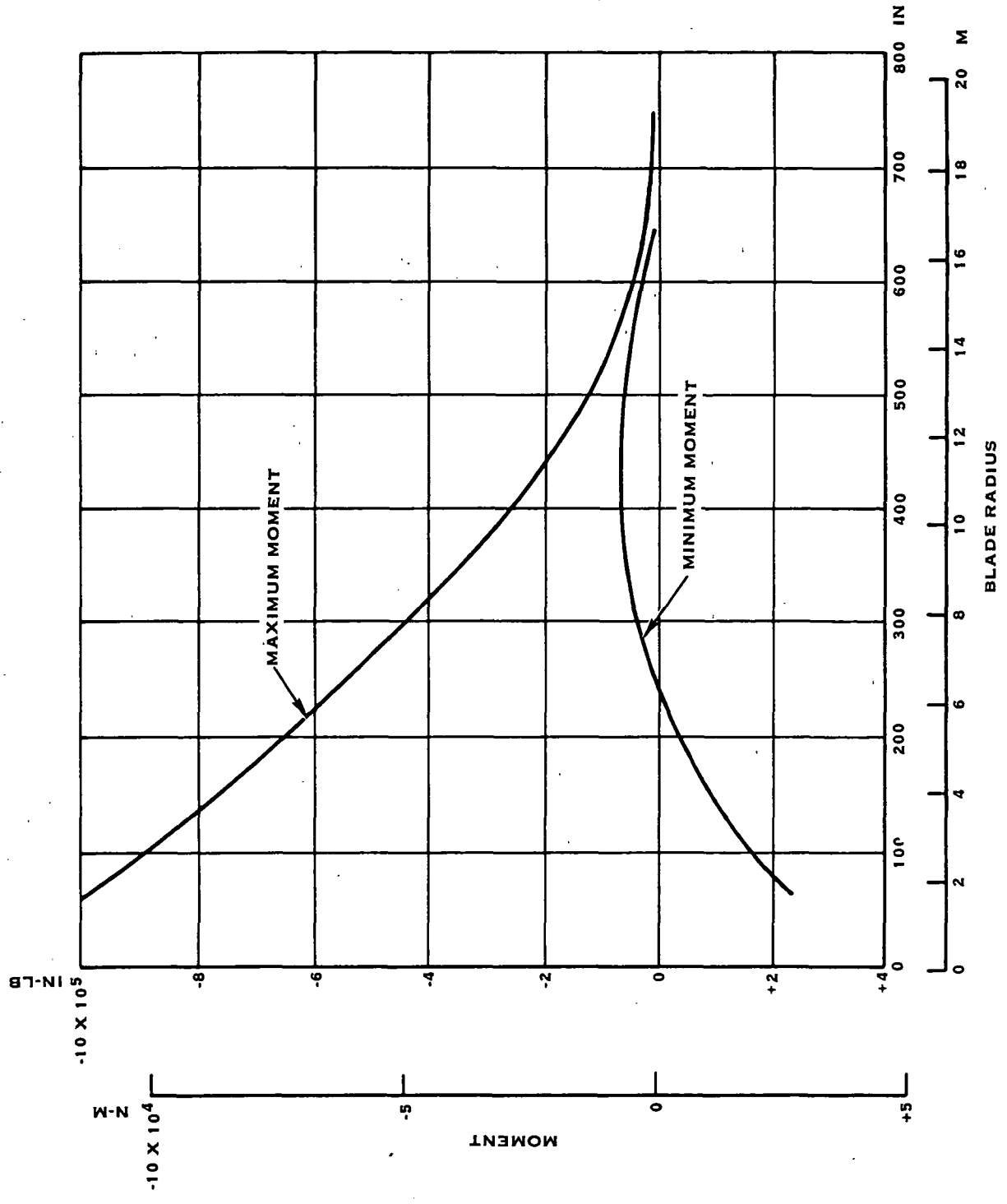
FIGURE 19. FLATWISE MOMENTS – CASE 1
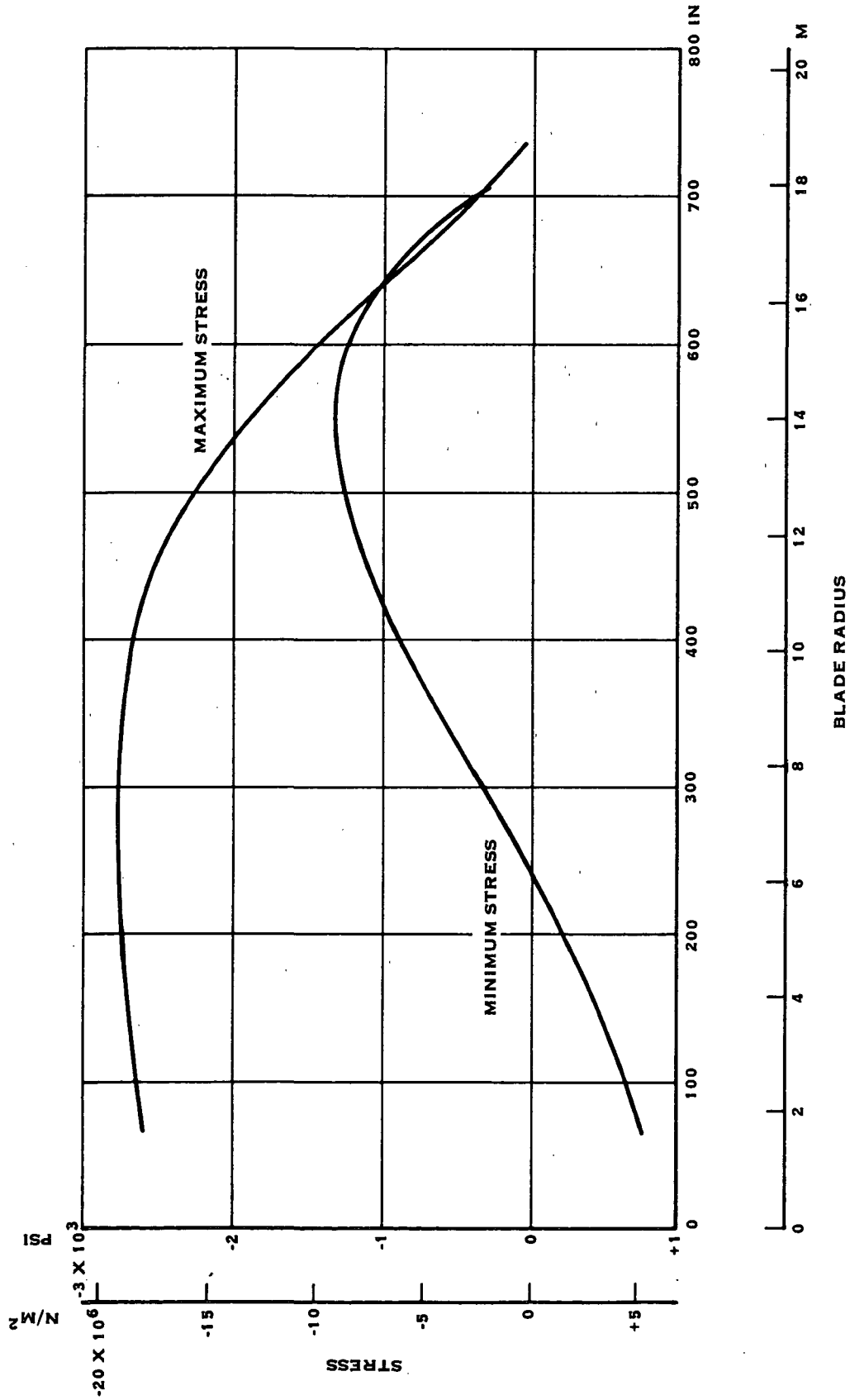
FIGURE 20. FLATWISE STRESSES – CASE 1
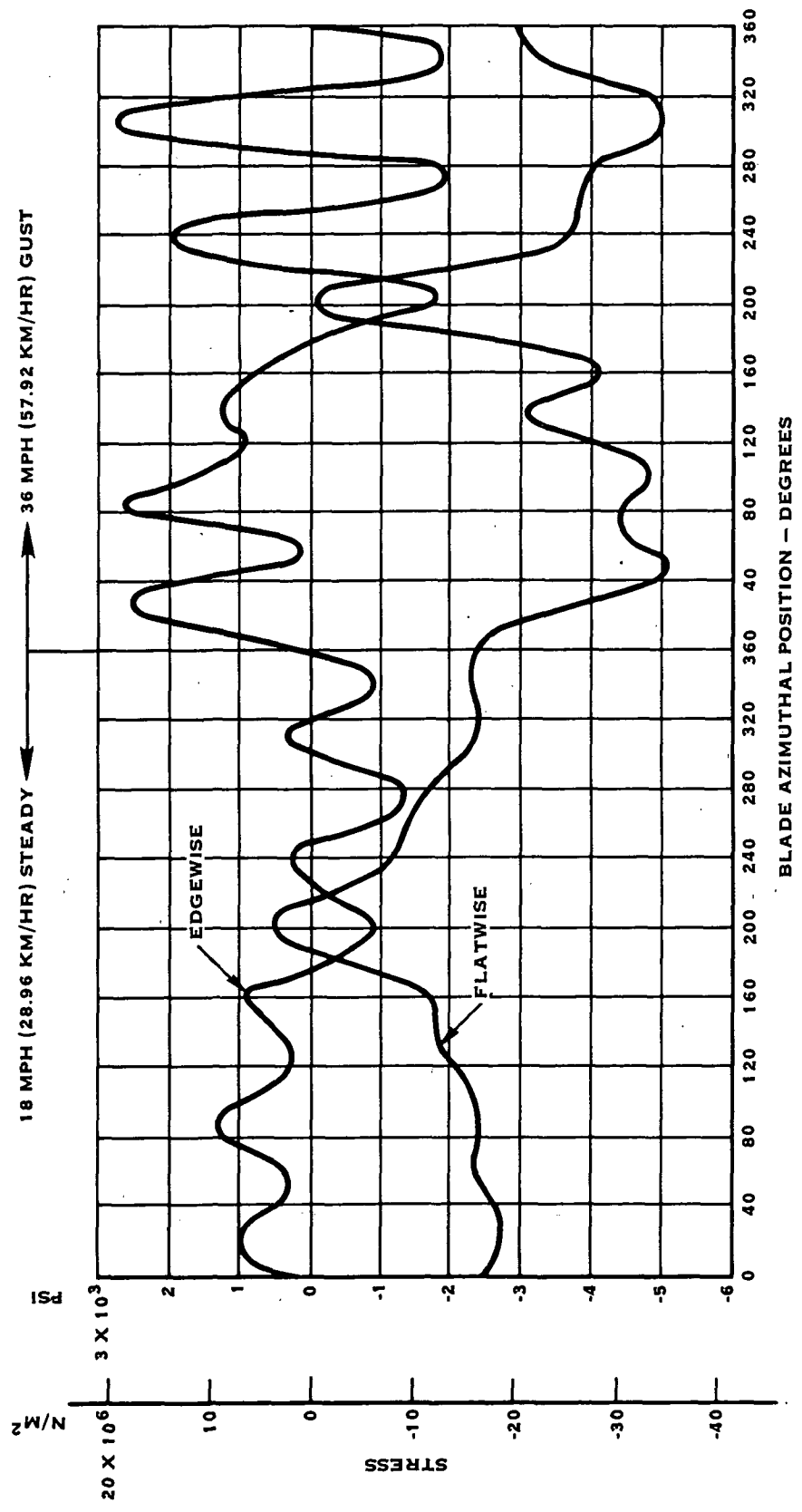
FIGURE 21. SHANK STRESSES – CASE 2
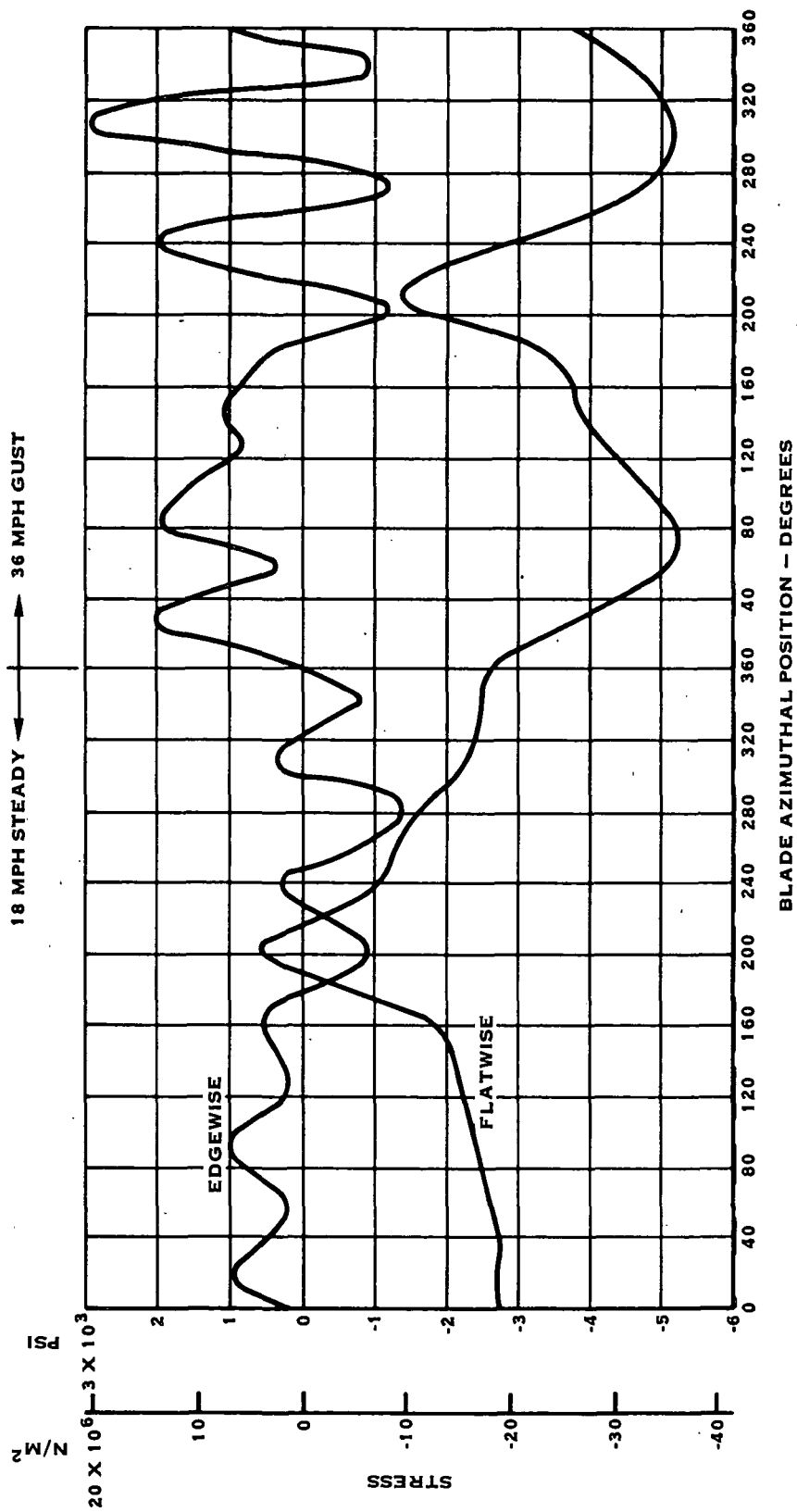
FIGURE 22. MID BLADE STRESSES — CASE 2
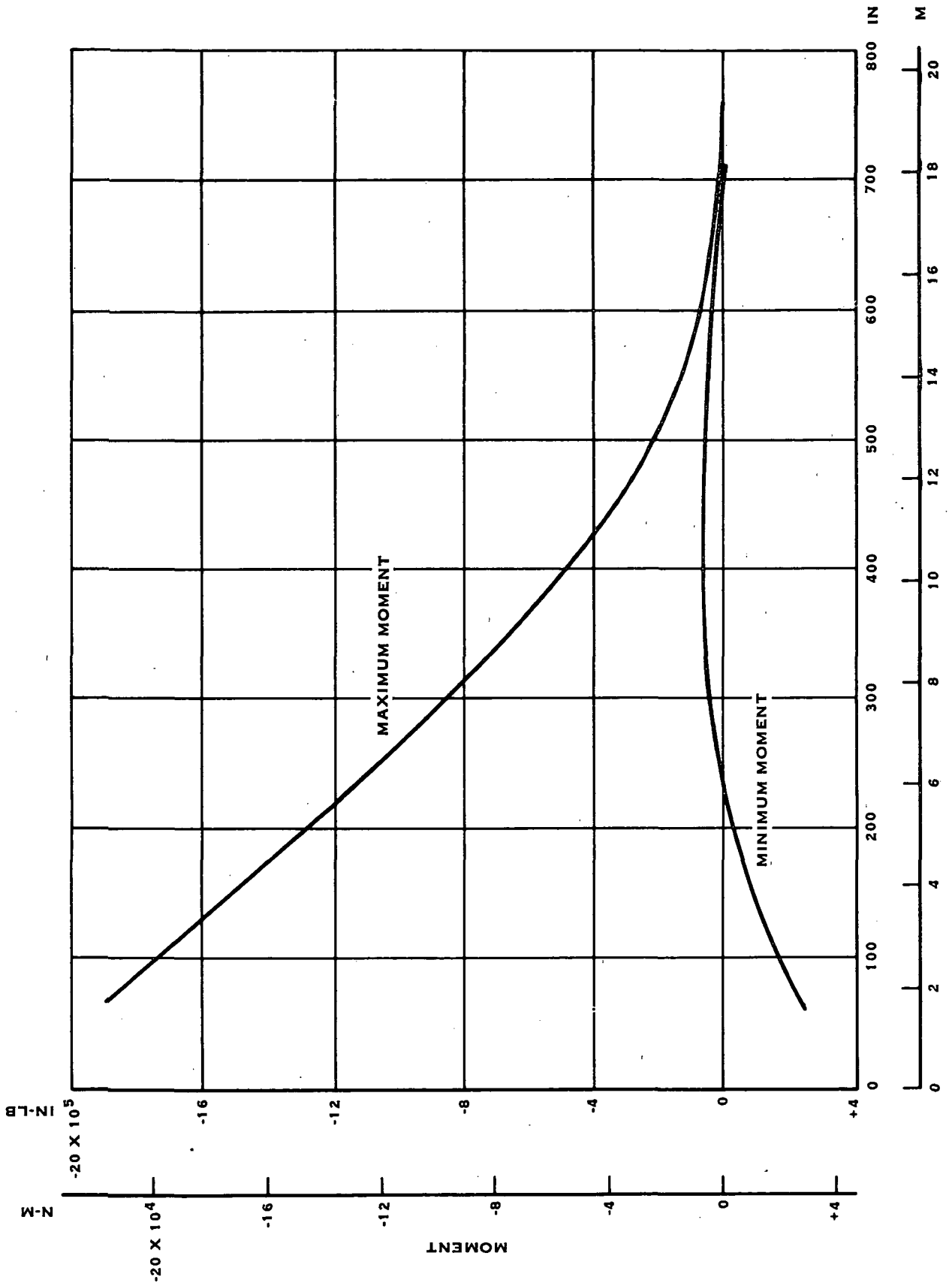
FIGURE 23. FLATWISE MOMENTS – CASE 2
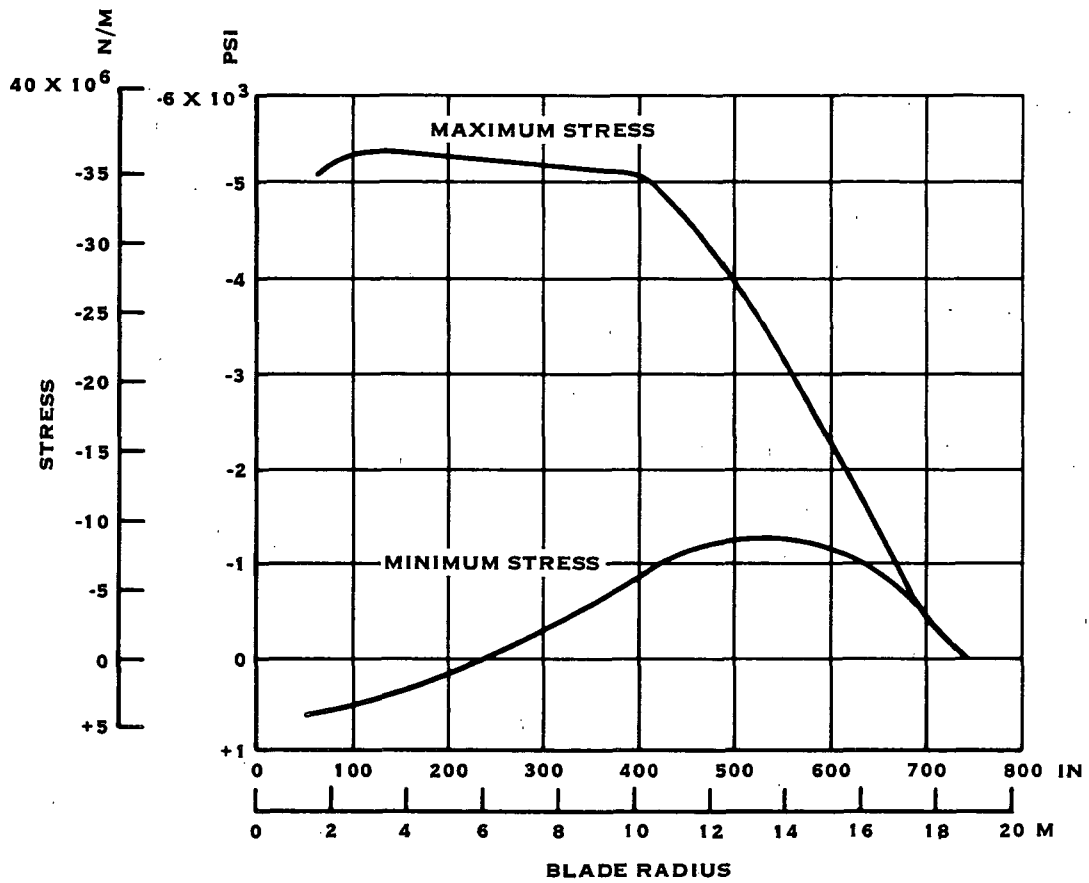
FIGURE 24. FLATWISE STRESES – CASE 2
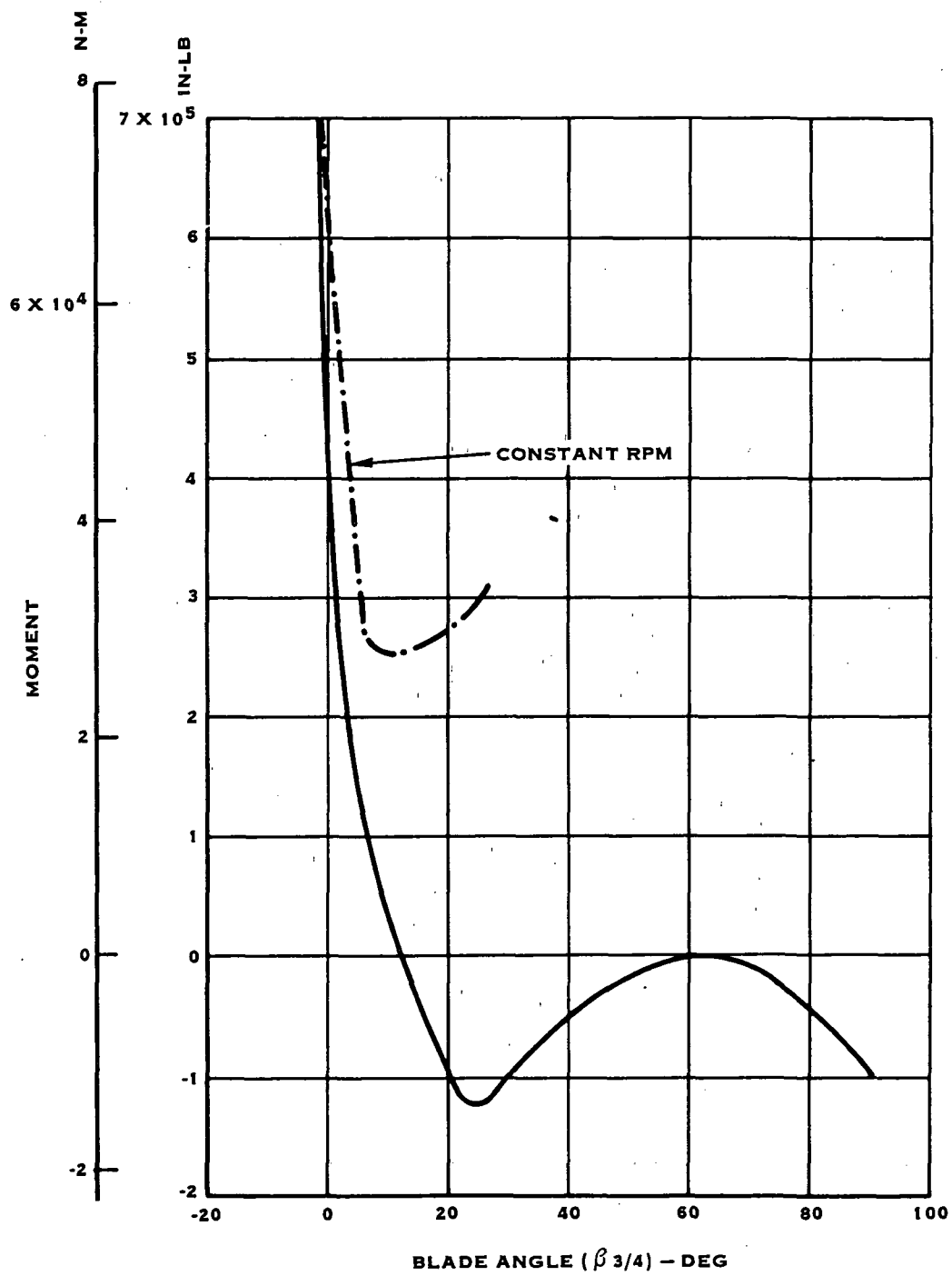
FIGURE 25. SHANK MOMENT — CASE 3
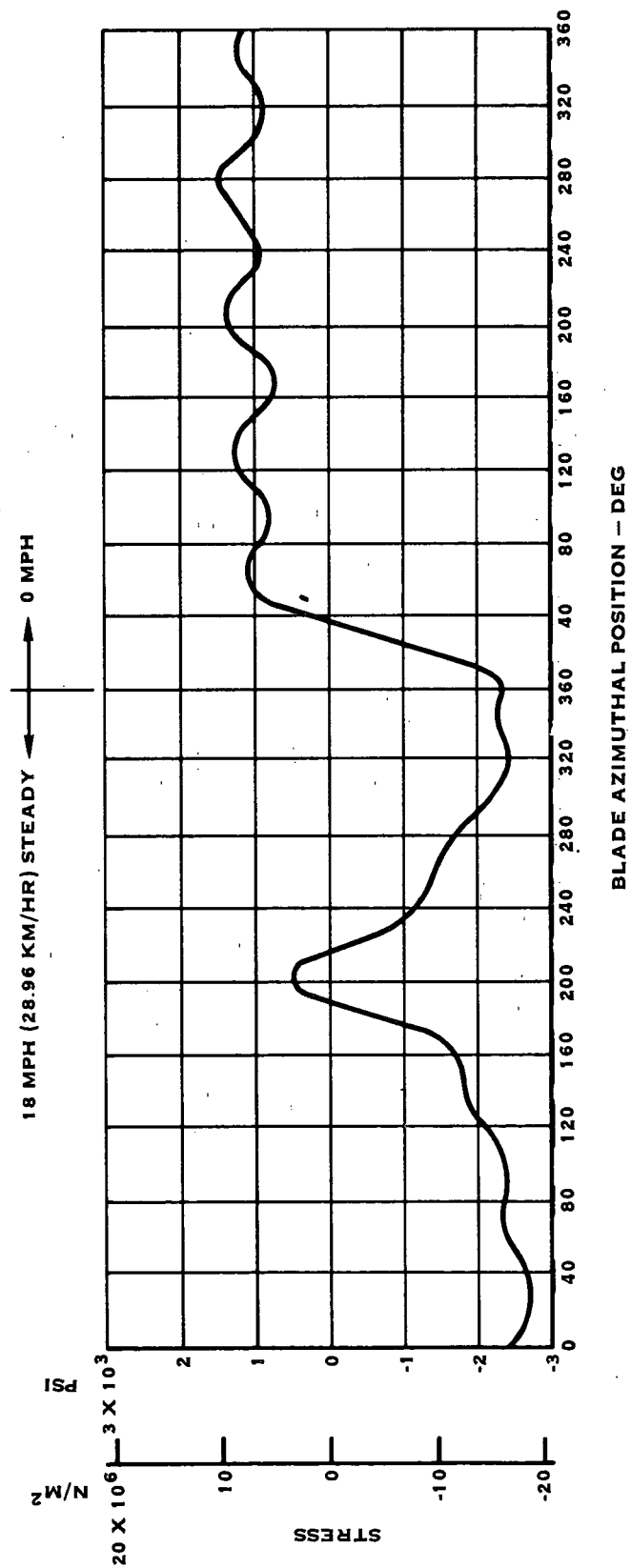
FIGURE 26. SHANK FLATWISE STRESS – CASE 4

40
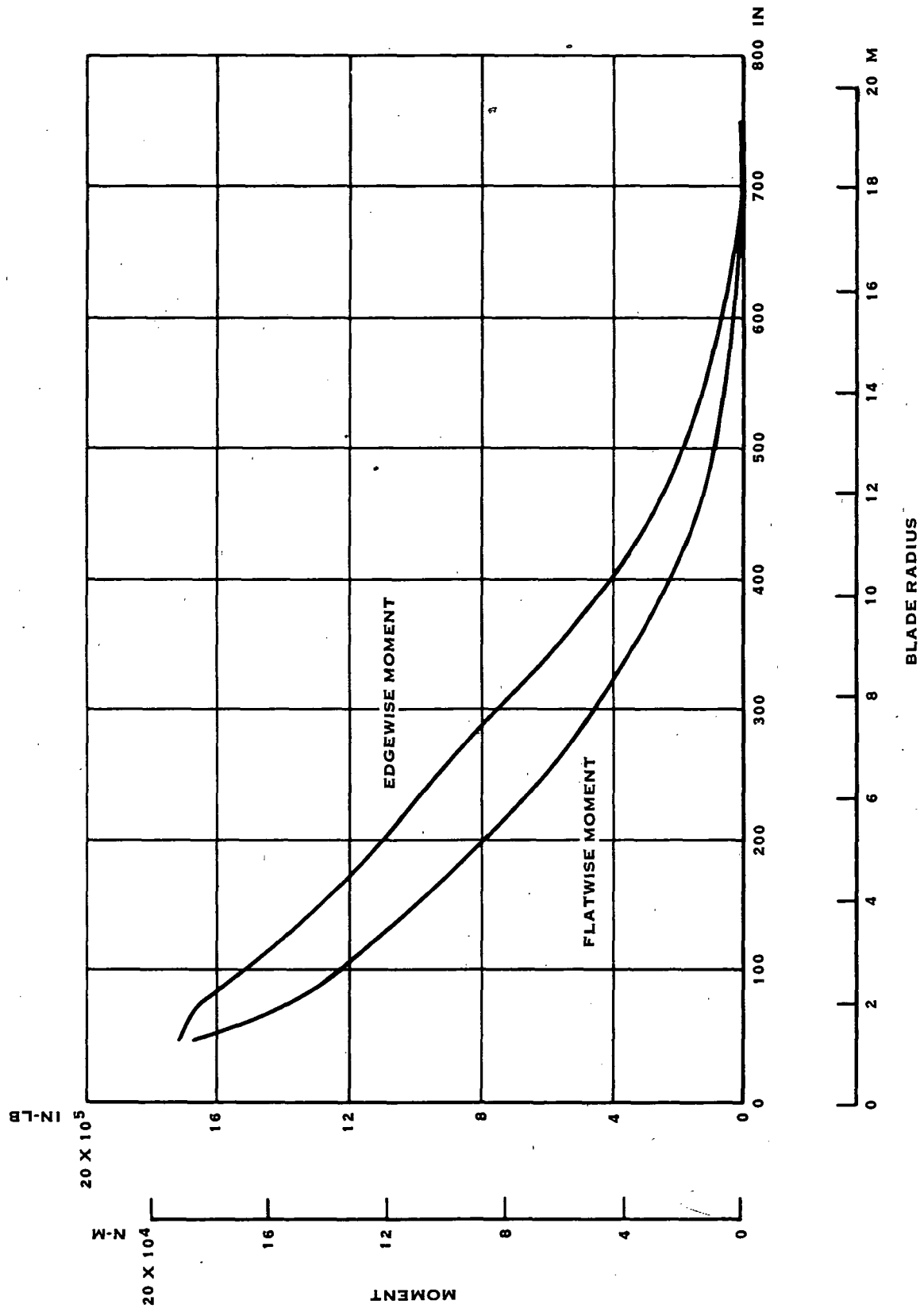
FIGURE 27. BLADE MOMENTS – CASE 2A

During the course of the design it became evident that the trailing edge shell would wrinkle under high loading conditions. A study was conducted to determine the effect on section properties, frequencies and stresses. To account for the wrinkling effect, one-half of the shell was removed for calculations of major moment of inertia, minor moment of inertia and torsional stiffness, but retained for mass calculations. Figures 28, 29 and 30 show this effect on major moment of inertia, minor moment of inertia and torsional stiffness respectively.

Mid blade stresses for the load cases of Table IV are plotted on the Goodman Diagram for the selected blade filament wound material in Figure 31. The numbers refer to the tabulated cases. Case 6 was identical to Case 1 except that blade shell wrinkling was accounted for by decreasing the section properties of the blade as explained above. Computer program G400 was run with this reduced section property blade. This explains that the stress relationship between Case 6 and Case 1 was not a stress increase by the relationship of inertias alone but also took into consideration the structural and dynamic characteristics of the blade. This curve showed that the blade met all life requirements for the load cases imposed.

The buckling capacity of the blade was examined based on Hamilton Standard established design criteria. The spar was analyzed as a flat plate with simply supported edges, the plate width was equal to the spar width at any given station and the effective plate modulus of elasticity was equal to the square root of the product of the axial and chordwise modulii. Based on this set of criteria, the allowable critical buckling stress of the spar was calculated and found to be below the predicted blade operating stress as shown in Figure 32. If the effective panel width was reduced to 70% of the total spar width the critical buckling stress was not raised sufficiently to encompass the specified loading conditions. In order to raise the critical buckling stress limit to an acceptable level a foam and fiberglass spar support was added to the blade design. Figure 32 also shows the predicted critical stress limit with the spar support included in the blade design.

The shell buckling level was determined using a finite element analysis. The shell cavity was modeled to simulate the 450 inch (11.55 meter) station as shown in Figure 33. A moment loading which would simulate 4000 psi $(27.58 \ N/M^2)$ in the spar was applied to the model and by iteration the spar moment level at which shell buckling was initiated was determined. The subsequent post buckling stress in the shell was also determined. Figures 34 and 35 show the buckled shell shape and resulting stress respectively. Figure 36 plots the resulting shell stress on the Goodman diagram for the shell material and shows that the stress levels are acceptable for infinite life.

The uncoupled bending-torsion frequencies for a blade assembly including a clamped hub, one-half effective trailing edge shell, and seven (7) pounds of tip balance weights were calculated and are shown on a Campbell diagram in Figure 37.

42
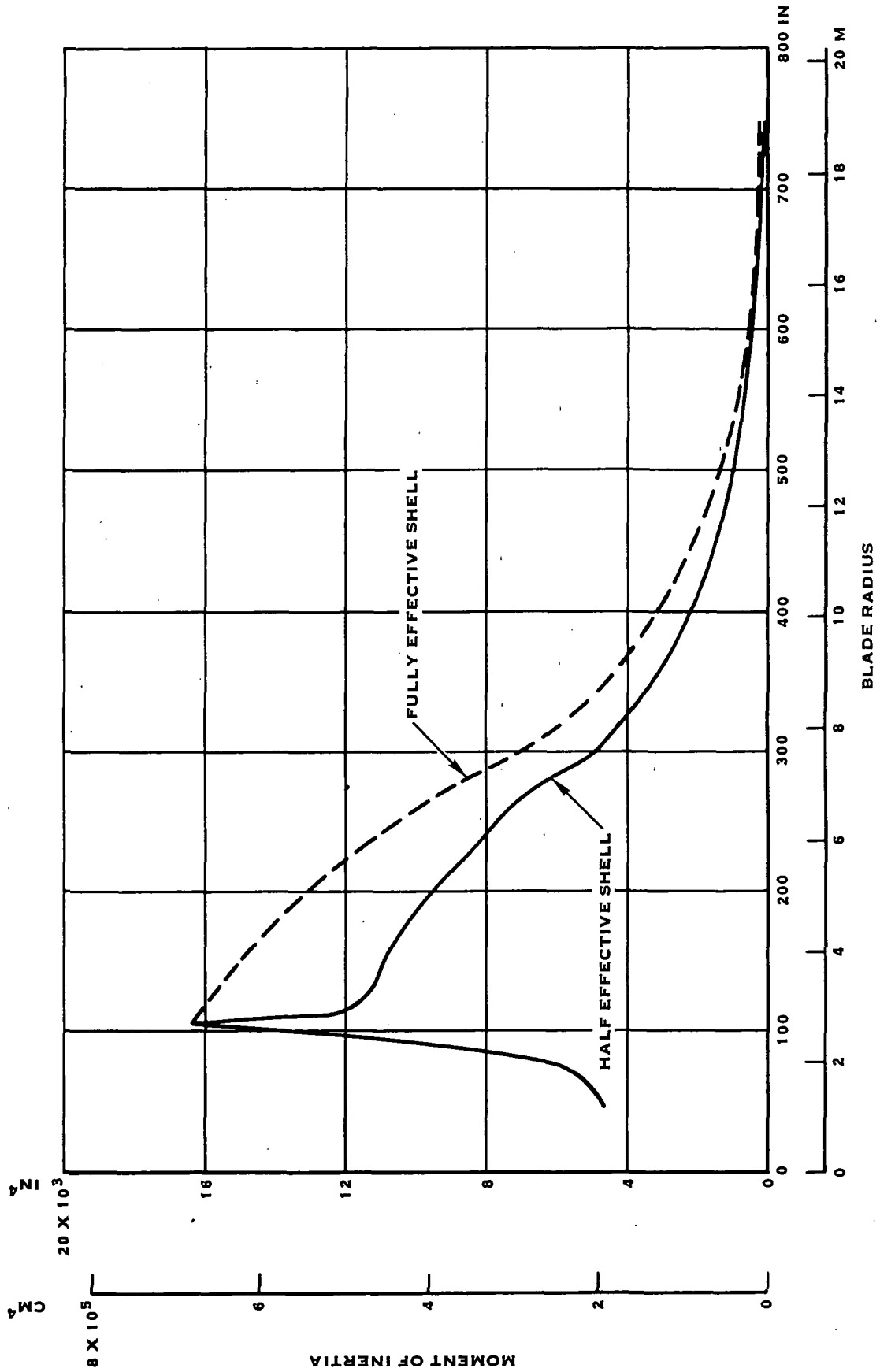
FIGURE 28. MAJOR MOMENT OF INERTIA

43
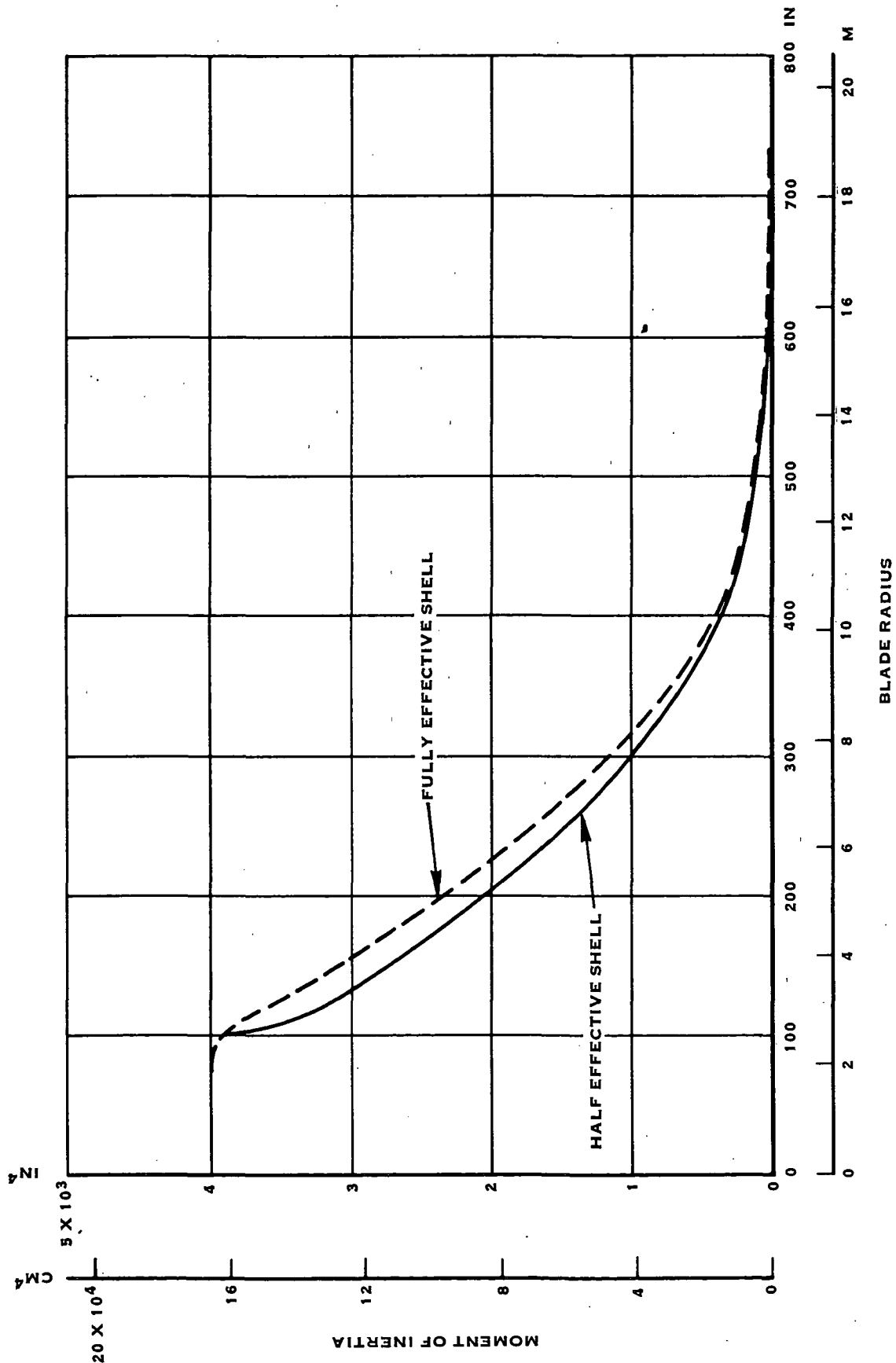
FIGURE 29. MINOR MOMENT OF INERTIA
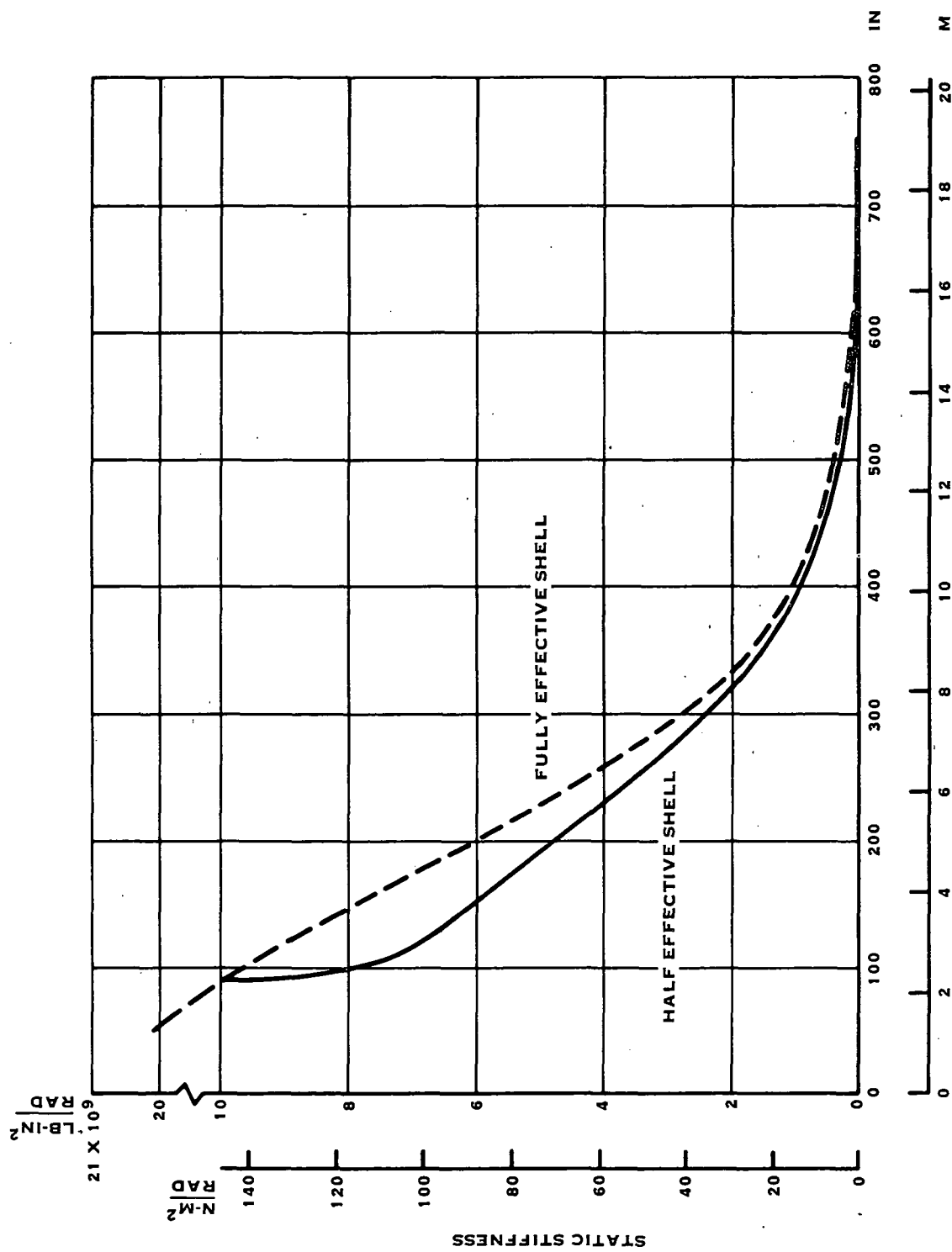
FIGURE 30. TORSIONAL STIFFNESS
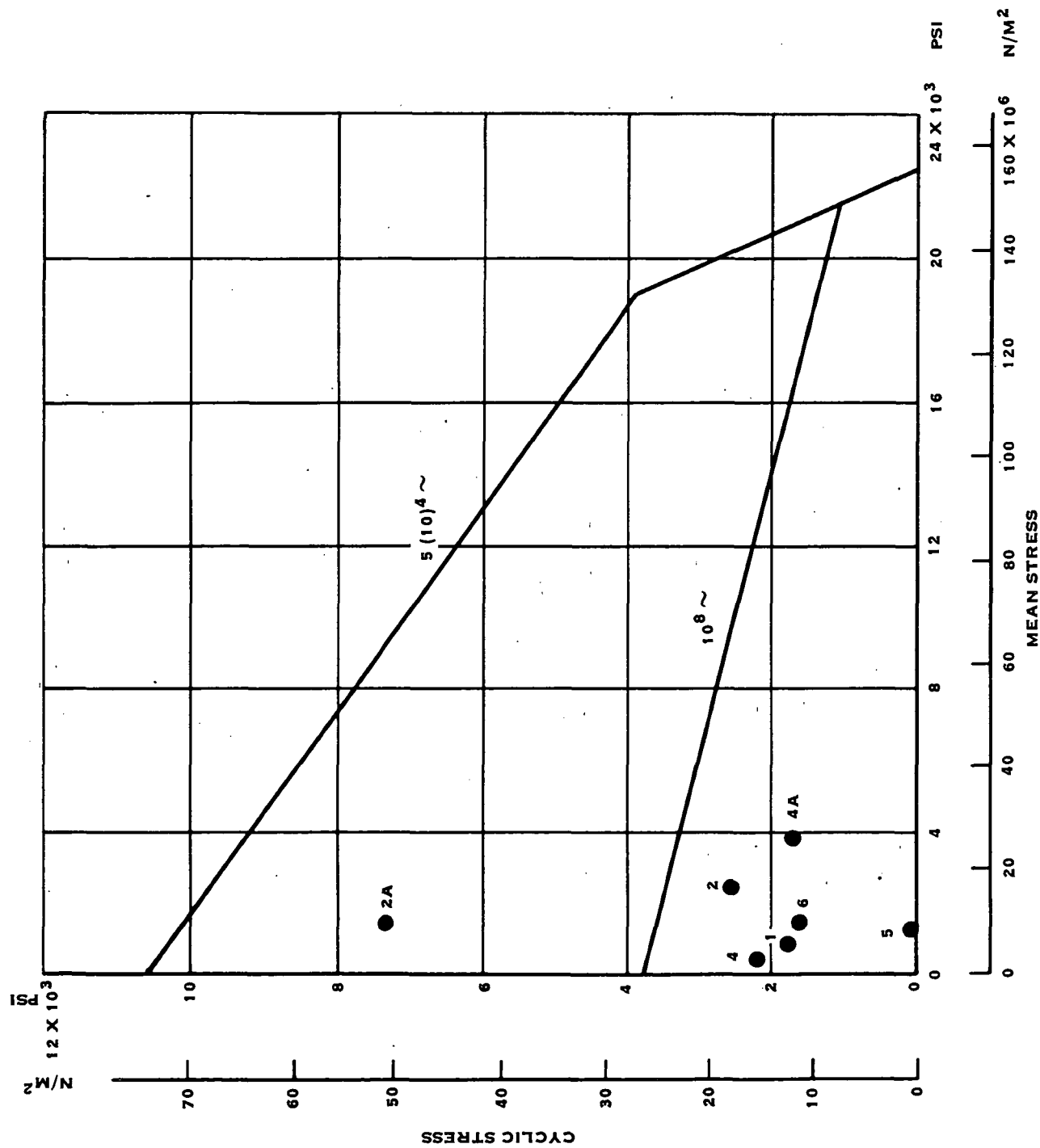
FIGURE 31. MID BLADE STRESSES
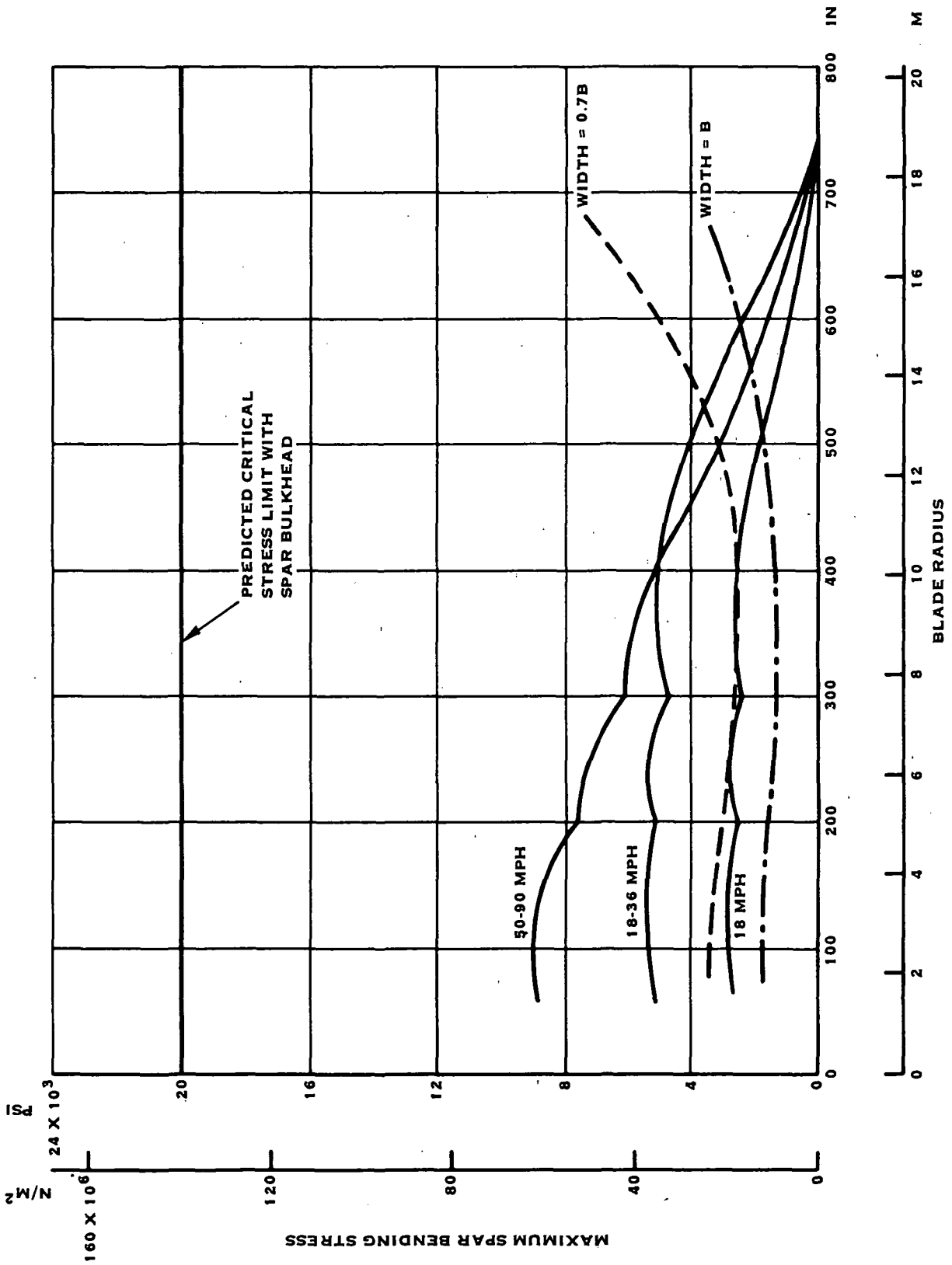
FIGURE 32. SPAR BUCKLING STRESSES
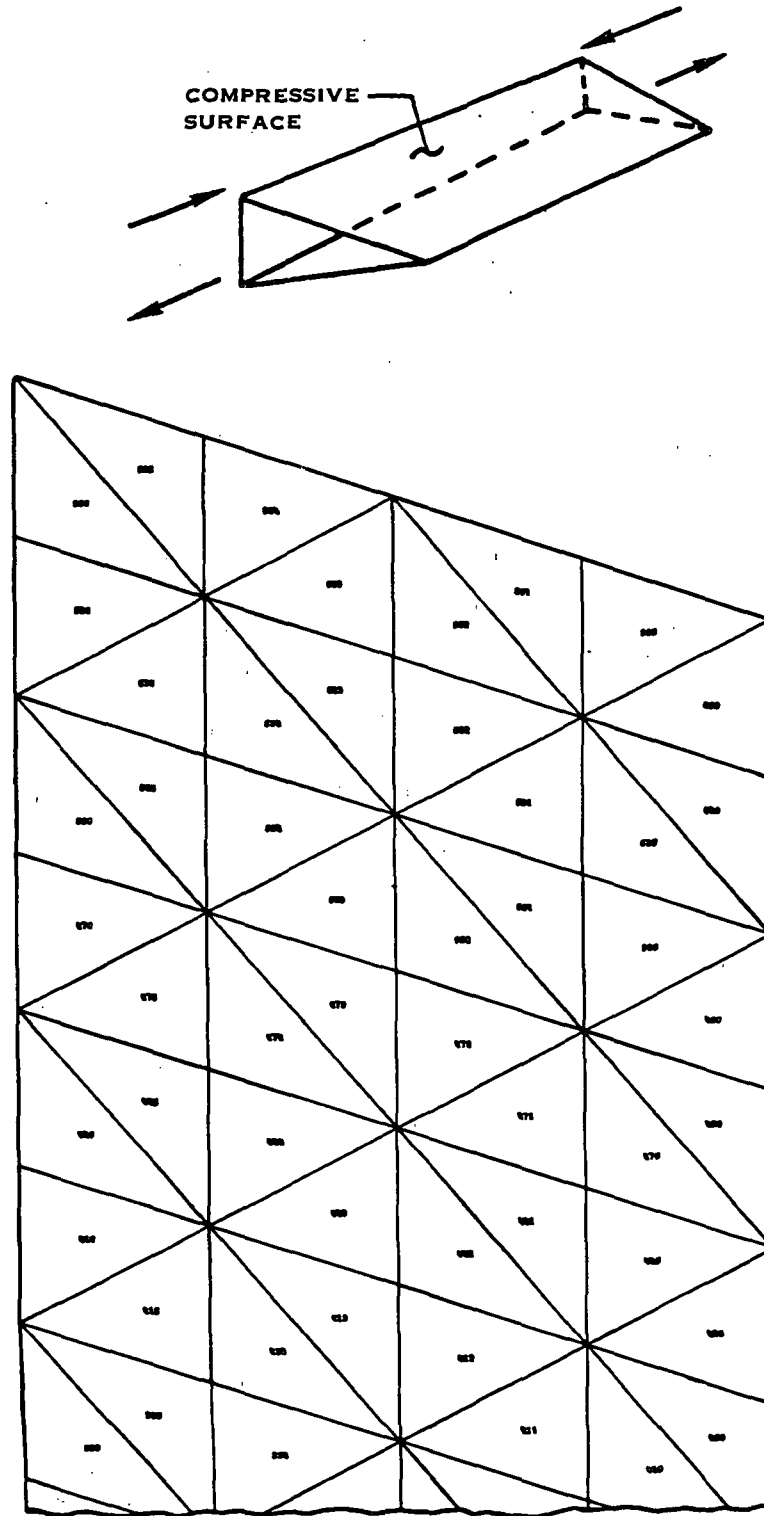
FIGURE 33.   SHELL WRINKLING FINITE ELEMENT MODEL

A. SPANWISE DEFLECTION

B. CHORDWISE DEFLECTION
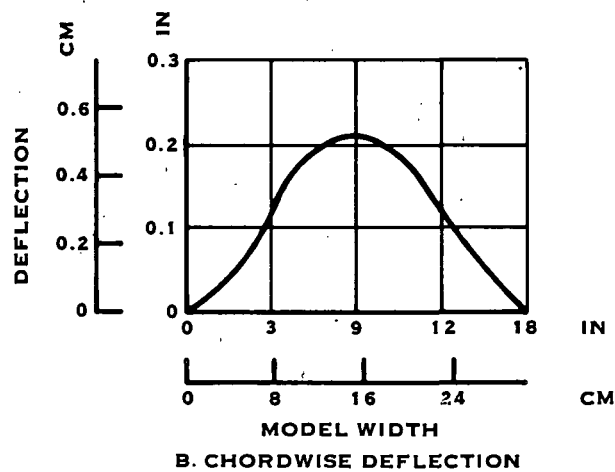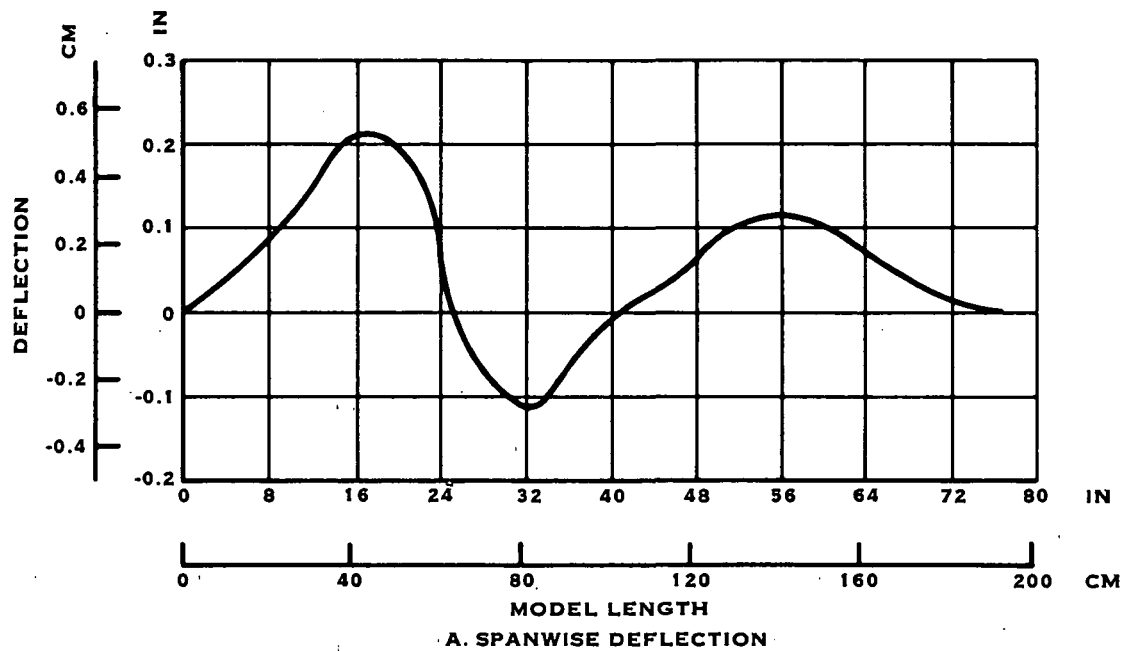
FIGURE 34. SHELL MODEL BUCKLE DEFLECTIONS
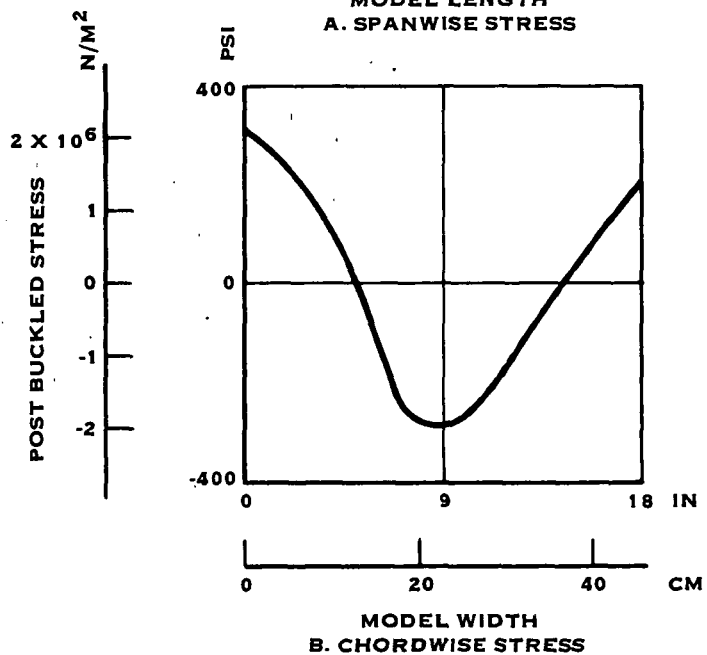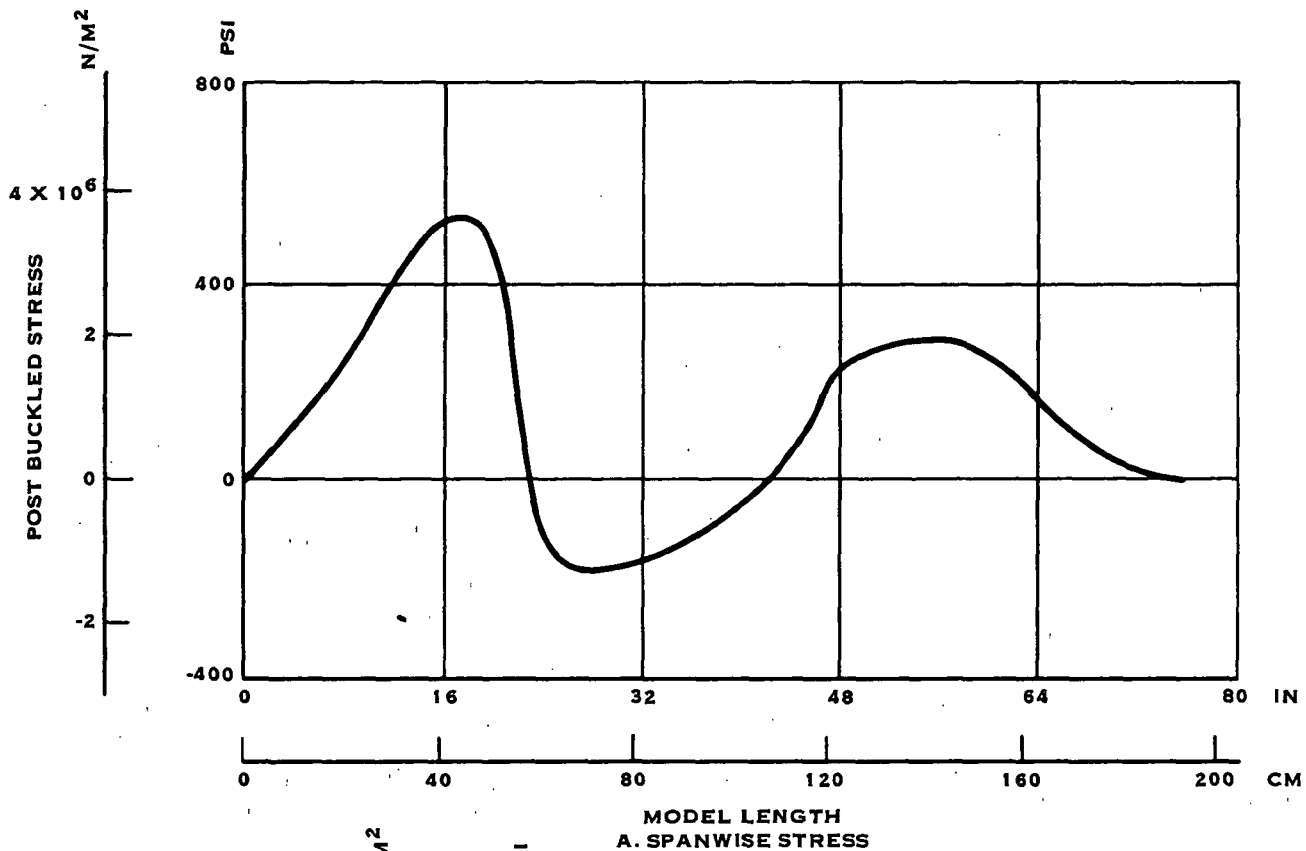
FIGURE 35. SHELL MODEL BUCKLE STRESSES

50
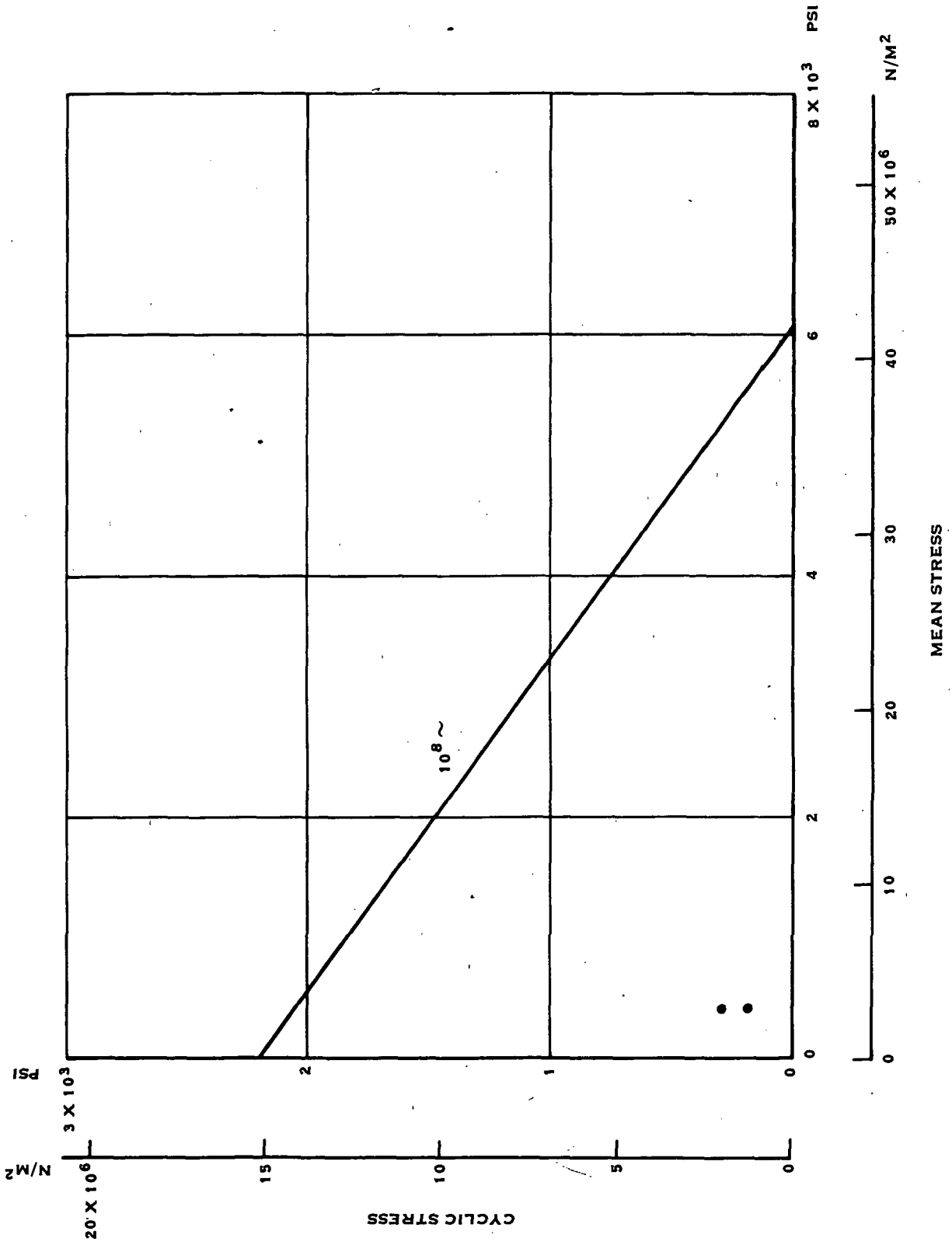
FIGURE 36. POST BUCKLED SHELL STRESS
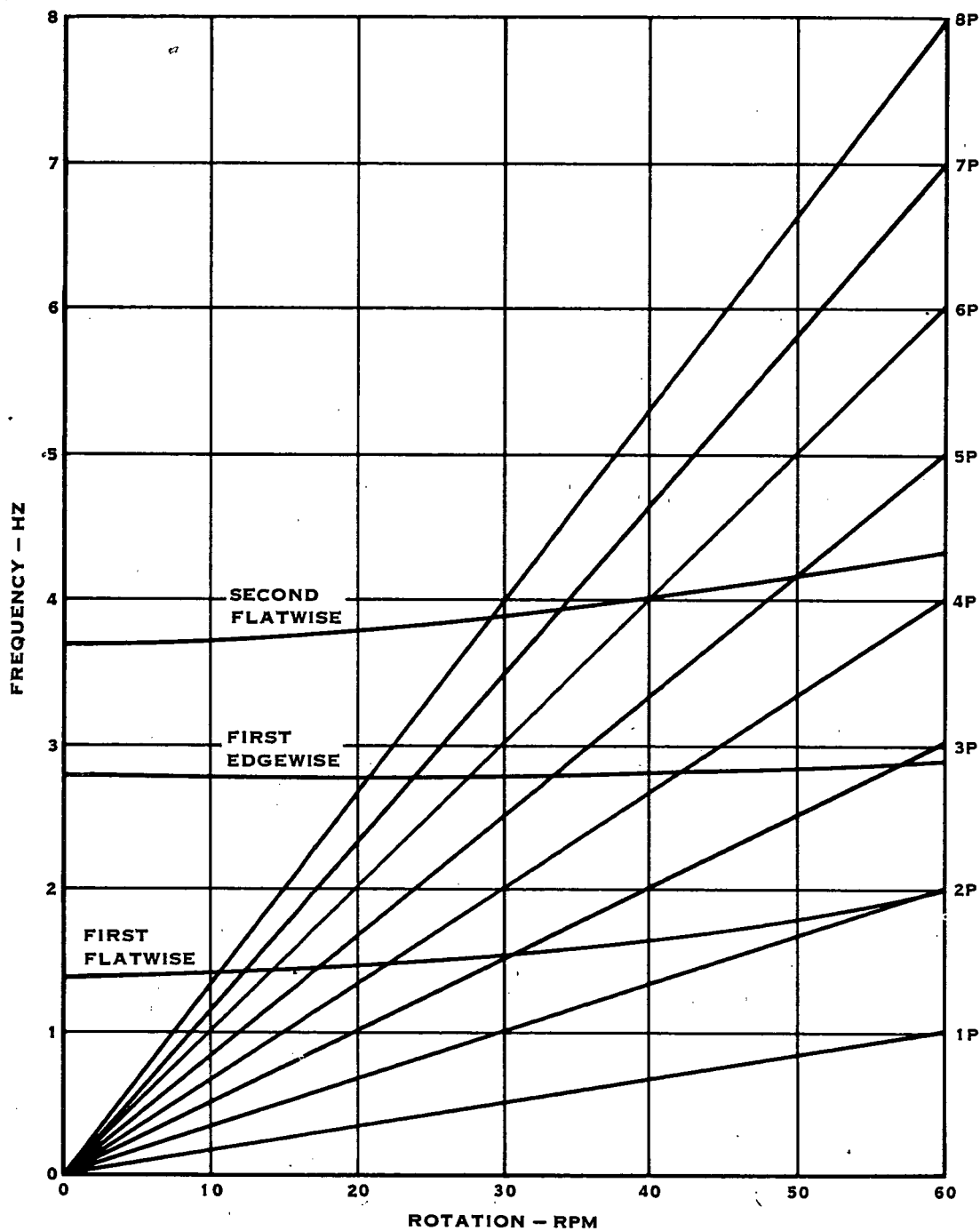
FIGURE 37. UNCOUPLED BLADE FREQUENCIES

The first edgewise frequency for the blade, if the shell were fully effective, would raise the natural frequency to operating frequency ratio (ω/Ω) from 4.2 to a ratio of 4.8. The steady state blade stress versus blade azimuthal position showed the edgewise stress variation to correspond with the edgewise frequency. It is important to note, however, that the time histories of blade stress were calculated using a rigid hub. The inclusion of the drive shaft, gear train, and generator spring rates would effect the edgewise response of the blade.

Blade stability was analyzed for three wind velocities; 18 mph (28.96 km/hr), 50 mph (80.45 km/hr), and 80 mph (128.72 km/hr); and a range of rotor speeds from 40 rpm to 80 rpm. Results of this analysis are shown in Figure 38a, b, and c. The solid torsion curve was comprised of 60% blade elastic torsion and 40% rigid body motion. The dashed torsion curve was composed of 95% blade elastic torsion and 5% rigid body motion. The results of the stability study indicated that the blade was stable over the steady state operating range.

The loading cases used for design of the blade-to-hub adapter were as shown in Table V. These loads were calculated based on computer program G400 with 100% tower shadow, wind shear, and smooth airfoils. The cases refer to the blade design conditions of Table IV. The resulting shank moments for the specified conditions were the vector sum of the flatwise and edgewise components. These detailed design loads are different from the loads used for the design study. The design study loads did not include the aeroelastic action of the blade because computer program G400 was not operational during the design study.

The inner and outer adapter sleeves were analyzed for two different load transfer mechanisms. The first was load transfer by shear only across the bonded joints equally to the inner and outer sleeves. The second was total load taken through the retention bolts.

The inboard section of the blade, the adapter sleeves, the bondjoint and the blade-to-hub adapter were analyzed using a shell of revolution computer program. The resulting configuration was modeled by finite elements from the NASA hub shaft to the 150 inch (3.81 meter) station as shown in Figure 39. The initial results of the finite element analysis of the blade shank transition area indicated high chordwise stresses. To lower these stresses to acceptable levels without necessitating a tooling change, woven fiberglass cloth layers were interleaved in the shell filament layers.

Figures 40 through 43 show Goodman diagrams for the different sections of the blade shank and retention. The numbers refer to the point on the blade where the stress was calculated. The symbols indicate the load condition from Table V. Figure 40 shows the blade-to-hub adapter stresses. Figure 41 shows the inner and outer adapter sleeve stresses. Figure 42 shows fiberglass stress in the transition area. Figure 43 shows the inner and outer adapter sleeve maximum adhesive shear stress.
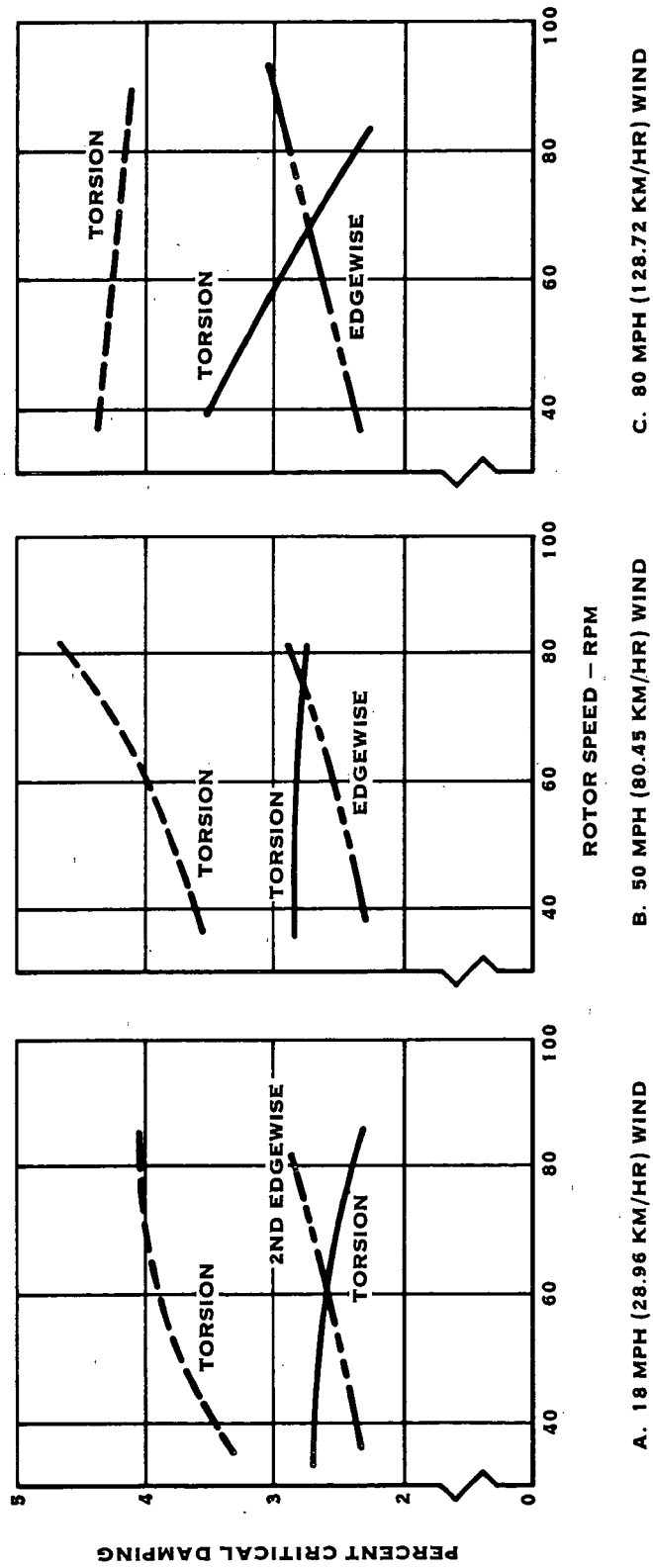
FIGURE 38. BLADE STABILITY

A. 18 MPH (28.96 KM/HR) WIND

B. 50 MPH (80.45 KM/HR) WIND

C. 80 MPH (128.72 KM/HR) WIND

ROTOR SPEED — RPM

PERCENT CRITICAL DAMPING

54

TABLE V
BLADE-TO-HUB ADAPTER DESIGN LOADS

Case	Moment	Type
1	$342,000 \pm 770,000$ in. -lb ($38,646 \pm 87,010$ N-m)	Infinite life ($10^8 \sim$)
2	$886,00 \pm 1,320,000$ in. -lb ($100,118 \pm 149,160$ N-m)	Finite life ($5 \times 10^4 \sim$)
2a	$2,393,000$ in. -lb ($270,409$ N-m)	Limit load
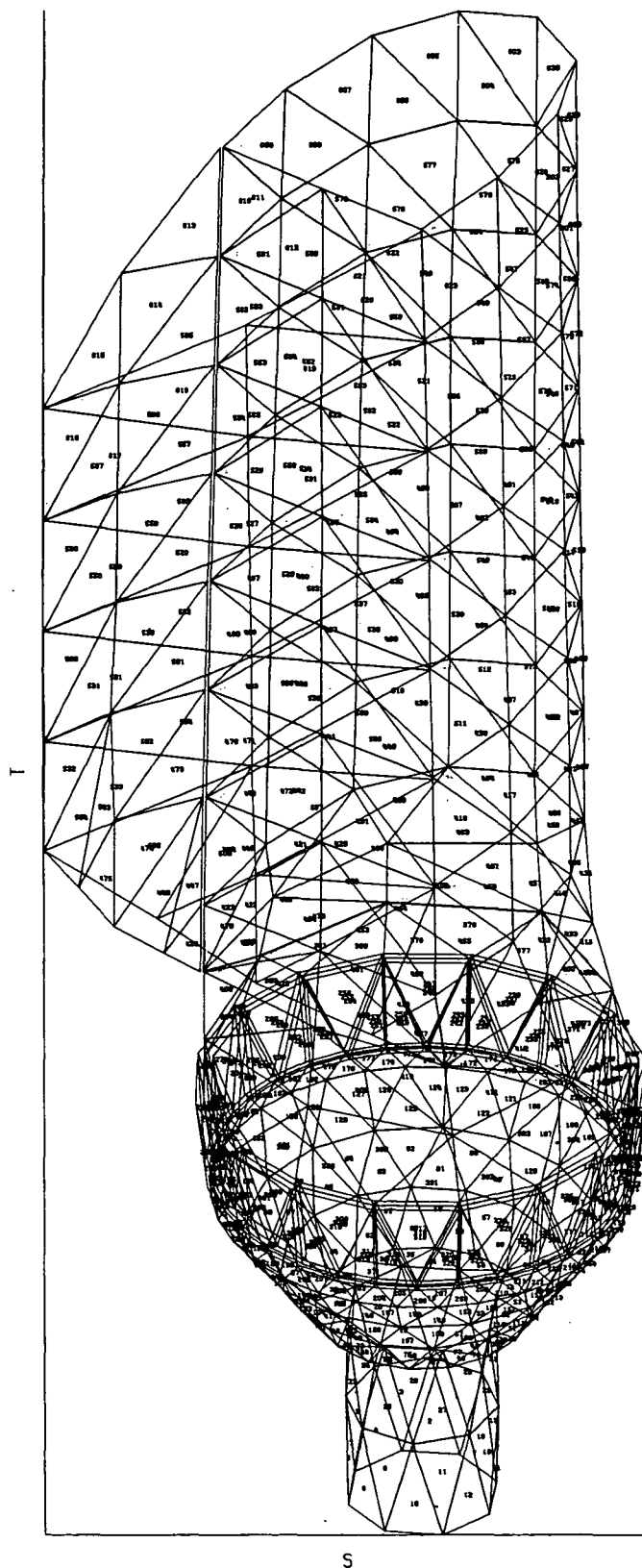
FIGURE 39. BLADE FINITE ELEMENT MODEL
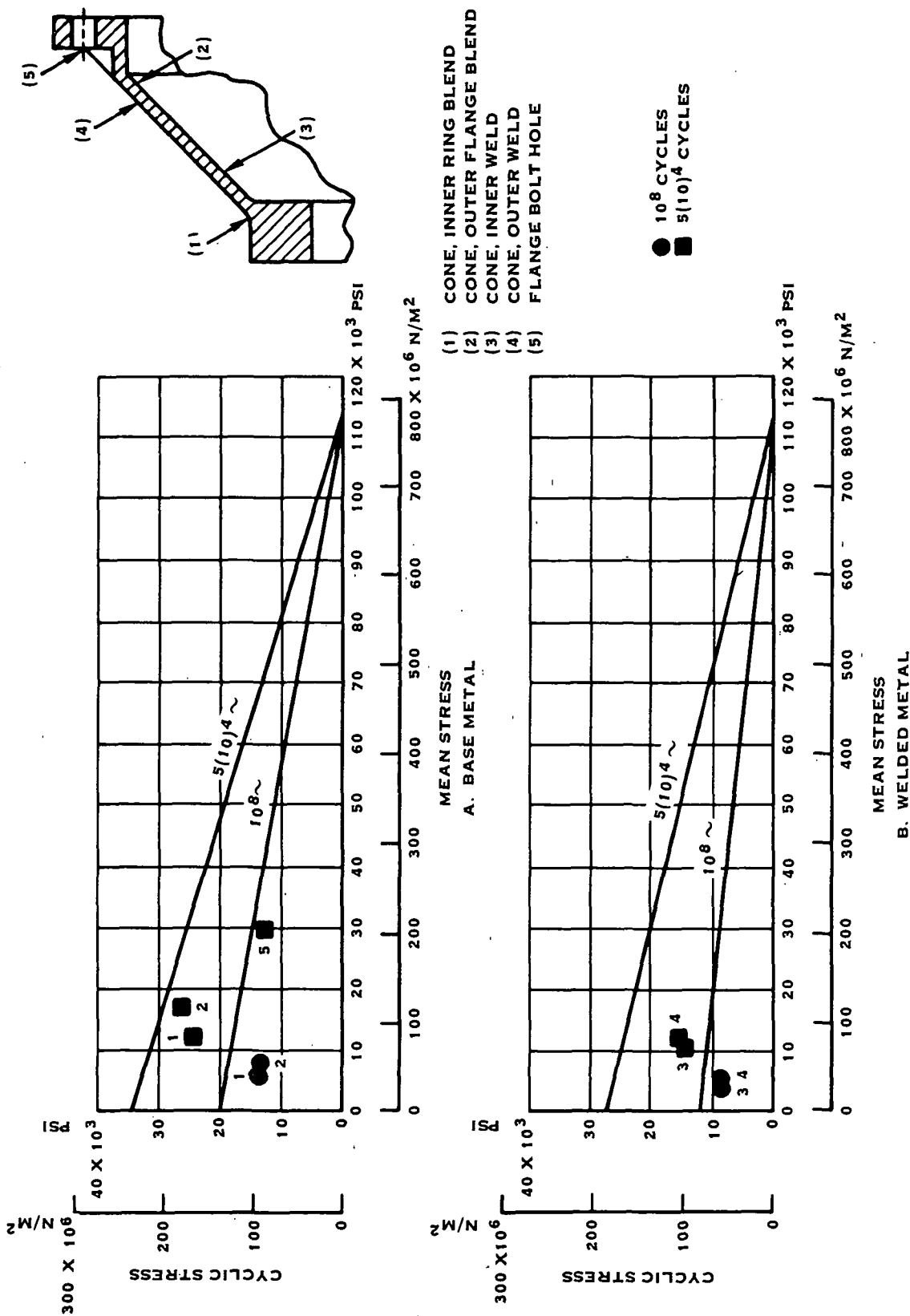
FIGURE 40. BLADE-TO-HUB ADAPTER STRESSES

(1) CONE, INNER RING BLEND
(2) CONE, OUTER FLANGE BLEND
(3) CONE, INNER WELD
(4) CONE, OUTER WELD
(5) FLANGE BOLT HOLE

● 10^8 CYCLES
■ $5(10)^4$ CYCLES
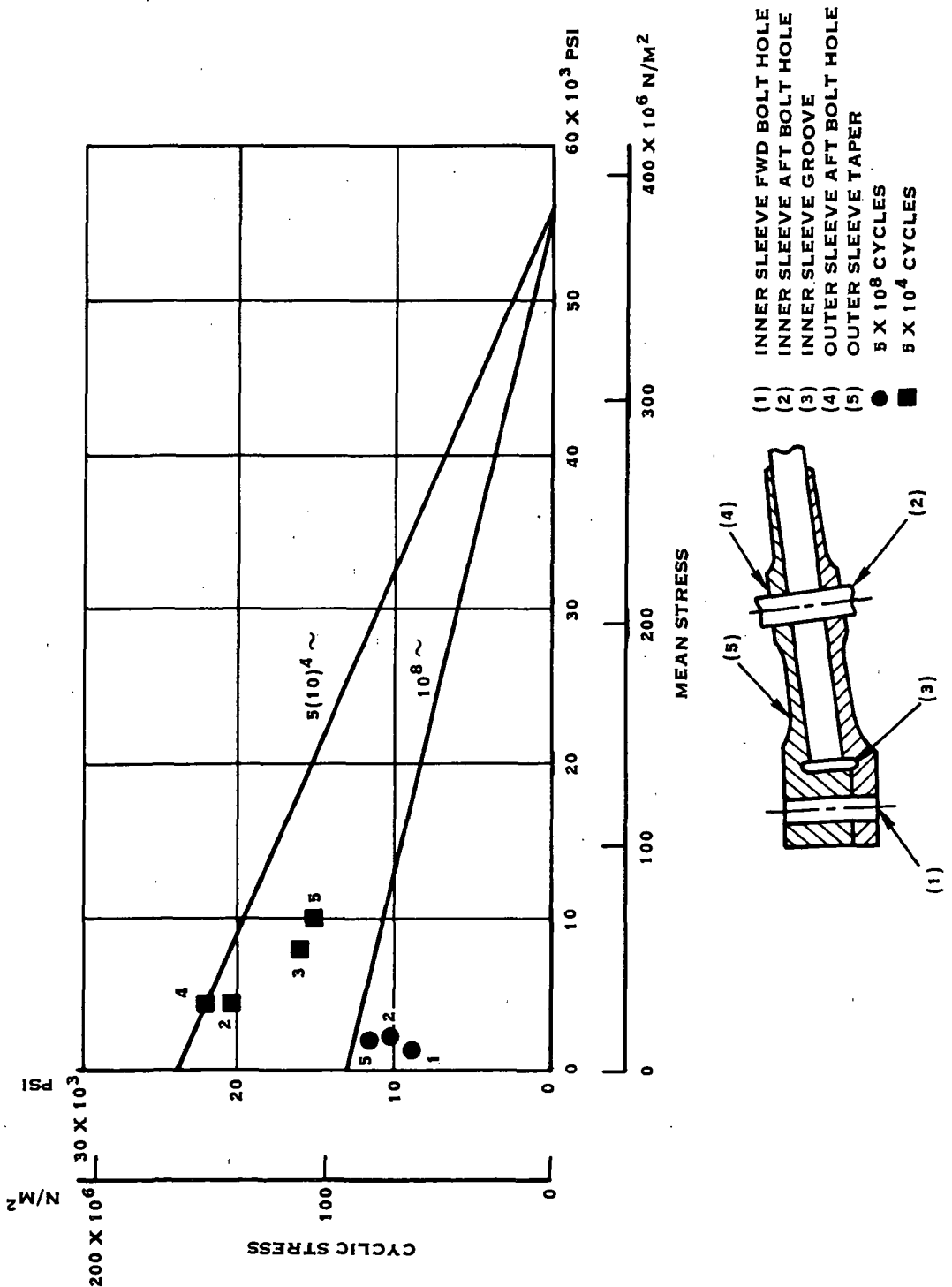
FIGURE 41. ADAPTER SLEEVE STRESSES
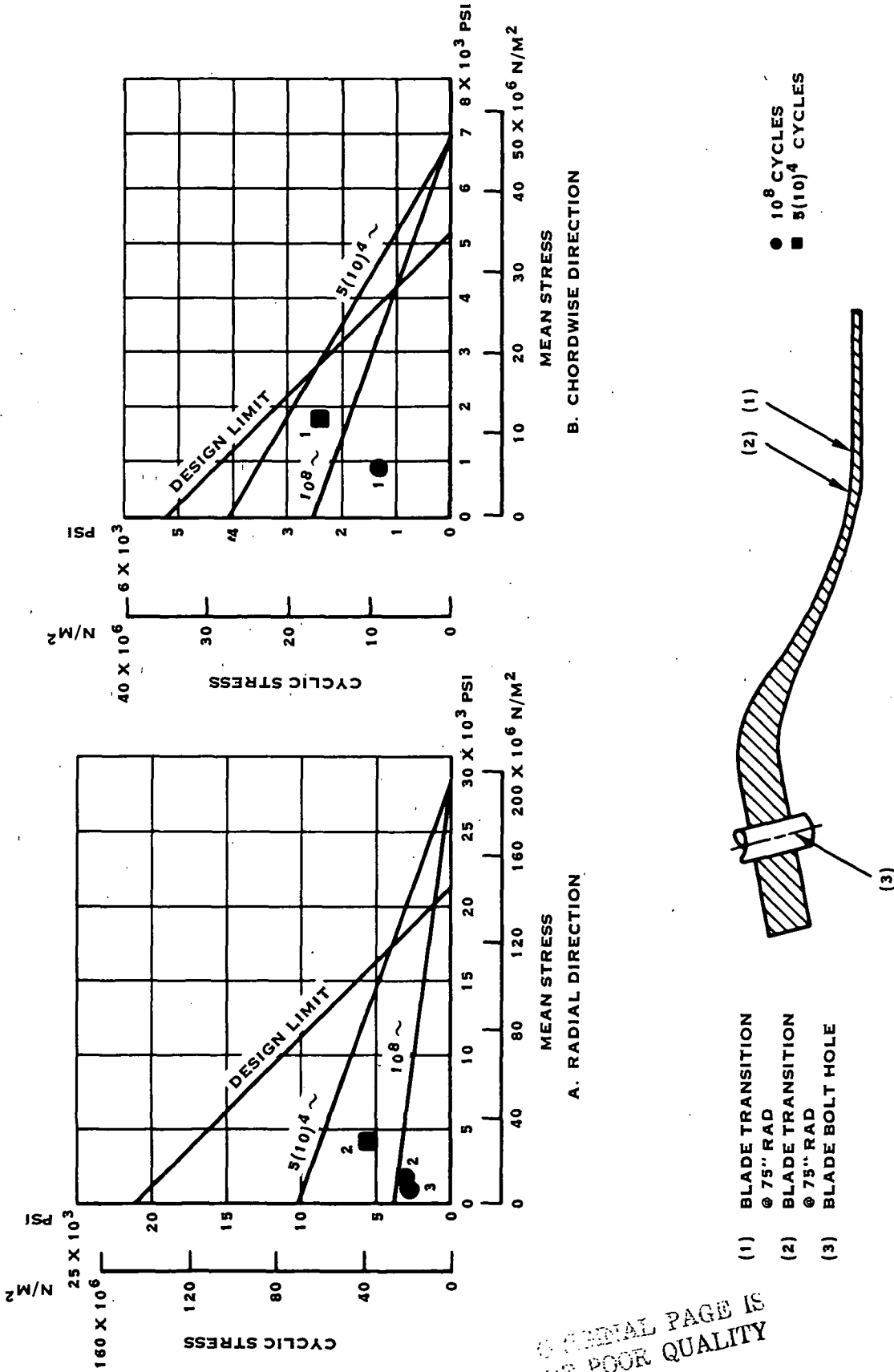
FIGURE 42. TRANSITION FIBERGLASS STRESSES

(1) BLADE TRANSITION @ 75" RAD
(2) BLADE TRANSITION @ 75" RAD
(3) BLADE BOLT HOLE

● 10⁸ CYCLES
■ 5(10)⁴ CYCLES

59
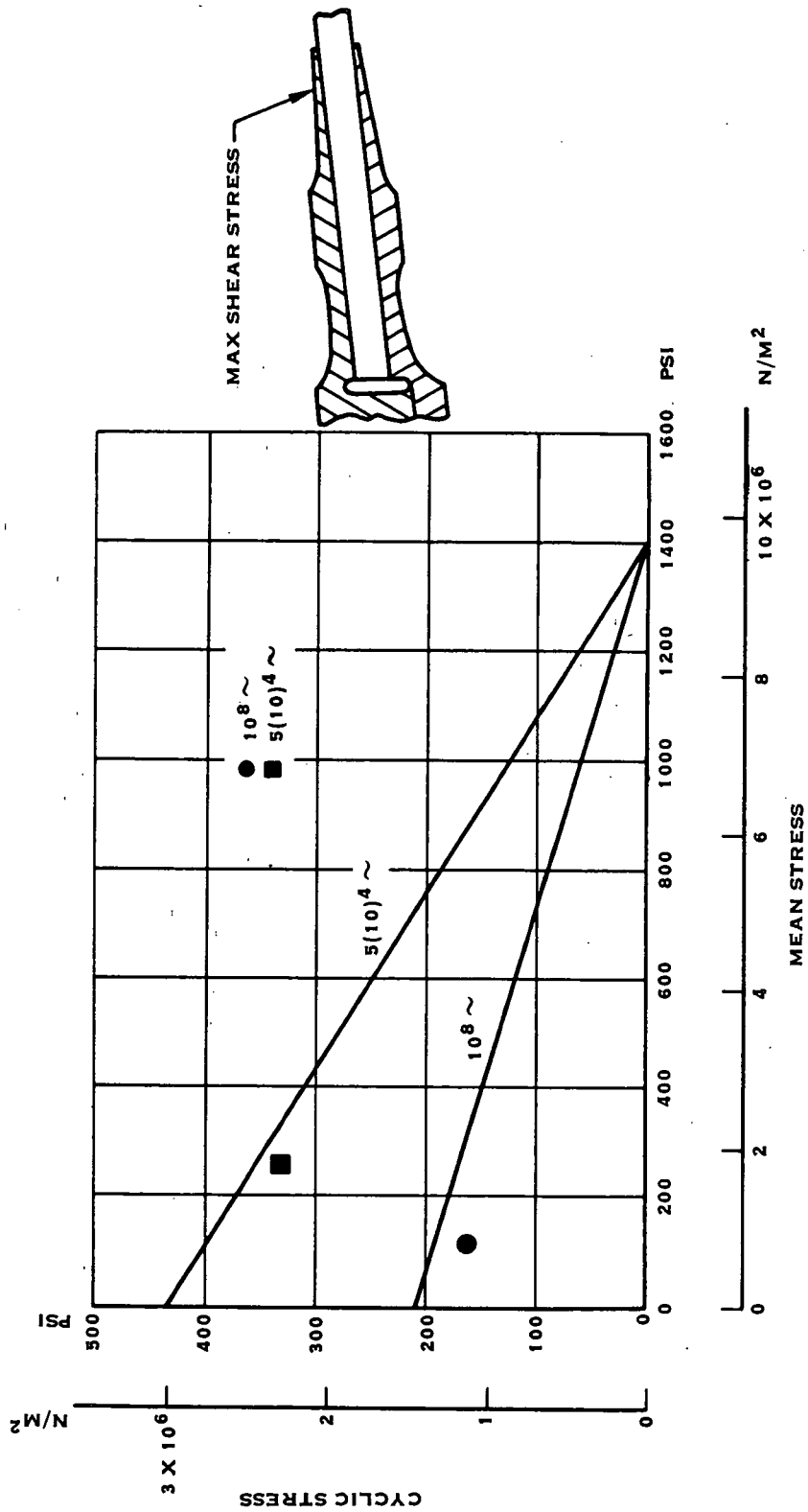
FIGURE 43.   ADAPTER SLEEVE ADHESIVE STRESSES

Structural adequacy of the blade design for operation in higher wind speed regimes was studied. Using smooth airfoil loadings, 100% tower shadow and wind shear, steady state operation was reviewed for 24, 36 and 50 mph (38.62, 57.92, and 80.45 km/hr). Figures 44 through 52 present the results of this study.

Figures 44, 45, and 46 show flatwise and edgewise shank stresses versus blade azimuthal position for 24, 36, and 50 mph (38.62, 57.92, and 80.45 km/hr) wind speeds respectively. All cases are steady state with the rotor at 40 rpm and a power output of 100 kW. Figures 47 and 48 show the variation of steady and vibratory moments with increasing wind speeds. The shank moments are the vector addition of the flatwise and edgewise moments and the mid blade moments are flatwise only. Figures 49 through 52 show the mean and cyclic stresses on Goodman diagrams for midblade filament wound material, blade-to-hub adapter, inner and outer adapter sleeves, and adapter sleeve adhesives respectively.

The limiting areas of the design for operation at higher wind speeds were the blade-to-hub adapter and the adapter sleeves. As designed, the blade is structurally adequate for an infinite life of steady state operation in wind velocities up to 30 mph (48.27 km/hr).

TOOL DESIGN

An interactive design system (IDS) was used as an aid in design of the spar and shell tooling. This IDS was a conversational computer-aided design system which provided for visual interactive geometric construction and dimensioning, storage, retrieval, manipulation, association, and reproduction of three dimensional and multi-view graphics. The system was employed to generate stacked views of the outside blade contour, the spar mandrel, and the shell mandrel. System input came from computer generated magnetic tapes defining the outside airfoil contours at 15 inch intervals. The inside coutours of the spar and shell were generated using spline and offset functions built into the system. The inside spar contours were stacked as shown in Figure 53 so that mandrel removal could be studied. Minor modifications were made to several stations so that one-piece mandrel removal could be accomplished if desirable. The inside shell contours were stacked in the same manner to insure that the mandrel could be removed. Engineering Approved Equivalent Duplicates (EAED) for each spar station and each shell station were prepared to aid in mandrel design and fabrication. Figure 54 is a typical EAED and shows the spar 75.0 inch (1.90 meter) station. The IDS was used to generate the blend between the blade airfoil and the retention. Figure 55 shows the resulting blend.
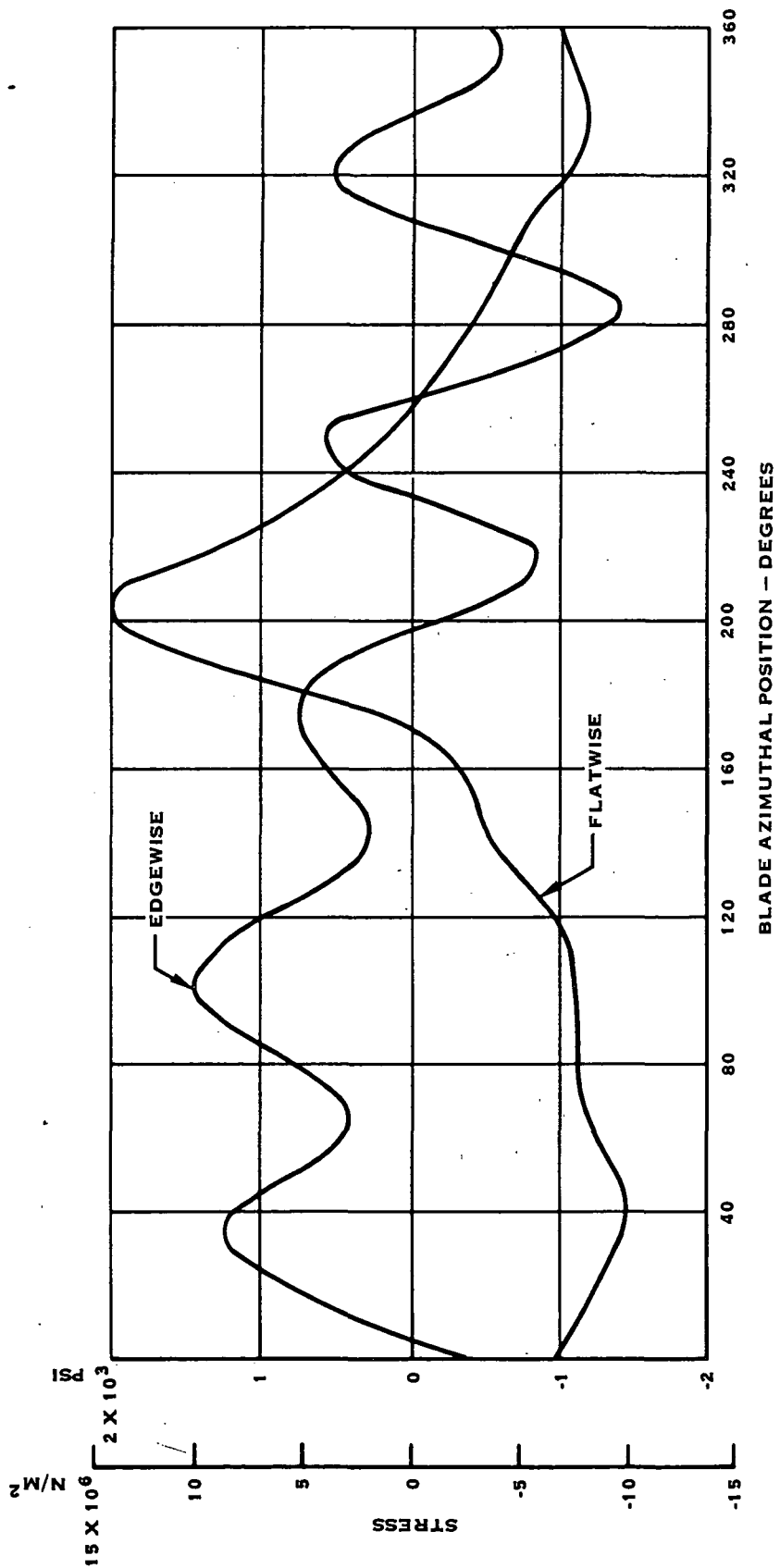
FIGURE 44. SHANK STRESSES – 24 MPH (38.62 KM/HR) WIND
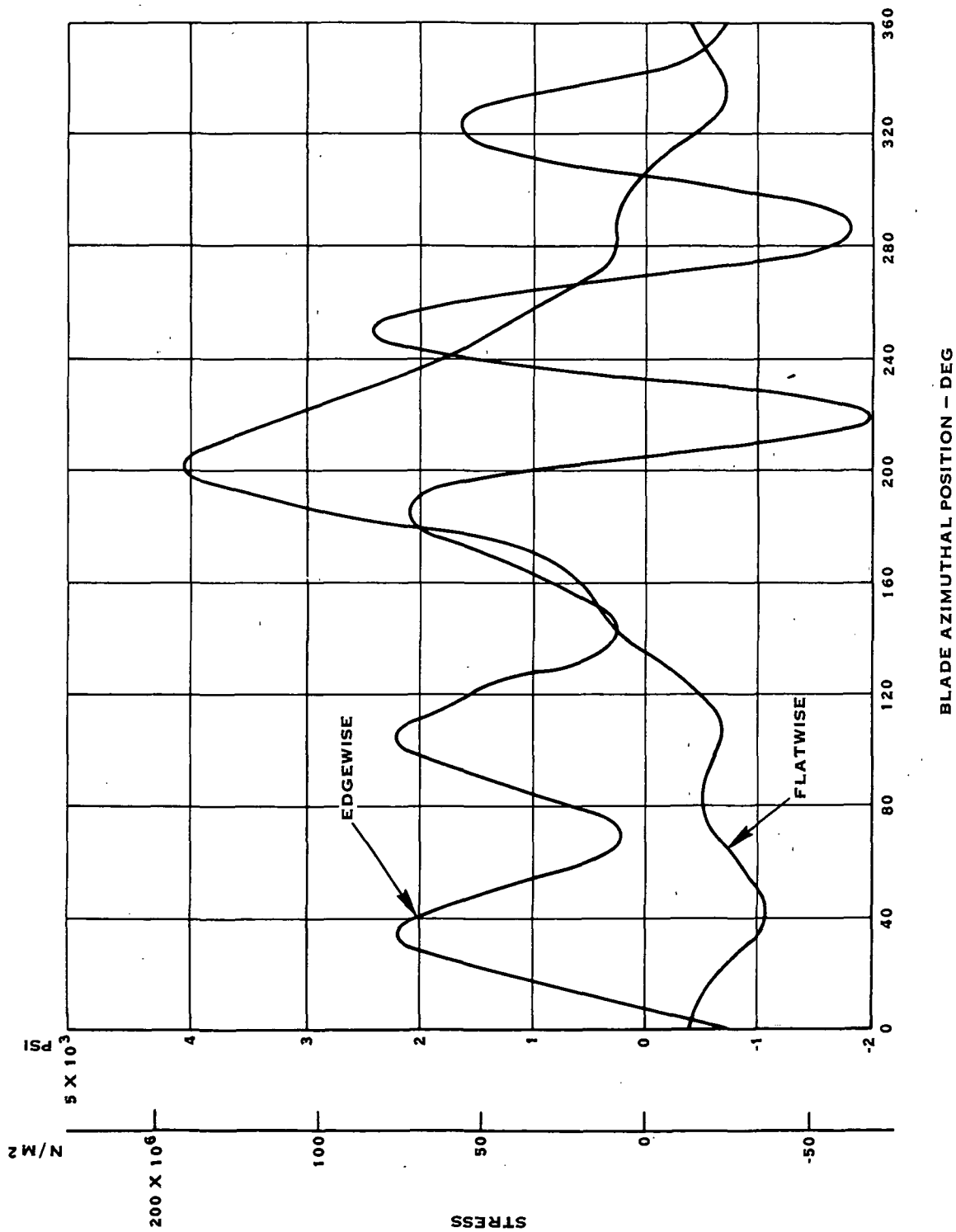
FIGURE 45. SHANK STRESSES — 36 MPH (61.31 KM/HR) WIND
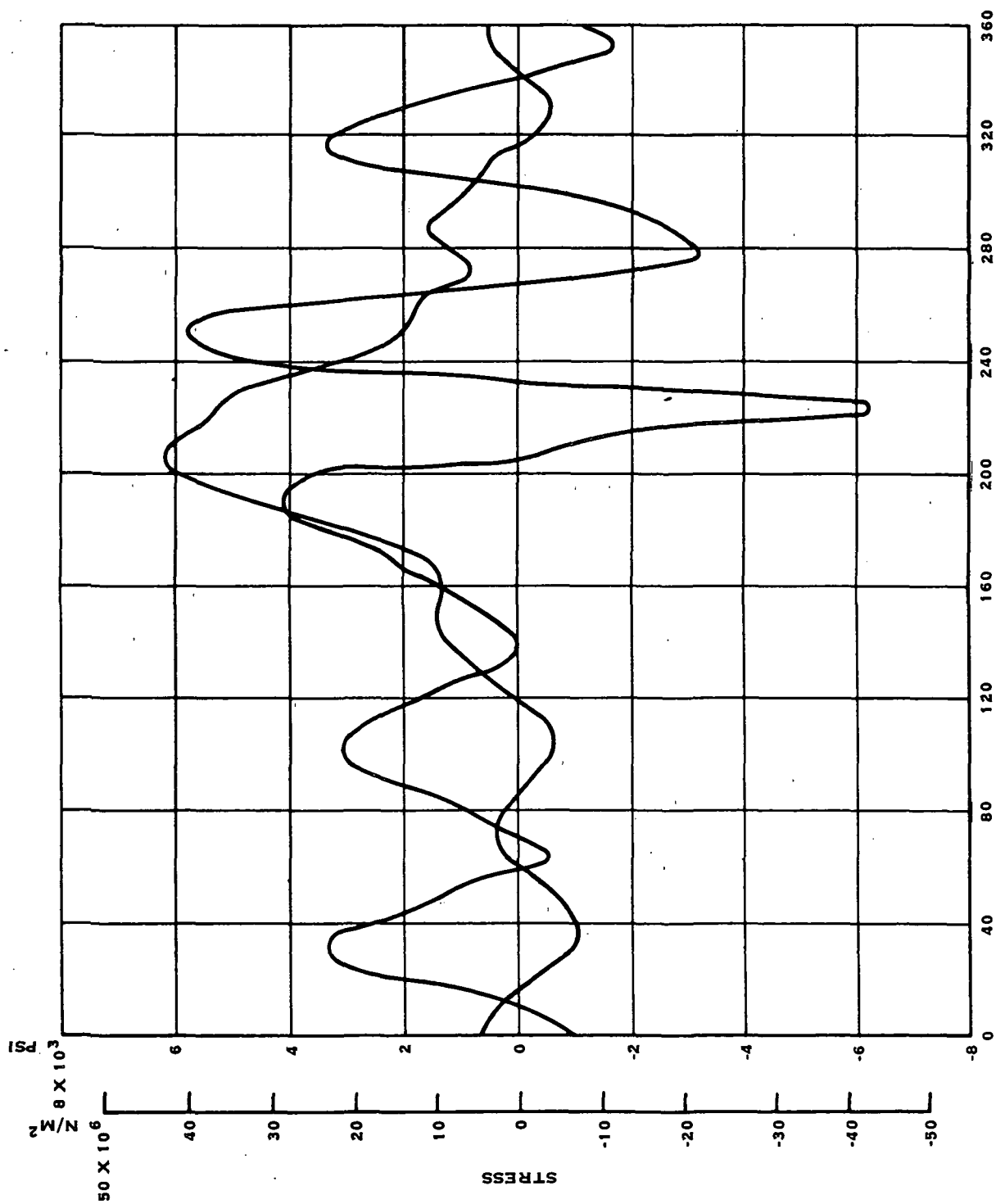
FIGURE 46. SHANK STRESSES — 50 MPH (80.45 KM/HR) WIND
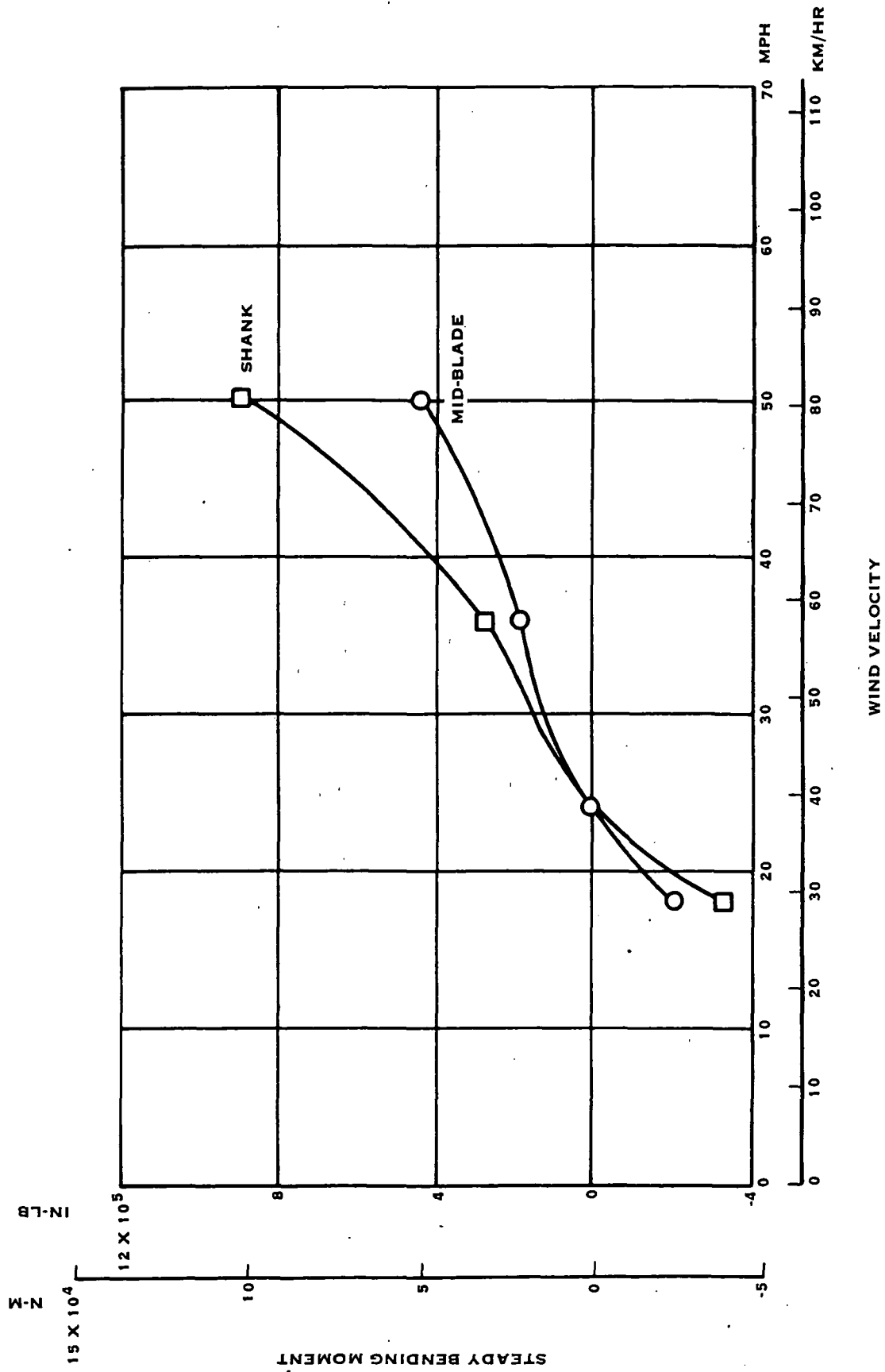
FIGURE 47. STEADY MOMENTS – INCREASED WIND SPEEDS
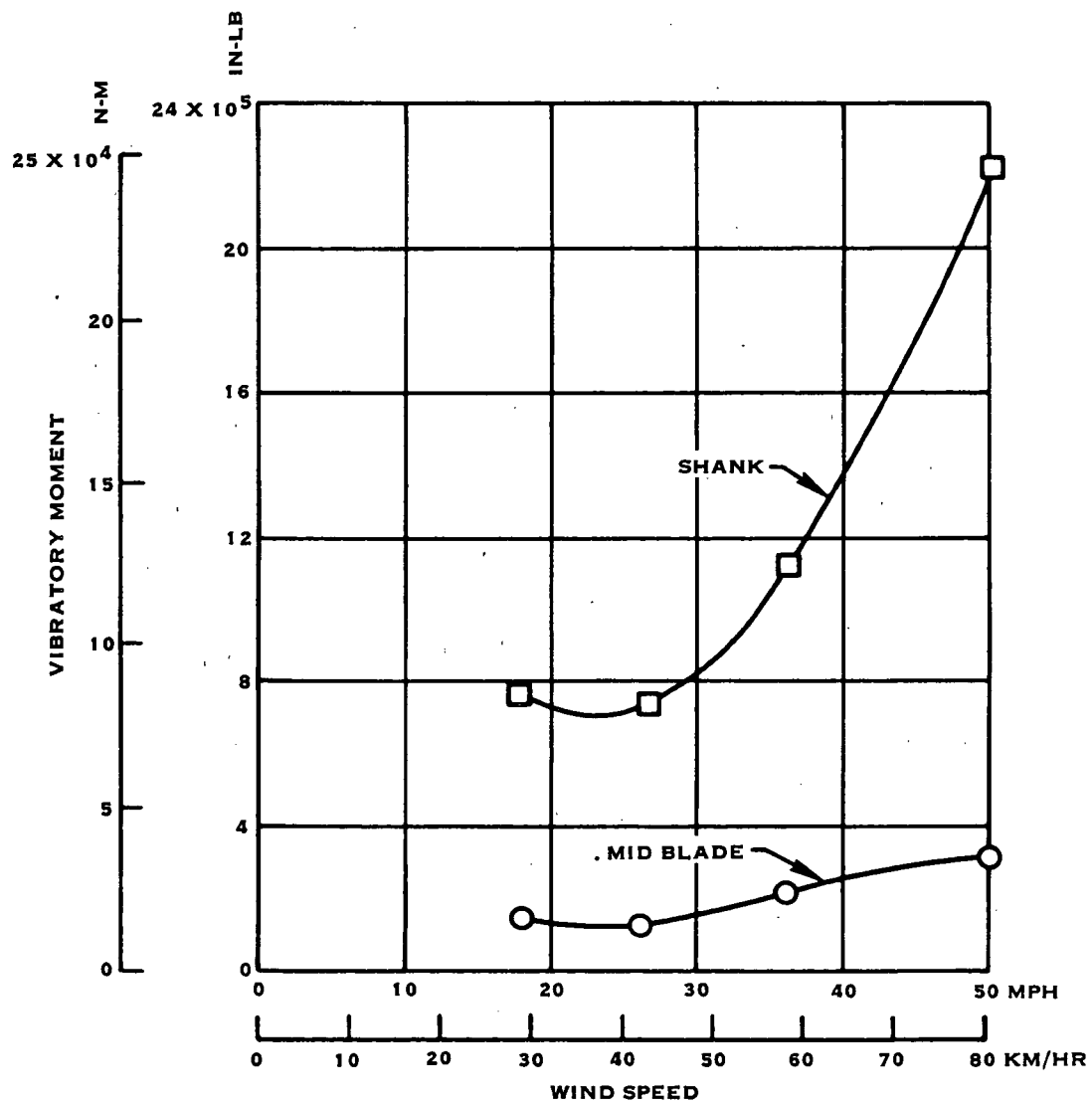
FIGURE 48. VIBRATORY MOMENTS – INCREASED WIND SPEED
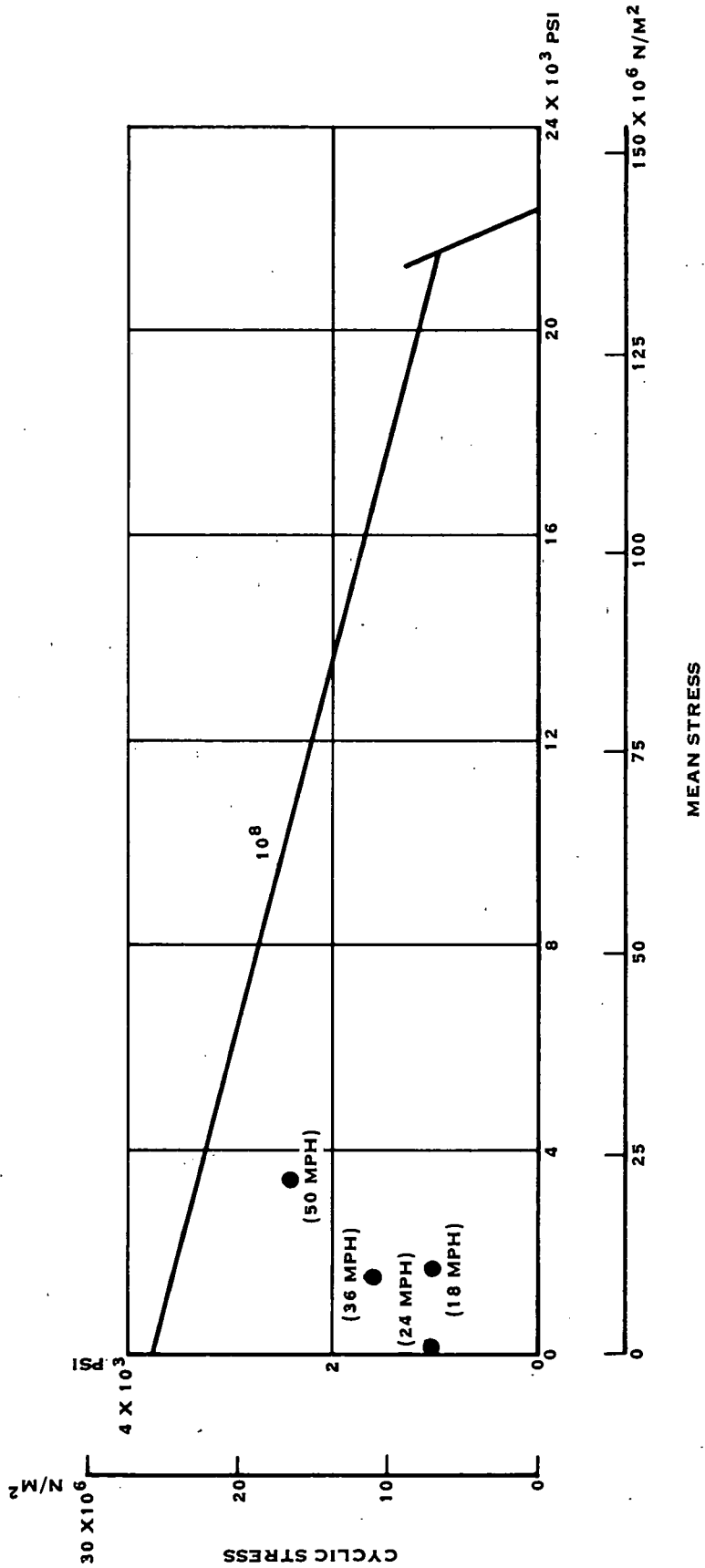
FIGURE 49. MID BLADE STRESSES — INCREASED WIND SPEED
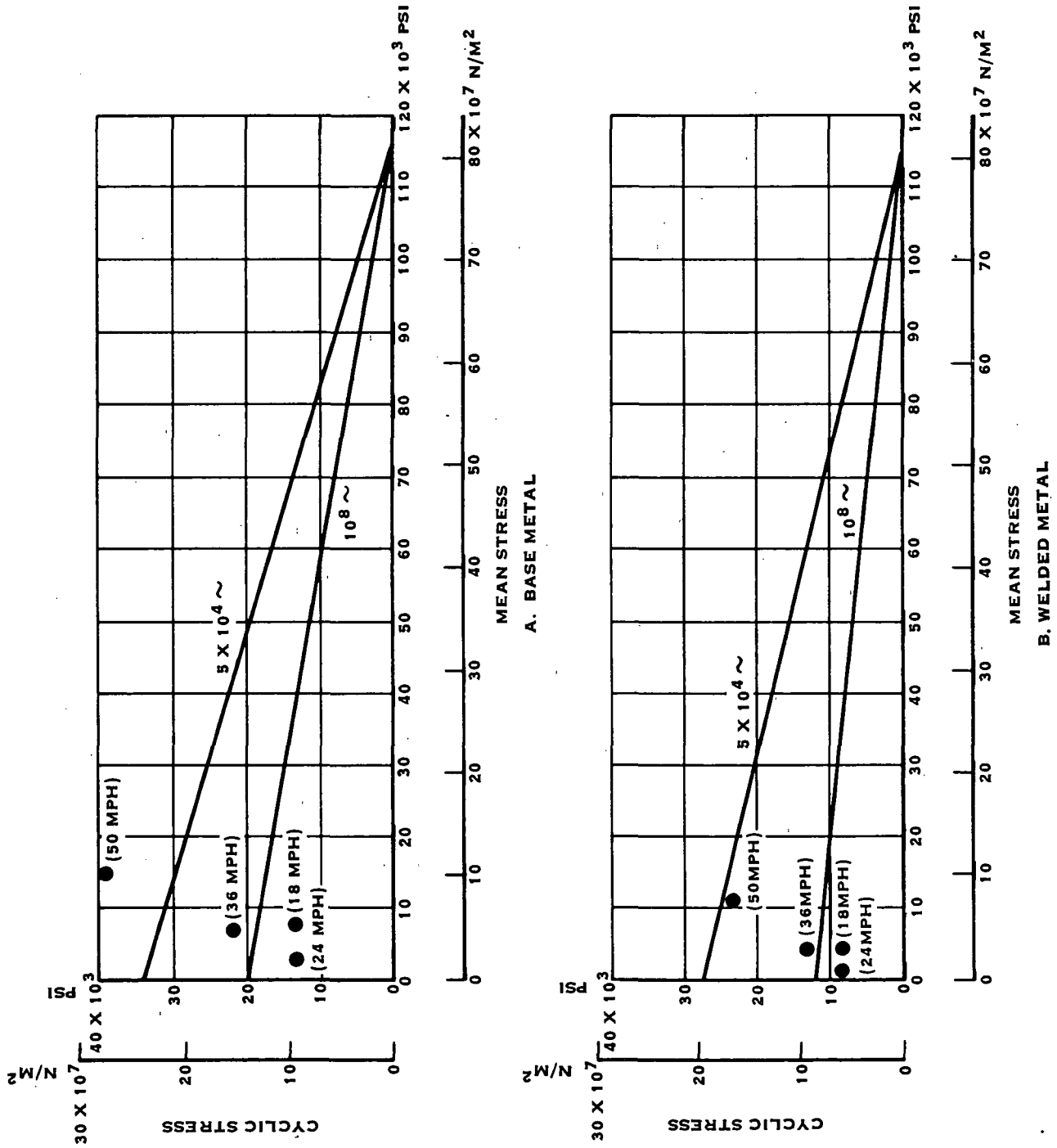
FIGURE 50. BLADE-TO-HUB ADAPTER MAXIMUM STRESS – INCREASED WIND SPEED
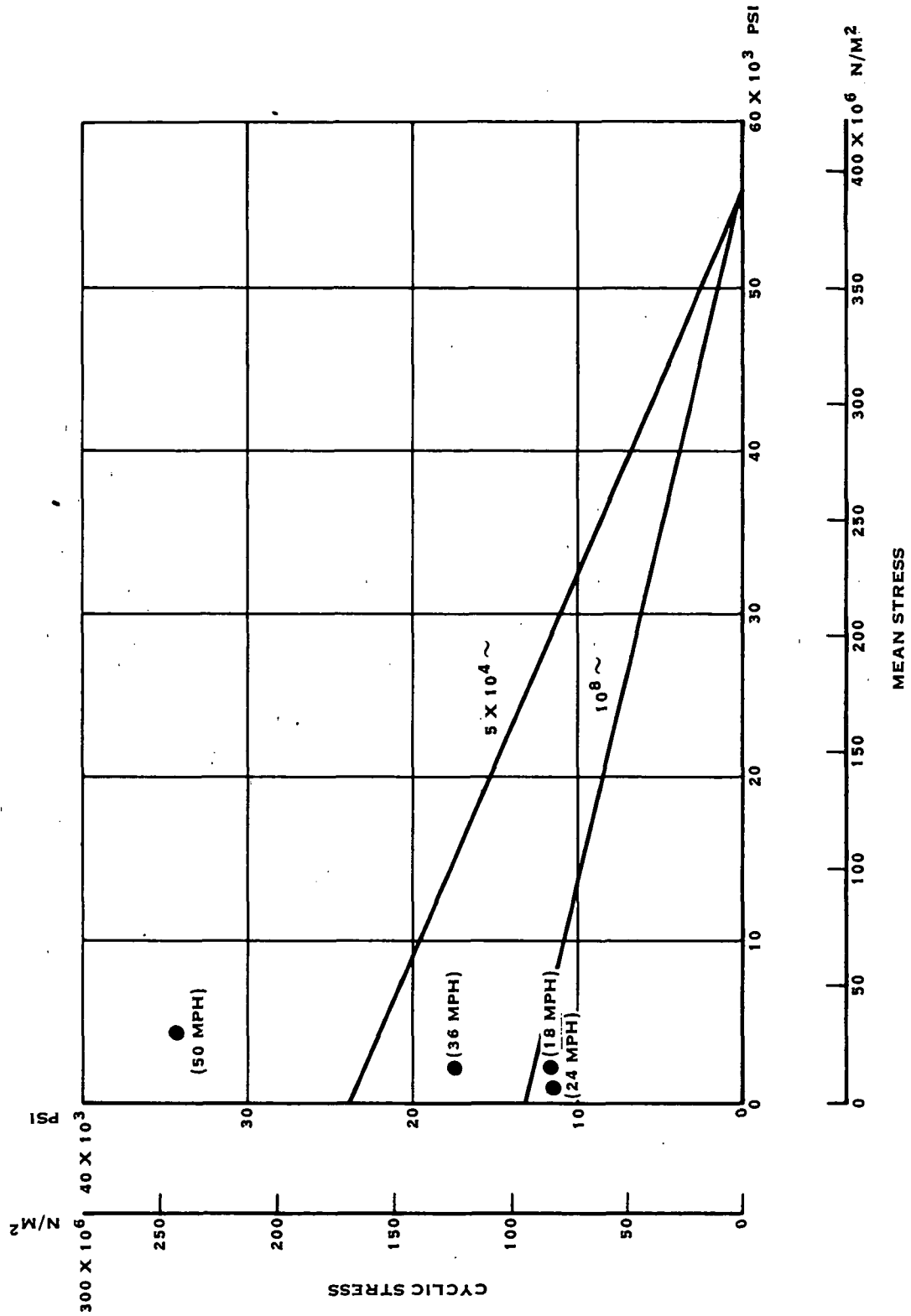
FIGURE 51. ADAPTER SLEEVE MAXIMUM STRESS – INCREASED WIND SPEEDS
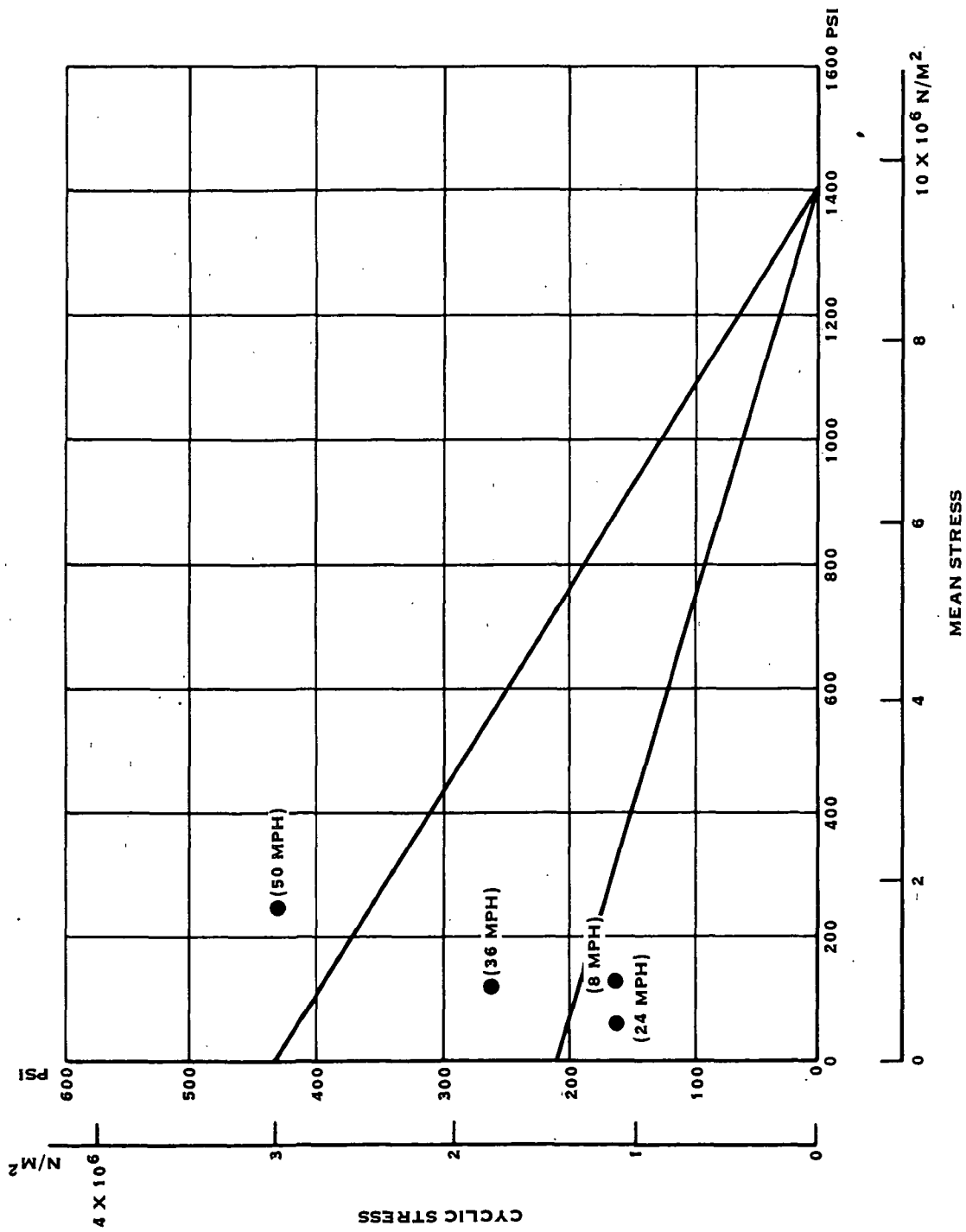
FIGURE 52.   ADAPTER SLEEVE ADHESIVE MAXIMUM STRESS – INCREASED WIND SPEEDS

AXIS X

FACE

LEADING EDGE

STACKING PLANE
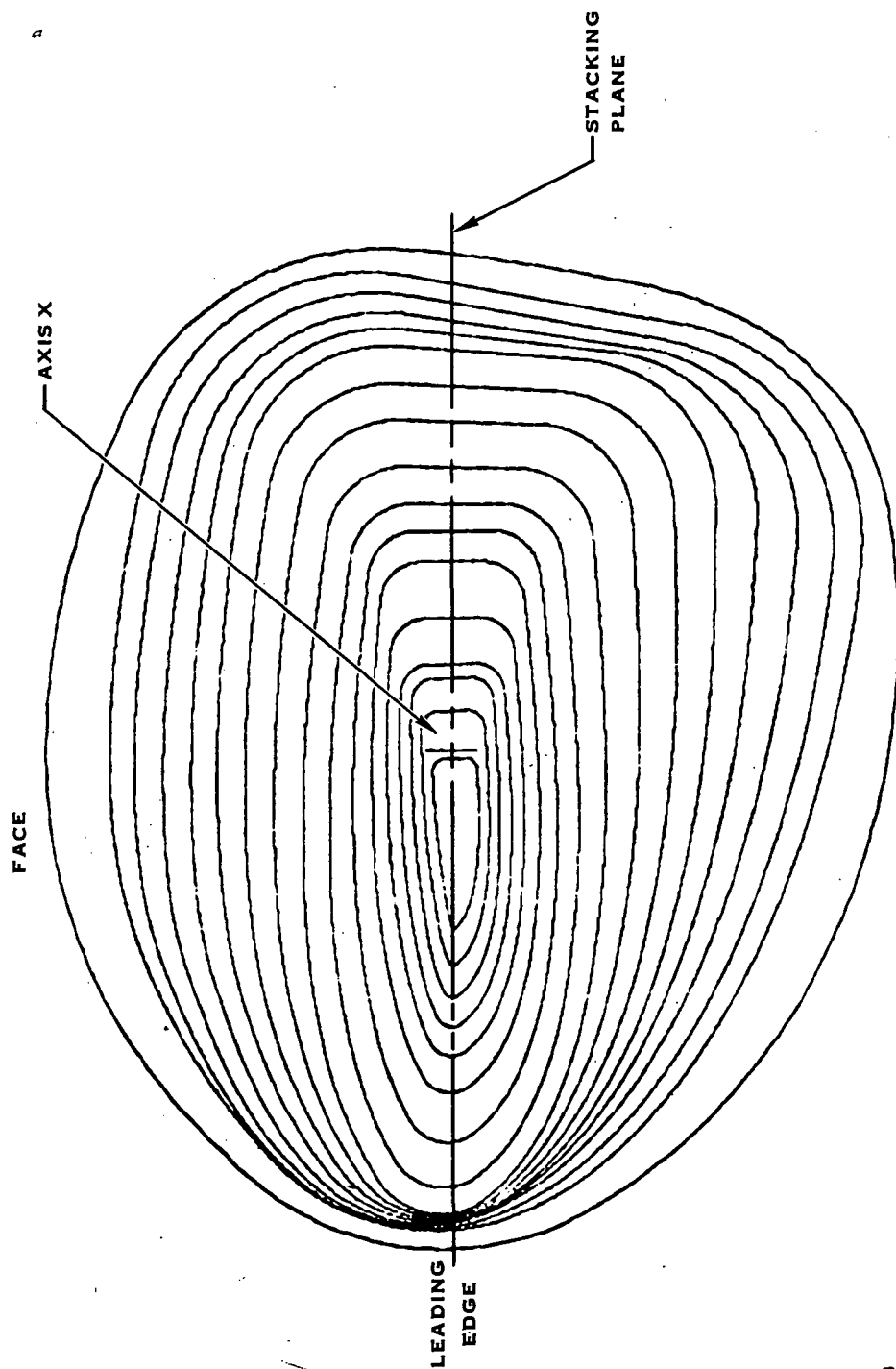
VIEW LOOKING TIP TO HUB

TEMPLATES SHOWN (INSIDE OF SPAR MINUS 0.06251 FOR
STATIONS   65.00, 75.00, 120.0, 165.0, 210.0, 255.0
300.0, 345.0, 390.0, 435.0, 480.0, 525.0,
570.0, 615.0, 660.0, 705.0 & 750.0

FIGURE 53.   STACKED SPAR CONTOURS

71

AXIS X

FACE

STACKING PLANE

LE

STA 75
VIEW LOOKING TIP TO HUB
SCALE: 1/1

ENGINEERING APPROVED
EQUIVALENT DUPLICATE

PROJECT
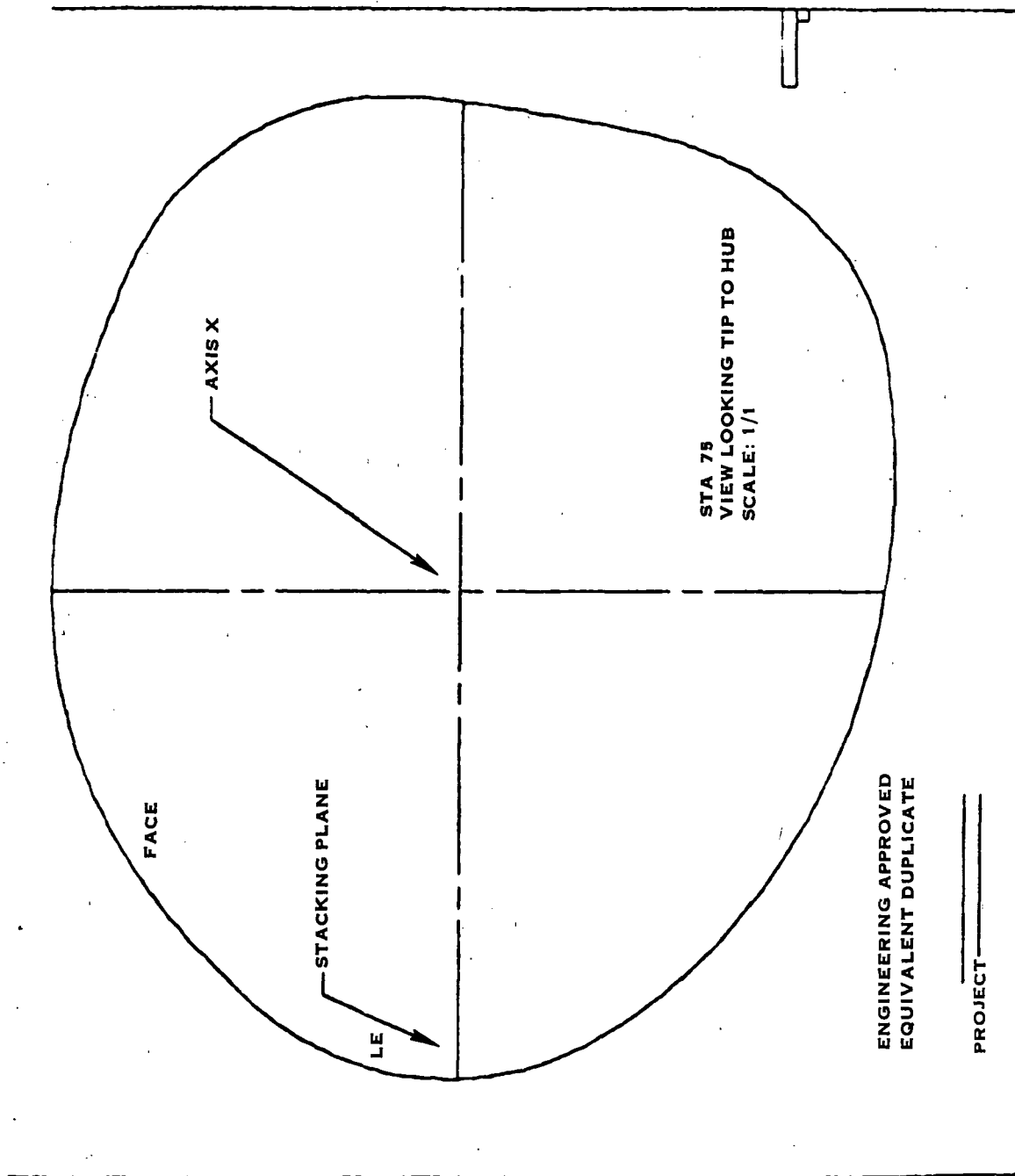
FIGURE 54. ENGINEERING APPROVED EQUIVALENT DUPLICATE

72

ORIGINAL PAGE IS
ON POOR QUALITY
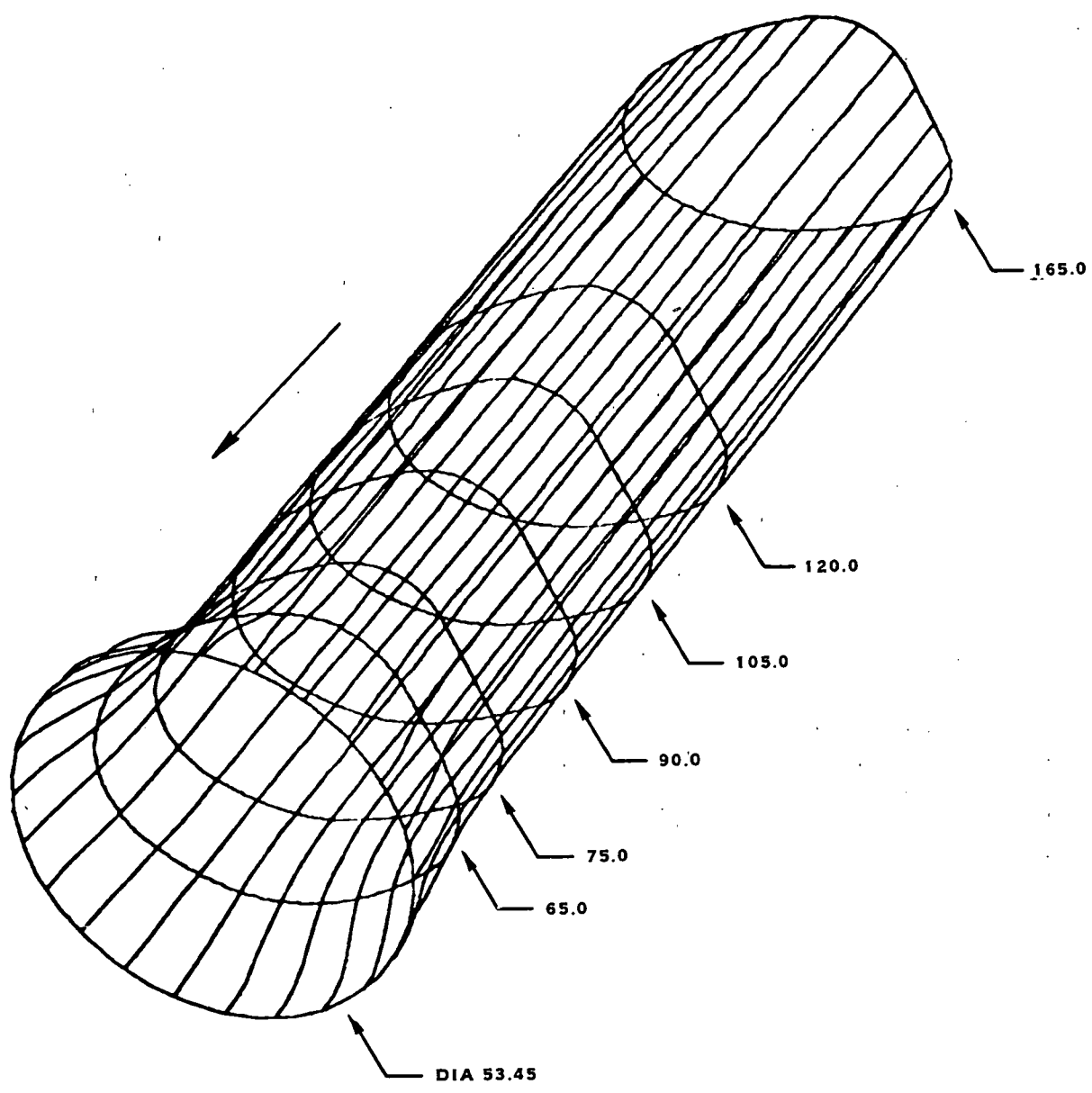
FIGURE 55.   AIRFOIL TO RETENTION BLEND

73

Tooling for the blade filament winding consisted of three major elements: the center steel supporting shaft, the spar mandrel formers and the shell mandrel formers. The shaft was designed using welded steel tubing, channel, and plate as shown in Figure 56. The mandrel was designed in 45 inch (114.3 cm) long segments assembled around the shaft as shown in Figure 57. Each segment employed an aluminum skin over airfoil shaped ribs on 15 inch (38.1 cm) centers. The shell mandrel employed an aluminum skin over airfoil shaped ribs on 15 inch (38.1 cm) centers aligned and keyed to the trail edge of the spar as shown in Figure 58. The sequence for removal of the spar mandrel was: (1) remove the continuous steel shaft, (2) remove the four retaining shafts thus releasing the wood keys (3) remove the keys, (4) remove leading edge section, and (5) remove trailing edge section. The sequence for shell mandrel removal was to remove the alignment keys then collapse and remove the mandrel section. Circular generating disks were designed to fit the spar and blade at two spar and one shell station to provide filament-turn-around near ply drop off locations to minimize material usage.

MANUFACTURE

The fabrication task consisted of three phases: (1) facilities preparations, (2) tool fabrication, and (3) manufacturing prototype blade fabrication. These activities were performed at Hercules, Inc., Allegany Ballistics Laboratory. The facilities preparations included modification of existing equipment and fabrication of new equipment to construct a filament winding machine with the needed capacity. Tool fabrication included the center steel shaft, spar mandrel formers, shell mandrel formers, shell winding offset fixture, generating disks, and mandrel removal equipment. Blade fabrication included spar winding, retention adapter sleeve bonding, shell winding, heat cure,mandrel removal, and inspection. The spar and shell were wound using PPG 1062TNT-15 glass rovings with a Silane finish and EPON 826 resin with Jeffamine D230 hardener.

FACILITIES PREPARATIONS

The filament winding machine fabricated to wind this wind turbine blade consisted of five major components: (1) head stock, drive shaft and drive system, (2) filament delivery carriage and filament delivery system, (3) filament delivery carriage rails and chain drive, (4) carriage program system, and (5) cure hood and hot air blower. Figure 59 shows the carriage rails and chain drive and the head stock. Figure 60 shows the drive shaft and bearings with the spar mandrel installed in the machine. Figure 61 shows the carriage rails and the filament delivery carriage.

STA 750

STA 705

3" TO 2" TAPER
SOLID STEEL

3" STEEL CHANNEL
BOX STRUCTURE

STA 570

4" STEEL CHANNEL
BOX STRUCTURE

STA 435

6" STEEL CHANNEL
BOX STRUCTURE

1/2" STEEL PLATE

12" X 8" X 1/2"
RECTANGULAR
STEEL TUBING

STA 210

ATTACHMENT PLATE

STA 43
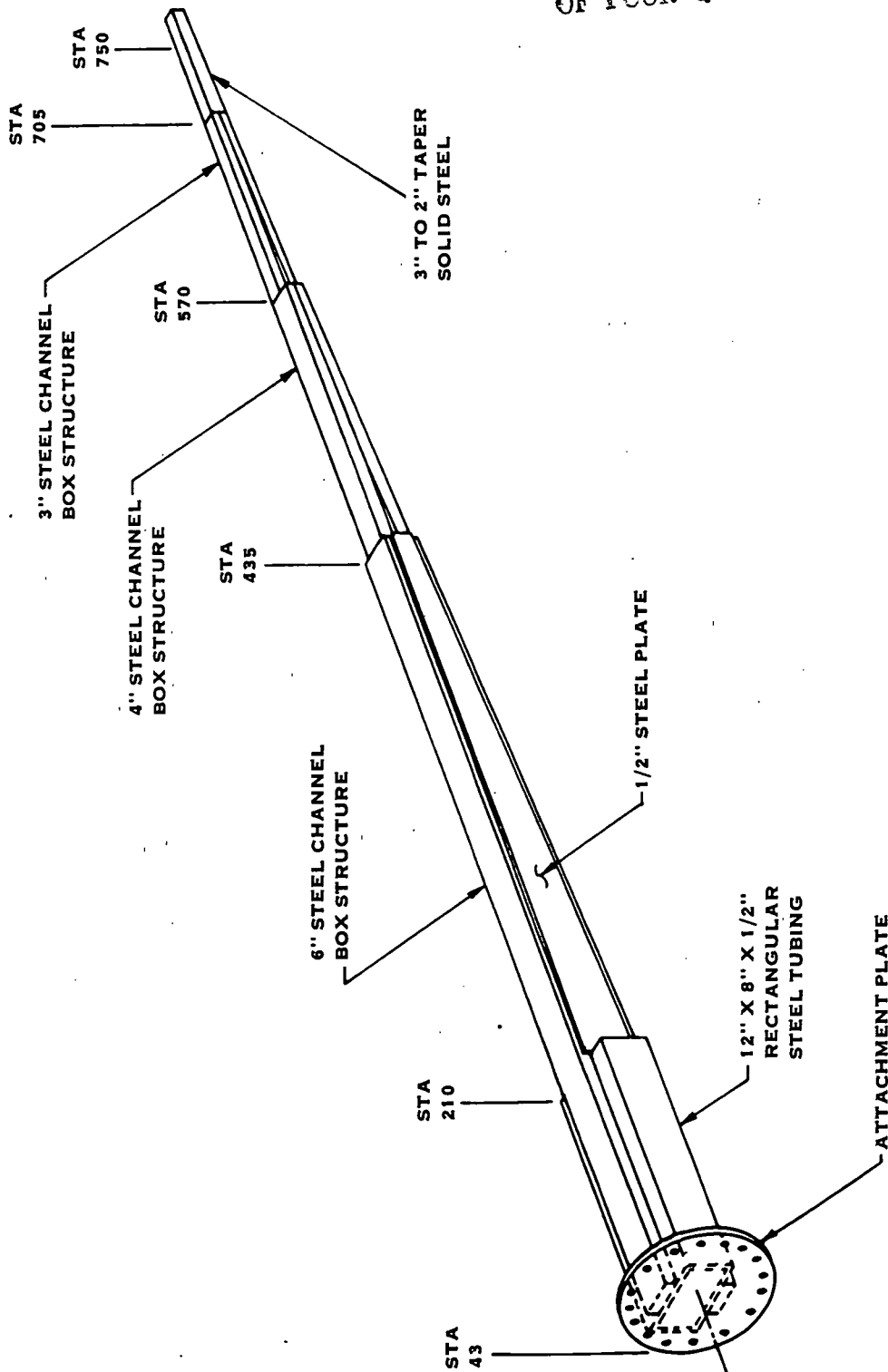
FIGURE 56.   SPAR MANDREL CENTER STEEL SHAFT

PLYWOOD RIBS

WOOD STRINGER

135" TYP

45" TYP

WOOD KEY
CONSTRUCTION

WOOD KEY
(135")

RETAINING SHAFT (PIPE)
(135")

CONTINUOUS
STEEL SHAFT
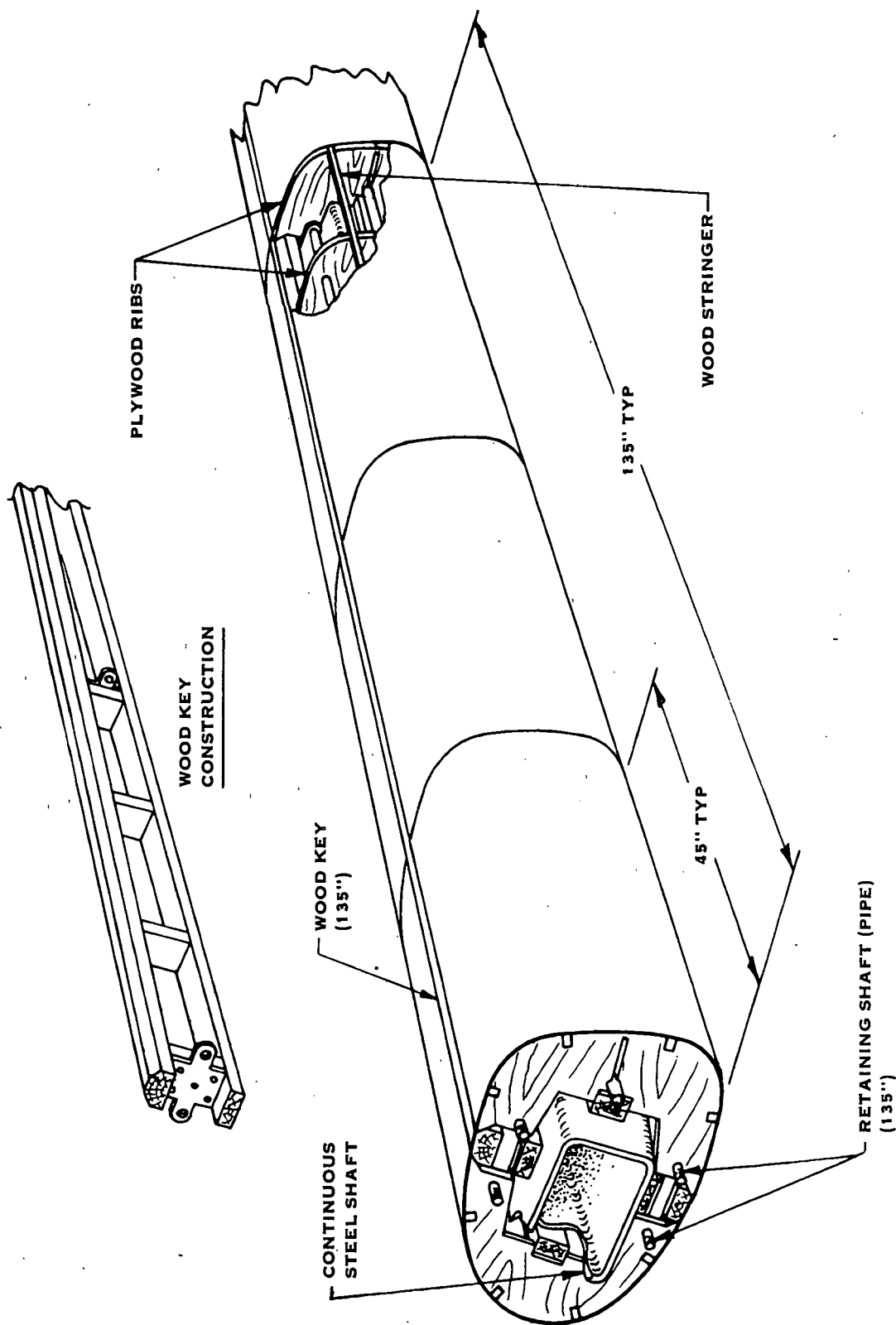
FIGURE 57. SPAR MANDREL SEGMENTS
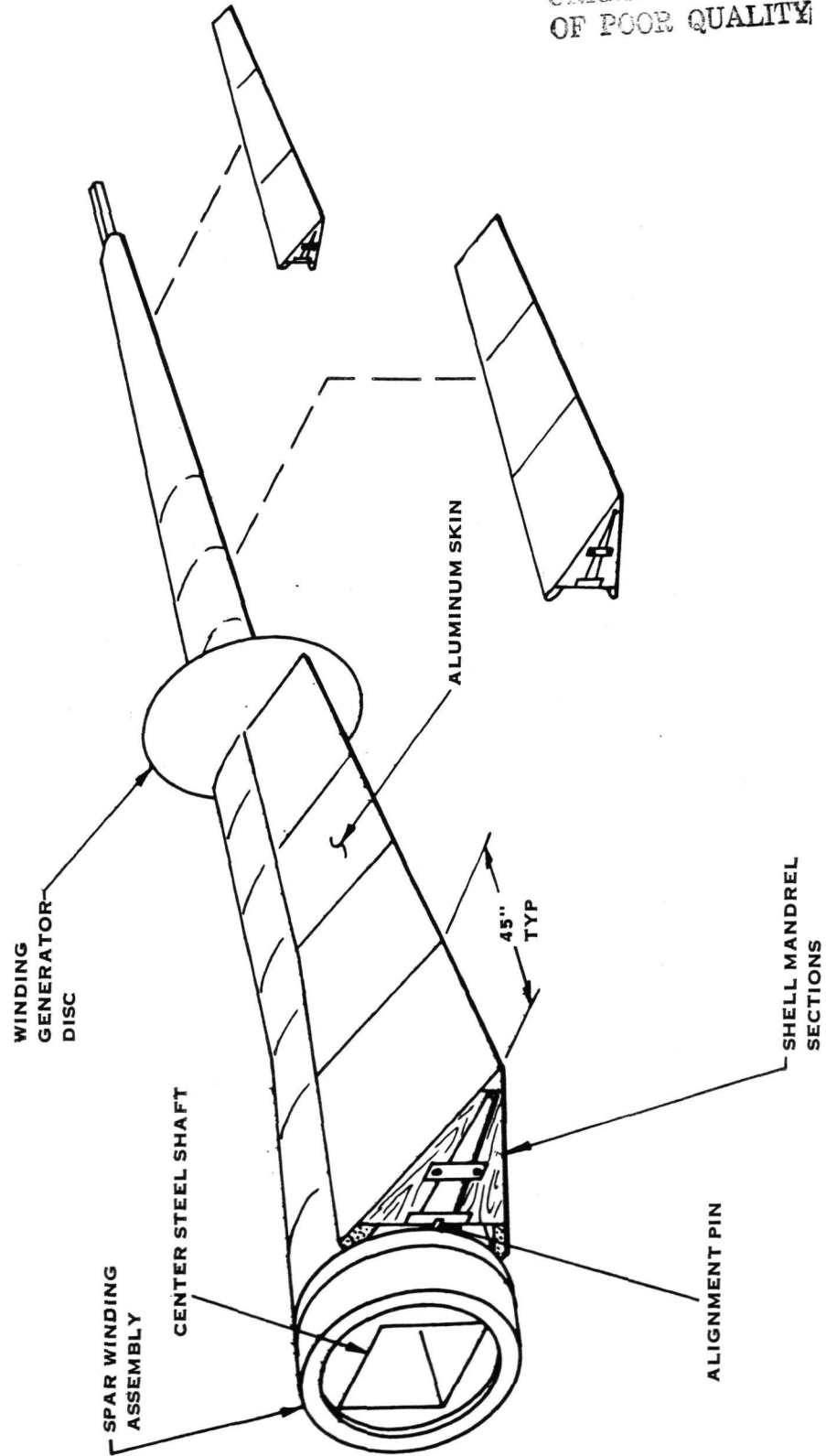
FIGURE 58.   SHELL MANDREL ASSEMBLY

ALUMINUM SKIN

WINDING
GENERATOR
DISC

SHELL MANDREL
SECTIONS

45" TYP

CENTER STEEL SHAFT

SPAR WINDING
ASSEMBLY

ALIGNMENT PIN
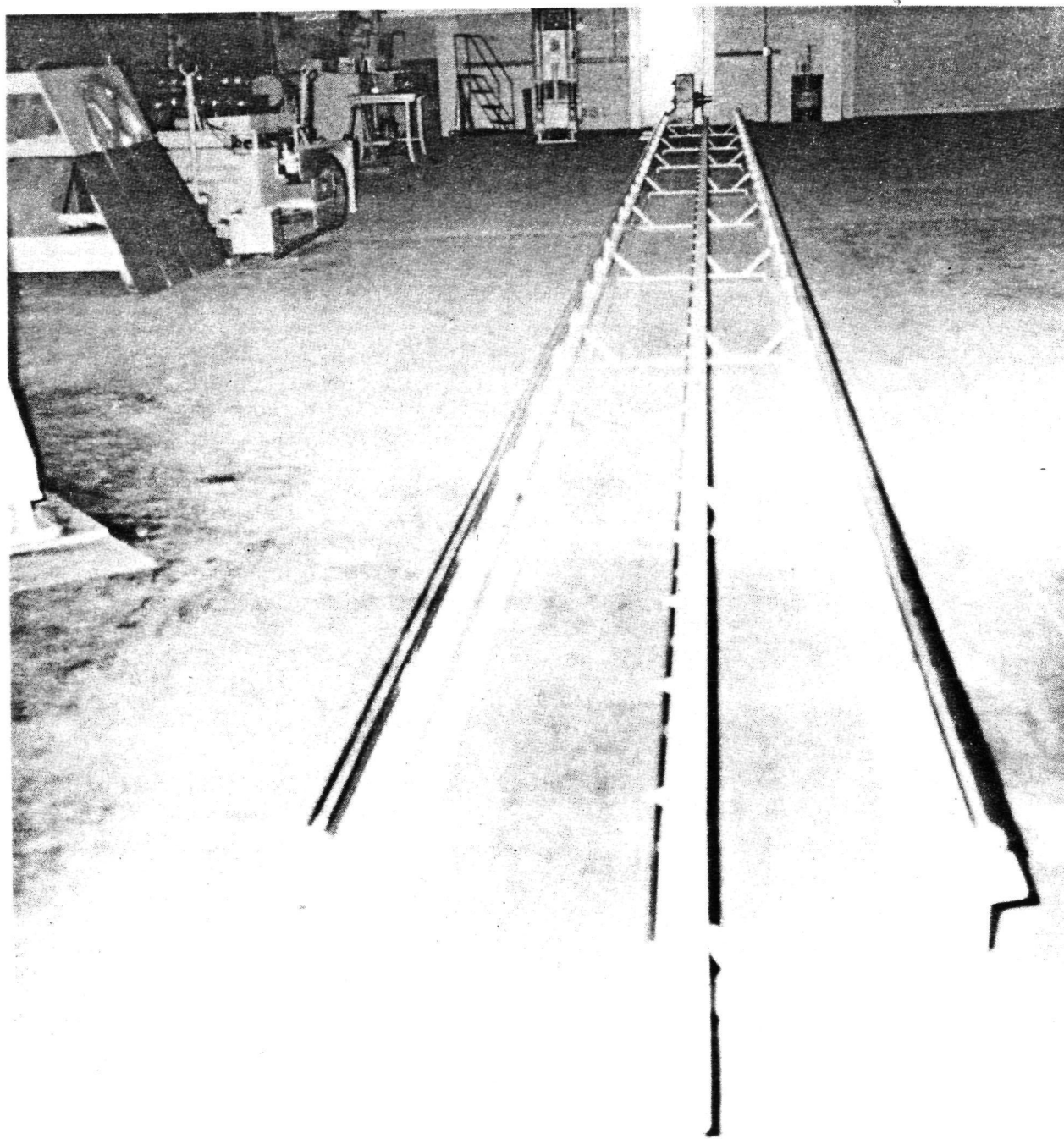
FIGURE 59. FILAMENT WINDING MACHINE PARTS
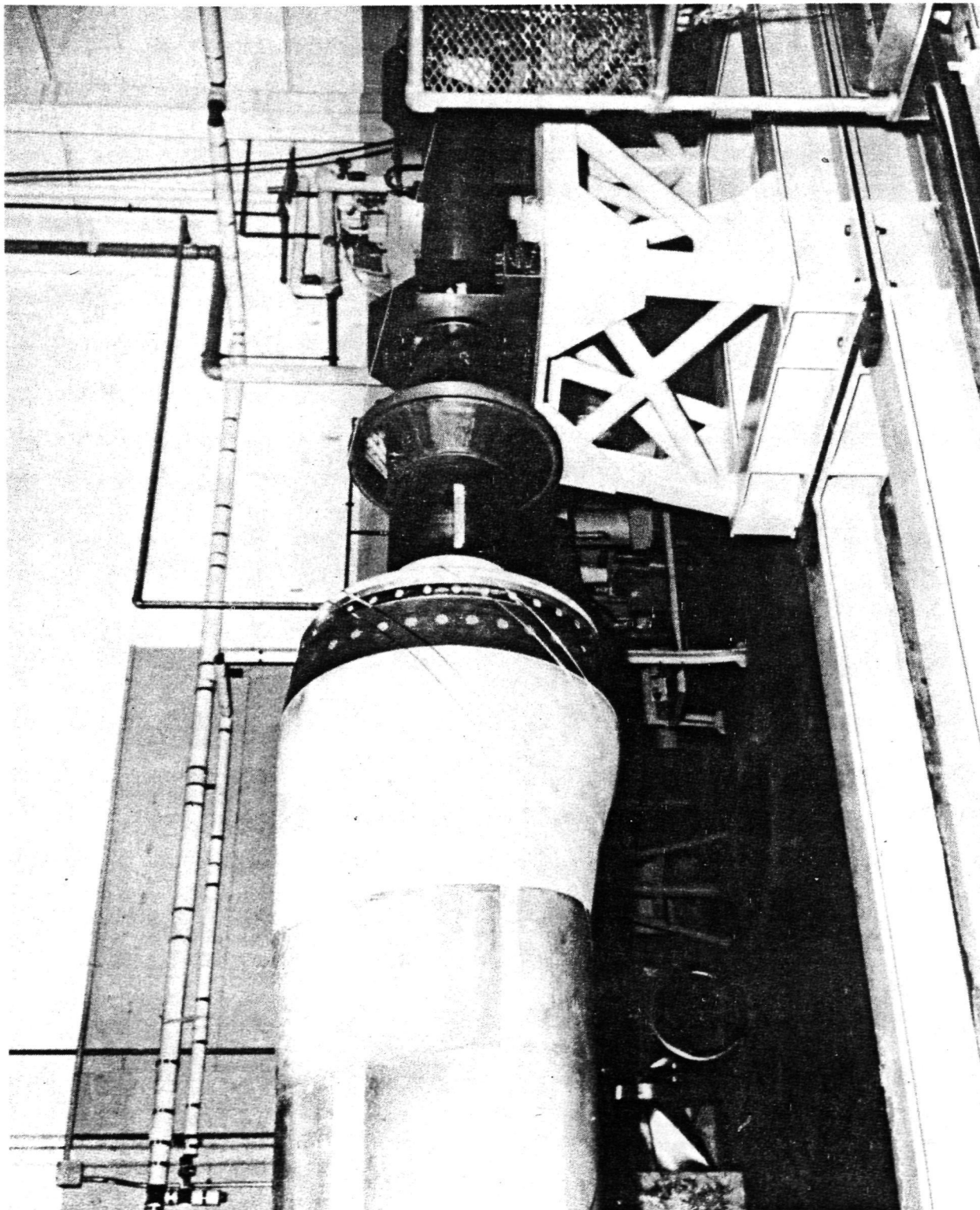
FIGURE 60. FILAMENT WINDING MACHINE PARTS
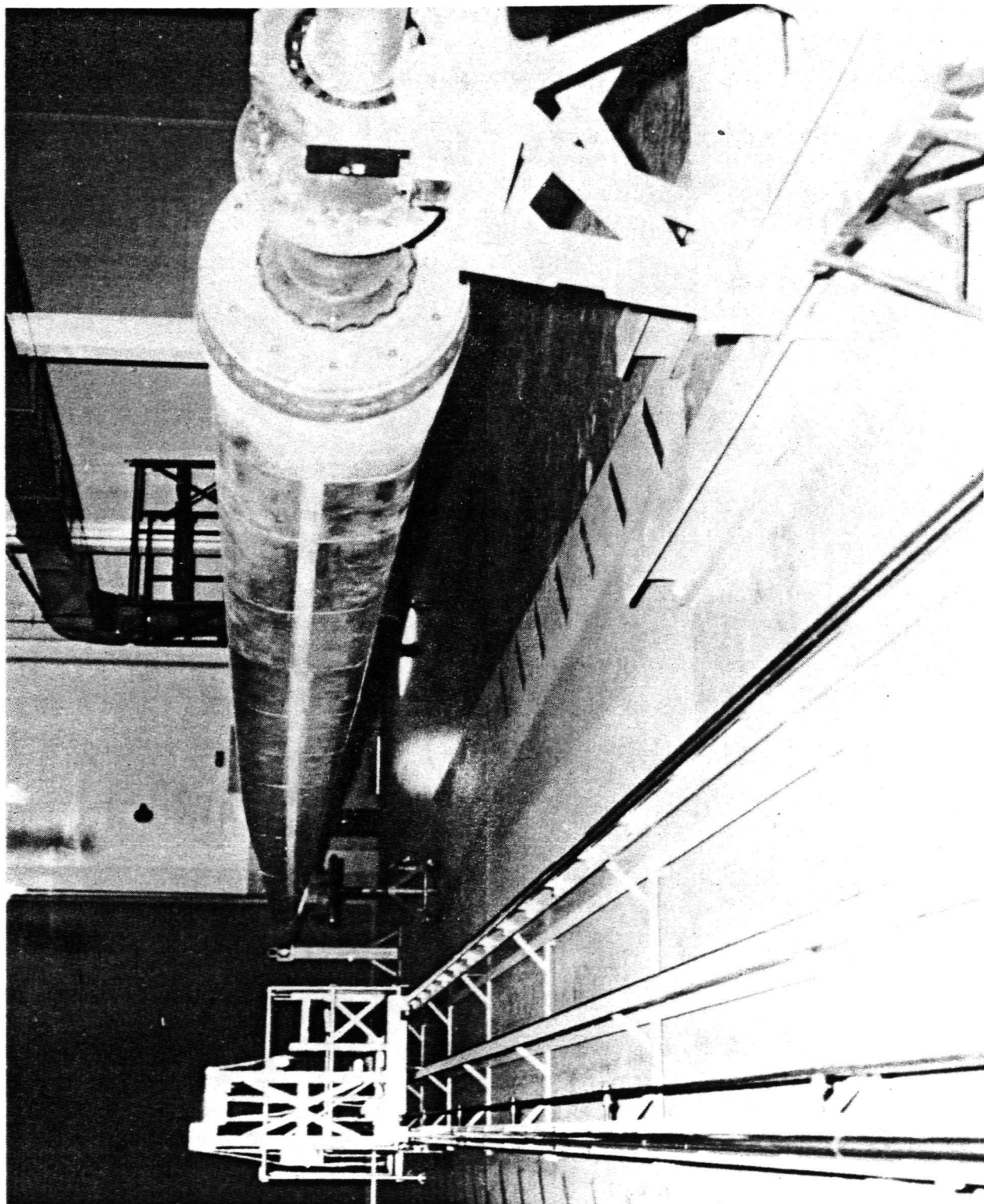
FIGURE 61. FILAMENT WINDING MACHINE

TOOL FABRICATION

Center Steel Shaft

The center steel shaft was a weldment constructed of rectangular box beams, channels, and flat plates. The inboard end of the shaft is shown in Figure 62. The completed shaft as it was installed in the winding machine is shown in Figure 63.

Spar Mandrel Formers

The spar mandrel formers were constructed in 45 inch (114.3 cm) lengths as shown in Figure 64. Each 45 inch (114.3 cm) length consisted of four airfoil shaped plywood bulkheads held in position by wood stringers and covered with an aluminum skin. Three 45 inch (114.3 cm) lengths were assembled together with the leading edge and trailing edge portions separated by 135 inch (342.9 cm) long wood keys which were held in place with metal rods. Each section was attached to the next section by steel cables to facilitate section removal. Figures 65 through 70 show a mockup of a 45 inch (114.3 cm) mandrel length and illustrate the disassembly procedure. The sequence for removing the spar mandrel formers was described in an earlier section under Tool Design. Briefly, the center shaft is extracted, then four retaining shafts are withdrawn which release the wood keys. After the keys are removed the leading and trailing edge forms may be taken out.

Shell Mandrel Formers

The shell mandrel formers were constructed in the same manner as the spar mandrel formers with airfoil shaped plywood bulkheads, wood stringers, and aluminum skins. Positioning on the trailedge of the spar was accomplished through the use of a slotted wood key placed over pins wound into the spar at various stations along the length.

Removal was accomplished by removing the key, collapsing the section away from the face and camber sides and sliding it along the spar. Figure 71 shows the 75 inch station bulkhead with details of the mandrel construction. Figure 72 shows the first three 45 inch (114.3 cm) lengths of shell mandrel formers.

The blend from the inner adapter sleeve to the first airfoil section at the 75 inch (1.9m) station was fabricated from wood blocks machined to template fit as shown in Figure 73. Some modifications to the blend contour were required due to filament bridging in this area. The modifications were studied on the interactive design system and incorporated by adding material to the mandrel surface.
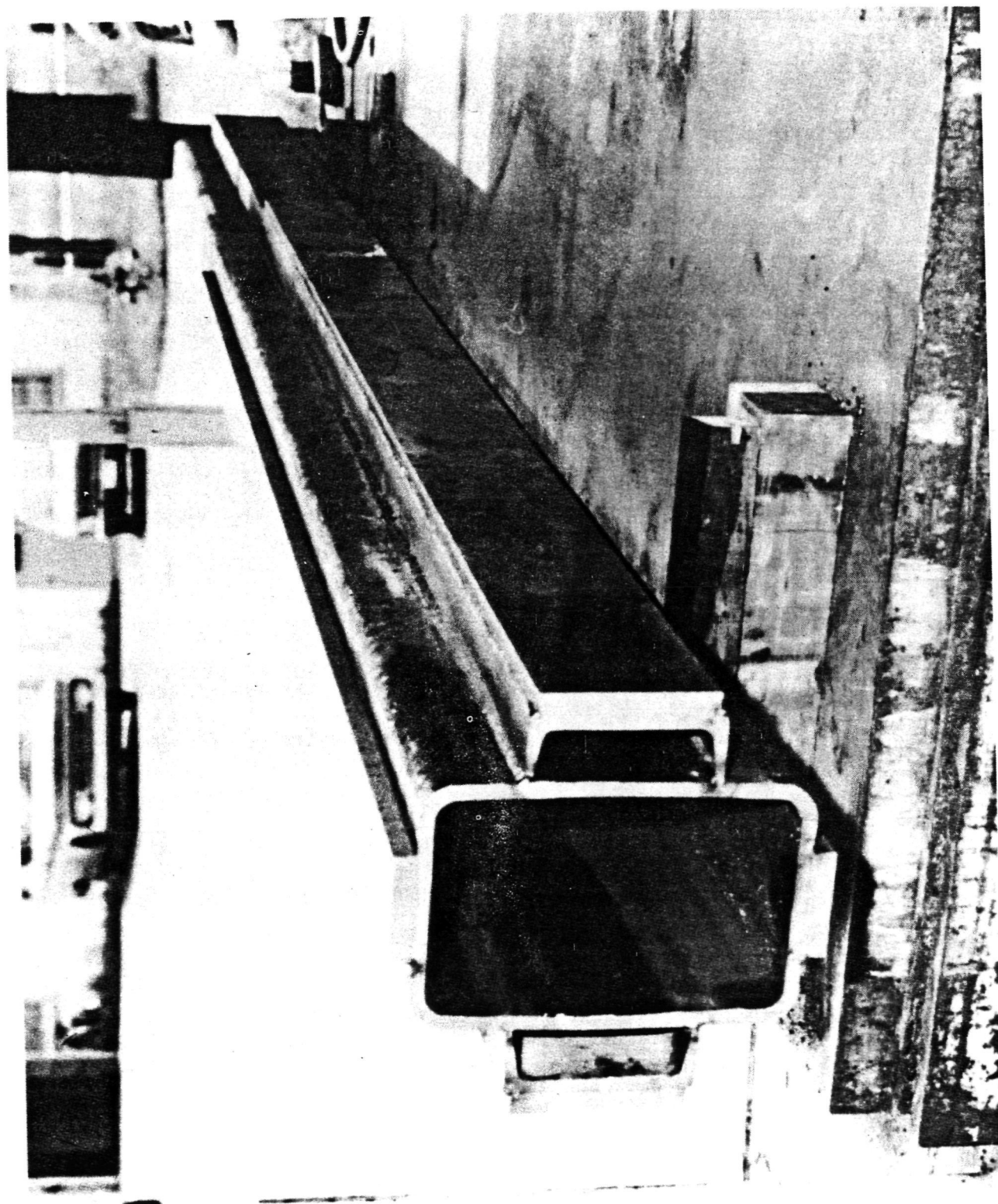
FIGURE 62. MANDREL CENTER STEEL SHAFT
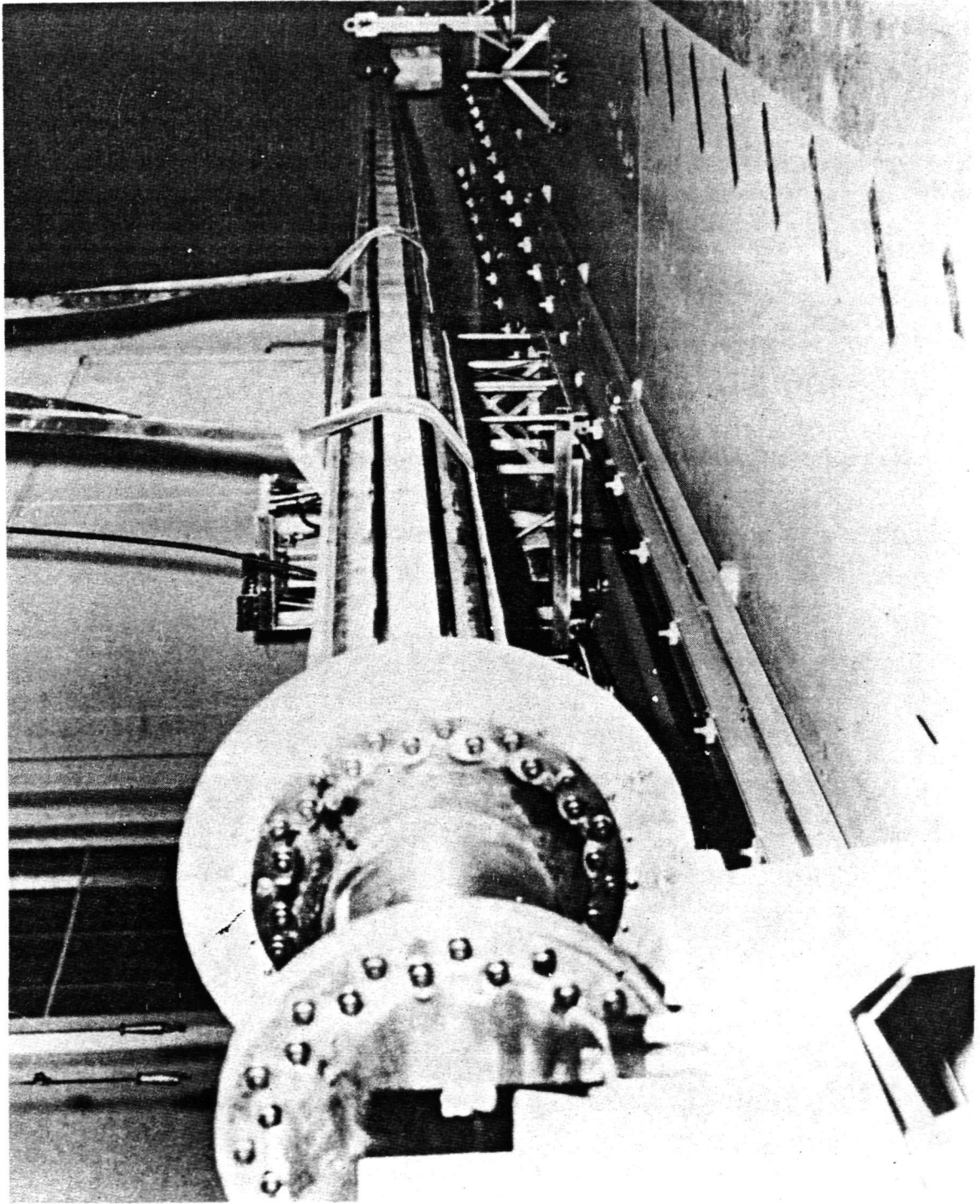
FIGURE 63. MANDREL SHAFT INSTALLATION
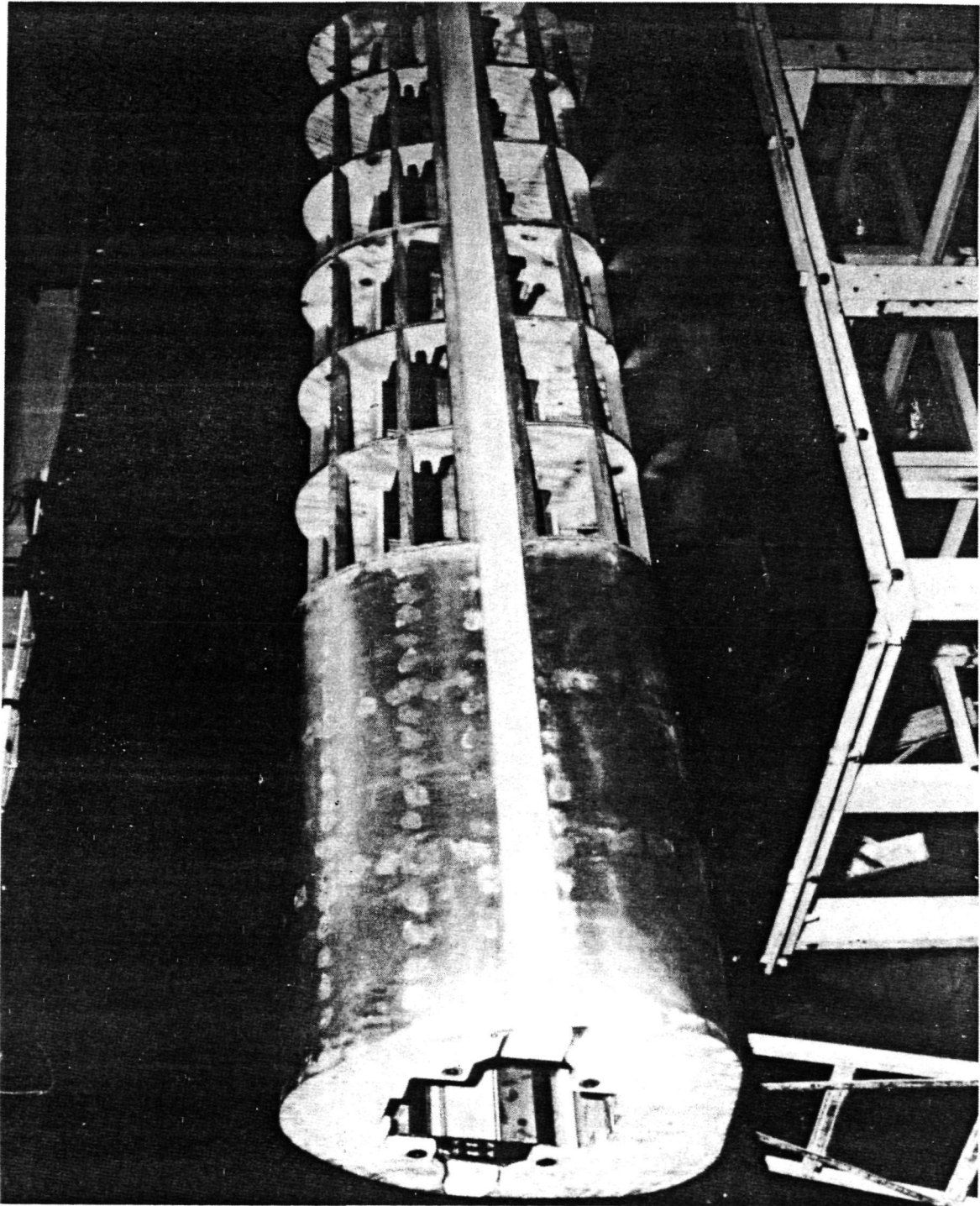
FIGURE 64. SPAR MANDREL FORMERS
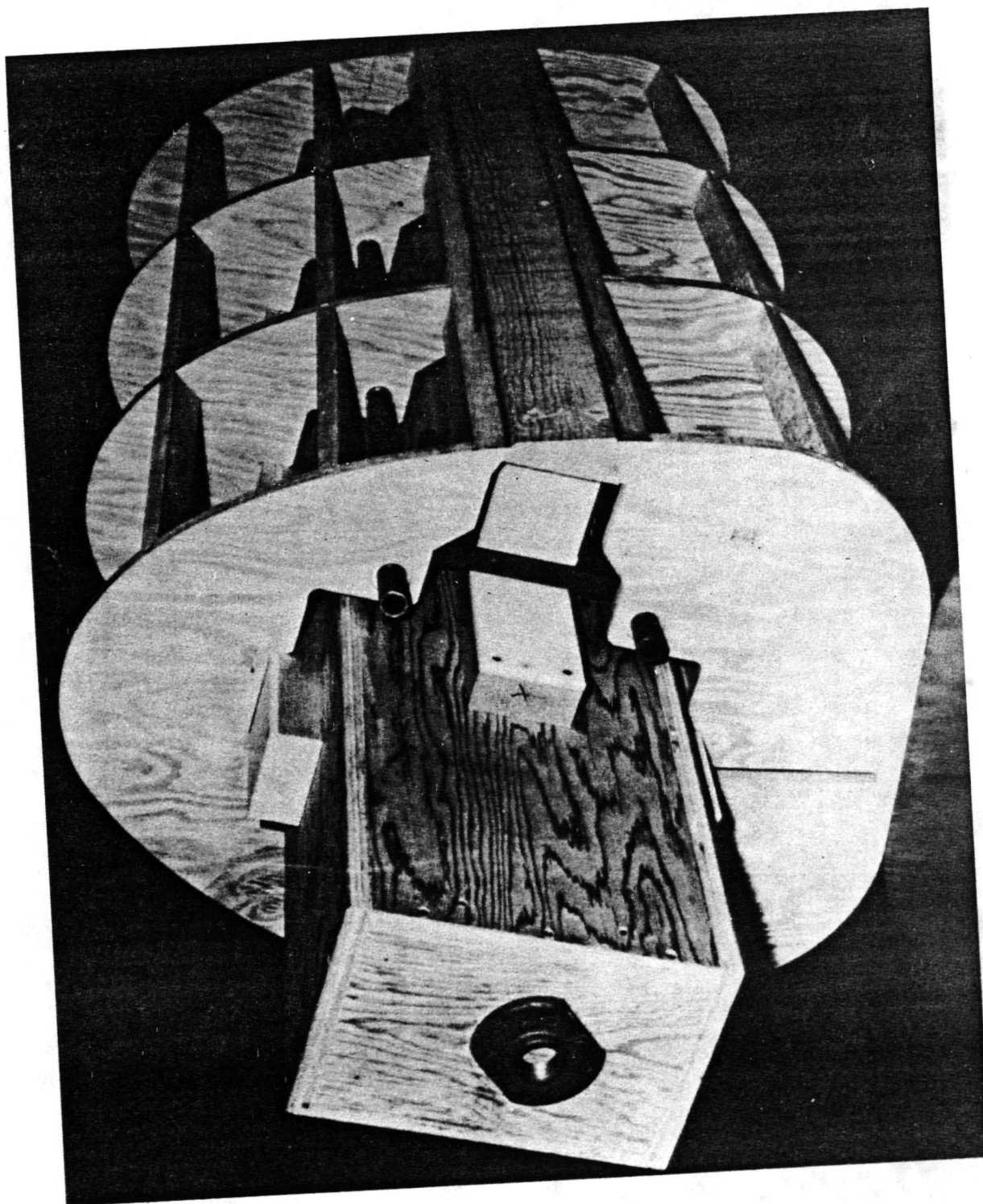
FIGURE 65. SPAR MANDREL FORMER MOCKUP
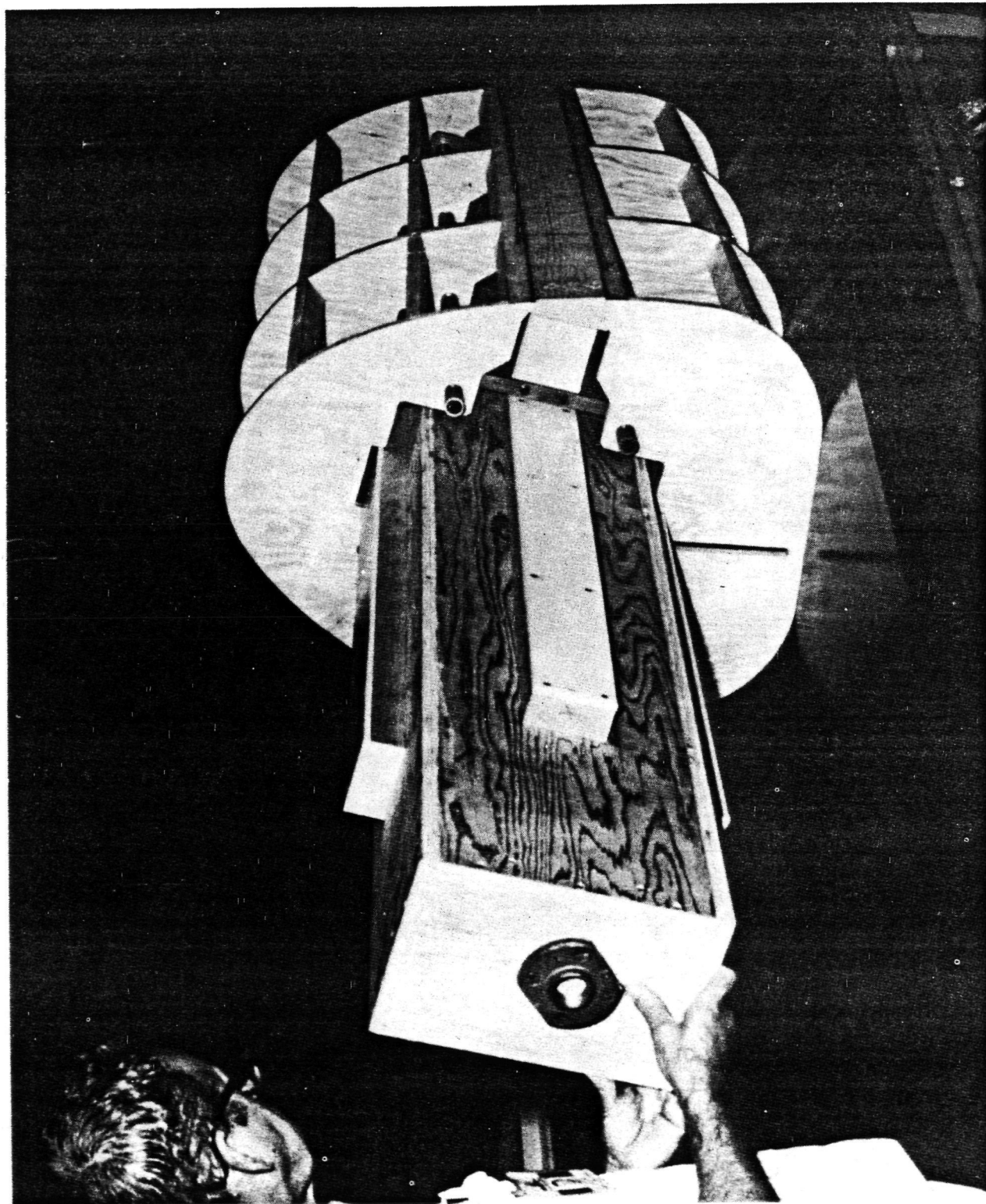
FIGURE 66. SPAR MANDREL FORMER DISASSEMBLY
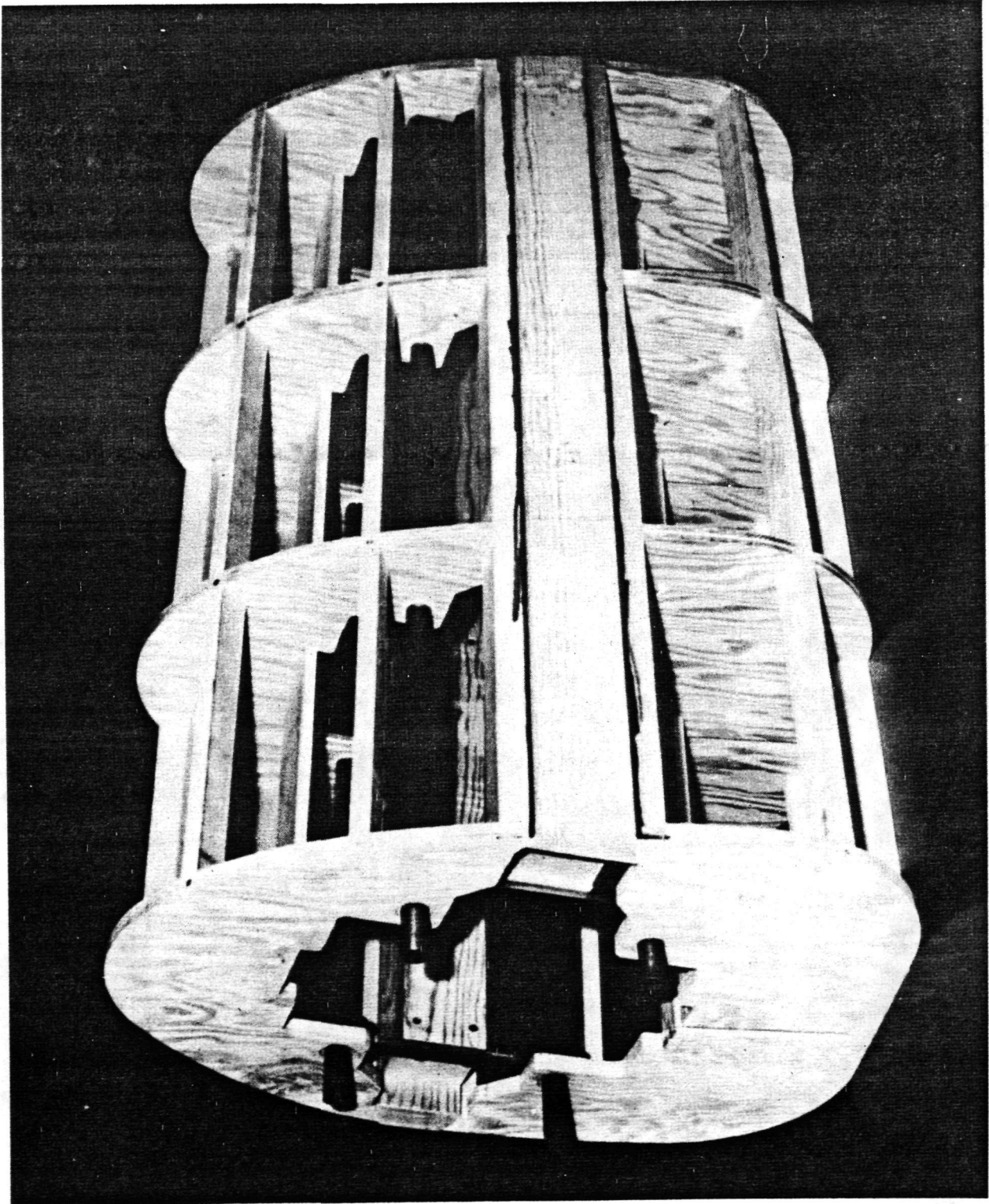
FIGURE 67. SPAR MANDREL FORMER DISASSEMBLY

C-2
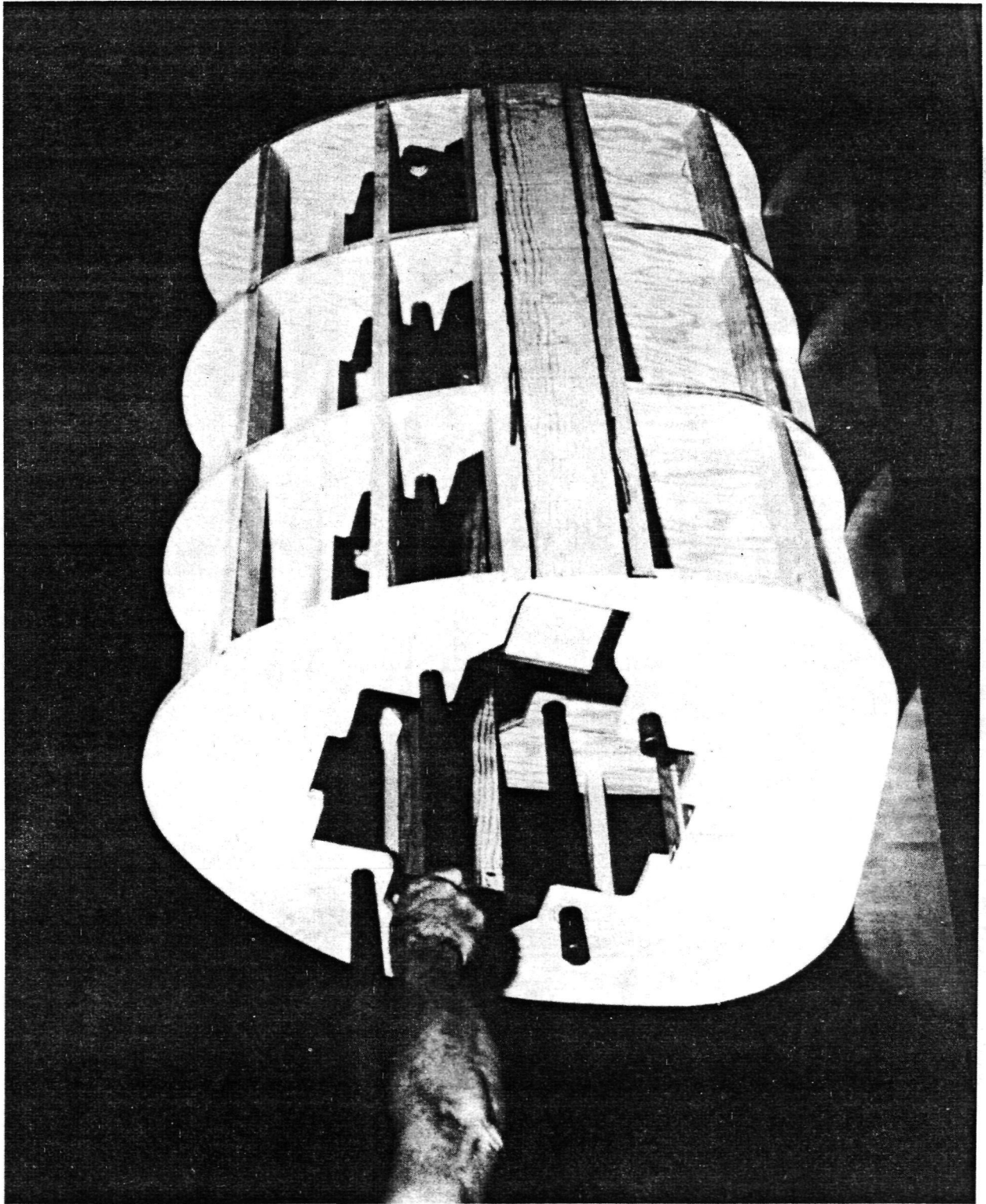
FIGURE 68. SPAR MANDREL FORMER DISASSEMBLY
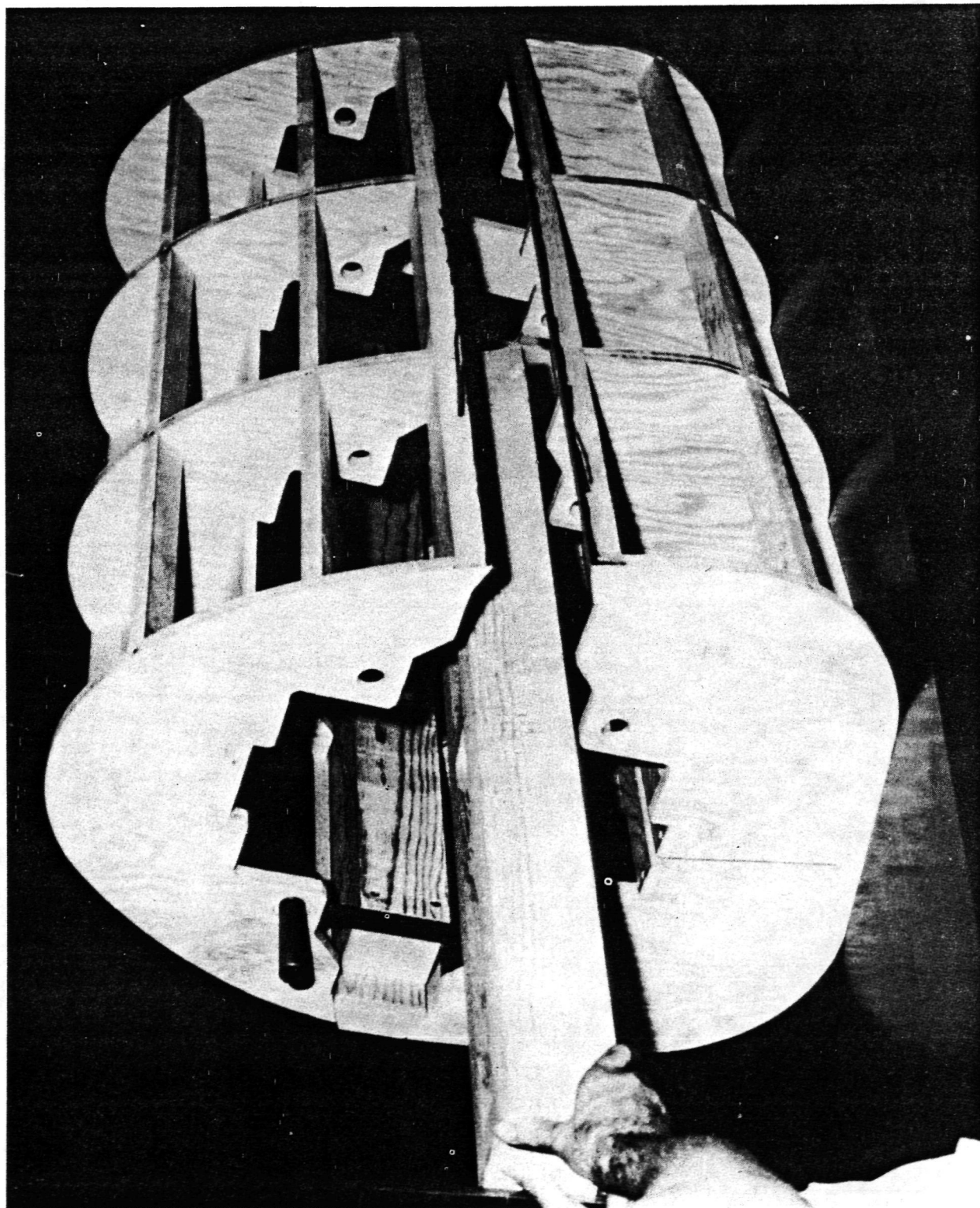
FIGURE 69. SPAR MANDREL FORMER DISASSEMBLY
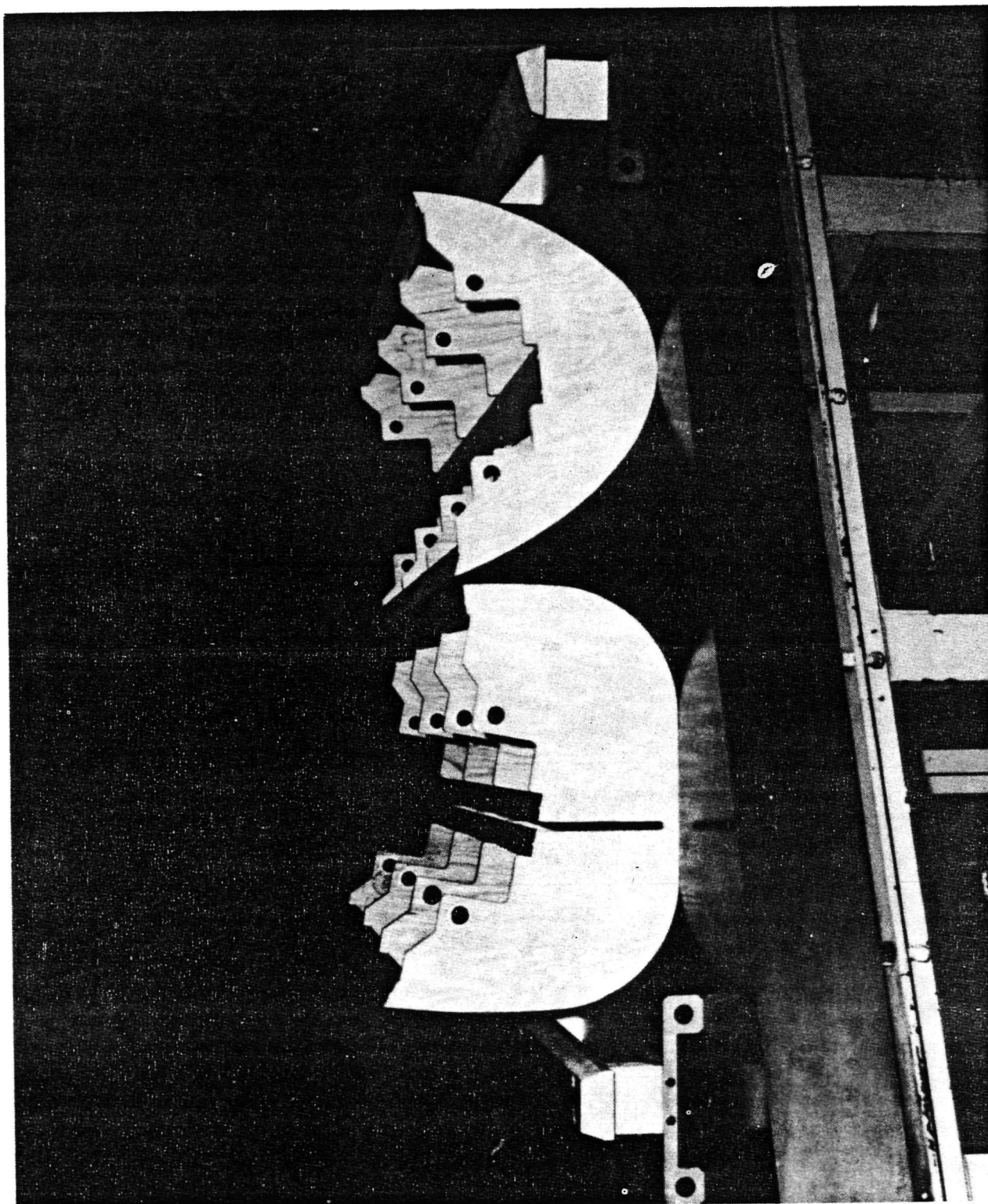
FIGURE 70. SPAR MANDREL FORMER DISASSEMBLED
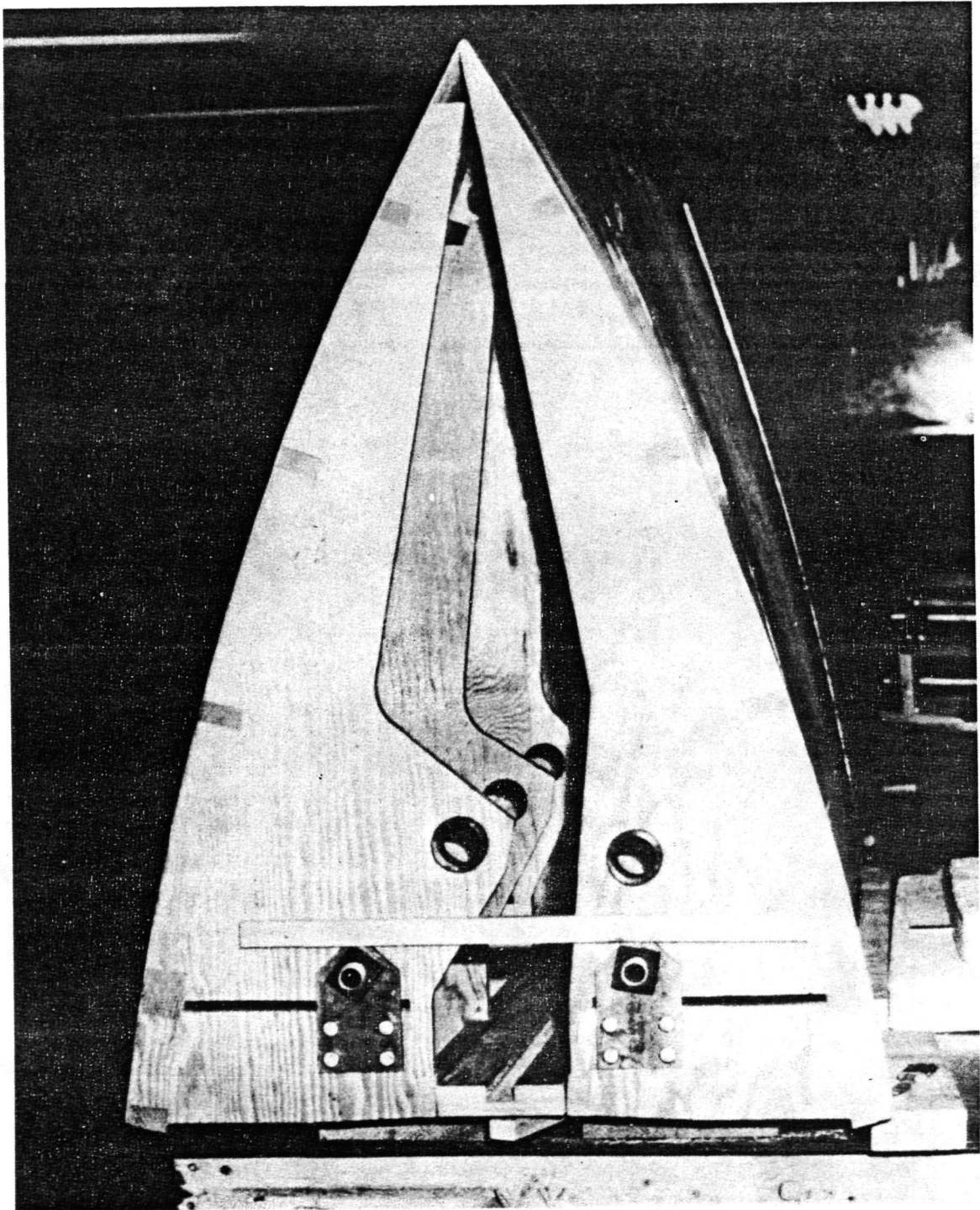
FIGURE 71. SHELL MANDREL FORMER
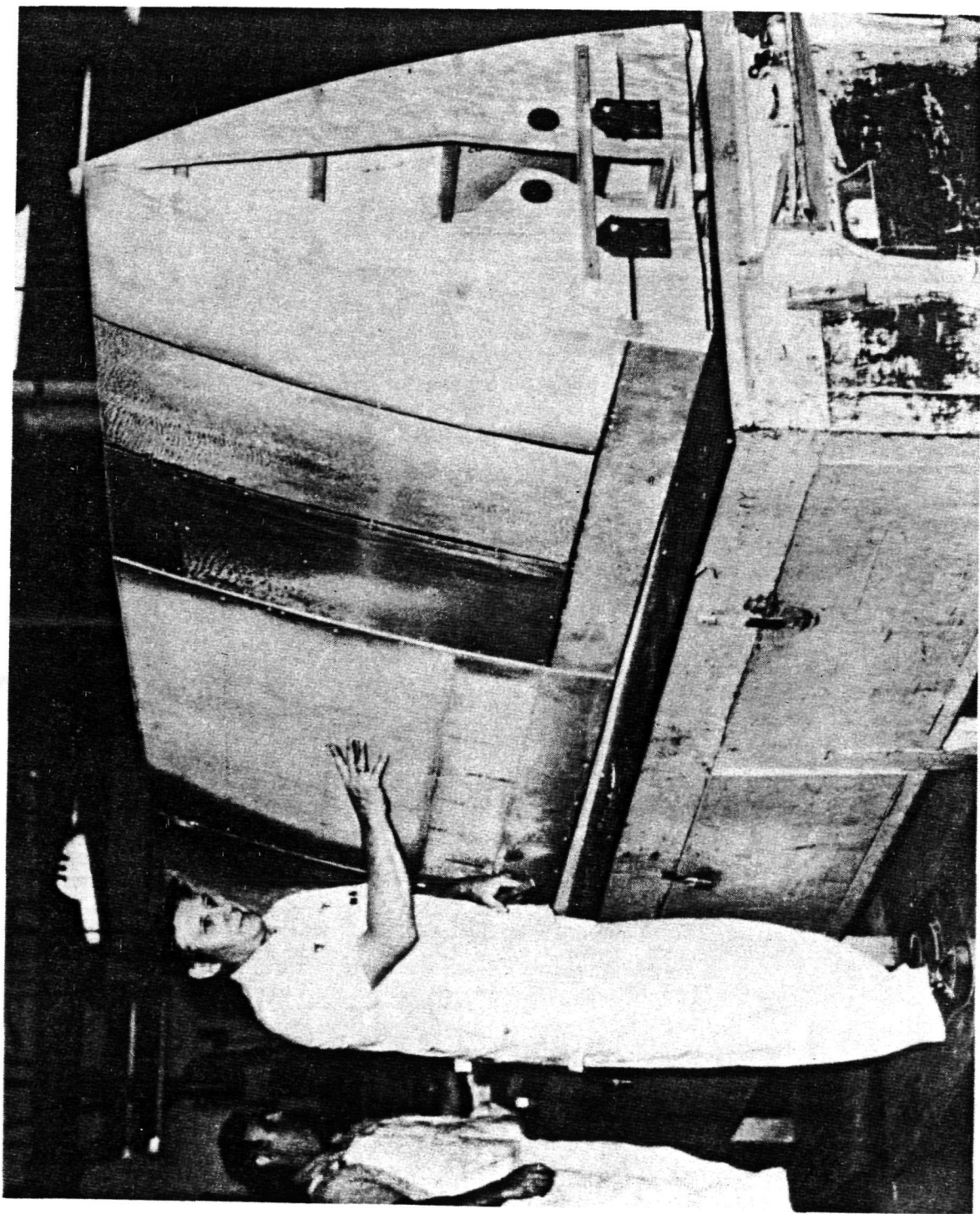
FIGURE 72: SHELL MANDREL FORMERS
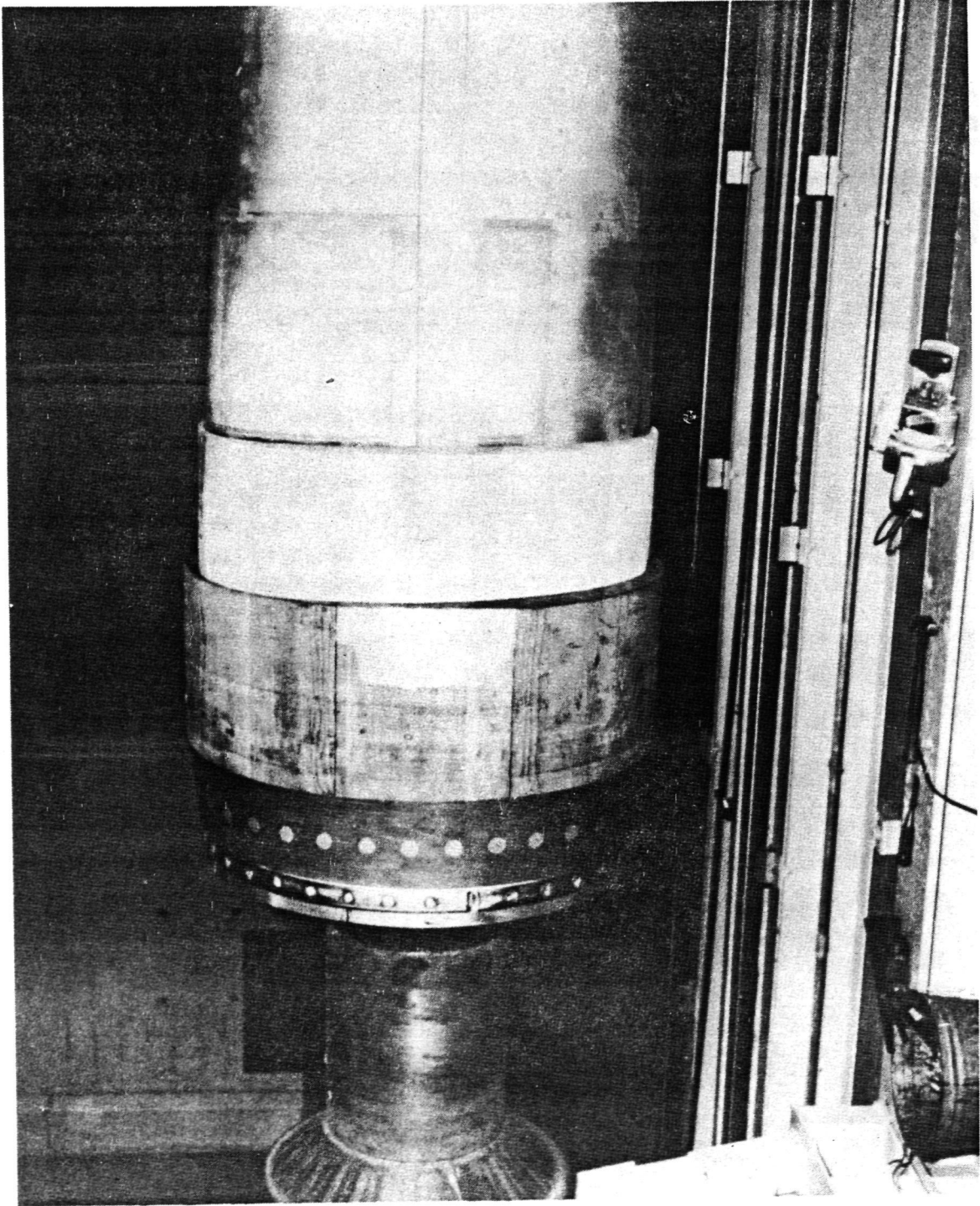
FIGURE 73. RETENTION-TO-AIRFOIL BLEND

93

Shell Mandrel Offset Fixture

Since it is necessary during filament winding to rotate the mandrel about the geometric center line of the part being wound it was necessary to fabricate an offset crank fixture for the shell winding operation. This fixture is shown as installed in Figure 74.

Generating Disks

In order to minimize material usage during filament winding parts with varying wall thickness it is desirable to terminate or drop off wound plies at various locations along the length of the part being wound. Through the use of symmetrical generating disks on the part it is only necessary to wind to the disk rather than to the end of the part thus less material is scrapped when part of the ply is cut and dropped off.

Trial Winding

The full spar mandrel was assembled on the center shaft and winding trials were conducted to program the winding machine to produce the desired filament pattern on the blade. The fully assembled spar mandrel is shown in Figures 61 and 75. The full length pattern was programmed first as shown in Figure 76. The mandrel sections were removed from the tip to the 570 inch (14.48 m) station where a generating disk was assembled. The pattern to the 570 inch (14.48 m) station disk was programmed by slight modifications to the full length program. Mandrel sections were then removed from the 570 inch (14.48 m) station to the 345 inch (8.65 m) station. The final spar pattern was programmed to complete the spar winding programs,

Shell winding patterns were programmed after spar fabrication and shell mandrel assembly in the same manner as the spar patterns were programmed.

BLADE FABRICATION

Adapter Sleeves

Both the inner and outer adapter sleeves were machined from ASTM A-36 steel. The finish machined sleeves were plated all over for corrosion protection. Undersize bolt holes were provided in the outer sleeve for use as drill bushings for drilling holes through the fiberglass and the inner sleeve. The surface around the location of the holes on the inner sleeve was not plated to preclude chipping, cracking, or delamination during the subsequent drilling operation.
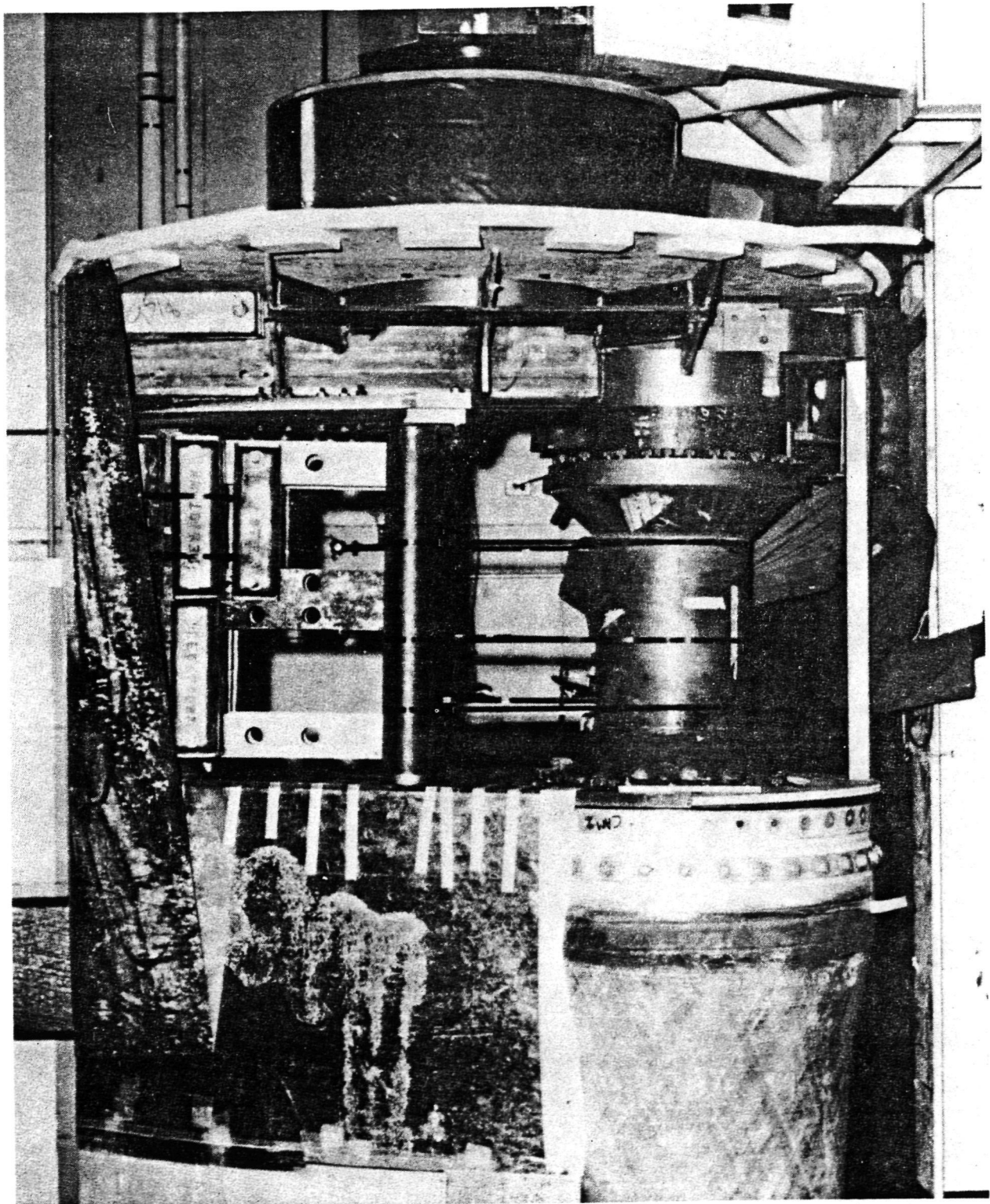
FIGURE 74. SHELL MANDREL OFFSET FIXTURE
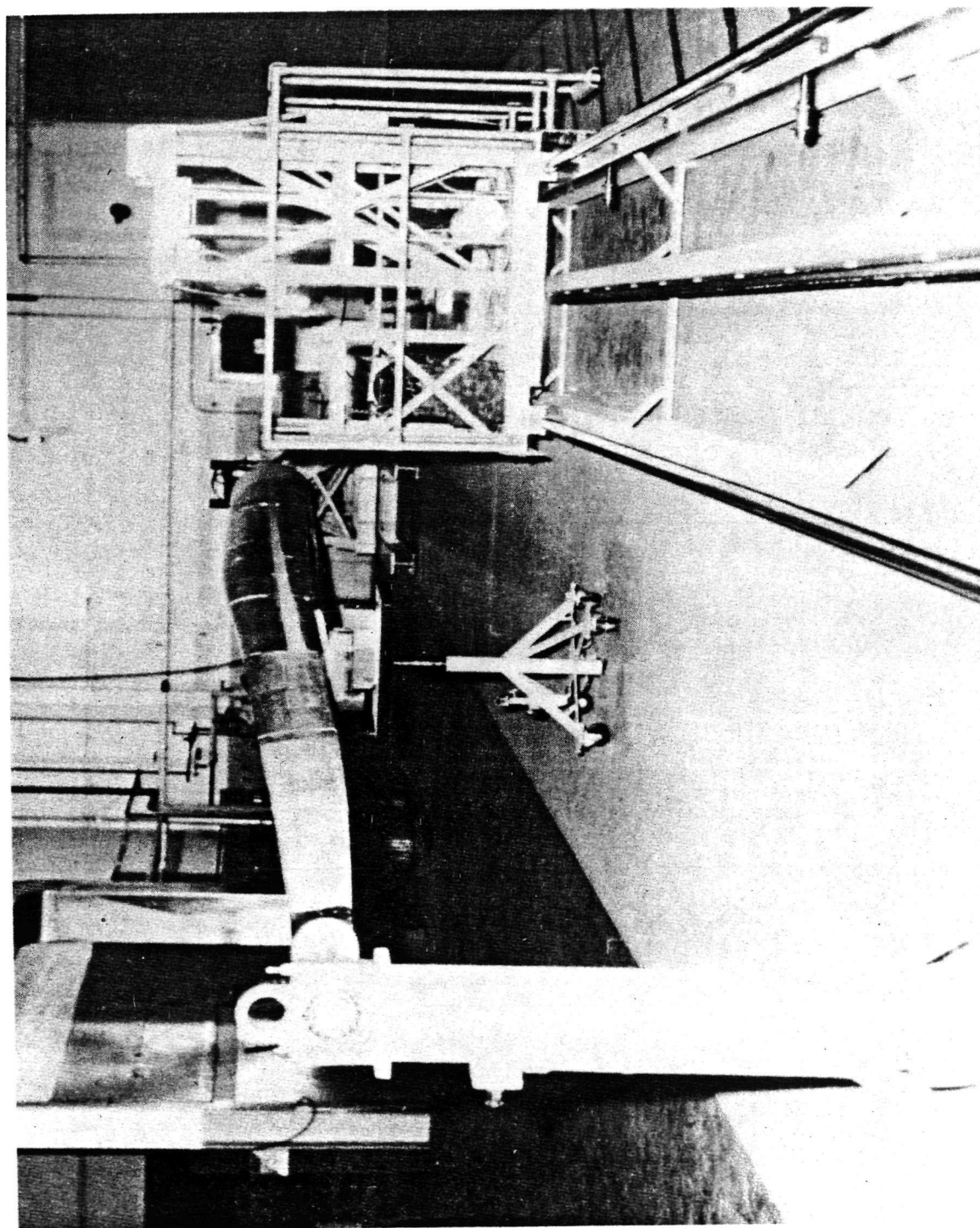
FIGURE 75. ASSEMBLED SPAR MANDREL FORMERS
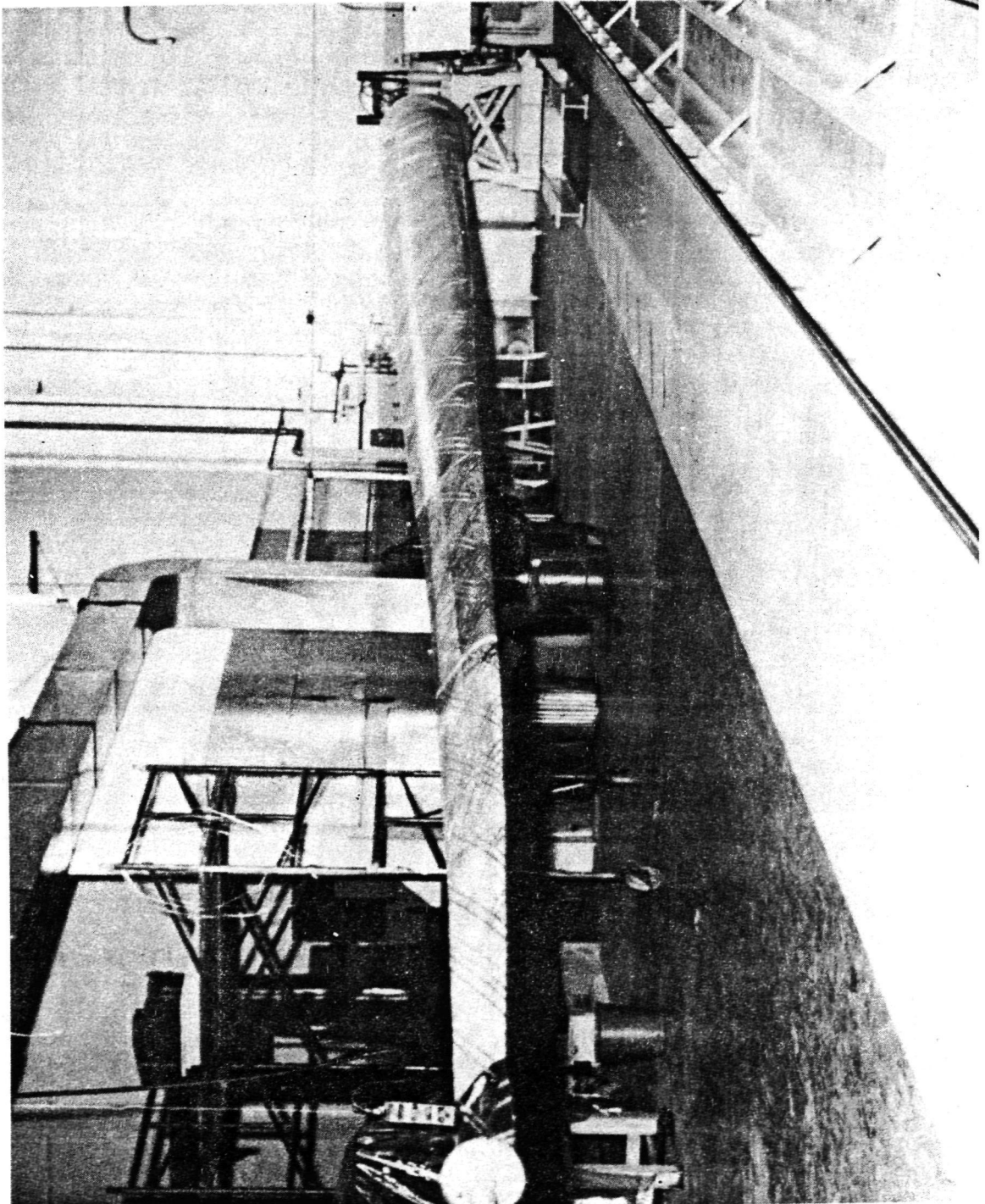
FIGURE 76. SPAR WINDING TRIAL PATTERN

Spar

The spar was integrally filament wound over the inner adapter sleeve.
Epoxy adhesive was applied to the bond surface of the sleeve as shown in
Figure 77. The fiberglass thickness required between the inner and outer
sleeves was achieved by interleaving fiberglass cloth with the filament
layers. The first plies of this cloth were applied directly over the adhe-
sive on the inner sleeve and the first filament helical layer was wound
over the cloth. Plies of fiberglass cloth were applied in the retention
area between each filament helical layer, Figure 78. The rapid build up
in thickness of the glass cloth resulted in some filament bridging, a
condition in which the filament being wound does not follow the mandrel
surface but bridges across "high spots" along the filament path on the
mandrel. This results in a lack of compression of the filament layer
since there is nothing under the lowest level for the upper levels to
push against. To eliminate the bridging extra layers of fiberglass cloth
were applied to the spar to fill up the bridging areas. This was a major
contributor to the increased spar weight. Figure 79 shows the completed
windings to the 345 inch (8.76 m) station with the spar mandrel formers
assembled through the 570 inch (14.48 m) station. After winding each
layer, a single 90° filament with a two inch spacing was wound over the
layer to hold it in place after it had been trimmed to the proper length.
Additional fiberglass cloth was applied in the retention area between
the helical layers wound to the 570 inch (14.48 m) station. After winding
helical layer four it was observed that some welds in the drive shaft had
fractured. This shaft was reinforced with steel gussets, seen in Figure 82
and presented no further problems. The remaining spar mandrel formers
were assembled and full length helical layers were wound completing the
spar filament winding. Figure 80 shows the completed spar with an ex-
ternal nylon peel ply which was applied to protect the spar surface from
contamination during subsequent adapter sleeve bonding operations.

Outer Adapter Sleeve Bonding

The finished wound spar was room temperature cured for 48 hours so that the
material in the retention area could be machined. The spar bonding surface
for the outer adapter sleeve was machined as shown in Figure 81. After
machining to obtain the proper bond line gap, epoxy adhesive was applied
to the spar and sleeve bonding surfaces. The sleeve was pushed onto the
spar to the proper radial location and held until the adhesive was cured.
The finished bonded sleeve is shown in Figure 82. Using the predrilled
holes in the outer sleeve as drill bushings the adapter bolt holes were
drilled and reamed to proper size. The hole drilling operation is shown
in Figure 83. The outboard row of retention bolts was assembled as shown
in Figure 74. Assembly of the inboard row of bolts was delayed until
mandrel removal due to interference with the mandrel structure preventing
their assembly.

Shell

The shell winding offset fixture was assembled as shown in Figure 74.
Figure 84 shows the cowling over this offset fixture to provide a filament
winding surface. It also shows the shell mandrel assembled to the spar and
held in place with metal straps so that trial windings could be accomplished.
Following completion of the winding trials, the shell was wound to the
525 inch (13.34 m) station as shown in Figure 85. The dark bands on the
blade indicate the location of shell ply drop offs. Shell helical layers
one and two were wound to the 525 inch (13.34 m) station generating disk.
During winding of shell helical layer two, the machine revolution counter
malfunctioned. This resulted in filament overlap and the need to apply
additional material to obtain a complete layer. These extra circuits
contributed to the shell overweight problem. A routine inspection of the
mandrel drive tooling revealed that some welds in the offset fixture were
fractured. Strengthening members were added to the fixture and the frac-
tured welds were repaired. This fixture caused no further problems during
subsequent winding. The shell mandrel was assembled to the tip and the
final shell layers were wound over the full length of the blade. The
pattern selected for winding the shell was an eighteen circuit pattern.
A circuit is defined as one pass of filament band from shank to tip to
shank. In an eighteen circuit pattern, eighteen circuits are required
before two filament bands end up side by side. This results in a multi-
tude of band cross overs commonly called "basket weaving," which produce
filament bridging. Surface voids associated with these problems were
filled by applying excess resin and a complete 90° filament overwrap.
This was a major cause of overweight in the shell. A two inch wide nylon
peel ply was wound over the shell for protection and to prevent filament
surface contamination during mandrel removal and blade shipping. The
nylon peel ply was applied with resin to insure that it would remain in
place during subsequent handling. The resin remaining in the blade follow-
ing removal of the peel ply also contributed to the shell overweight
problem.
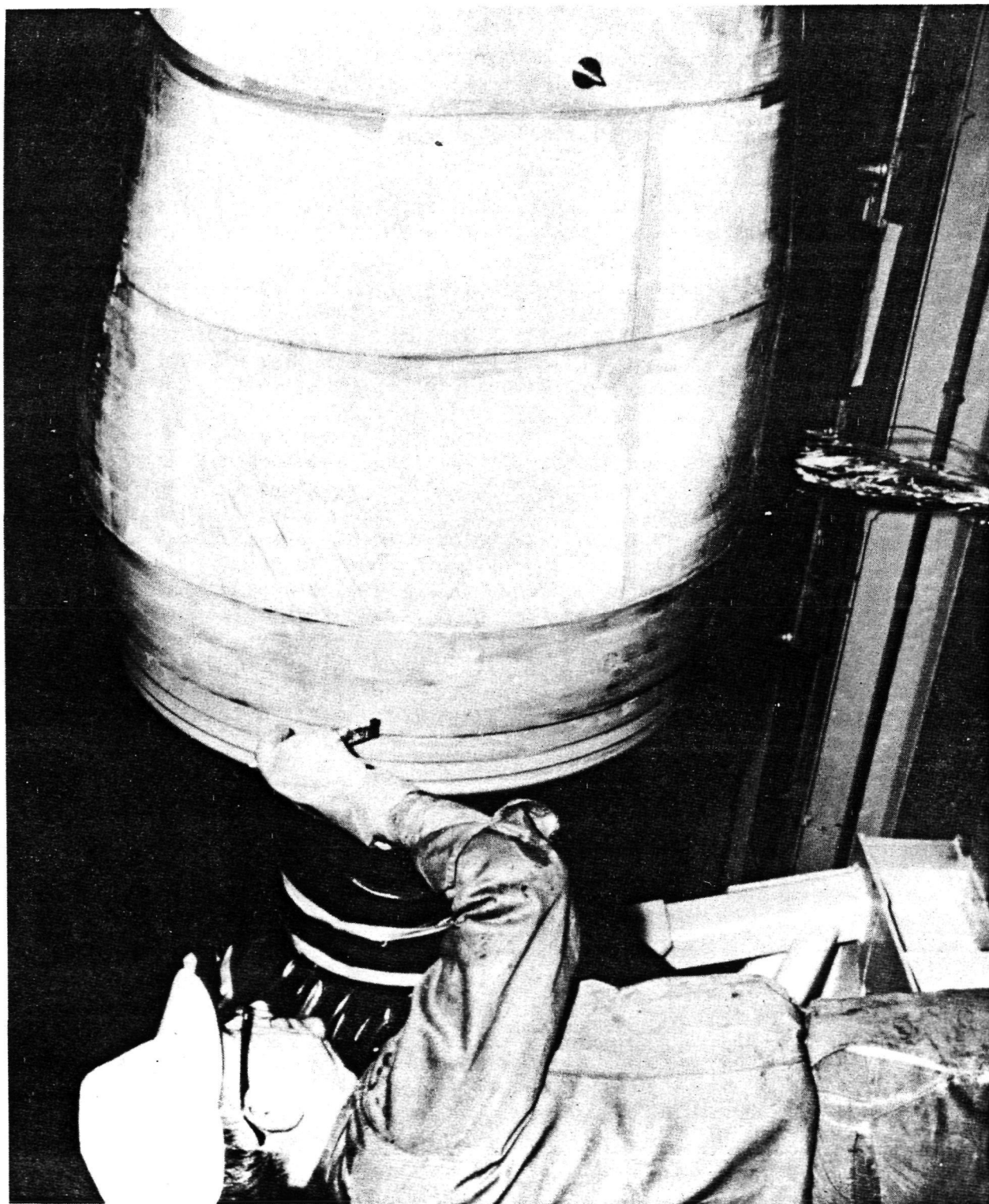
FIGURE 77. INNER RETENTION SLEEVE ADHESIVE APPLICATION
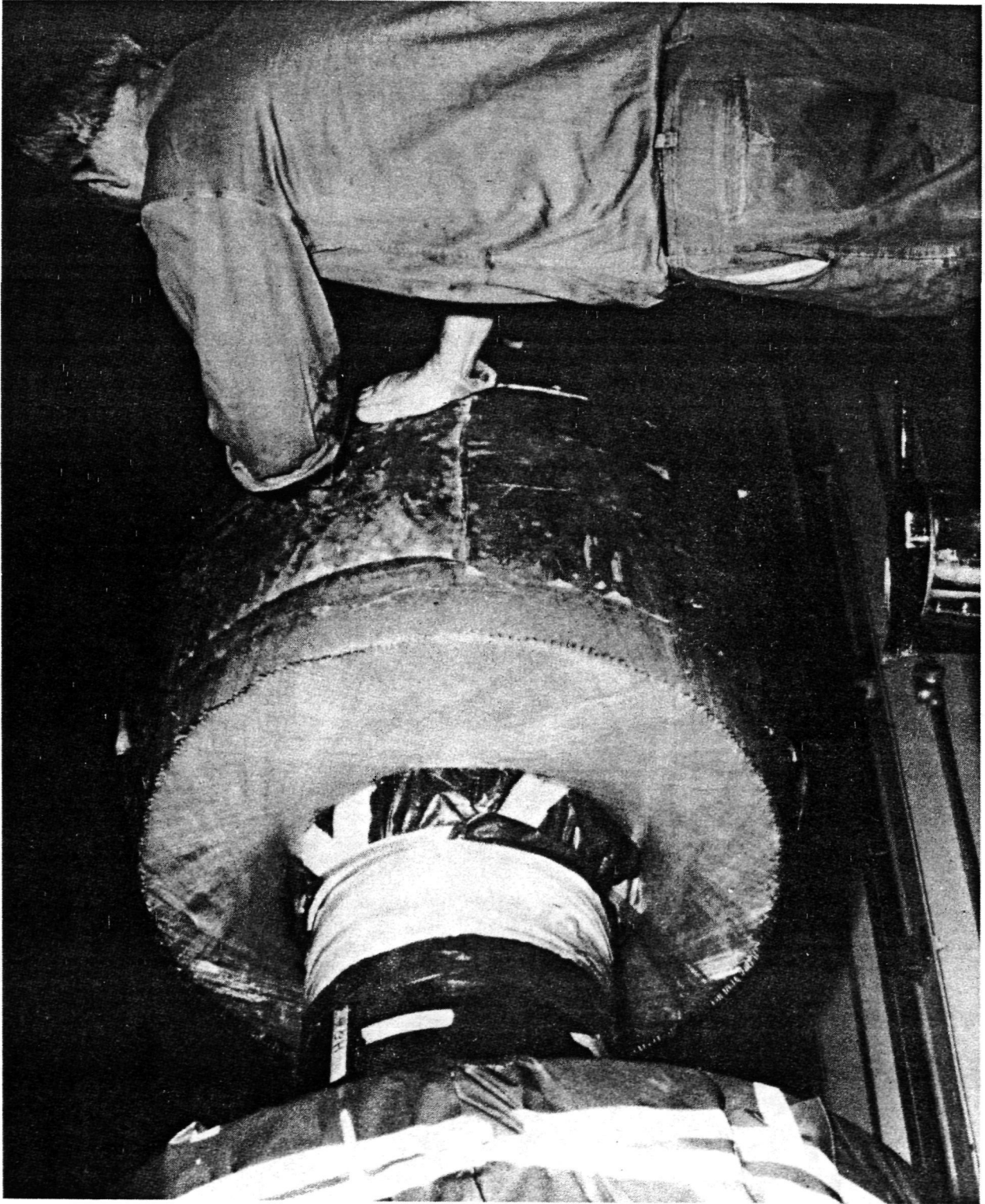
FIGURE 78. FIBERGLASS CLOTH INTERCLEAVING
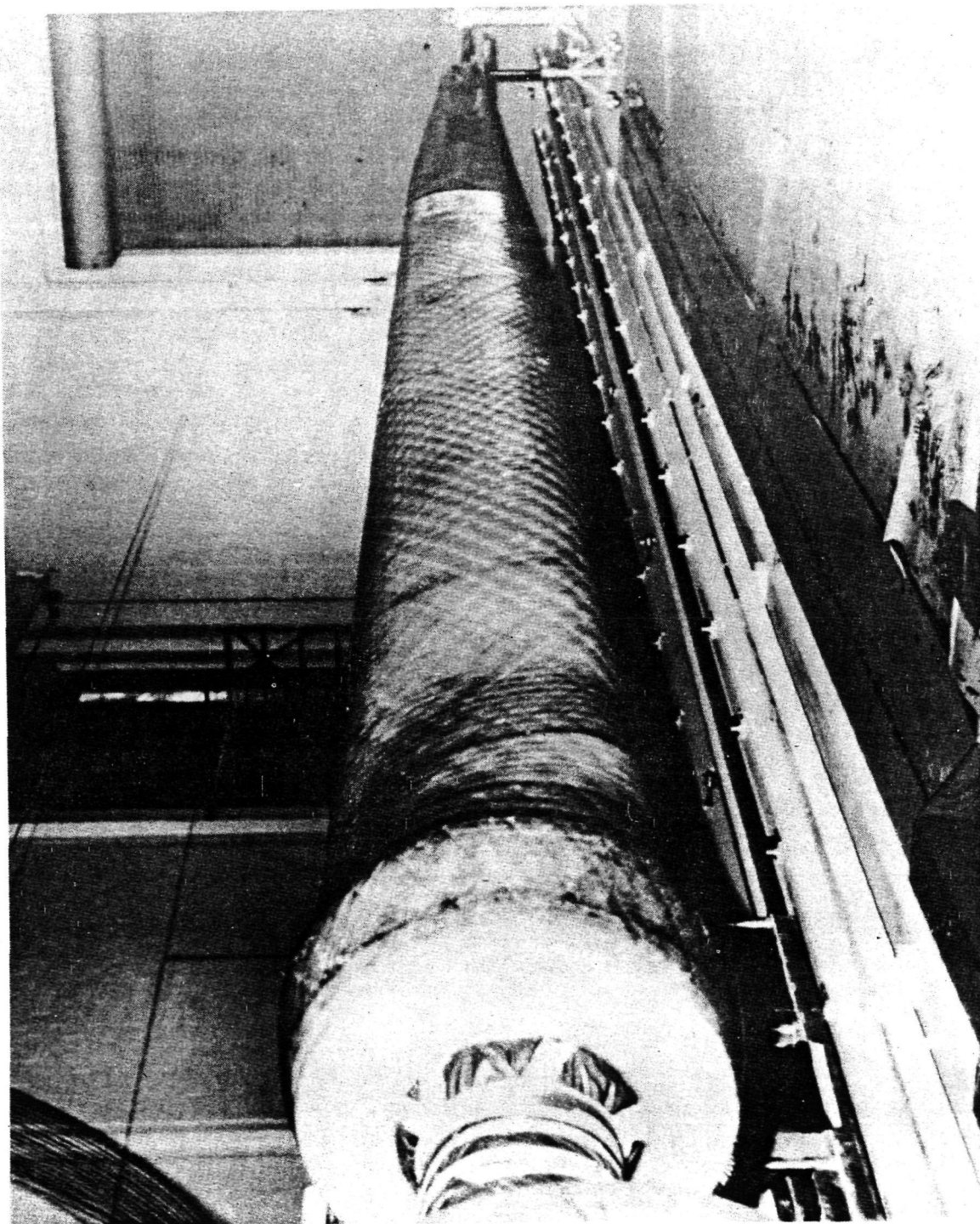
FIGURE 79. SPAR HELICAL WINDING TO STATION 345
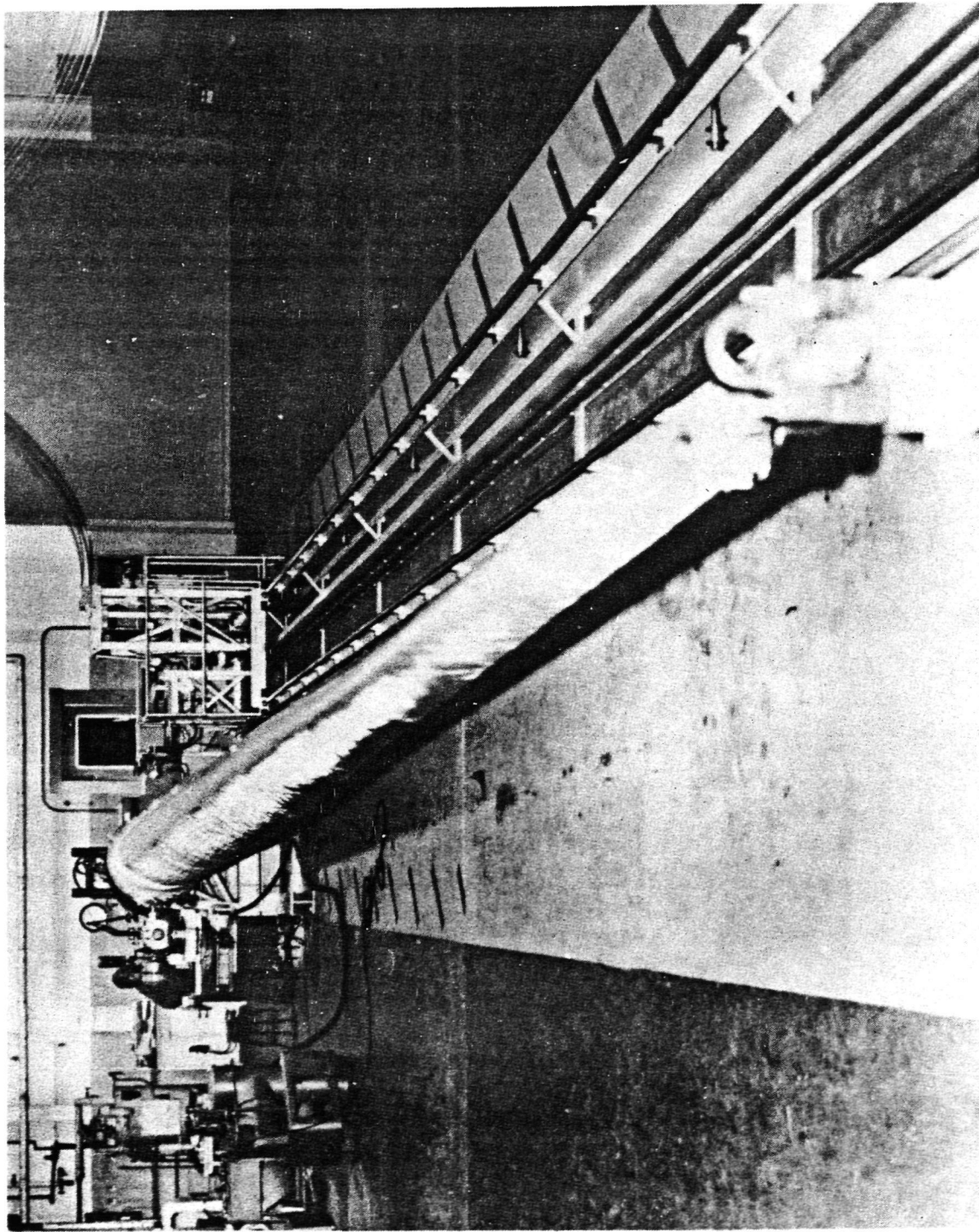
FIGURE 80. FINISH WOUND SPAR
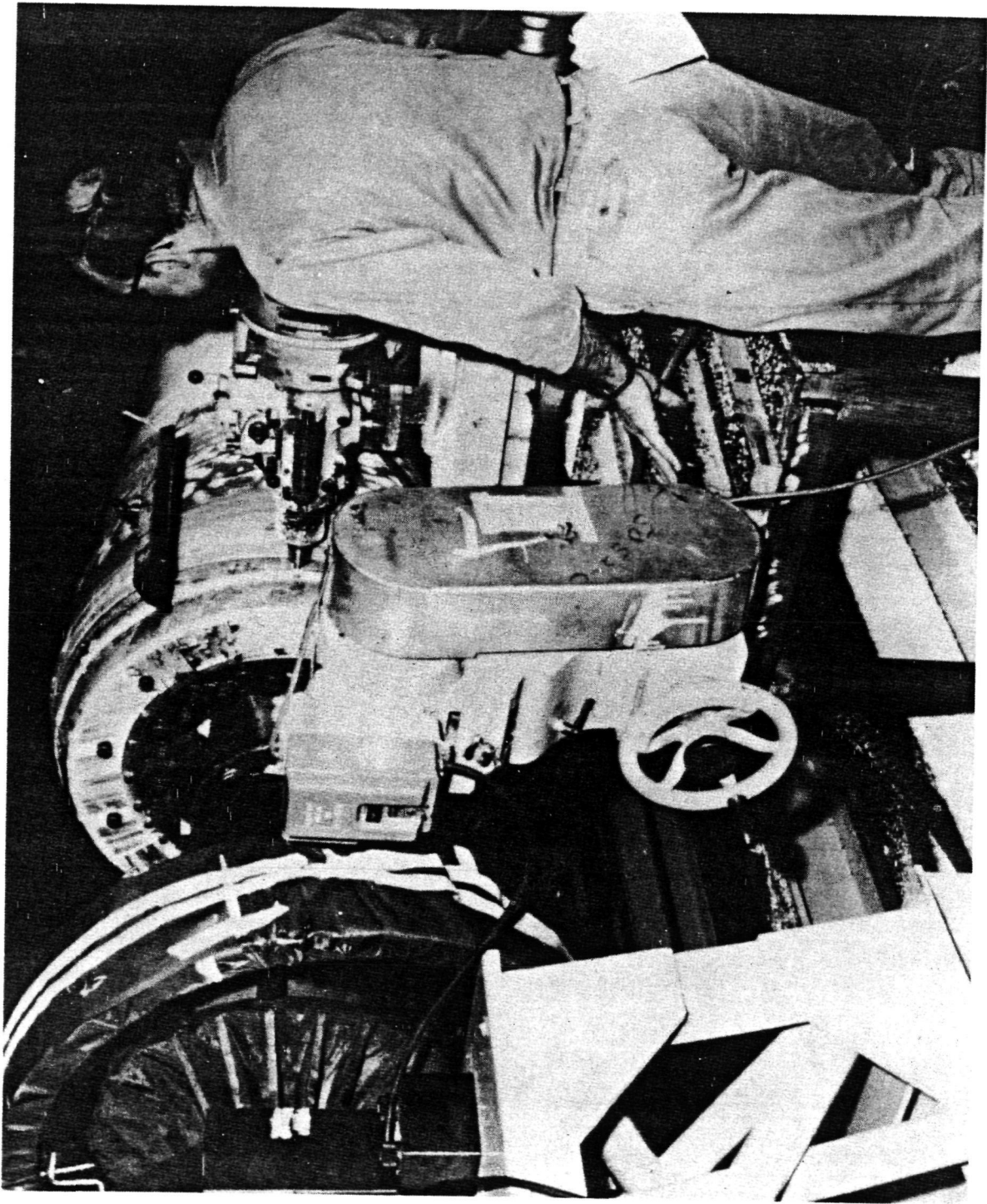
FIGURE 81. SPAR MACHINING FOR OUTER ADAPTER SLEEVE
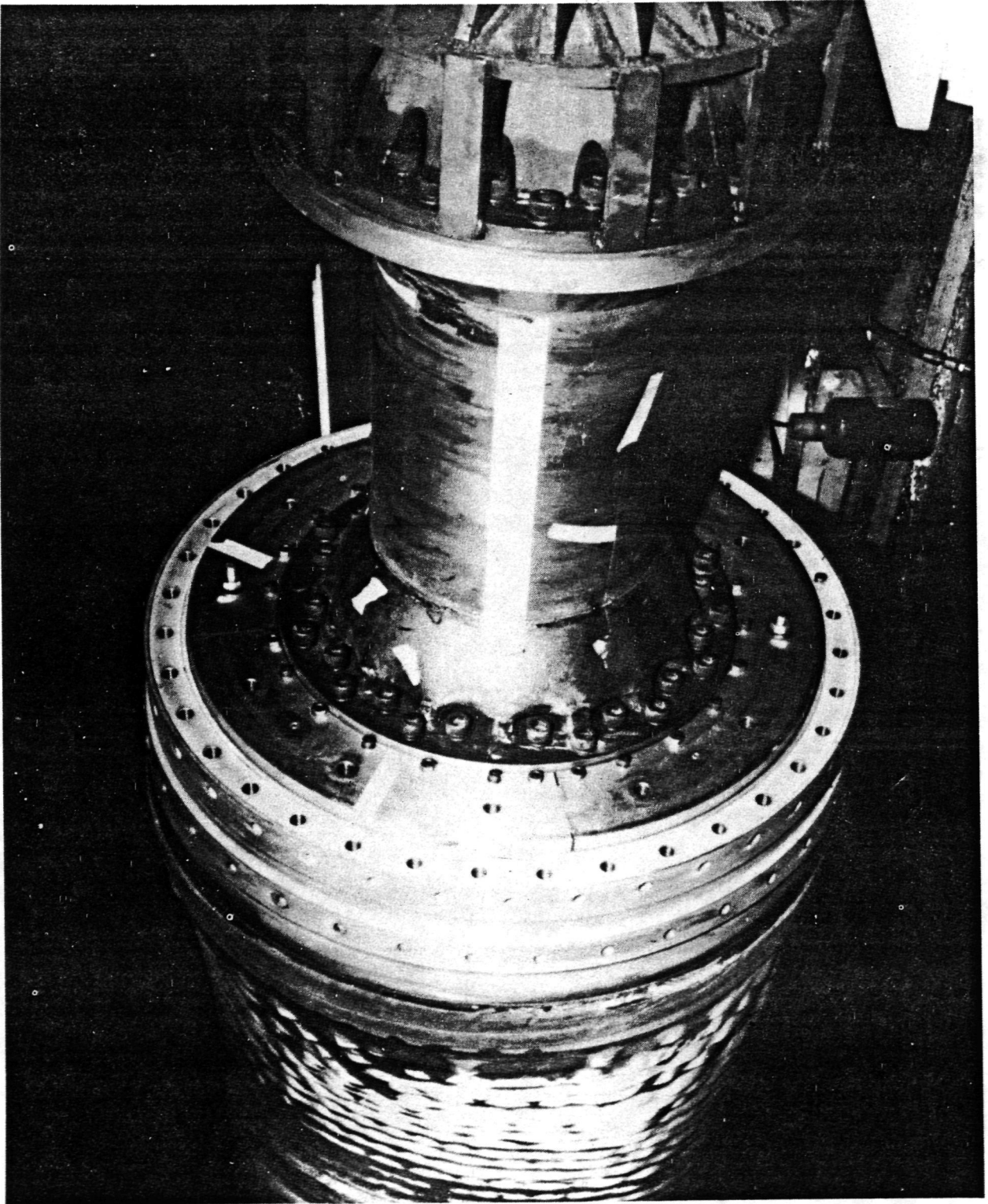
FIGURE 82. FINISH BONDED OUTER ADAPTER SLEEVE
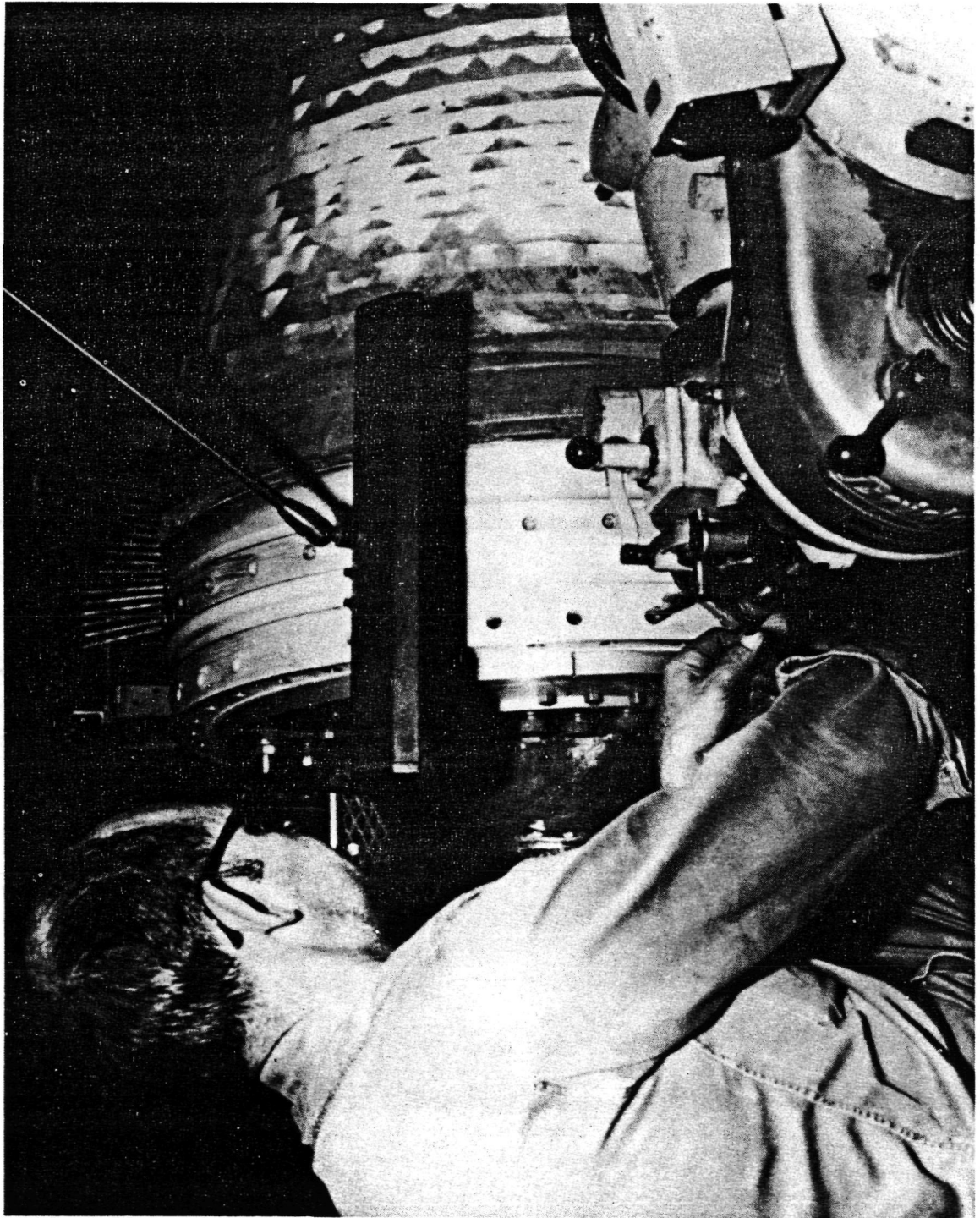
FIGURE 83. ADAPTER SLEEVE BOLT HOLE DRILLING
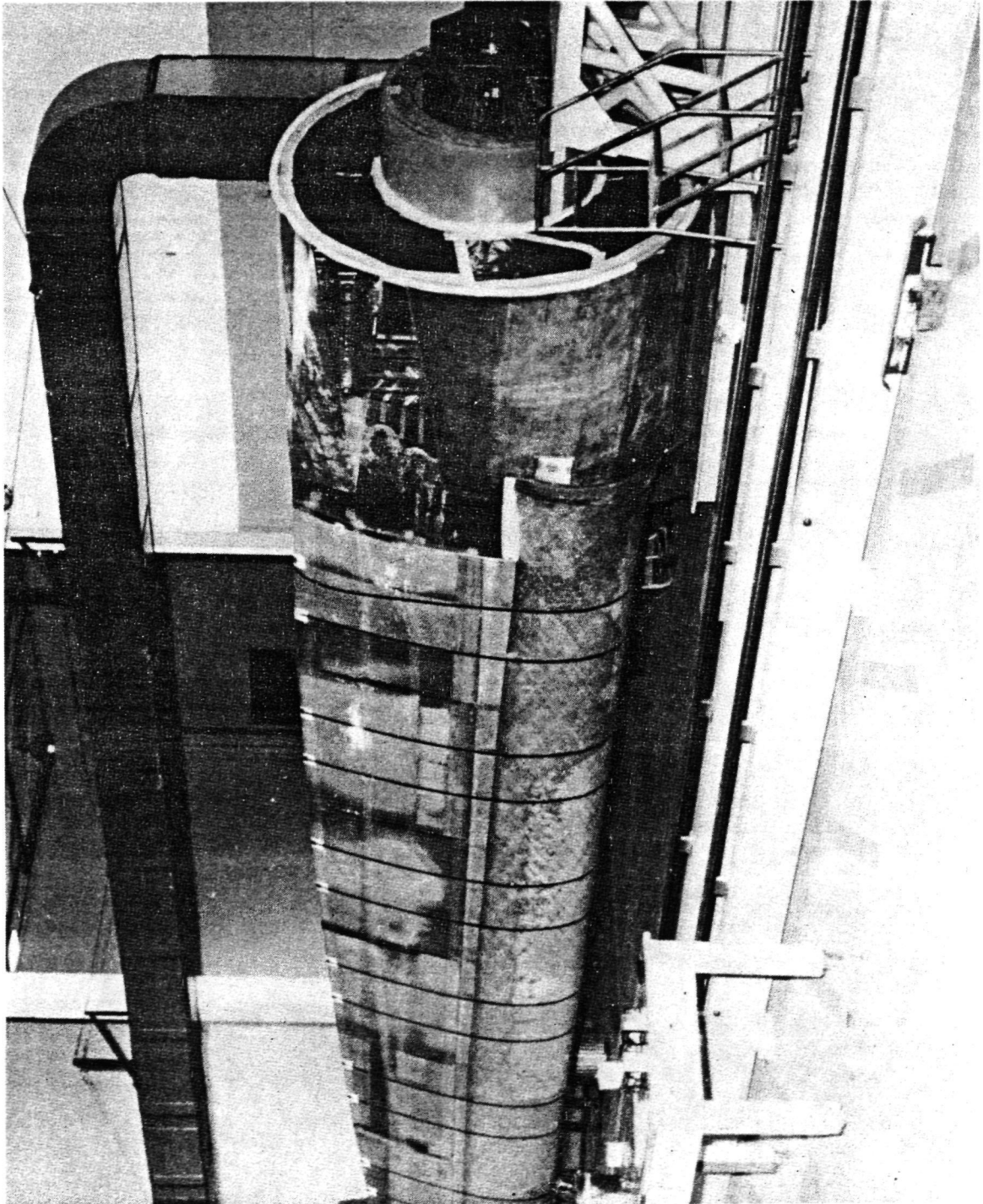
FIGURE 84. SHELL MANDREL FORMER INSTALLATION
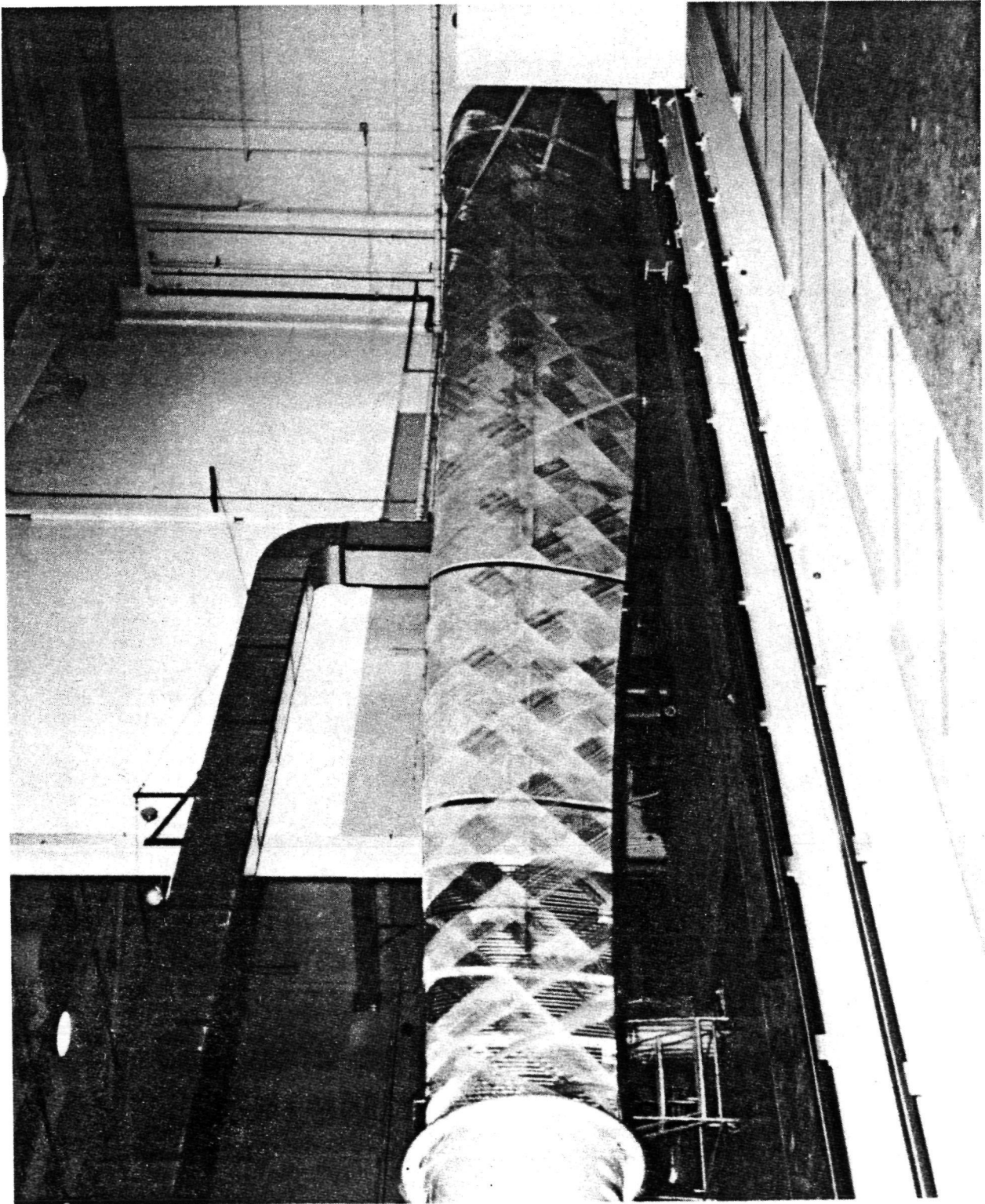
FIGURE 85. SHELL HELICAL WINDING TO STATION 525

Heat Cure

An insulated plywood cure hood was positioned over the finish wound blade as shown in Figure 86. Hot air was circulated through the hood to cure the blade at 175°F (353°K) for 16 hours. Thermocouples were applied to the blade at various locations to monitor material temperature to assure proper cure cycle.

Mandrel Removal

The tip of the blade and the inboard end of the shell were trimmed to facilitate mandrel removal. The tail stock was removed and the blade held as shown in Figure 87. Hydraulic jacks were used to release the center steel shaft and the blade was pushed off the shaft as shown in Figure 88. Spar mandrel formers were collapsed and removed with minimal difficulty and shell mandrel removal progressed satisfactorily up to mid blade. At this point the shell mandrel sections were found to be jammed against the spar and could not be collapsed as planned. It was necessary to remove the plywood bulkheads and then collapse the aluminum skins to pull the mandrel out. In the removal process, the shell mandrel formers were damaged to such an extent that they were not reuseable. If additional blades had been manufactured the former configuration would have been modified to provide increased clearance with the spar thus avoiding any jamming problems and allowing mandrel removal without damage.

Following mandrel removal the inboard row of retention bolts was installed.

The finish wound blade was installed on a shipping fixture as shown in Figure 89. The blade was covered with a six inch layer of foam rubber and a nylon reinforced plastic tarp and shipped to Hamilton Standard.

Inspection

During the filament winding operations the blade was inspected visually for band placement coverage, and band angle. Dimensional inspection during layup was limited to positioning of shank filler material and diameter buildup in the retention area. Table VI summarizes the results of these inspections as noted in the Manufacturing and Inspection Record log sheets. After the spar windings were completed, the resin was allowed to cure at room temperature prior to incorporation of the offset winding fixtures at each end. The spar was tap test inspected at that time while it was on the winding mandrel. No tonal changes indicating voids or other than continuous laminated structure were noted during the spar tap test inspection.

After shipment to Hamilton Standard the blade laminate was inspected visually, by tap test, and by bright light. Areas of small voids up to 2 inches (5.08 cm) across near the outer surface of the shell, were detected by tap test as well as a limited quantity of (17) voids up to 5 inches (12.7 cm) across. All of these were reviewed and found accep-
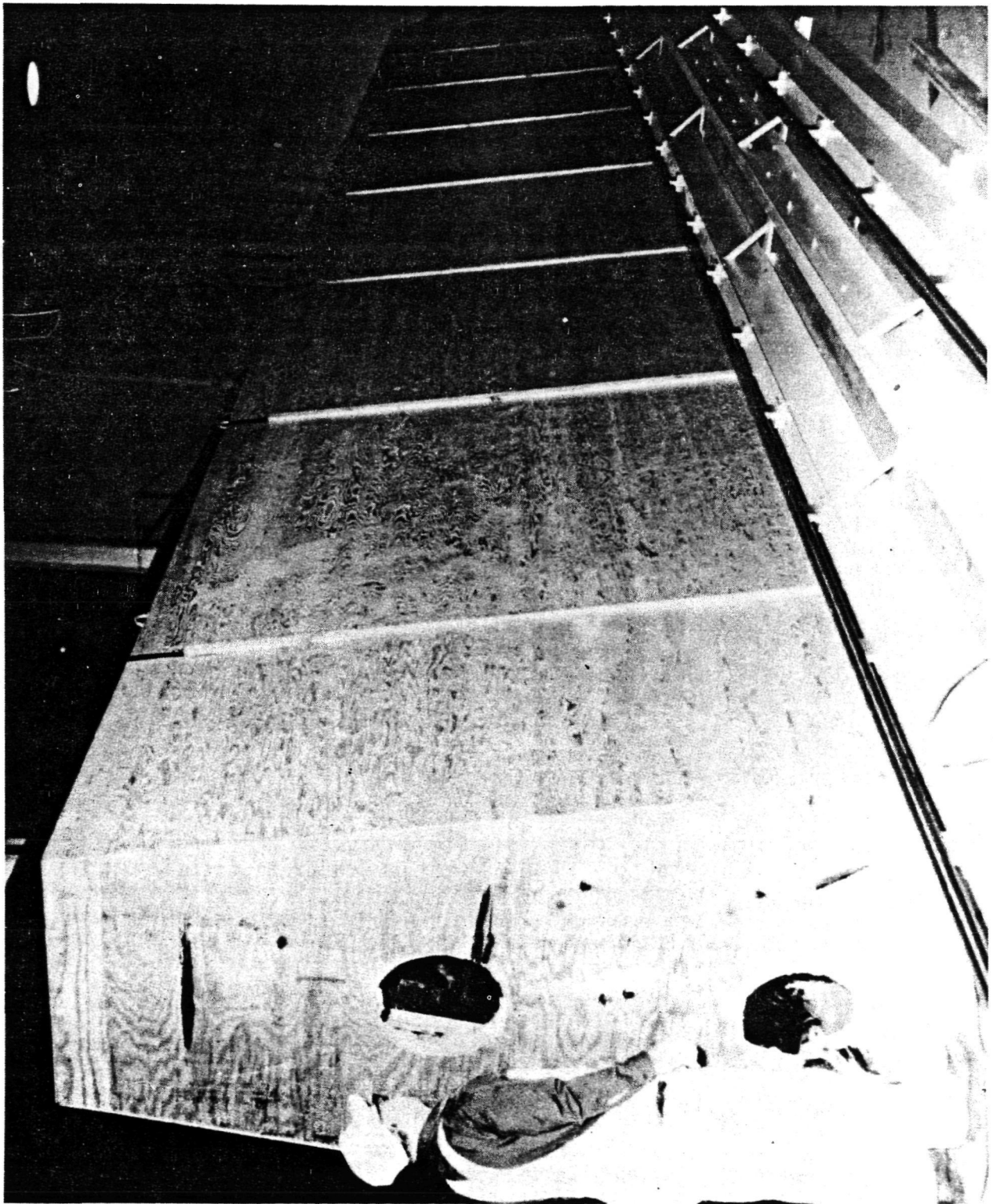
FIGURE 86. BLADE CURE HOOD INSTALLATION
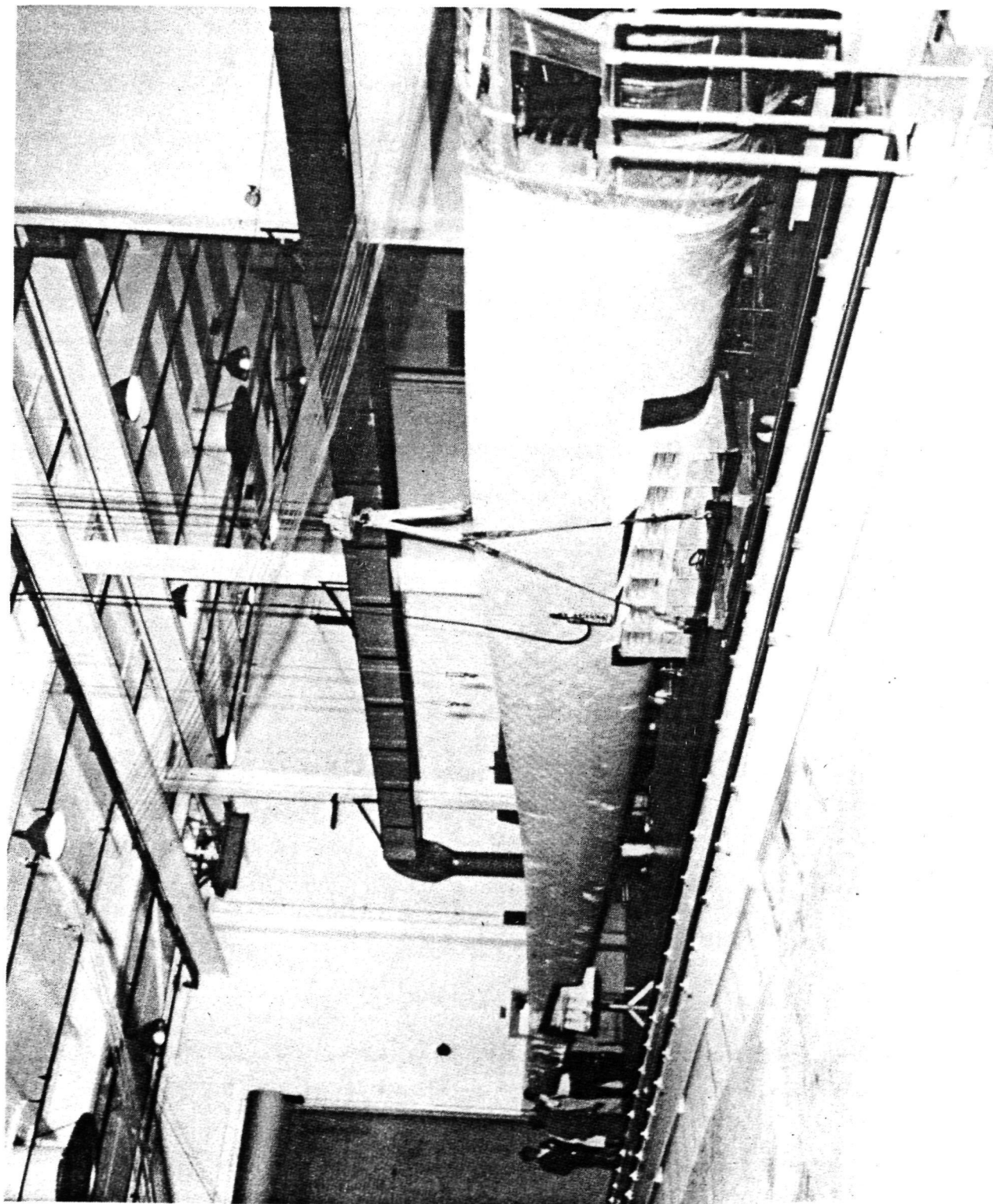
FIGURE 87. FINISH WOUND BLADE
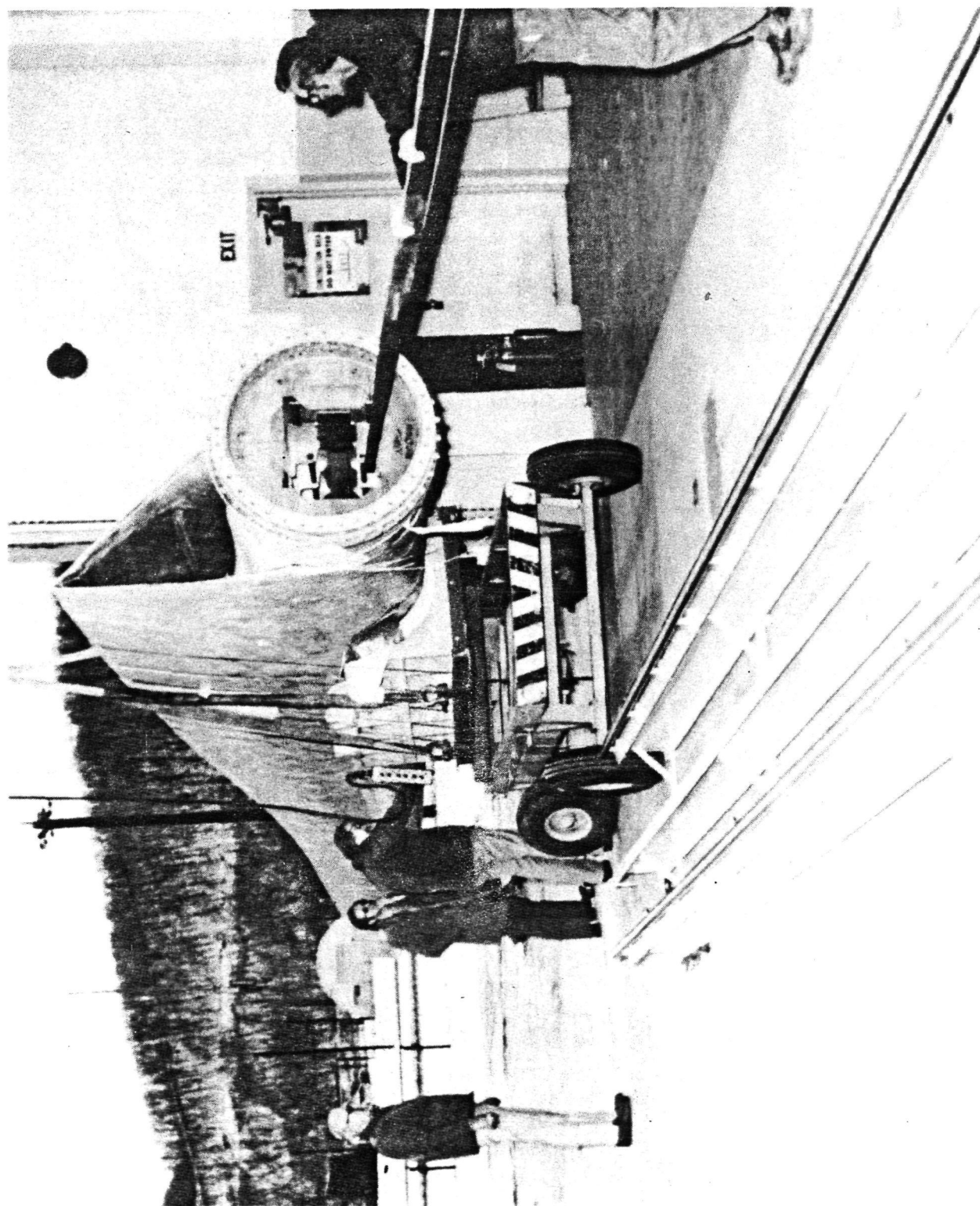
FIGURE 88. BLADE REMOVED FROM WINDING MACHINE
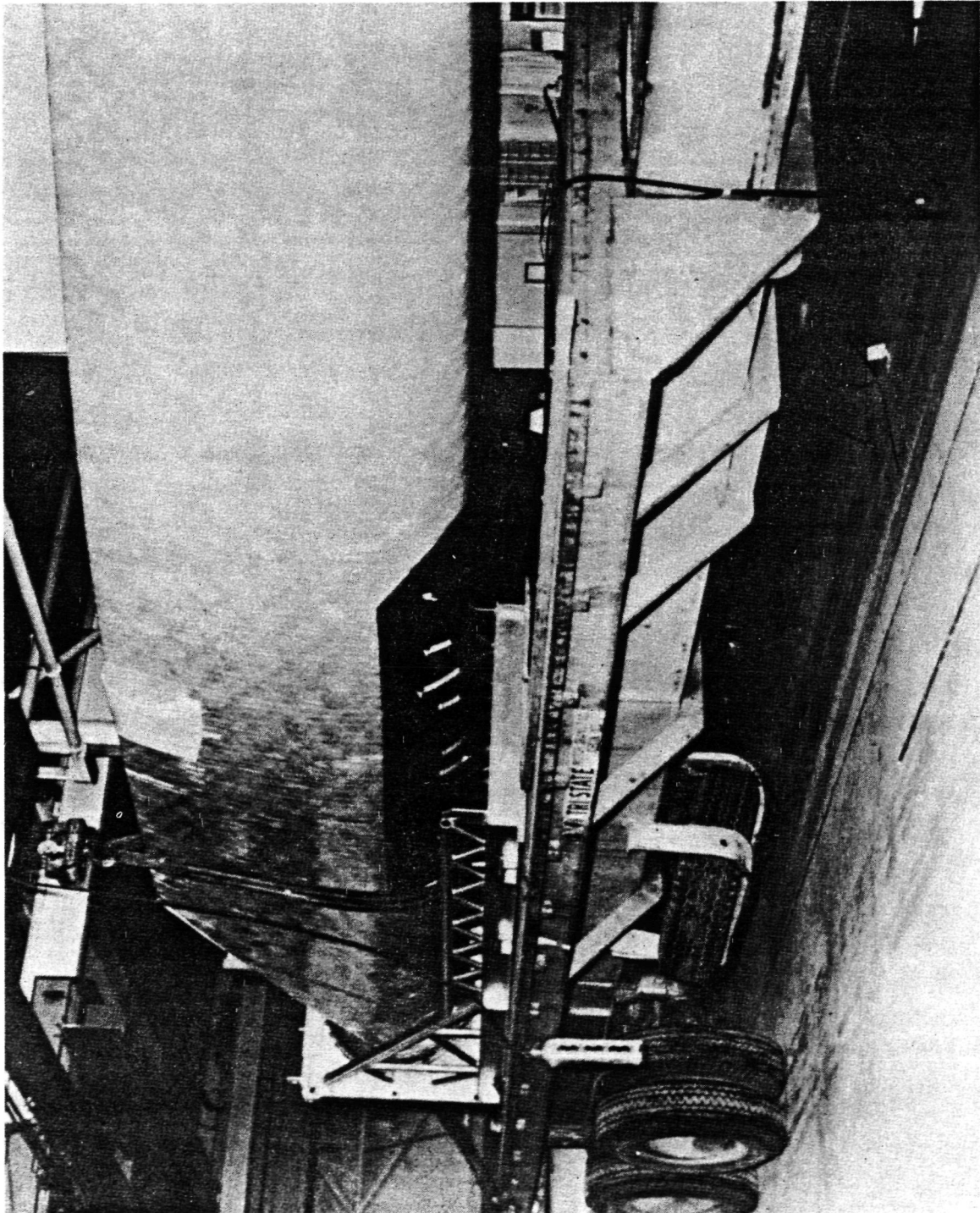
FIGURE 89. FINISHED BLADE ON SHIPPING FIXTURE

TABLE VI
SUMMARY OF MANUFACTURING AND INSPECTION RECORDS FOR
MANUFACTURING PROTOTYPE BLADE

ITEM	CORRECTIVE ACTION
Band gaps around locating pins on spar.	Filled gaps with resin impregnated roving strands.
After wrap 2, 3, 4, 5, and 6, the 53.5 sta. dia. oversize and bridging 58 to 120 sta.	Adjusted cloth fillers to reduce diameter buildup and fill bridged area.
Layup interrupted due to drive shaft weld failure after wrap #4.	Spar blocked in position and covered with peel ply to protect surface. Spar surface was resin coated prior to resumption of winding.
Inner ring scored on land that mates to outer ring (32.033 dia.).	Locally dressed out marks 0.010 to 0.020 deep and coated with Zinc Chromate primer.
Layup exposed on root cutoff trim surface.	Coated the exposed trim edge with outer ring bonding adhesive at outer ring bonding operation.
Rough surface on spar wrap.	Smoothed surface by screening with filled resin prior to srapping shell.
Y-joint cloth strips locally irregular.	Ground off smooth and reapplied cloth to smooth gap between spar and shell mandrel.
Spar surface preparation.	Spar surface lightly sanded with 80 grit just prior to initiating shell wraps.
Machine indexing problem due to counter malfunction.	Continued shell wrap #2 to close pattern adding 88 circuits. Indexing checked on each circuit. Counter replaced with better functioning unit.
Local shell outer surface bridging due to indexing and 18 circuit pattern results.	Filled gaps with resin and chopped glass and overwound 1/2 layer of 90° wrap to improve compaction of outer surface.
Shell Mandrel sections between stations 344 and 750 stuck.	Shipped with mandrel sections in place and removed at Hamilton Standard. Clearance between shell mandrel section and spar rear face to be increased in this area.
Shell cutoff at trailing edge was 1.46 inches O.H.L.	Accepted for shipment.

table without repair with respect to their size, location and local blade operational stresses. Bright light examination indicated acceptable laminate throughout the blade structure. The retention area was radiographically inspected and no discrepancies were found. Dimensions including width, thickness, edge alignment, face alignment, and angle were within acceptable tolerance levels proportional to aircraft propeller blades. Wall thickness measurements taken in the shell trailing edge cavity indicated an over-thick condition of the shell which was ascribed to filament bridging problems on the inboard transition section of the blade and basket weaving conditions associated with using a winding pattern that required several circuits before laying down bands next to each other. Voids associated with these problems were filled by applying excess resin and a 90° wind was applied to improve shell compaction. Since this program Hamilton Standard has developed computer programs to define non-bridging blade surfaces and winding techniques to eliminate the basket weave problem.

The blade was weighed by a two-point suspension setup and horizontal balance computed from the two load-cell readings. It was found to be overweight by 682 lbs. (309.4 kg) which was primarily ascribed to the aforementioned shell thickness and added materials.

Tap Test

The tap test technique of inspection has been used for inspection of propeller blades since the advent of hollow blade structures over 20 years ago. The finish wound blade structure was tap tested over its entire external surface. Two sizes of tap hammers were used, both of which consisted of a large bearing ball silver soldered to a small diameter tubular shaft. A four ounce size hammer was used to tap test the shell aft of the spar and the tip area of the blade. An eight ounce size hammer was used to tap test the heavier wall thickness of the spar from the 600 inch (15.24 m) station inboard. Table VII lists the items noted by tap test indications. Due to the number of small (2" across) surface voids present in the shell outer surface, it was found to be beneficial in interpretation of the tonal changes to move the hammer in the $\pm$ 30° general direction of the band angle. The effect of these noted conditions on the blade structure were assessed by conservatively assuming the hole of the specified size went through the complete blade wall. Tentative acceptance criteria based on the part size and local stressing were formulated and are listed in Table VIII. All of the items found on the tap test inspection were acceptable within the definition of these criteria.

TABLE VII
TAP TEST DATA SHEET

Item	Sta.	Dist. From TE	Size/Inches	Remarks
1	145.0	19–23	5 x 5	C/S shell void 2 bands (B) wide
2	145.0	27–31	4 x 4	C/S shell void 2 bands (B) wide
3	150.0	14–18	3 x 4	C/S shell void 2B x 1B
4	160.0	17–21.5	4.5 x 4.25	C/S shell void 3B x 2 1/2 B
5	166.0	29–34	4 x 5.5	C/S shell void 2B x 3B
6	172.0	34–37.5	2 x 3	C/S shell boid 1B x 2B
7	160.0	25–31	5.5 x 6	C/S shell void 3B x 2 1/2 B
8	167.0	21–26.5	5 x 5	C/S shell void 3B x 3B
9	197.0	26.5–31	3 x 4.5	C/S shell void 2B x 2B deeper in shell
10	252.0	20.5–25	3.5 x 4	C/S shell void 2B x 2B deeper in shell
11	172.0	33.5–35.5	2 x 3	C/S shell void 1B x 2B
12	278.0	38–41.5	2 x 4	C/S shell void 1B x 2B
13	320.0	17–20.5	3.5 x 3.5	C/S shell void 2B x 2B
14	340.0	27–29	2 x 3	C/S shell void 1B x 2B
15	340.0	31–33.5	2.5 x 3	C/S shell void 2B x 2B
16	706.0	0–4	1 x 4	C/S & F/S FOD at edge of mandrel section
17	731.0	2–3	0.5 x 3	F/S shell void 1B x 2B

Voids inside 2" band of winding pattern are numerous and are located on both face and camber sides. They are visible with a bright surface light.

C/S – Camber Side
F/S – Face Side

TABLE VIII
TAP TEST ACCEPTANCE CRITERIA

- Existing design allowables include effects of voids $\leq$ 2" size.

- Voids 2" to 5" square size acceptable if local stress is a % of design

    allowable = $\dfrac{W_S - W_D}{W_S}$

    where W_S = Width of spar

    W_D = Width of void

    Providing the void area bright light indicates no band damage.

- > 20 square inches area will be dispositioned for repair.

- Shell trail cavity area < 20 sq. in. is acceptable.

Bright Light

Bright light viewing of laminated parts has been done on Hamilton Standard propeller products for nearly twenty years. These parts were generally made of a darker resin system and woven cloth reinforcements. The lightly colored resin system seemed amenable to this form of inspection even in the thicknesses used on the MOD-0 wind turbine blade. The entire blade, except for the laminate sandwiched between the retention load rings was inspected by use of 500 watt/120 volt Sylvania Photo-ETC bulbs with 3200°K illumination. The technique requires internal and external observation of the blade. Wherever possible the blade is entered for direct internal observation and the light is hand held and passed back and forth in a spray painting motion for complete area coverage. Distance of the lamp from the surface can be varied to adjust brightness and readability on the viewing surface. At the same time the external illuminated surface is viewed by the person holding the light. Where the blade is inaccessible to direct internal view, mirrors and borescopes were used to view the structure. The light sources were also passed through the spar and shell cavities with the blade being viewed from the outside. At the 600 inch (15.24 m) station, the bulbs were too large to pass through either cavity to the tip. Since the laminate is thinner in this area, the bulbs were placed on the outside and the light passed through both walls for external viewing. Four additional items were noted during this inspection. The aforementioned voids due to band pile up at the spar locator buttons was observed and typical bright light view of this condition is illustrated in Figure 90. Some band pile-up was noted near the blade tip as previously mentioned. Small shell subsurface voids were seen from the illuminated side. During removal of the shell mandrel former sections, some local crazing was incurred at the inboard end of the last 45 inch (114.3 cm) long section. This was noted on tap test but was much more reliably noted on bright light inspection. Figure 91 illustrates acceptable bright light inspected material and Figure 92 illustrates unacceptable bright light inspected material in a heavy walled test piece filament wound prior to the blade. Figures 93 and 94 illustrate typical blade shell structure and spar structure respectively.

Retention X-Ray

The adapter sleeve area was radiographically inspected by use of a tridium 192-20 Curie Source placed in the center of the blade-root with film cassettes wrapped around the outer surface. Two exposure times were used to observe (1) the laminate termination and (2) the remaining part of the structure. No discrepancies were found in the retention area.

118

G49461
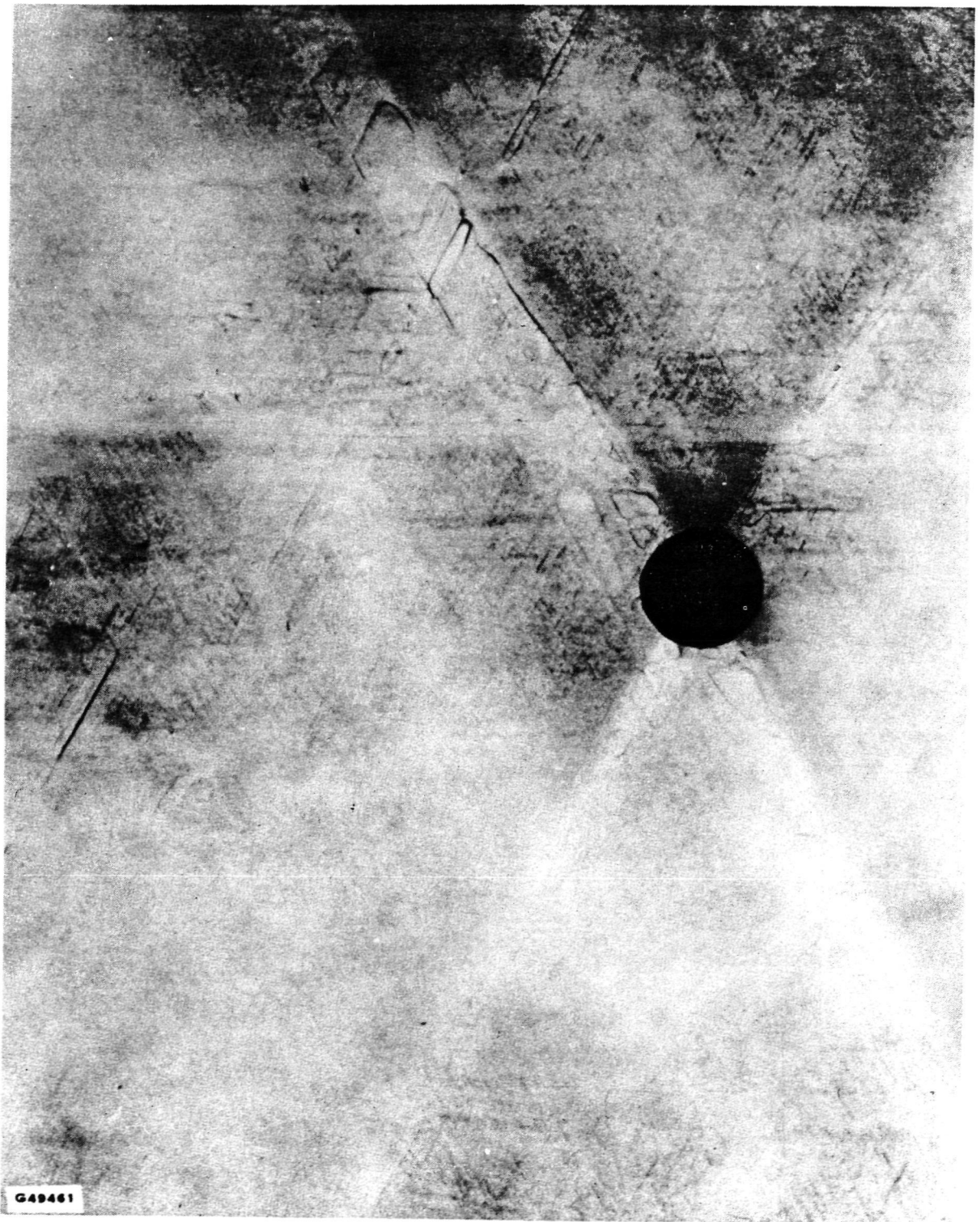
FIGURE 90. INTERNAL BRIGHT LIGHT INSPECTION
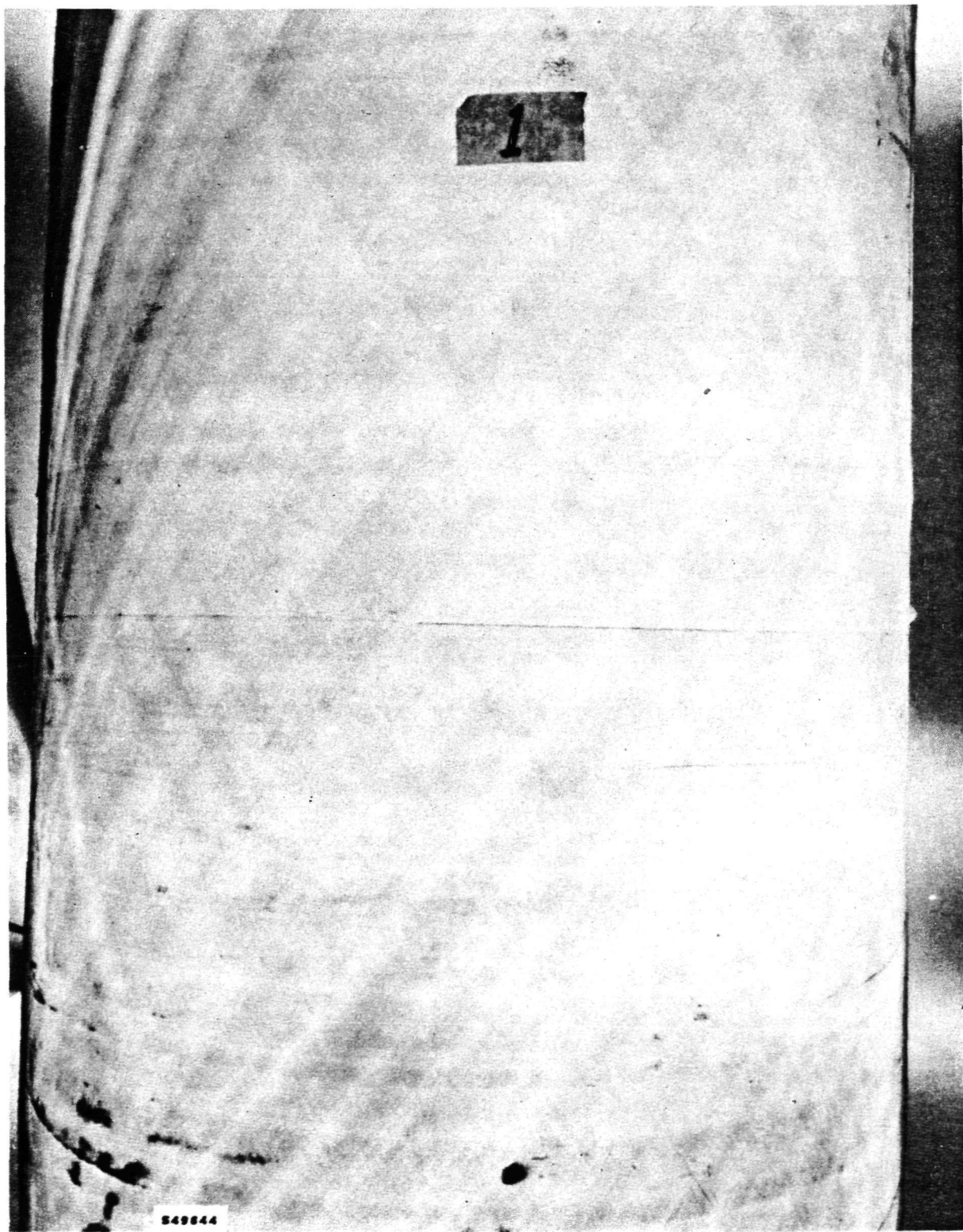
FIGURE 91. ACCEPTABLE BRIGHT LIGHT INSPECTION
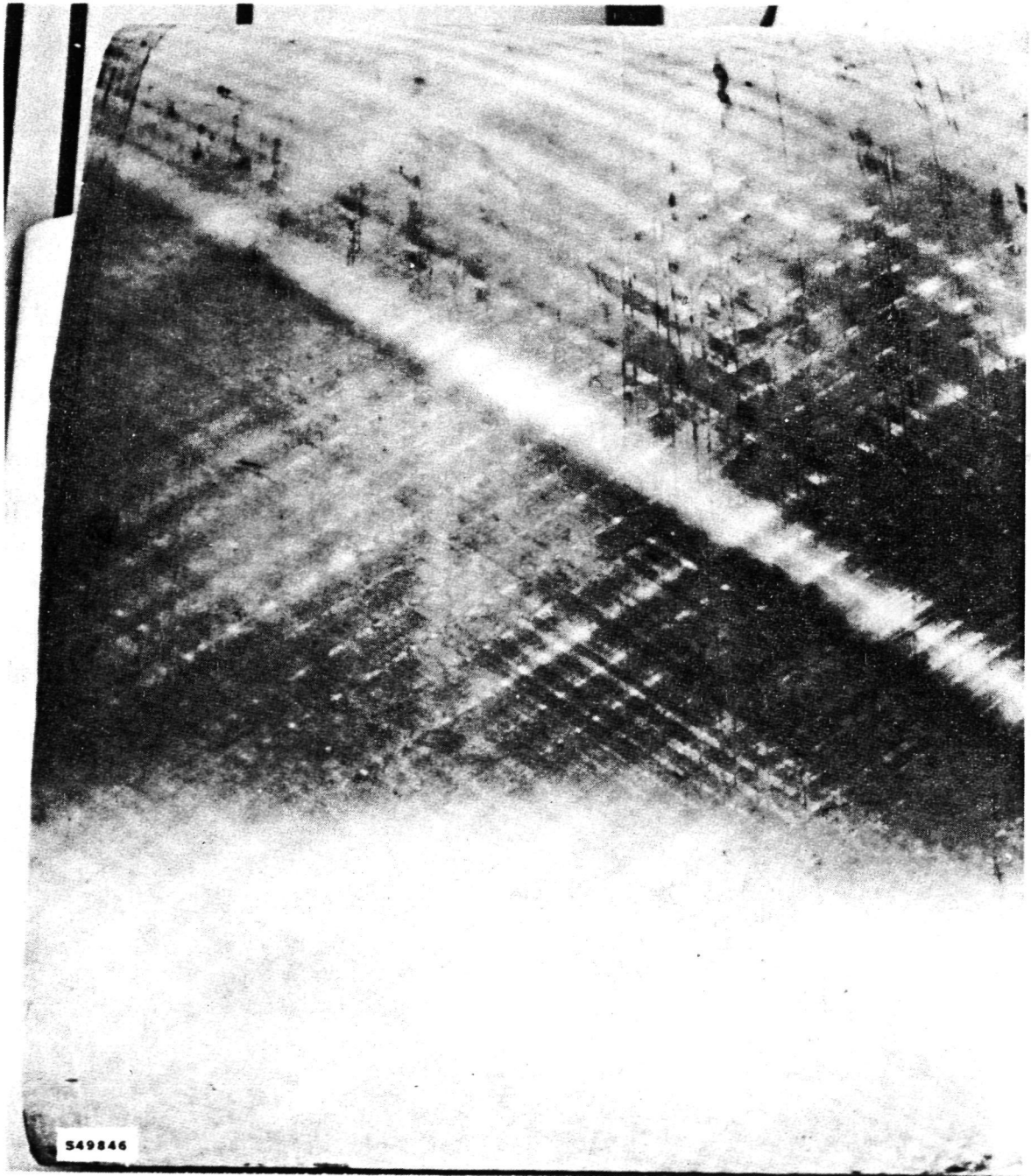
FIGURE 92. UNACCEPTABLE BRIGHT LIGHT INSPECTION   121

122   FIGURE 93. TYPICAL SHELL BRIGHT LIGHT INSPECTION

G49399
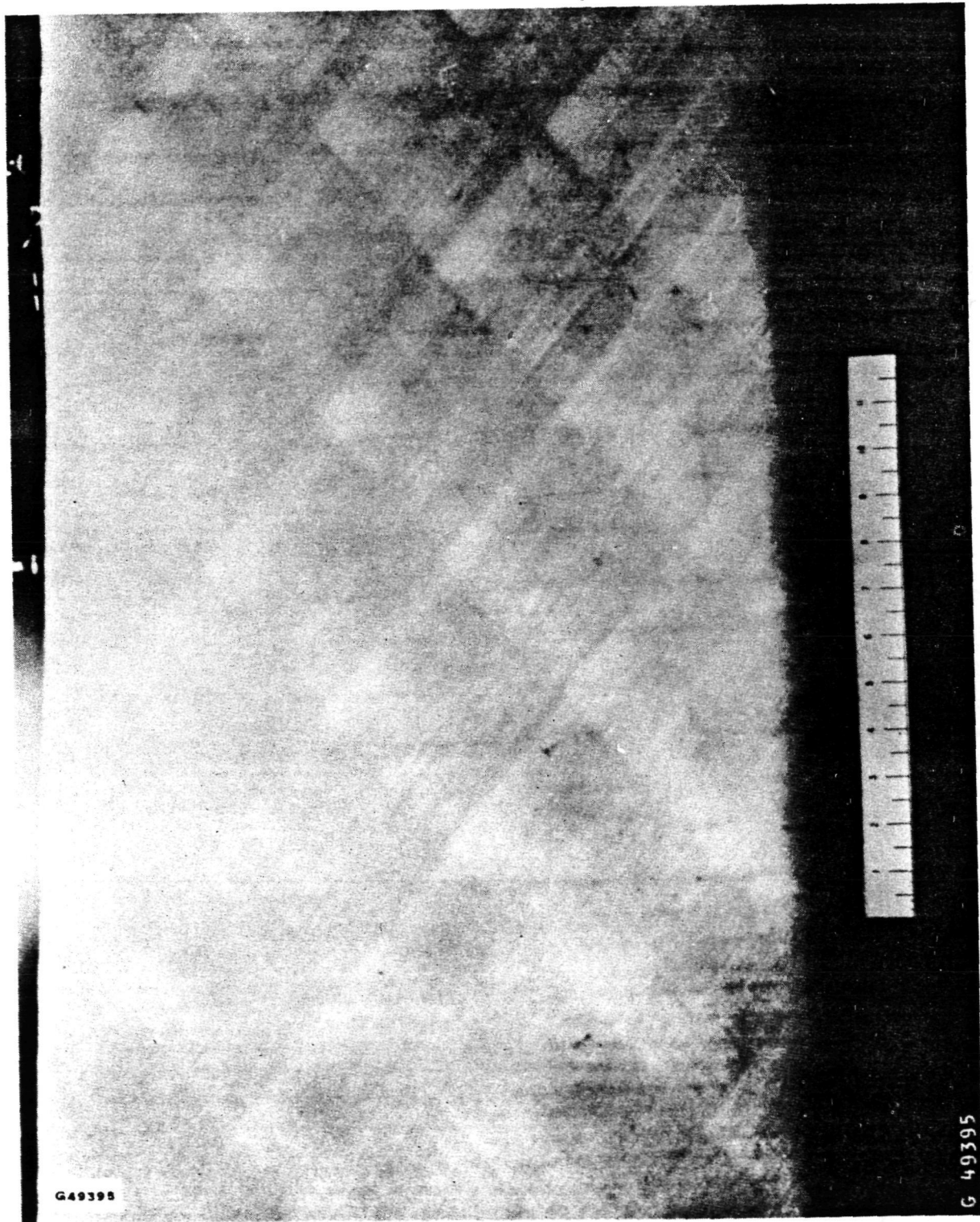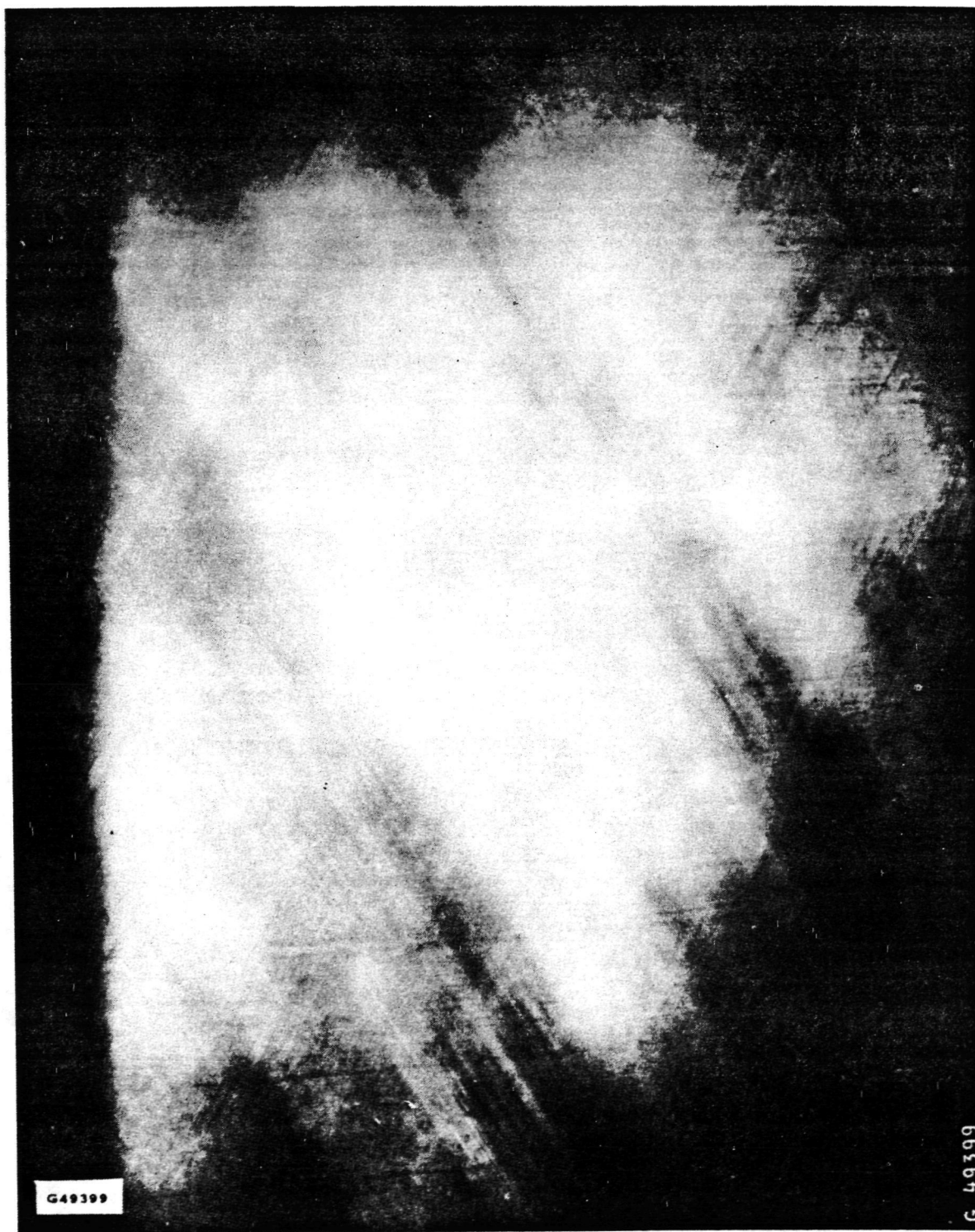
FIGURE 94. TYPICAL SPAR BRIGHT LIGHT INSPECTION

123

Dimensional

Since the manufacturing prototype blade was the first fabricated on the tooling, several dimensional inspections were made to define the aerodynamic shape of the blade. Additional measurements were made in order to define the structure of the blade for a computer model which was used to calculate blade resonant frequencies and deflections.

Contour inspection was accomplished in accordance with requirements of the blade drawing. Figure 95 contains the maximum deviation AJ at each station. A 0.035 inch (.89 mm) diameter wire was stretched across the surface of the blade with a weight to keep the wire under tension. Feeler gages were used to check gaps between the wire and the blade surface. No gaps were found in excess of the listed values of AJ.

Width inspection was accomplished by using squares and a long scale, Table IX lists the measured and required values. Figure 96 shows the measured values compared to the design width distribution. The variations noted are well within the normal tolerances used on propeller blades on a proportional basis.

Thickness of the blade airfoil was measured by use of calipers and a scale. Table IX lists the measured and required values. Figure 96 shows the measured values compared to the design distribution thickness. The comparison shows a consistent over thickness condition accentuated at the tip. Most of this variation was ascribed to the effects of the shell wall thickness discussed below which proportionally has a greater effect on airfoil thickness at the tip area of the blade.

Angle measurements were taken at four tip area stations where airfoil templates were available. The method of performing this measurement is illustrated in Figure 97. The blade was rotated into a chordline vertical position by use of the retention ring locating keyway and a protractor/level. The face side template for the station was placed against the blade face side and positioned for best fit. A propeller pitch protractor was aligned to the template's back edge and an angle deviation from vertical read from the protractor's level and vernier scale. These variations are listed in table IX. The comparison to design requirements is shown in Figure 96 where a correction has been allowed in the manufacture of the blade adapter.

Edge alignment and face alignment were measured by use of transit, levels, plumb lines, and a taut reference wire offset from the blade. The hub centerline, as defined by the inside diameter of the inner adapter sleeve and the butt face of the outer adapter sleeve and a centerline jig hole established at the blade tip using drawing dimensional definition of the tip station were used to maintain blade centerline and offset taut line parallelism during rotation for measurements of face and edge alignment

STA	AJ
75.00	~
105.00	0.053
150.00	0.051
195.00	0.049
240.00	0.046
285.00	0.042
330.00	0.039
375.00	0.037
420.00	0.036
465.00	0.035
510.00	0.033
555.00	0.031
585.00	0.030
630.00	0.028
690.00	0.027
735.00	0.026

MAX ALLOWABLE DEPRESSION
AT ANY STATION SHALL NOT EXCEED DIM. AJ

AIRFOIL CONTOUR ESTABLISHED
BY A TAUT CORD CIRCUMSCRIBING
THE AIRFOIL STATION

SCALE: NONE
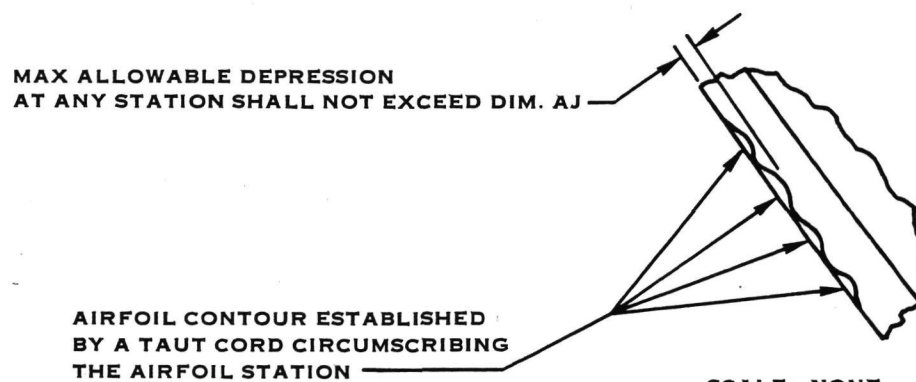
FIGURE 95. AIRFOIL CONTOUR INSPECTION

TABLE IX
MANUFACTURING PROTOTYPE BLADE
DIMENSIONAL INSPECTION RESULTS

Station	Face Alignment Actual/Dwg.	Edge Alignment Actual/Dwg.	Width Actual/Dwg.	Thickness Actual/Dwg.	Angle ~° Actual/ Variation
105	11.916/11.469	16.312/16.166	69.280/69.31	24.28/23.297	10.23/–
195	9.687/9.529	16.250/15.986	65.375/65.34	20.07/19.214	7.46/–
285	7.750/7.748	16.125/15.742	57.562/57.24	16.08/15.287	3.32/–
375	5.500/5.803	16.000/15.523	46.409/46.38	11.91/11.160	1.68/–
465	3.812/3.460	14.125/13.715	36.875/36.84	8.45/7.804	0.18/–
555	2.875/2.978	11.000/10.739	29.937/30.03	6.09/5.428	-0.99/-0.5
630	2.187/2.265	9.125/9.116	25.125/25.19	4.45/3.967	-1.47/-2.0
690	1.875/1.784	7.687/6.786	21.250/21.54	3.53/2.981	-1.97/-1.5
735	1.625/1.450	6.687/6.709	18.281/18.39	2.82/2.292	-2.26/-0.2

All linear dimensions in inches
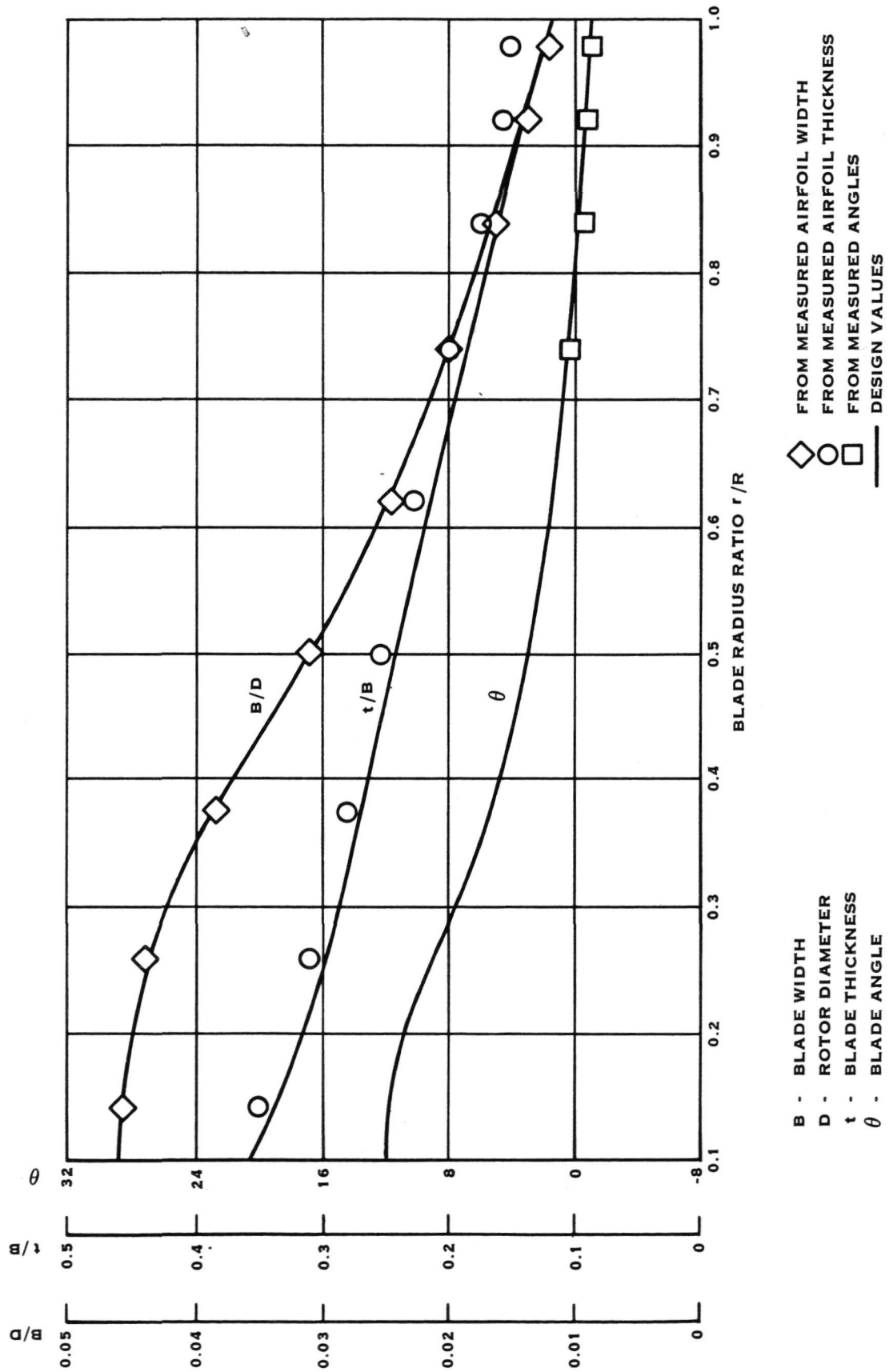
FIGURE 96. MEASURED AERODYNAMIC SHAPE

◇ FROM MEASURED AIRFOIL WIDTH
○ FROM MEASURED AIRFOIL THICKNESS
□ FROM MEASURED ANGLES
— DESIGN VALUES

B - BLADE WIDTH
D - ROTOR DIAMETER
t - BLADE THICKNESS
θ - BLADE ANGLE
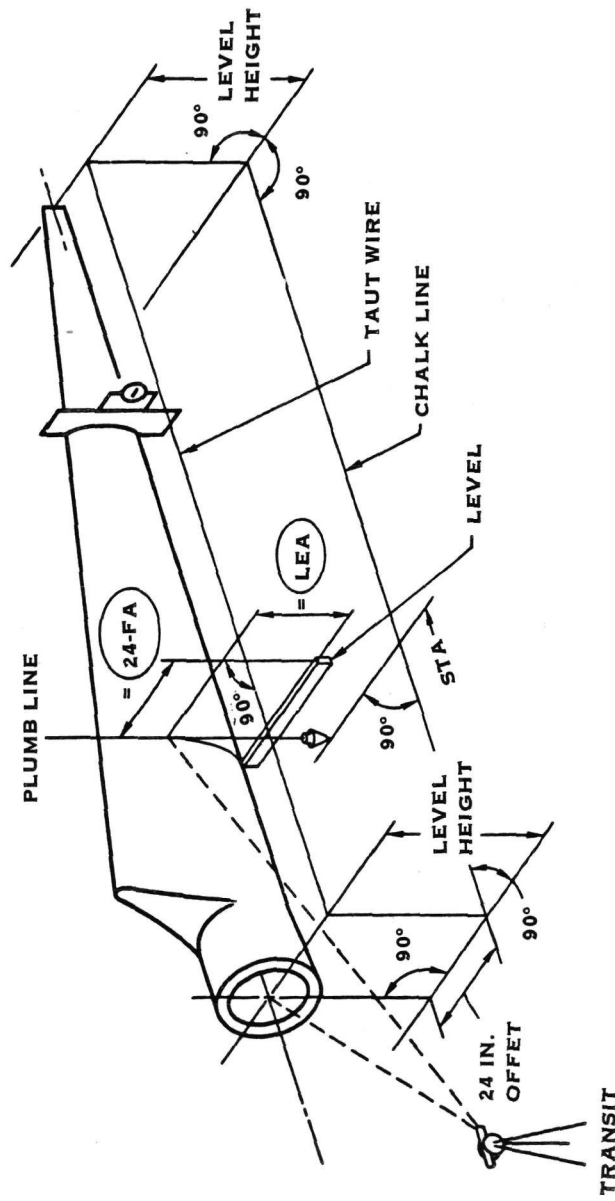
FIGURE 97. BLADE DIMENSIONAL INSPECTION SETUP

128

at each station. A detailed step by step procedure is listed in Table X. The blade was supported by a saddle and one sling, generally with the trailing edge upward. Measurements taken are listed in Table IX. The variations noted are well within the variations acceptable to propeller blade manufacture on a proportional basis.

Shell wall thickness was measured by use of a permanent magnet and a Gauss meter. The procedure for using this equipment is listed in Table XI. The calibration curves mentioned in the procedure are contained in Figures 98 and 99. Two full scale settings were used to accommodate the range of wall thickness present in the blades.

The measurements were made just aft of the spar rear face. At each location the magnet was moved slightly to the root and tip so that three readings were obtained and averaged as representative of the station. Table XII lists the readings and thicknesses taken. The measured shell data in the table indicates an excessively thick condition of the shell. No direct measurements were available on the spar. The extra shell material added during shell winding partially accounts for the increase in thickness. The rest can be accounted for by lack of compaction of the shell material.

Weight and Moment

The blade weight and horizontal moment were determined by suspending the blade with slings at two stations and calculating the weight and moment from load cell readings.

The test setup used is shown in Figure 100. The heavy end of the blade at the root was suspended from an overhead traveling crane with a calibrated resistance gage type load cell. A spreader was inserted in the sling to protect the exposed edges of the shell cut-off. A tare weight reading including the slings, spreader, shackles, and unsupported parts of the load cell was read prior to hoisting. The tip end was hoisted from a traveling "A" frame with a chain-fall. The same type of load cell was used to read the tip support point. Tare weight at this support point consisted of slings, shackles, and unsupported parts of the load cell. The load cells were driven with a regulated 6 volt power supply and read with a digital voltmeter. Load cell calibration was in terms of milli- volt per volt of driving voltage per force pound applied to the load cell. The readings and computations are shown in Table XIII. Station location for the slings and the blade centerline marks were derived from the dimensional inspection setup. The blade centerline was positioned level to a horizontal plane. The load cells were adjusted to the vertical plane by use of a level and by moving the traveling "A" frame.

The net blade weight was 2412 lb (1094.1 kg) and a horizontal C.G. posi- tion at the 255 inch (6.48 m) station was calculated. Table XIV lists the design weight breakdown for this blade. The asterisked items were not present on the blade during the weighing and are not included in the

TABLE X
LEA AND FA INSPECTION PROCEDURE

1. Mount shank in saddle

2. Sling support blade at 441" station.

3. Plumb key slots vertical trailing edge up.

4. Mount 1/8" aluminum plate to face of outer sleeve.

5. Locate center of sleeve oval plate and drill 0.125" hole.

6. With transit establish height of sleeve center.

7. Mount cap on blade tip.

8. With transit and scale locate 735" station working from shank end.

9. With scale or level measure up from 735" station leading edge to locate blade center axis.

10. With transit set at sleeve center elevation swing to 735" station and adjust sling so blade center axis is at same elevation as sleeve center elevation.

11. With level carry blade center axis line out to blade tip and mark across tip cap.

12. Locate center intercept on blade tip cap and drill 0.125" hole.

13. Set height and lateral position of center pin stands so 0.125" center pins will slide into sleeve plate and tip cap center holes.

14. Mount 24" horizontal bar at tip, fixed to floor, same height as tip center, level and out perpendicular 24" from center hole.

15. Mount 24" swivel plate to rotate at center of sleeve plate, level and lock.

16. Draw 1/32 steel cable between horizontal bar and swivel plate 24" out from center holes on face side.

17. Set propeller protractor on horizontal shelf of sleeve plate, zero. Transfer this zero setting to a permanent beam, a mark for reference.

18. Retract centering pins.

19. Set propeller protractor to 3.73° C.W. and rotate sleeve C.C.W., as viewed from shank end, until protractor levels.

20. Level and lock swivel plate.

21. Re-engage centering pins. If necessary position sling to engage tip centering pin.

22. From inner face of swivel plate measure out 61.645" on cable to locate 105" station. Transfer this location on the vertical plane of blade face with machinist scale. Set horizontal intersect on face vertical line to establish centerline. With plumb, level a straight edge carry station line to tip and leading edge.

TABLE X (Continued)
LEA & FA INSPECTION PROCEDURE

23. With level against leading edge at station mark, measure up to centerline for L.E.A.

24. With level and scale measure from centerline out to cable and subtract from 24.00" for F.A.

25. For remaining stations repeat steps 19-22.

Sta.	Step 22	Protractor Angle
195	151.645	5.5
285	241.645	10.14
375	331.645	12.28
465	421.645	13.78
555	522.645	14.95
630	586.645	15.43
690	646.645	15.93
735	691.645	16.22

TABLE XI
THICKNESS INSPECTION PROCEDURE

1. Use F.W. Ball Gauss Meter Model 640.

2. Using eleven 2' square glass blocks milled from 0.200 - 0.700 inches in 0.050 increments establish meter reading with probe placed on one side and magnet on other side of each block. Plot meter reading versus block thickness on graph.

3. At each desired station (105, 195, 285, 375, 465, 555, 630, 690, 735) place magnet on inner shell at trailing edge side of spar (both sides) and check for peak meter reading. On graph determine thickness from max meter reading.

4. At completion of all 18 readings recheck calibration against calibration blocks.

5. With outside calipers measure thickest portion of blade at each station being certain caliper jaws are level.

FW BELL GAUSSMETER
MODEL 640
PROBE SER #58194
SET FULL SCALE RANGE AT 100
ZERO SUPPRESS OFF
CHECK CALIBRATION ON 1.0
SET ZERO
CHECK KNOWN THICKNESS

O CAL. JAN. 31, 1977

FOR 100 RANGE

THICKNESS – INCHES

GAUSSMETER READING
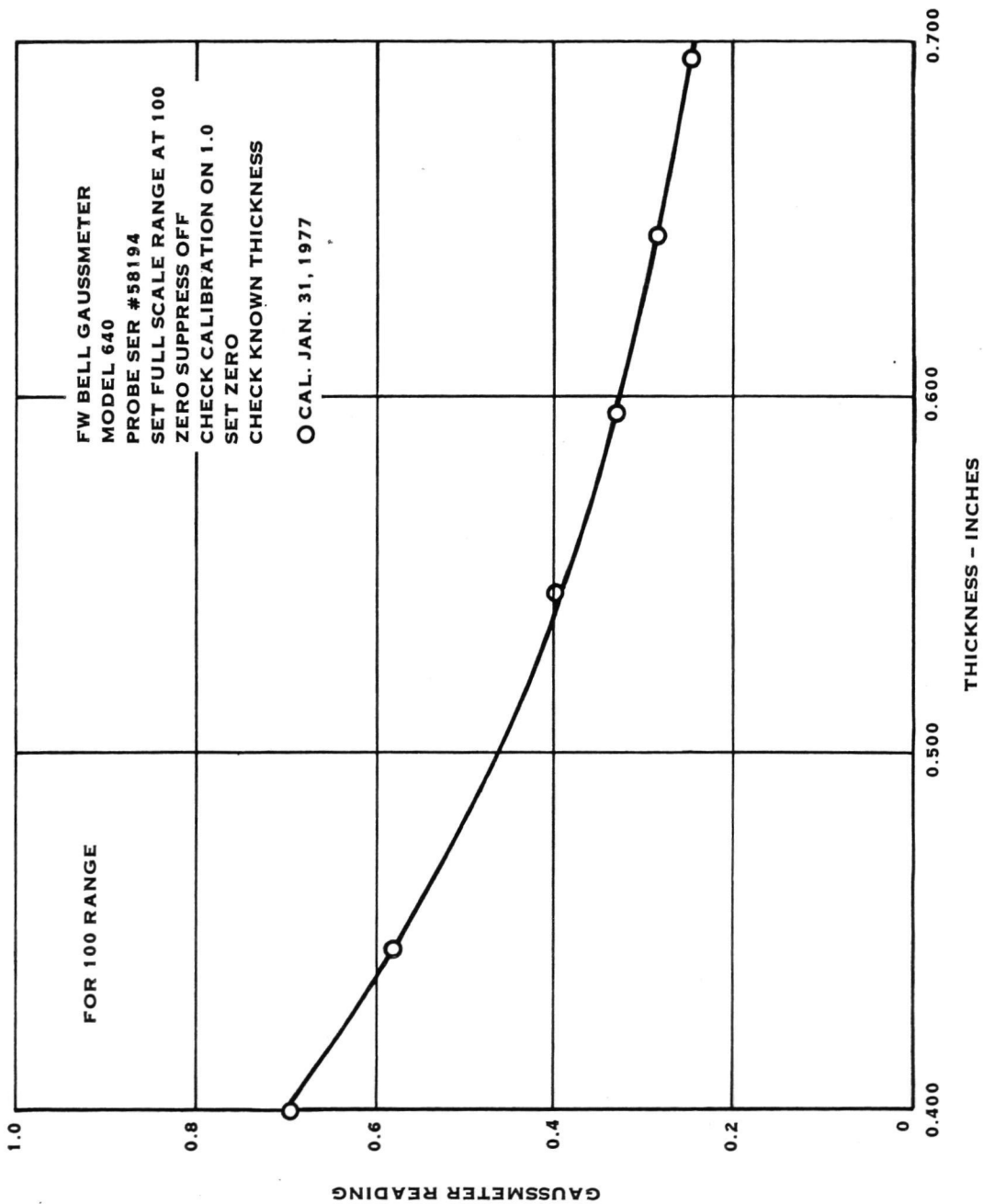
FIGURE 98. 100 RANGE GAUSS METER CALIBRATION
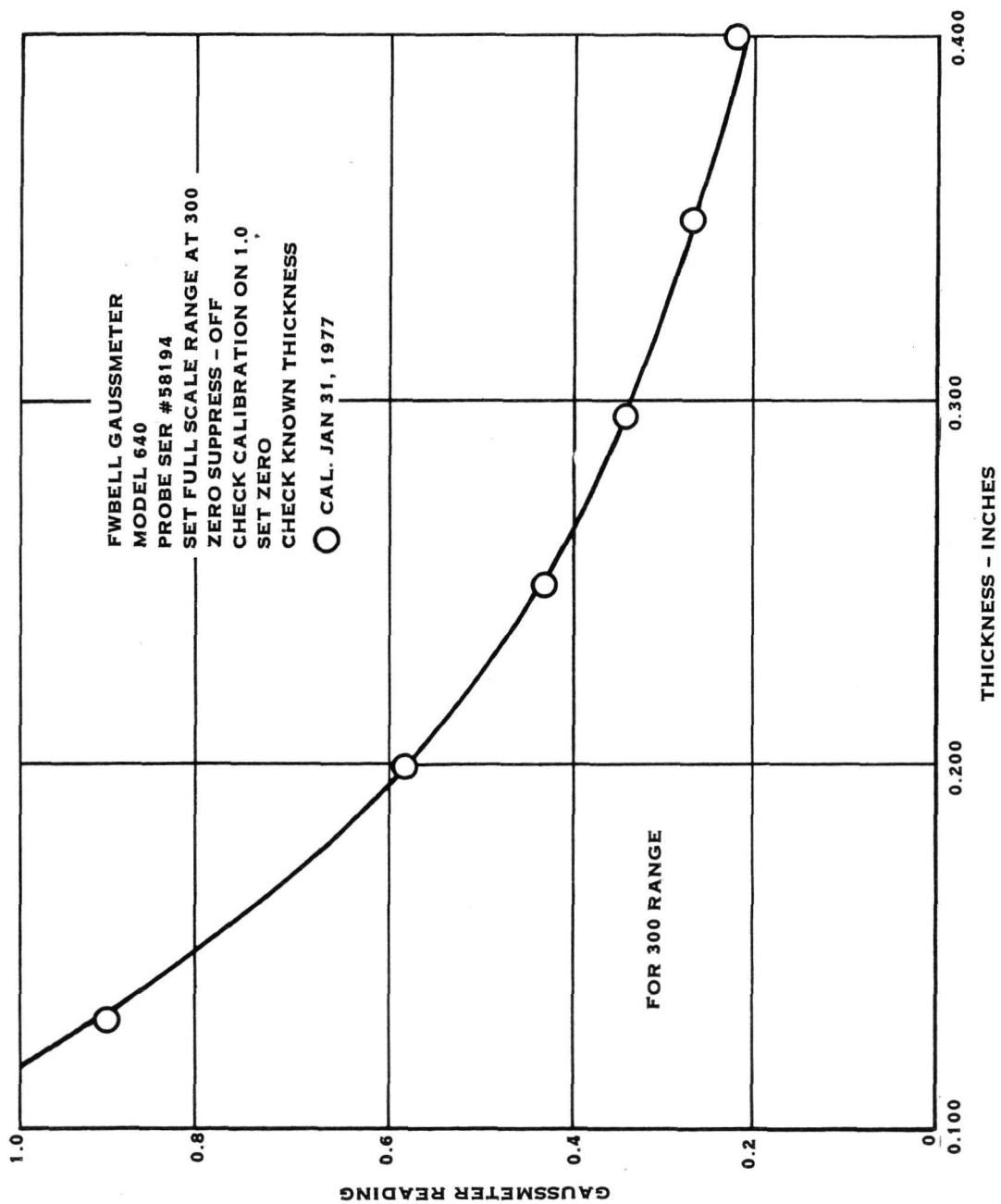
FIGURE 99. 300 RANGE GAUSS METER CALIBRATION

134

TABLE XII
BLADE AND BLADE WALL THICKNESSES

Sta. Face	Scale/Read	Thickness	Sta. Cam	Scale/Read	Thickness	Max. Thickness
105"	100 / 695	0.401	105"	100 / 700	0.400	24.25
	710	0.398		680	0.407	24.30
	730	0.395		770	0.378	24.32
		0.398 Avg			0.395 Avg	24.24 Avg
195	100 / 780	0.375	195	100 / 760	0.381	20.1
	810	0.366		840	0.358	20.02
	920	0.337		820	0.363	20.08
		0.359 Avg			0.397 Avg	20.05 Avg
285	100 / 730	0.390	285	100 / 750	0.384	16.12
	670	0.411		650	0.418	16.06
	665	0.413		730	0.390	16.05
		0.405 Avg			0.397 Avg	16.18 Avg
375	100 / 510	0.475	375	100 / 370	0.448	11.90
	520	0.470		580	0.445	11.92
	535	0.463		560	0.452	11.90
		0.469 Avg			0.448 Avg	11.91 Avg
465	100 / 810	0.366	465	300 / 410	0.261	8.45
	810	0.366		400	0.266	8.45
	300 / 325	0.307		360	0.286	8.45
		0.346 Avg			0.271 Avg	8.45 Avg
555	100 / 980	0.323	555	100 / 750	0.384	6.10
	880	0.347		750	0.384	6.10
	890	0.344				6.09
		0.338 Avg			0.384 Avg	6.09 Avg

TABLE XII (Continued)
BLADE AND BLADE WALL THICKNESSES

Sta. Face	Scale/Read	Thickness	Sta. Cam	Scale/Read	Thickness	Max. Thickness
630	100 / 995	0.319	630	300 / 320	0.309	4.45
	300 / 116	Out. Cal.		450	0.243	4.45
	115	Out. Cal.		445	0.245	4.45
	0.319 Avg			0.266 Avg		4.45 Avg
690	300 / 120	Out. Cal.	690	300 / 460	0.239	3.51
	137	Out. Cal.		470	0.235	3.55
	112	Out. Cal.				3.52
				0.237 Avg		3.53 Avg
735	100 / 880	0.347	735	300 / 300	0.323	2.83
	300 / 275	0.343		315	0.313	2.85
						2.85
	0.345 Avg			0.318 Avg		2.84 Avg
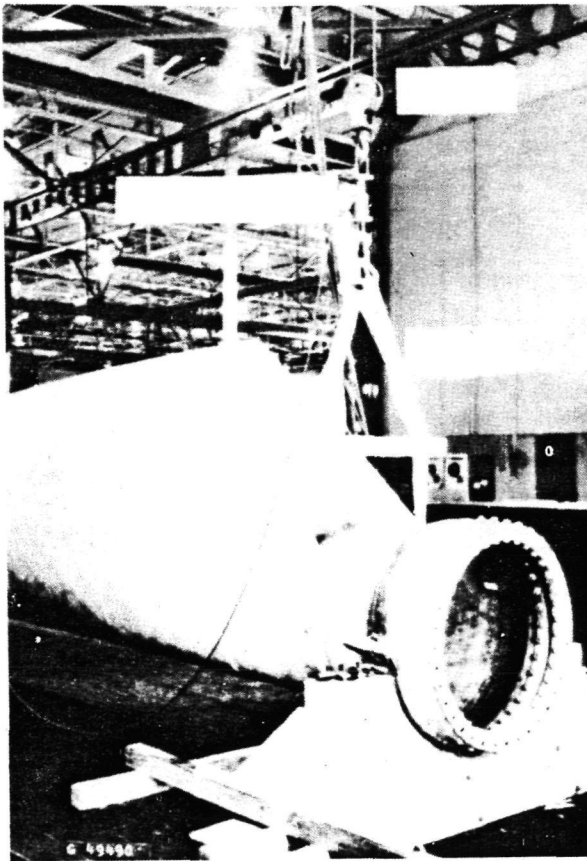
ROOT END SUSPENSION
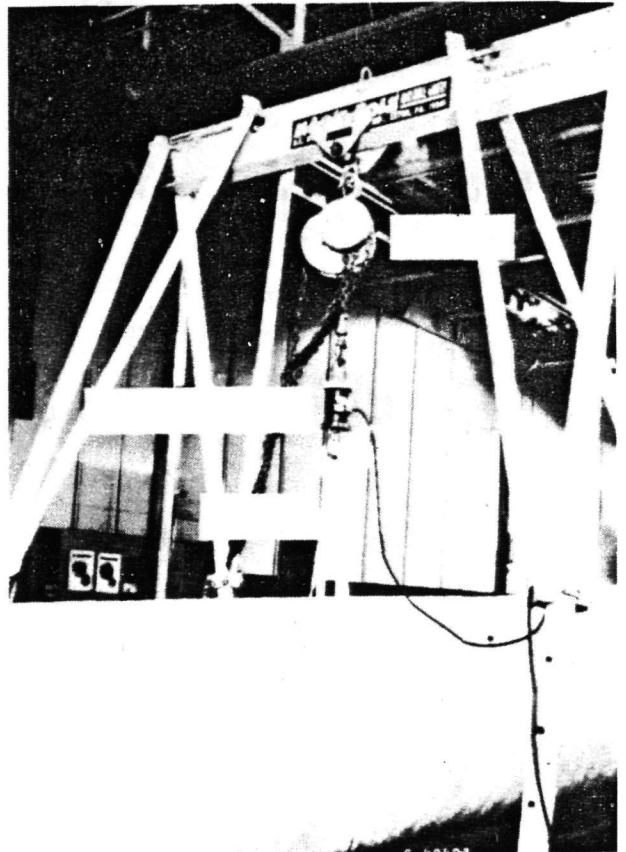
TIP END SUSPENSION

FIGURE 100. BLADE WEIGHT AND MOMENT DETERMINATION

137

TABLE XIII
BLADE WEIGHT DATA AND CALCULATIONS

FORMULA: Blade WT (lb) = $\dfrac{\text{(load cell \#1 output - tare)}}{\text{load cell \#1 sensitivity}} + \dfrac{\text{(load cell \#2 output - tare)}}{\text{load cell \#2 sensitivity}}$

C.G. position (STA) = $\dfrac{\dfrac{\text{(load cell \#2 output - tare)}}{\text{load cell \#2 sensitivity}} \times \text{(Distance between lines of action, 1)}}{\text{Blade WT}} + 75$

TEST DATA:

	LOAD CELL #1	LOAD CELL #2
LOAD	OUTPUT - MVDC	OUTPUT - MVDC
TARE	- 0.338	- 0.518
BLADE	- 8.952	- 11.950
	8.614 = 1445.9 lbs.	11.432 = 965.6 lbs.

LOAD CELL DATA:

K_1 = 0.0009929 MV/V/lb.

K_2 = 0.00197318 MV/V/lb.

EXCITATION = 6.000 V dc

TABLE XIII (Continued)
BLADE WEIGHT DATA AND CALCULATIONS

CALCULATIONS:

WT = 1445.9 + 965.6 = 2411.5 lbs.

C.G. position (STA) = $\dfrac{965.6 \times (525 - 75)}{2411.5}$ + 75"

= 255. in.

TABLE XIV
BLADE WEIGHT BREAKDOWN

	Type I Design	Manufacturing Prototype	Cause	Amount Over Design Weight
Blade spar & shell	1470 lb	2145 lb	Spar	
Inner and outer rings	260 lb	267 lb **	Cloth in transition	50
			Surface fill	23
*Adapter & bolts	236 lb		Ply tie down	36
			Alignment pin fill	10
*Balance weights	45 lb		Total	119
*Spar bulkhead	194 lb		Shell	
			Mandrel tie down	45
*Paint	36 lb		Extra circuits	95
			Ply tie down	23
*Tip and root closures	11 lb		90° overwrap & fill	240
			Peel ply resin	70
			Total	473
*Lightning Protection	25 lb		Adapter Sleeves	
Net Wt.	1730 lb	2412 lb	Over nominal tolerance	5
			Total Blade	597

*Not included in manufacturing prototype blade
**From separate scales weighing

140

net as weighed comparison. The manufacturing prototype blade as fabricated through filament winding was 682 lb (309.4 kg) over the nominal design weight. Examination of the fabrication records indicated that 597 pounds (270.8 kg) could be accounted for; 5 lb (2.3 kg) in the retention rings, 119 lb (54.0 kg) in the spar, and 473 lb (214.6 kg) in the shell, as shown also in Table XIV.

STRUCTURAL TEST

The blade structural testing consisted of an Experimental Modal Analysis (EMA) to evaluate mode shapes and resonant frequencies, an Experimental Stress Analysis (ESA) to evaluate the blade stress response and load deflection and a Proof Load Test to evaluate the blade plate buckling resistance. Several items were not included in the blade for these tests. They included the tip balance cup assembly, lightning protection, erosion protective coating, and the spar support. Only the spar support was structurally significant to the tests. A computer model of the test blade was used to predict blade response for comparison to the test results.

EXPERIMENTAL MODAL ANALYSIS

The blade was subjected to an experimental modal analysis (EMA) while mounted on a NASA furnished hub as shown in Figure 101. A separate hub EMA was not conducted. A fifty force pound (224.4 N) electrodynamic shaker was attached to the blade through an aluminum adapter which was temporarily bonded to the blade. The shaker was attached first to excite edgewise modes as shown in Figure 102a and second to excite flatwise and torsion modes simultaneously as shown in Figure 102b. An accelerometer was moved from point to point on the blade while the force and motion signals were acquired, processed and written onto the memory disk of a digital vibration analyzer. The blade frequencies, damping, amplitudes and phase angles and the blade mode shapes were extracted from the data using various modal parameter and mode shape extraction techniques. Zoom analysis was also used to help determine accurate modal damping.

Testing was conducted with a random force input from the shaker, exciting all blade modes simultaneously. This method is faster than swept sine methods and is similar to impact testing where the force gage is mounted on the head of a hammer. When a shaker is used however, the force gage is attached directly to the blade and significantly more low frequency energy is available since the impact duration may be much longer.

Table XV compares the actual blade frequencies to the analytically modeled frequencies for the first three flatwise, first three edgewise and first torsion modes. An average 6% variation existed between the two values. Figures 103 and 104 are comparisons of the predicted and actual mode shapes for the first three flatwise and first three edgewise modes. The agreement between analysis and test is good for the first two flatwise and first two edgewise modes, but shows some mode displacement and magnitude difference for the third flatwise and edgewise modes.
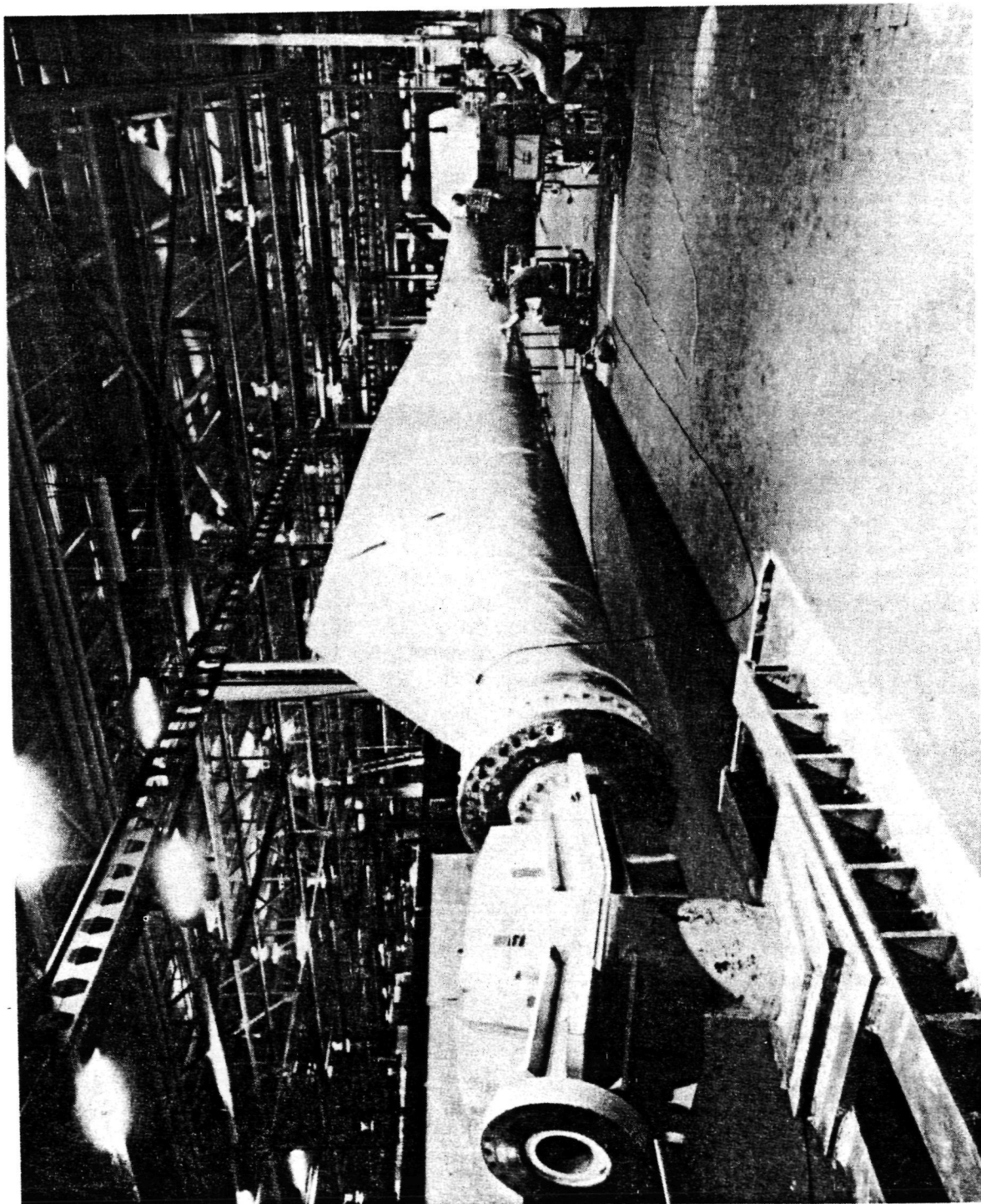
FIGURE 101. BLADE MOUNTED IN TEST HUB
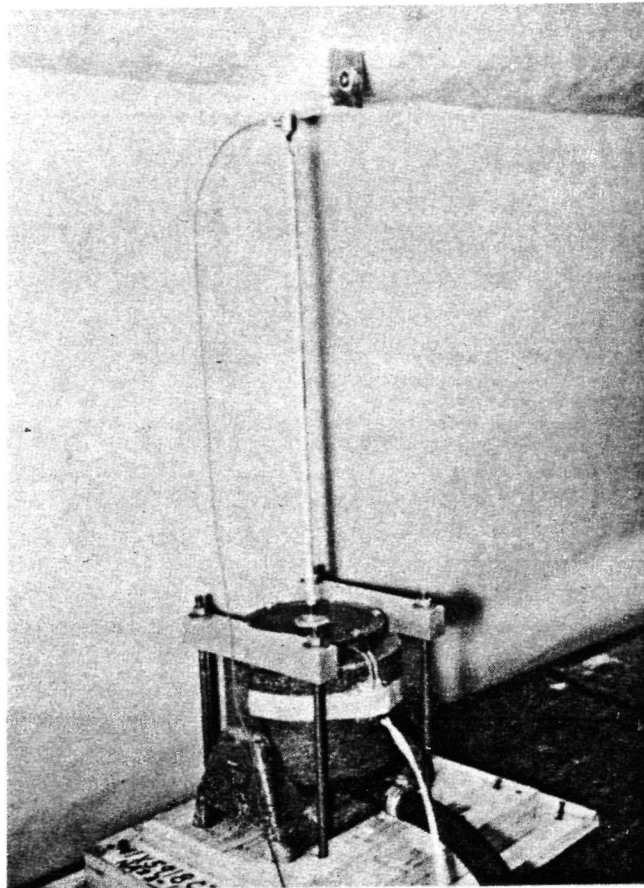
A. EDGEWISE MODE
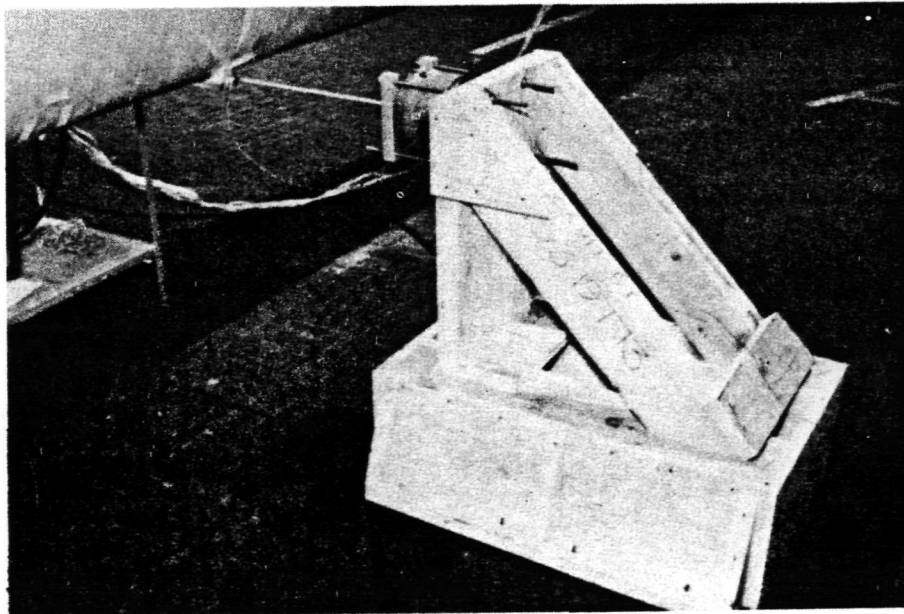
B. FLATWISE MODE

FIGURE 102. EXPERIMENTAL MODAL ANALYSIS SHAKER ARRANGEMENTS

TABLE XV
BLADE FREQUENCY COMPARISON

Mode	EMA (Hz)	Calculated (Hz)
First Flatwise	1.53	1.45
Second Flatwise	4.05	3.70
Third Flatwise	8.59	8.08
First Edgewise	2.63	2.51
Second Edgewise	9.36	9.86
Third Edgewise	22.38	24.75
First Torsional	29.26	28.59
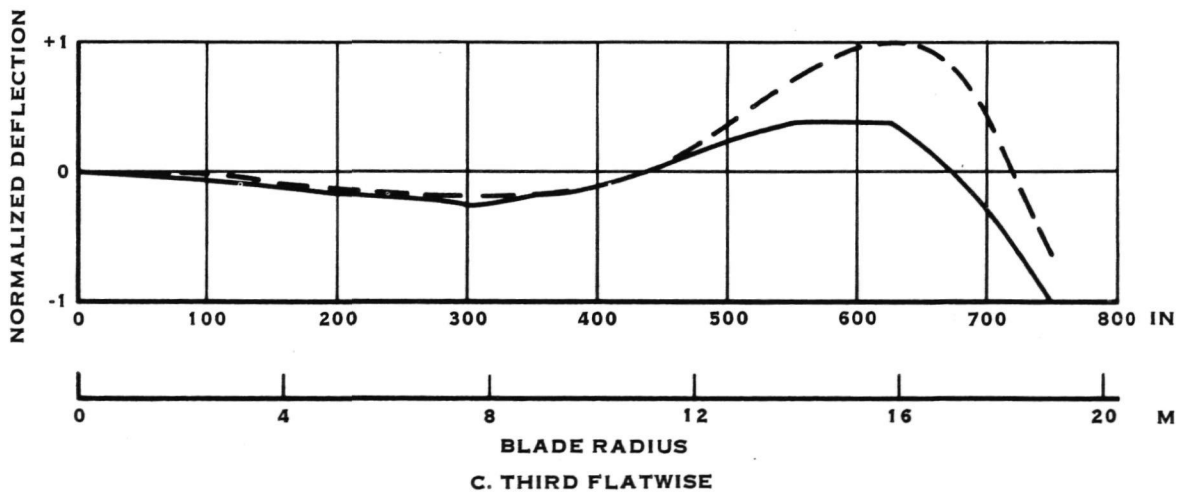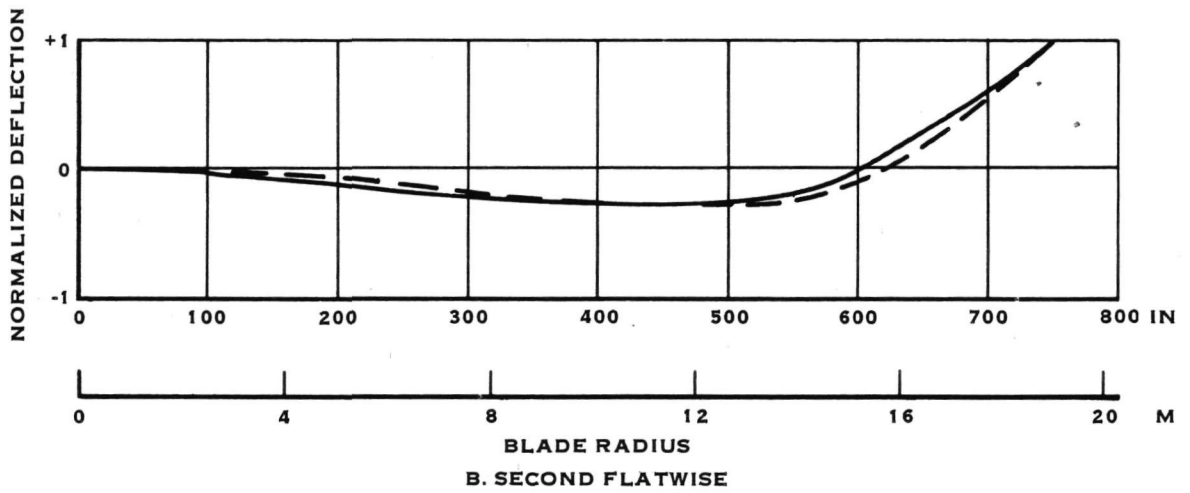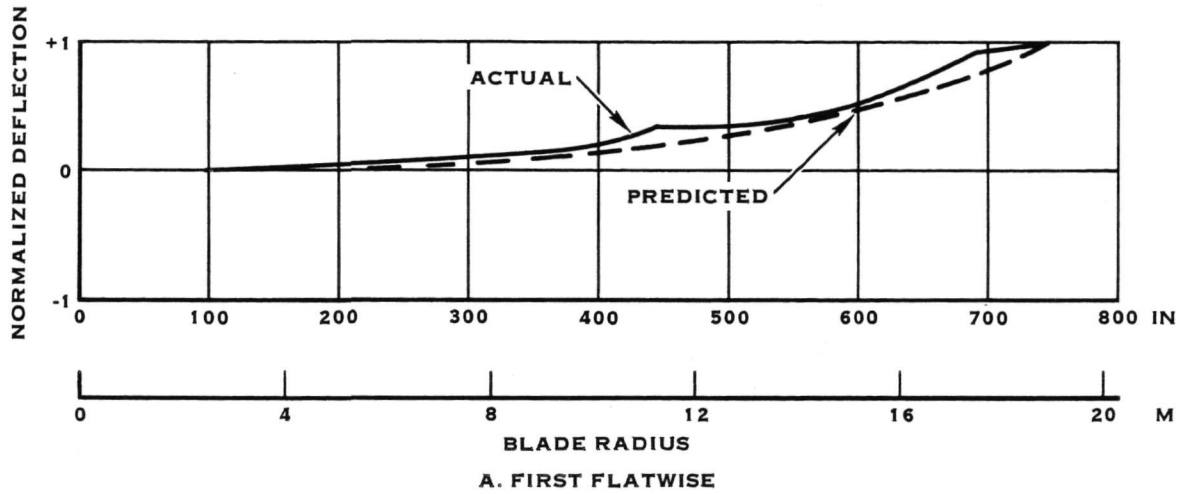
FIGURE 103. FLATWISE MODE SHAPES

145
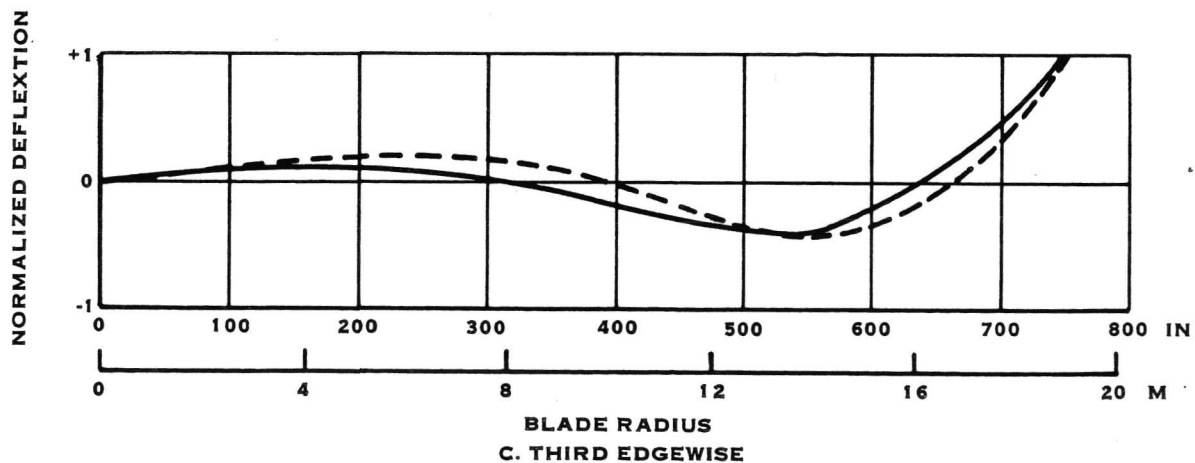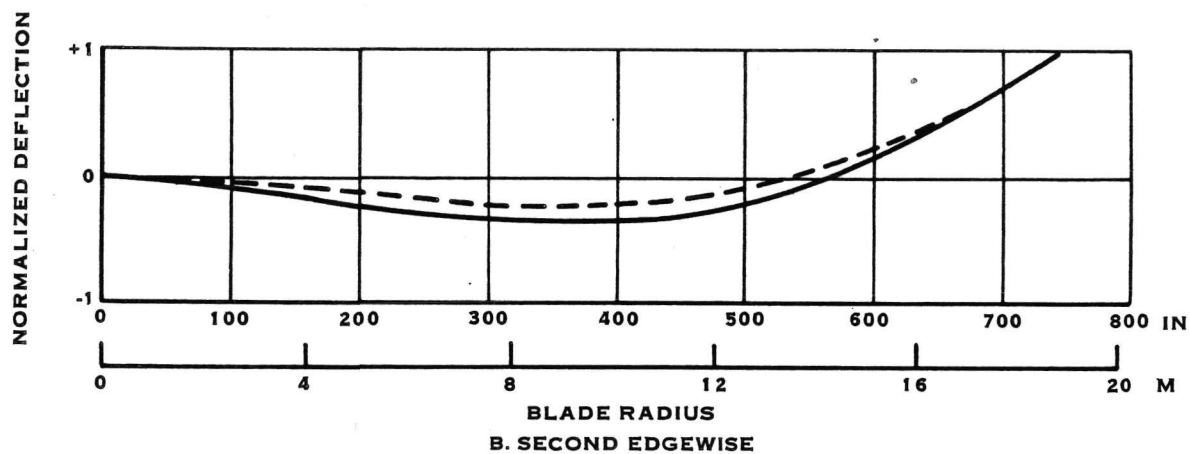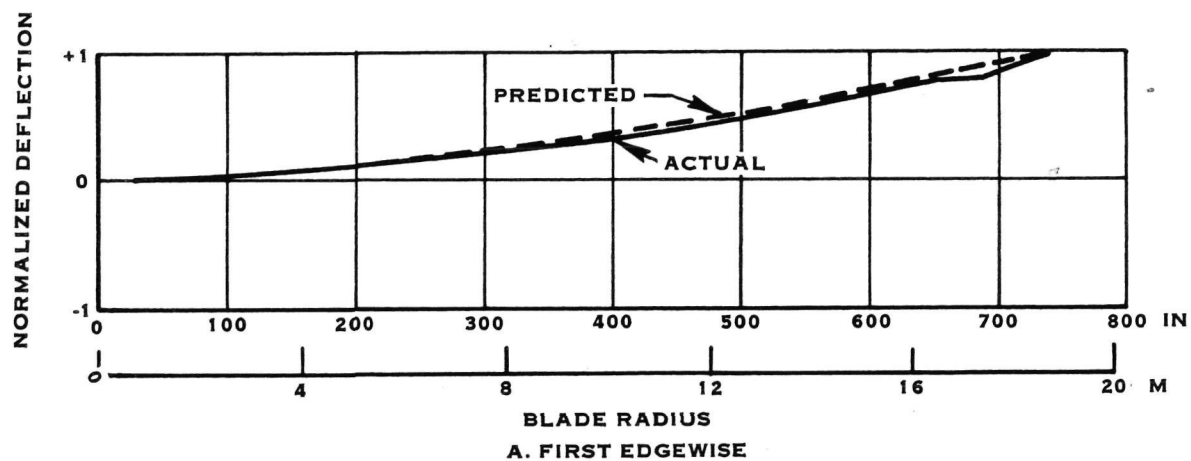
FIGURE 104. EDGEWISE MODE SHAPES

The analytical frequency and mode shape predictions accounted for hub rotational flexibility but not translation flexibility because of limitations in the computer program. The hub flexibility data was obtained in static stiffness tests. The damping values obtained in the tests include an unknown amount of interface and support structure damping. The fixed-free damping values in the test indicate smaller fixture and interface participation than in some other blade experience. It was not possible to separate the fixture damping from the blade damping and air damping.

When the blade is coupled to a hub, platform and tower, it is expected that much of the modal damping will come from interface damping in the pitch change mechanism, blade interface and other structural connections. Thus, accurate evaluation of the static blade damping properties may be relatively unimportant. Conversely, the modal damping coefficients of the installed, rotating blade are very important to accurately predict blade vibration stress levels and blade life resulting from operational blade excitations.

EXPERIMENTAL STRESS ANALYSIS

The blade was subjected to an experimental stress analysis (ESA) while mounted camber side up on a NASA furnished hub as shown in Figure 105. An array of electrical resistance foil strain gages was applied to the surface of the blade per Table XVI, and Figure 106. A concentrated load was applied at the 600 inch (15.24 M) station by use of a clamping fixture and an overhead crane. The load was monitored by a load cell and applied in increasing steps to define the linearity of the strain gage outputs. Strain gage readings were recorded on a Hamilton Standard Structures Laboratory, Strain Gage Data Logger (SGDL) System or read on a digital indicator. Deflection in the direction of loading were measured by graduated scales at various stations both of the lead edge and the trail edge. Deflections of the test hub were measured by dial gages and results used to correct indicated blade deflections. Pendumum type protractors were used to measure angular rotations of the blade upper surface in the longitudinal plane at several stations.

The ESA load was applied in 200 lb (889.6 N) increments up to a maximum load of 1000 lbs. (4448.0 N). The blade dead weight moment of 510,668 in-lb. (57705 N-M) at the retention was alleviated by applying a 917 lb (4079 N) force at the load point which was 556.6 inches (14.14 M) from the retention. The load values for the ESA were measured from the dead weight moment position.

The ESA results are tabulated in Tables XVII and XVIII. The results shown in Table XVII were obtained using the SGDL system. Selected gages were tied into a strain indicator and the testing repeated in order to minimize the data acquisition time and hence the drift. A comparison between the two strain recording systems is also shown in Table XVIII for the 1000 lb (4448 N) load condition. Good agreement was demonstrated by

148
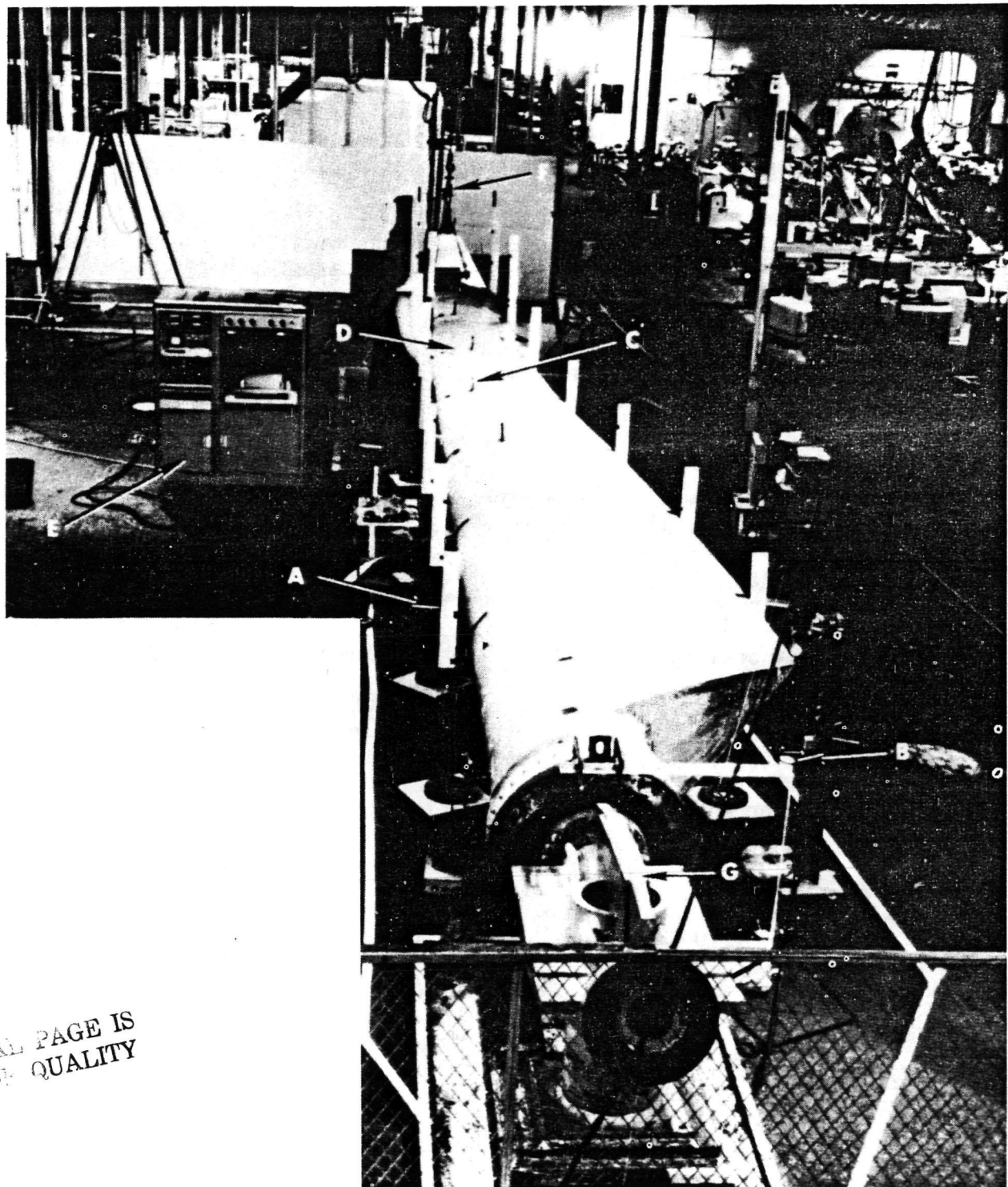
FIGURE 105. EXPERIMENTAL STRESS ANALYSIS SETUP

TABLE XVI
ESA STRAIN GAGE LOCATIONS

Station		% Chord	Side	Direction	Gage S/N
52.0-inch	(1.32-meter)	Spar C_L	Camber	Longitudinal	1
75.0	(1.90)	25			2
150.0	(3.81)				3
225.0	(5.72)				4
300.0	(7.62)				5
375.0	(9.52)				6
382.5	(9.72)				7
390.0	(9.91)				8
397.5	(10.10)				9
405.0	(10.29)				10
412.5	(10.48)				11
420.0	(10.67)				12
427.5	(10.86)				13
435.0	(11.05)				14
442.5	(11.24)				15
450.0	(11.43)				16
450.0	(11.43)			45°	17
450.0	(11.43)			Transverse	18
457.5	(11.62)			Longitudinal	19
465.0	(11.81)				20
472.5	(12.00)				21
480.0	(12.19)				22
487.5	(12.38)				23
495.0	(12.57)				24
502.5	(12.76)				25
510.0	(12.95)				26
517.5	(13.14)				27
525.0	(13.34)				28
562.5	(14.29)				29
450.0	(11.43)	0	Lead Edge		30
		5	Camber		31
		15			32
		40			33
		60			34
		80			35

149

TABLE XVI (Cont.)
ESA STRAIN GAGE LOCATIONS

Station		% Chord	Side	Direction	Gage S/N
450.0	(11.43)	100	Trail Edge	Longitudinal	36
		80	Face		37
		60			38
		40			39
		25			40
		15			41
		5			42
77	(1.96)	Main Joint	Camber		43
		See Fig 107		45°	44
				Longitudinal	45
450	(11.43)	Main Joint		45°	46
				Transverse	47
				Longitudinal	48
375	(9.52)	25	Face		49
412.5	(10.48)				50
487.5	(12.38)				51
525.0	(13.34)				52
532.5	(13.53)		Camber		53
540.0	(13.72)				54
547.5	(13.91)				55
555.0	(14.10)				56
570.0	(14.48)				57
577.5	(14.67)				58
585.0	(14.86)				59
592.5	(15.05)				60
600.0	(15.24)				61
607.5	(15.43)				62
615.0	(15.62)				63
622.5	(15.81)				64
630.0	(16.00)				65
637.5	(16.19)				66
645.0	(16.38)				67
652.5	(16.57)				68
660.0	(16.76)				69
562.5	(16.57)		Face		70
600.0	(15.24)				71
637.5	(16.19)				72
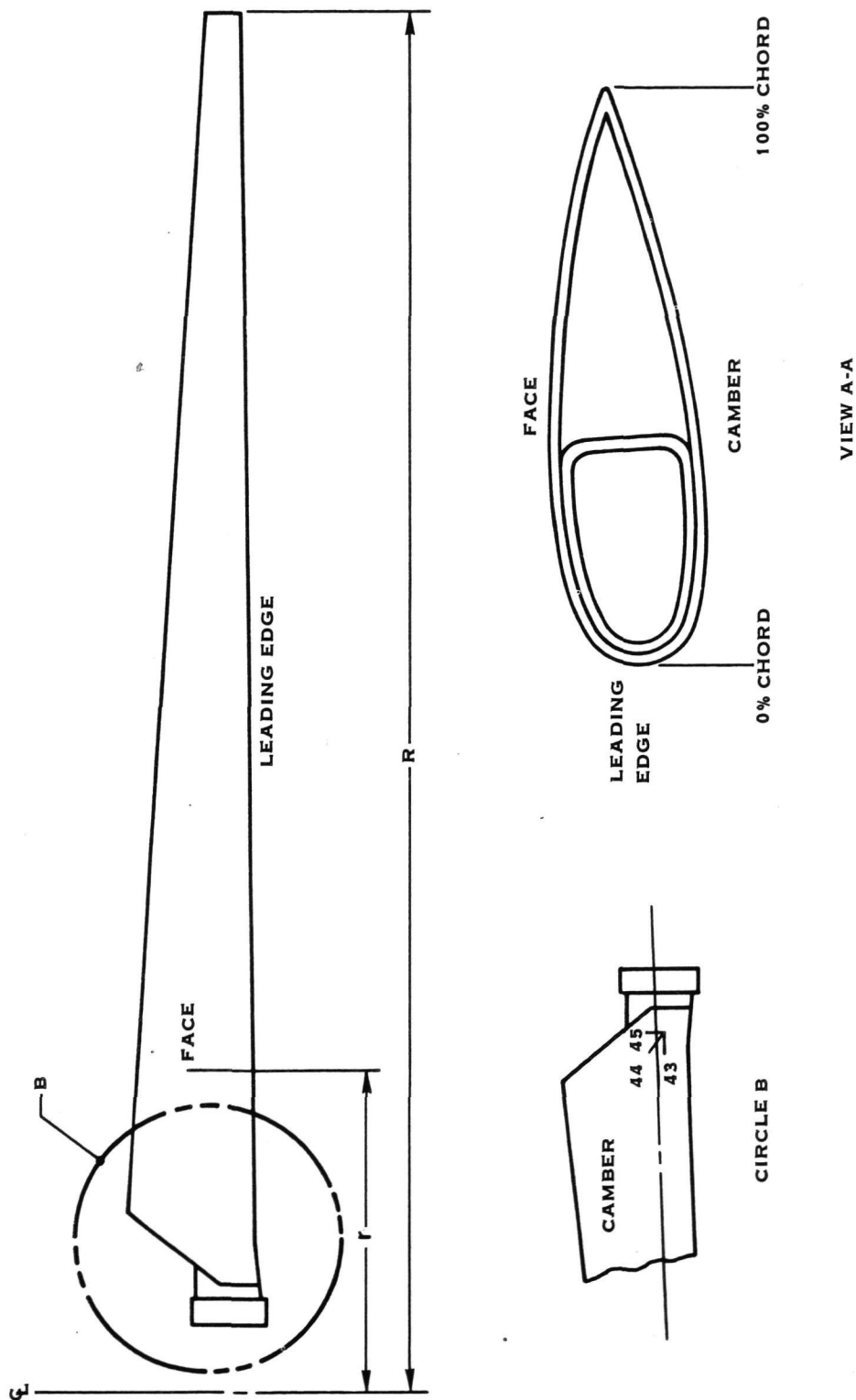
FIGURE 106. STRAIN GAGE INSTALLATION

TABLE XVII
ESA STRAIN GAGE READINGS
$\Delta\epsilon, \mu''/''$

SGDL

Gage #	0 Load Return	0 Load Set	200 lb	400 lb	600 lb	800 lb	1000 lb	0 Load Offset	Blade Sta. In.	r/R	% Chord	Side of Blade
1	-149	0	-36	-69	-102	-139	-175	3	52	0.07	₵	C
2	-269	0	-64	-120	-180	-247	-307	-3	75	0.1	25	C
3	-292		-71	-128	-196	-269	-336	11	150	0.2		
4	-364		-85	-159	-239	-326	-406	-6	225	0.3		
5	-459		-107	-201	-301	-409	-511	-11	300	0.4		
6	-563		-131	-250	-374	-508	-635	-9	375	0.5		
7	-539		-125	-240	-360	-489	-611	-9	382.5	0.51		
8	-363		-102	-171	-275	-376	-469	49	390	0.52		
9	-534		-123	-231	-346	-466	--	-2	397.5	0.53		
10	-496		-117	-220	-334	-452	-565	4	405	0.54		
11	-556		-127	-246	-366	-494	-616	-11	412.5	0.55		
12	-443		-102	-194	-291	-392	-487	2	420	0.56		
13	-557		-125	-243	-362	-487	-607	-10	427.5	0.57		
14	-508		-125	-232	-353	-477	-595	20	435	0.58		
15	-322		-88	-154	-242	-329	-409	46	442.5	0.59		
16	-601		-135	-263	-392	-527	-657	-7	450	0.6		
17	-95		-120	-143	-169	-196	-222	-95	450	0.6		
18	301		56	110	159	209	256	5	450	0.6		
19	-575		-130	-253	-378	-507	-633	-9	457.5	0.61		
20	-573		-125	-245	-366	-492	-615	-6	465	0.62		
21	-649		-145	-283	-422	-568	-709	2	472.5	0.63		
22	-561		-123	-241	-358	-482	-601	-5	480	0.64		
23	-574		-124	-246	-366	-490	-612	-6	487.5	0.65		
24	-576		-124	-247	-367	-492	-614	-5	495	0.66		
25	-553		-120	-239	-356	-477	-596	-1	502.5	0.67		
26	542		-120	-237	-353	-475	-593	9	510	0.68		
27	-533		-119	-236	-349	-468	-581	-2	517.5	0.69		

TABLE XVII (Cont.)
ESA STRAIN GAGE READINGS
$\Delta\epsilon, \mu''/''$

SGDL

Gage #	0 Load Return	0 Load Set	200 lb	400 lb	600 lb	800 lb	1000 lb	0 Load Offset	Blade Sta. In.	r/R	% Chord	Side of Blade
28	-485	0	--	-207	-306	-410	-511	-3	525	0.70	25	C
29	-357		-78	-151	-225	-301	-375	4	562.5	0.75	25	→ LE
30	92		23	46	68	92	114	8	450 →	0.6 →	0	C
31	-295		-66	-125	-187	-251	-314	3			5	
32	-505		-112	-218	-324	-436	-544	1			15	
33	-468		-104	-202	-300	-404	-504	-5			40	
34	-409		-93	-181	-271	-366	-458	1			60	
35	-238		--	-99	-145	-194	-240	-1			80	→ TE
36	59		14	27	40	54	67	7			100	F
37	304		70	138	204	274	342	12			80	
38	383		86	171	253	340	424	8			60	
39	620		137	269	399	539	673	15			40	
40	611		138	268	400	539	674	7			25	
41	593		131	258	382	515	643	17			15	
42	444		100	197	292	394	493	10			5	
43	-220		53	98	148	202	252	4	77	0.1		C →
44	-146		33	65	95	128	160	-18	77	0.1		
45	123		31	53	81	110	110	-7	77	0.1		
46	-431		-100	-195	-290	-392	-489	-8	450	0.6		
47	-64		-15	-27	-40	-52	-62	0	450	0.6		
48	257		61	121	181	249	315	4	450	0.6		F →
49	644		147	280	417	566	706	15	375	0.5	25	
50	585		142	265	397	537	670	-5	412.5	0.55	25	
51	628		140	277	410	552	689	12	487.5	0.65	25	
52	537		117	233	345	463	577	12	525	0.7	25	

TABLE XVIII
ESA STRAIN GAGE READINGS
$\Delta\epsilon, \mu''/''$

Gage #	0 Load Set	Vishay						SGDL		Blade Sta. In.
		200 lb	400 lb	600 lb	800 lb	1000 lb	0 Load Offset	1000 lb	0 Load Offset	
1	0	-32	-64	-97	-133	-171	-3	-175	3	52
2		-63	-120	-178	-239	-301	-4	-307	-3	75
3		-73	-140	-207	-277	-349	-4	-335	11	150
4		-80	-156	-233	-314	-397	-4	-406	-6	225
5		-101	-197	-294	-394	-497	-6	-511	-11	300
6		-126	-247	-368	-496	-624	-7	-635	-9	375
7		-118	-233	-350	-472	-595	-3	-611	-9	382.5
8		-121	-233	-346	-463	-580	2	-469	49	390
9		-120	-235	-348	-465	-580	5	-466(1)	-2	392.5
10		-122	-236	-350	-470	-587	-3	-565	4	405
11		-120	-238	-356	-480	-603	-3	-616	-11	412.5
12		-103	-202	-299	-400	-499	1	-487	2	420
13		-116	-233	-349	-470	-589	0	-607	-10	427.5
14		-131	-256	-382	-511	-638	9	-595	20	435
15		-108	-208	-306	-406	-502	18	-409	46	442.5
16		-131	-259	-386	-520	-649	-6	-657	-7	450
17		-28	-52	-77	-105	-132	0	-222	-95	450
18		60	112	163	212	258	13	256	5	450
19		-127	-249	-371	-499	-623	-6	-633	-9	452.5
20		-125	-246	-366	-493	-615	-5	-615	-6	465

(1) @ 800 lb

154

TABLE XVIII (Cont.)
ESA STRAIN GAGE READINGS
$\Delta\epsilon, \mu''/''$

Gage #	Vishay							SGDL		Blade Sta. In.
	0 Load Set	200 lb	400 lb	600 lb	800 lb	1000 lb	0 Load Offset	1000 lb	0 Load Offset	
21	0	-141	-282	-422	-568	-711	-4	-709	2	472.5
22		-122	-239	-357	-479	-598	-5	-601	-5	480
23		-124	-244	-364	-488	-609	-6	-612	-6	487.5
24		-123	-244	-364	-489	-610	-5	-614	-5	495
25		-123	-241	-360	-482	-600	-6	-596	-1	502.5
26		-124	-243	-362	-486	-605	-7	-593	9	510
27		-122	-238	-354	-473	-588	-7	-581	-2	517.5
28		-107	-208	-308	-412	-513	-7	-511	-3	525
29		-79	-155	-233	-311	-386	-7	-375	4	562.5

the results. Table XIX contains the deflection results.

Figure 107 is a plot of the theoretical strain distribution for the blade
with load applied at the 600 inch (15.24 M) station. Experimentally ob-
tained strain points at approximately 75 inch (1.90 M) intervals were
normalized to the 450 inch (11.43 M) station strain value and the results
were superimposed on the figure. Good agreement is indicated between the
experimental and computer model analysis results. Figure 108 is a compari-
son of computer model analysis and experimental chordwise distributions of
radial strain. A divergence from analysis is noted locally at the 40%
chord position. This may be accounted for as the result of local shell
deflections associated with proximity to the spar backface. Figure 109 is
a plot of theoretical deflection distribution with the experimental leading
edge and trailing edge distributions superimposed. Excellent agreement is
evidenced with the exception of the trailing edge value at the 600 inch
(15.24 M) station. Since this is the load application station and the
load transfer fixturing did not extend across the entire chord, the dis-
parity between the leading and trailing edge deflections apparently results
from slight twisting at this station. The coincidence of leading and
trailing edge deflections at the other stations demonstrates the absense of
twisting inboard.

PROOF LOAD TEST

Following completion of the experimental stress analysis and a review of
the test data the blade was subjected to a proof load test to evaluate
plate buckling resistance. From the review of the ESA results it was ap-
parent that the test hub would be damaged if the intended proof load were
applied at the 600 inch (15.24 M) station. To preclude damage to the hub
the hub was reinforced and the load application point was moved to the 712
inch (18.08 M) station. This resulted in moving the peak strain from the 450
inch (11.43 M) station to the 590 inch (14.99 M) station. The load applied
to the 712 inch (18.08 M) station necessary to produce the desired stress
at the 590 inch station produced less moment at the hub than the load needed
at the 600 inch station to produce the desired stress at the 450 inch (11.43 M)
station. The two one inch (2.54cm) holes in the shell next to the spar
trailing edge which were drilled to facilitate loading fixture application
were now at the maximum strain station. The holes were repaired using the
standard fiberglass cover propeller blade technique of scarfing the fiber-
glass around the hole and laying up fiberglass cloth in the hole. The
integrity of these patches was maintained throughout the proof load even
though they were at the maximum strain station.

The basis for selecting the proof load moment is shown in Figure 110. This
figure shows the ultimate moment where buckling would occur for each station
and the design moment curve which could not be exceeded at any station for
any load case. To establish that the blade had buckling capacity above the
design curve it was tested to 120% of the design buckling moment at the 590
inch (14.99 M) station. The blade moment distribution for an 18 to 36 mph
(28.96 to 57.92 km/hr) gust is also shown in Figure 110. The proof test
moment at the 590 inch (14.99 M) is 320% of the moment caused by this gust.

TABLE XIX
ESA DEFLECTIONS, INCHES OR DEGREES

Blade Sta. In.	Edge of Blade	200 lb	400 lb	600 lb	800 lb	1000 lb	0 Off-set	Type of Deflection
150	LE	0.150	0.200	0.280	0.370	0.470	0.050	Vertical
225		0.200	0.400	0.560	0.780	0.930	0.050	
300		0.350	0.650	0.970	1.310	1.630	0.100	
375		0.600	1.112	1.650	2.220	2.800	0.100	
450		0.940	1.750	2.640	3.500	4.470	0.125	
525		1.470	2.860	4.150	5.700	7.150	0.200	
600		2.210	4.240	6.340	8.460	10.610	0.320	
150	TE	0.060	0.140	0.230	0.280	0.350	0.060	
225		0.150	0.300	0.450	0.620	0.770	0.020	
300		0.300	0.600	0.890	1.250	1.550	0.070	
375		0.550	1.050	1.500	2.100	2.670	0.120	
450		0.920	1.740	2.560	3.470	4.440	0.160	
525		1.480	2.800	4.150	5.680	7.320	0.285	
600		2.180	3.200	5.200	7.500	9.600	0.360	
75	LE	0.017	0.034	0.051	0.071	0.089	0.008	
105	LE	0.036	0.068	0.101	0.140	0.176	0.015	
105	TE	0.028	0.054	0.080	0.110	0.140	0.010	
Hub	Top	0.0105	0.0215	0.033	0.046	0.0595	0.009	Horizontal
	Bottom	0.004	0.0075	0.012	0.018	0.0232	0.0035	
	Retent.	--	--	--	--	0.0215	0	Vertical
300	0	0	0	0.5	1.0	1.0	0.25	Angular
375	1.0	1.0	1.0	1.5	2.0	2.0	1.0	
450	1.0	1.0	1.0	1.5	2.0	2.0	1.0	
525	3.0	2.5	2.5	4.0	4.5	4.5	3.0	
600	2.0	2.5	3.0	3.5	4.0	5.0	2.0	
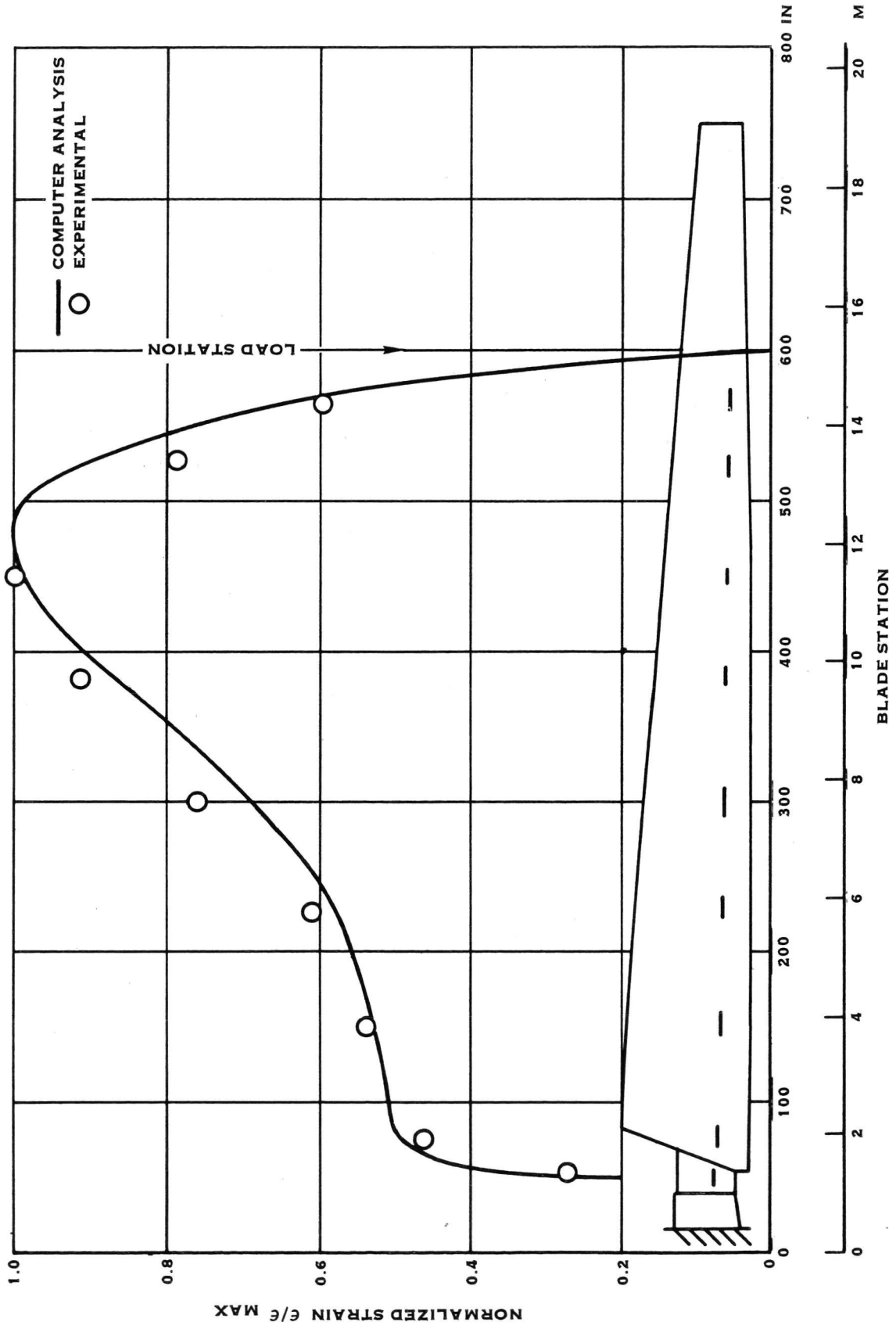
FIGURE 107. LONGITUDINAL STRAIN DISTRIBUTION
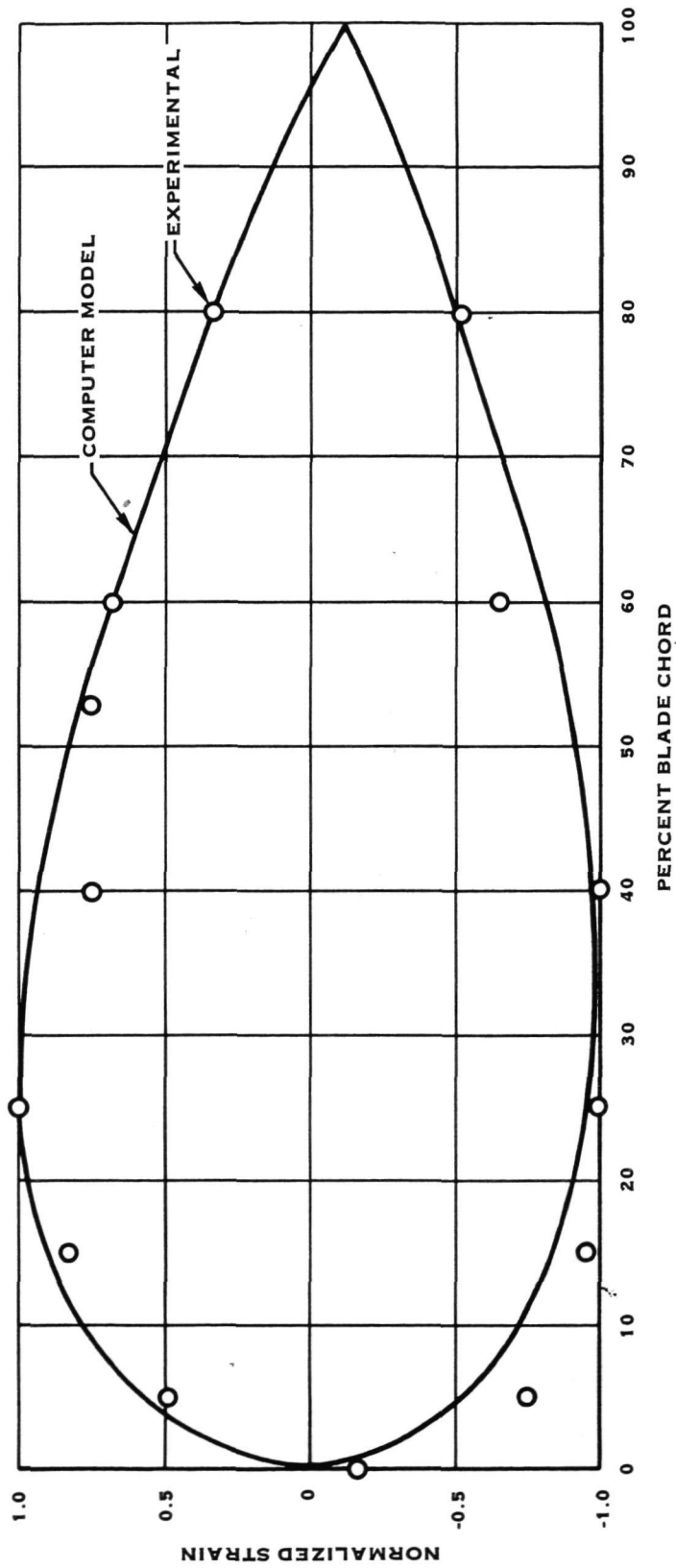
FIGURE 108. CHORDWISE STRAIN DISTRIBUTION
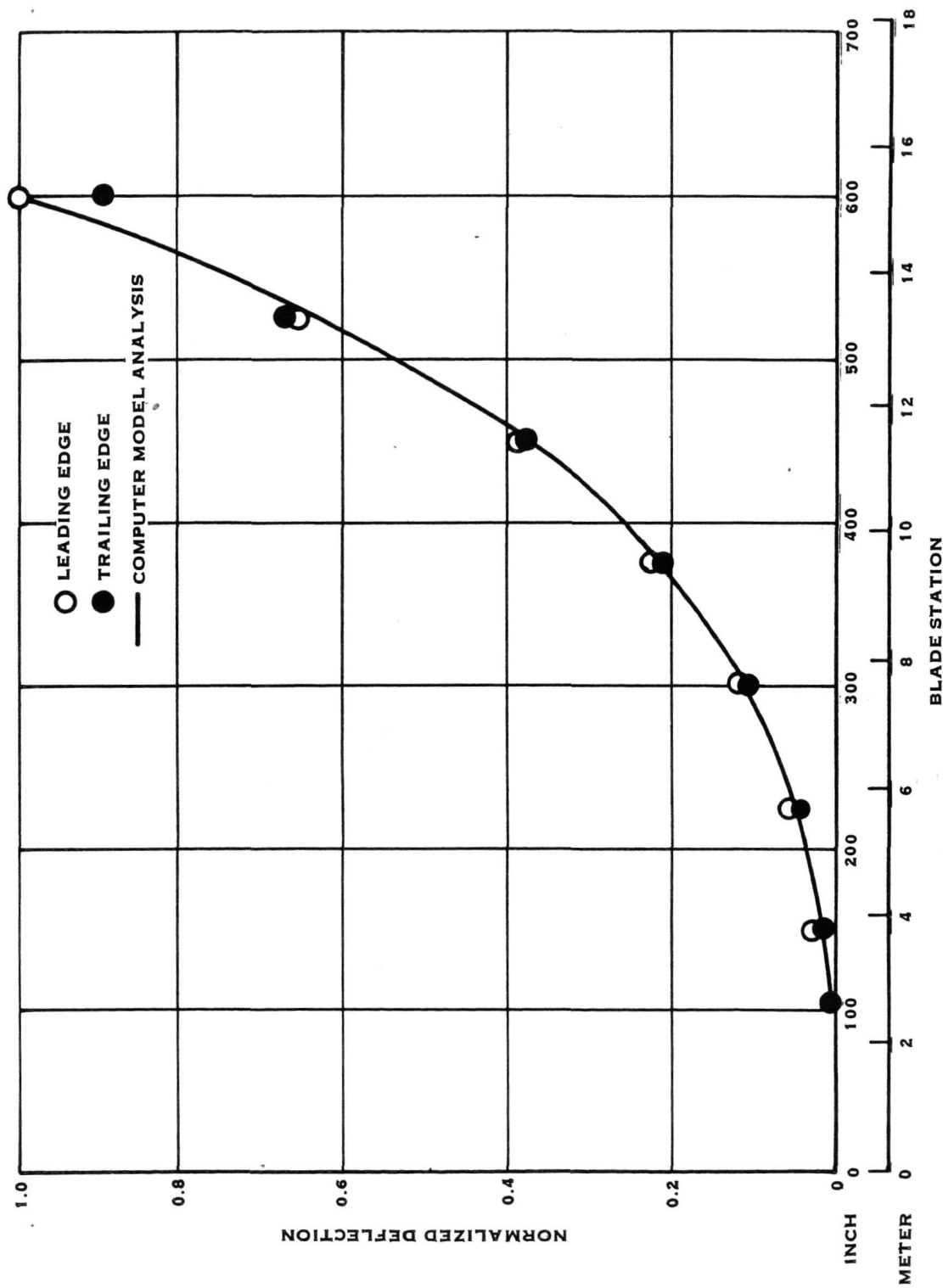
FIGURE 109. BLADE DEFLECTION DISTRIBUTION
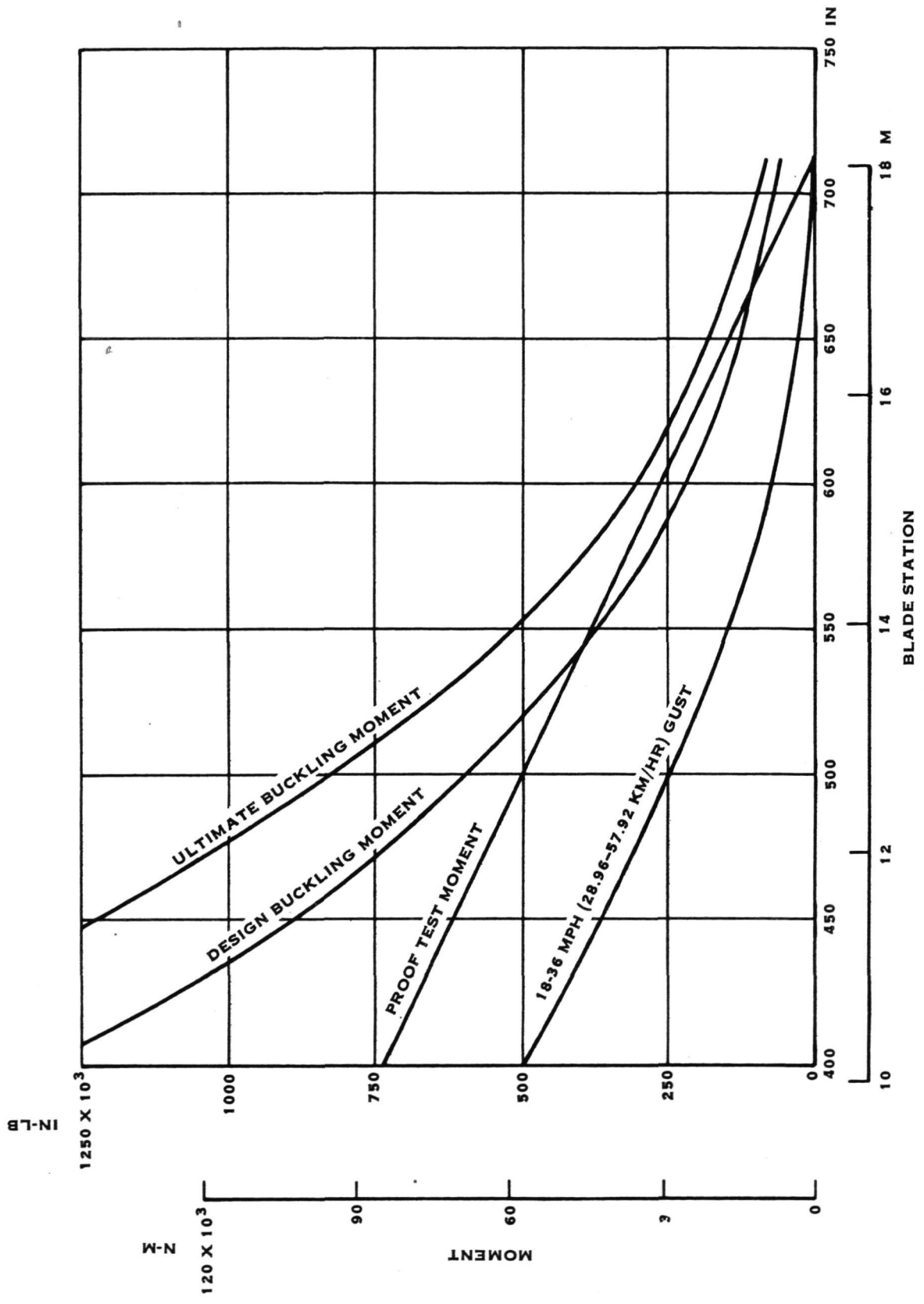
FIGURE 110. PROOF TEST MOMENT DISTRIBUTION

Set up, loading technique, and instrumentation for the proof test were the same as used for the ESA test. The buckling moment calculations included the effect of the blade dead weight loading and hence the load values for the proof test were measured from the dead weight downward position. Strains and deflections were measured at each of the loads applied to the blade. During the loading up sequence, selected strain gage outputs were plotted to detect possible departure from linearity which could represent the on-set of buckling. Blade surfaces were examined visually for occurances of local rippling and deformation instability. Figures 111 and 112 show the blade at its final load of 2365 lb (10520 N). The foam rubber and plywood seen in these figures were used as a safety damper to absorb the energy in the blade should the loading fixtures fail.

Figure 113 plots the experimental strain distribution for the proof load mode and shows the strain peaking near the 600 inch (15.24 M) station where the two shell holes were patched. Strains and deflections for the proof test are shown in Tables XX and XXI, respectively.

Figure 114 is a plot of strain versus load for several stations around the peak strain area of the blade. Figure 114 also shows the tip deflection measured at the end of a 27 inch (68.58 cm) boom attached to the end of the blade. The linearity of the displays is apparent, confirming the absence of buckling up to and including the maximum applied load of 2365 lb (10520 N).
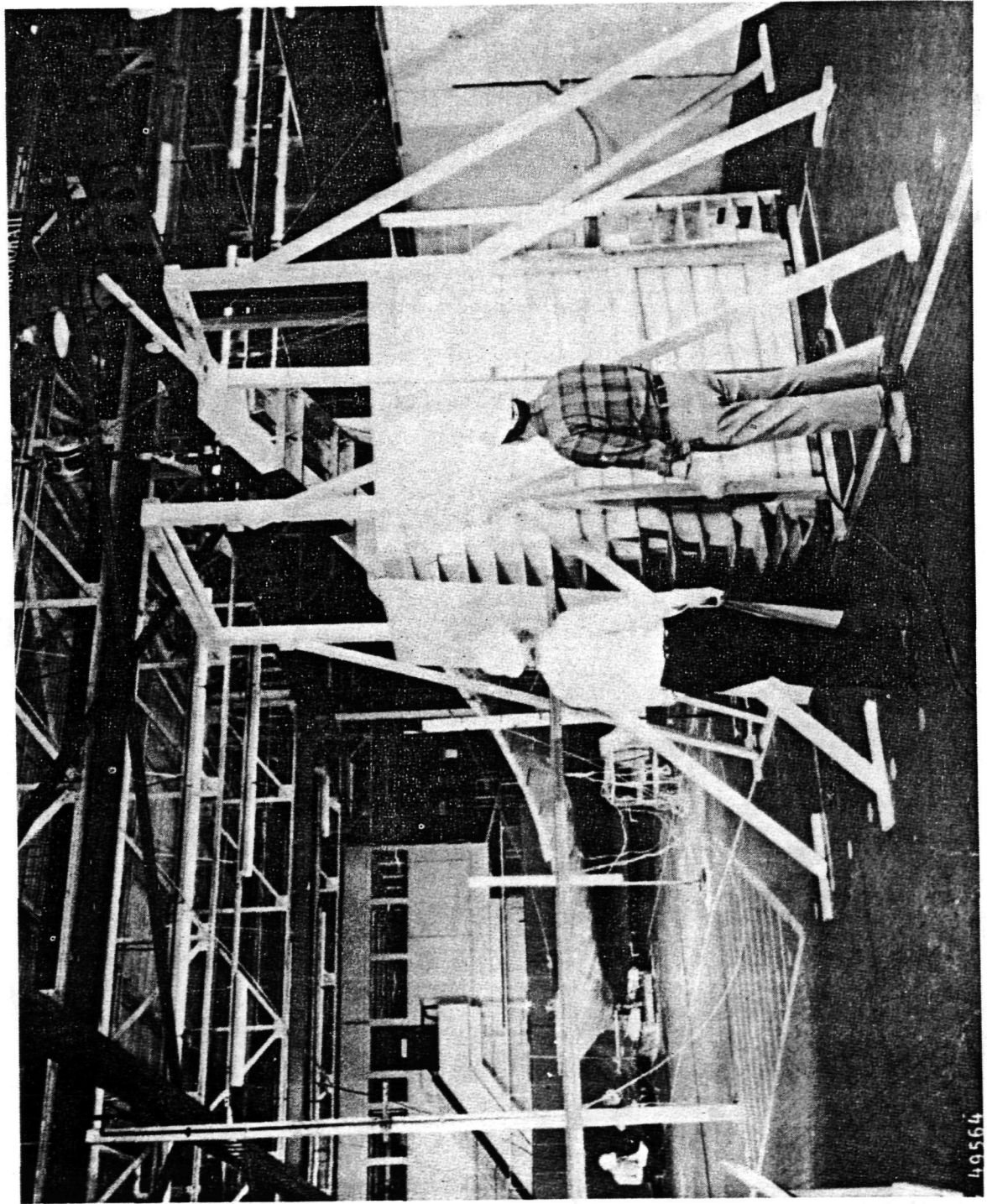
FIGURE 111. PROOF TEST FINAL LOAD
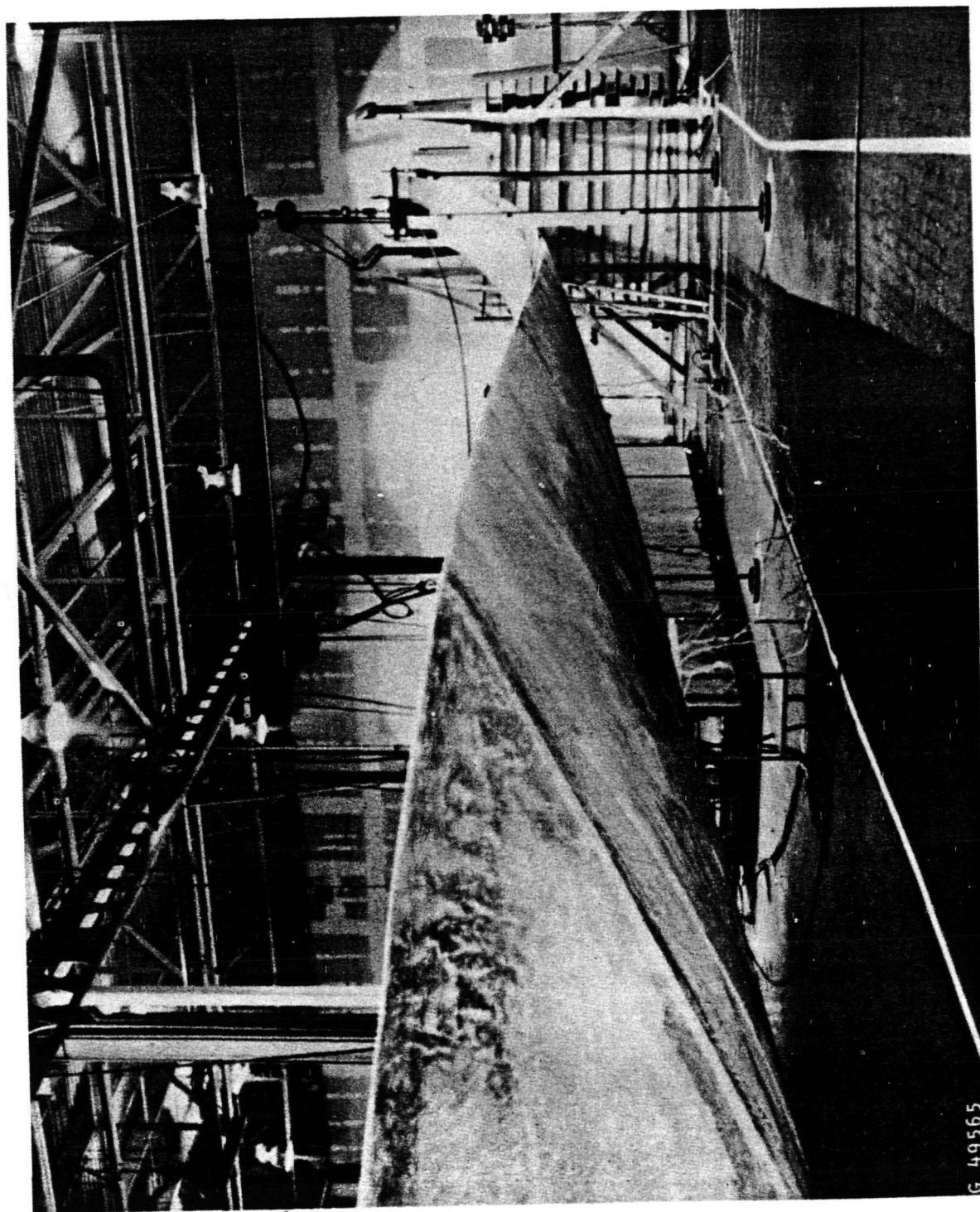
FIGURE 112. PROOF TEST FINAL LOAD
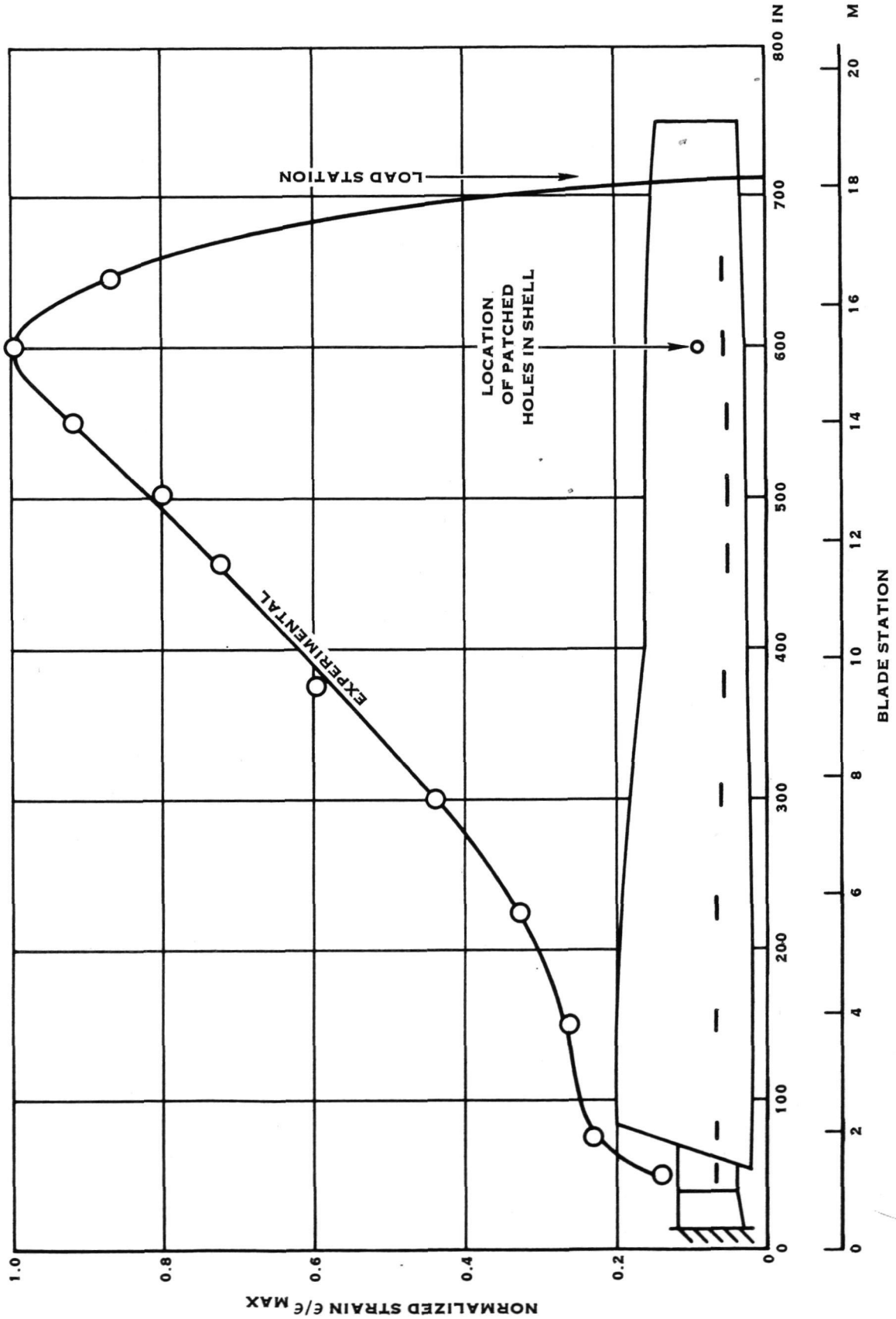
FIGURE 113. PROOF TEST LONGITUDINAL STRAIN DISTRIBUTION

TABLE XX
BLADE PROOF TEST STRAINS
$$\Delta\epsilon, \mu''/''$$

Vishay

Gage No.	0 Load Set	500 lb	1000 lb	1200 lb	1400 lb	1600 lb	1700 lb	1800 lb	1900 lb	1971 lb
20	0	-564	-1145	-1380	-1616	-1818	-1935	-2050	-2170	-2240
21		-672	-1358	-1638	-1919	-2170	-2300	-2440	-2570	-2660
22		-580	-1173	-1657	-1657	-1872	-1982	-2100	-2220	-2290
23		-608	-1229	-1481	-1736	-1962	-2080	-2200	-2320	-2400
24		-637	-1287	-1553	-1820	-2060	-2180	-2310	-2440	-2530
25		-650	-1316	-1587	-1861	-2110	-2230	-2370	-2500	-2580
26		-680	-1376	-1657	-1943	-2200	-2330	-2470	-2610	-2690
27		-703	-1416	-1704	-1993	-2250	-2380	-2520	-2660	-2740
28		-648	-1304	-1569	-1836	-3070	-2190	-2320	-2450	-2520
53		-585	-1009	-1194	-1321	-1454	-1478	-1546	-1610	-1621
54		-808	-1637	-1975	-2320	-2620	-2770	-2930	-3100	-3200
55		-700	-1382	-1632	-1880	-2110	-2210	-2330	-2450	-2510
56		-724	-1460	-1756	-2060	-2320	-2450	-2590	-2740	-2830
29		-784	-1576	-1894	-2210	-2490	-2630	-2780	-2930	-3020
58		-859	-1756	-2120	-2490	-2820	-2980	-3160	-3350	-3460
59		-716	-1451	-1749	-2050	-2310	-2440	-2590	-2730	-2820
60		-785	-1590	-1914	-2240	-2520	-2660	-2820	-2970	-3070
61		-770	-1552	-1864	-2180	-2440	-2570	-2720	-2870	-2950
62		-725	-1476	-1776	-2080	-2340	-2460	-2610	-2750	-2840
63		-732	-1485	-1784	-2080	-2350	-2470	-2050	-2770	-2850
64		-725	-1475	-1778	-2080	-2350	-2480	-2630	-2780	-2860
65		-731	-1490	-1796	-2100	-2370	-2500	-2650	-2800	-2890
66		-702	-1428	-1717	-2010	-2260	-2380	-2510	-2660	-2740
67		-680	-1365	-1628	-1890	-2110	-2210	-2330	-2440	-2500
68		-623	-1260	-1510	-1760	-1971	-2070	-3190	-1310	-2380

TABLE XX (Continued)
BLADE PROOF TEST STRAINS
$\Delta\epsilon, \mu''/''$

Vishay

Gage No.	0 Load Set	500 lb	1000 lb	1200 lb	1400 lb	1600 lb	1700 lb	1800 lb	1900 lb	1971 lb
69	0 →	-517	-1043	-1245	-1450	-1615	-1692	-1788	-1885	-1935
70		-592	-1209	-1452	-1690	-1902	-1998	-2120	-3240	-2200
71		-709	-1555	-1868	-2190	-2480	-2620	-2770	-2930	-3020
72		-773	-1579	-1906	-2240	-2540	-2680	-2840	-3000	-3100
73		-655	-1286	-1500	-1720	-1920	-1981	-2090	-2190	-2220
1	0 →		-212							
2			-362							
3			-423							
4			-510							
5			-674							
6			-914							
7			-882							
8			-850							
9			-717							
10			-900							
11			-955							
12			-788							
13			-980							
14			-1036							
15			-798							
16			-1127							
17			-219							
18			-510							
19			-1114							

TABLE XX (Continued)
BLADE PROOF TEST STRAINS
$\Delta\epsilon, \mu''/''$

Vishay

Gage No.	2050 lb	2168 lb	2220 lb	2300 lb	2365 lb	0 Load Offset	Blade Station In.	$\frac{r}{R}$	% Chord	Side of Blade
20	-2330	-2470	-2540	-2630	-2700	-31	465	0.62	25	Camber
21	-2780	-2940	-3020	-3120	-3210	-31	472.5	0.63		
22	-2340	-2520	-2590	-2680	-2750	-33	480	0.64		
23	-2500	-2650	-2730	-2810	-2890	-41	487.5	0.65		
24	-2630	-2790	-2880	-2970	-3050	-33	495	0.66		
25	-2690	-2850	-2940	-3040	-3120	-27	502.5	0.67		
26	-3810	-2970	-3060	-3160	-3240	-10	510	0.68		
27	-2860	-3020	-3110	-3210	-3290	-24	517.5	0.69		
28	-2630	-2770	-2860	-2950	-3030	-29	525	0.70		
53	-1650	-1714	-1723	-1754	-1779	-620	532.5	0.71		
54	-3330	-3530	-3640	-3760	-3850	-37	540	0.72		
55	-2590	-2730	-2790	-2870	-2930	-392	547.5	0.73		
56	-2940	-3110	-3210	-3310	-3400	-9	555	0.74		
29	-3140	-3310	-3420	-3510	-3600	-38	562.5	0.75		
58	-3610	-3830	-3960	-4080	-4200	-47	570	0.76		
59	-2940	-3100	-3210	-3310	-3390	-33	577.5	0.77		
60	-3190	-3370	-3480	-3580	-3680	-53	585	0.78		
61	-3070	-3230	-3340	-3430	-3510	-42	592	0.79		
62	-2950	-3110	-3220	-3340	-3420	-74	600	0.80		
63	-2960	-3130	-3230	-3330	-3410	-10	6075	0.81		
64	-2980	-3150	-3260	-3350	-3430	-34	615	0.82		
65	-3000	-3170	-3290	-3380	-3470	-43	622.5	0.83		
66	-2840	-3000	-3100	-3190	-3270	-7	630	0.84		
67	-2570	-2690	-3760	-2820	-2870	-71	632.5	0.85		

TABLE XX (Continued)
BLADE PROOF TEST STRAINS
$\Delta\epsilon, \mu''/''$

Gage No.	2050 lb	2168 lb	2220 lb	2300 lb	2365 lb	0 Load Offset	Blade Station In.	$\frac{r}{R}$	% Chord	Side of Blade
68	-2460	-2600	-2690	-2760	-2820	-3	645	0.86	25	Camber
69	-2000	-2110	-2180	-2230	-2280	-36	652.5	0.87		↓
70	-2380	-2510	-2610	-2670	-2730	-44	660	0.88		Face
71	-3140	-3320	-3420	-3530	-3610	-57	375	0.75		Face
72	-3240	-3420	-3530	-3530	-3650	-88	412.5	0.80		Face
73	-2280	-2380	-2420	-2470	-2510	-464	450	0.85		Camber
1					-530	-8	52	0.07		
2					-847	-7	75	0.1		
3					-966	-18	150	0.2		
4					-1199	-17	225	0.3		
5					-1588	-21	300	0.4		
6					-2190	-25	375	0.5		
7					-2120	-21	382.5	0.51		
8					-1811	-199	390	0.52		
9					-2012	-11	397.5	0.53		
10					-2087	-25	405	0.54		
11					-2261	-20	412.5	0.55		
12						-16	420	0.56		
13					-2271	-11	427.5	0.57		
14					-2329	-98	435	0.58		
15					-1628	-192	442.5	0.59		
16					-2551	-6	450	0.60		
17					-583	-23	450	0.60		
18					-939	-62	450	0.60		
19					-2665	-35	452.5	0.61		

Vishay

169

TABLE XXI

BLADE PROOF TEST DEFLECTIONS, INCHES OR DEGREES

Blade Station In.	Type of Deflection	500 lb	1000 lb	1200 lb	1400 lb	1600 lb	1700 lb	1800 lb	1900 lb
777 (1)	Vertical	20.25	40.75	49.25	57.75	65.25	69.0	73.5	77.37
Top	Horizontal	0.0200	0.0410	0.0490	0.0580	0.0660	0.0700	0.0738	0.0778
Bottom	Horizontal	0.0135	0.0280	0.0342	0.0390	0.0442	0.0465	0.0500	0.0520
Retention	Vertical	0.006	0.0115	0.0142	0.0168	0.0200	0.0220	0.0230	0.0242
777 (1)	Angular, °	5	10	11.5	13.5	15.5	16.5	17	18

| Blade Station In.	Type of Deflection	1971 lb	2050 lb	2168 lb	2220 lb	2300 lb	2365 lb	0 Load Offset
777 (1)	Vertical	80.25	84.5	89.5	92.25	95.5	98.125	2.5
Top	Horizontal	0.0810	0.0850	0.0901	0.0918	0.0942	0.0976	0.005
Bottom	Horizontal	0.0542	0.0561	0.0590	0.0603	0.0628	0.0640	0.008
Retention	Vertical	0.0250	0.0260	0.0271	0.0284	0.0292	0.0301	0.007
777 (1)	Angular, °	19	20	21	21.5	22.5	23	1

(1) Boom 27" from blade tip
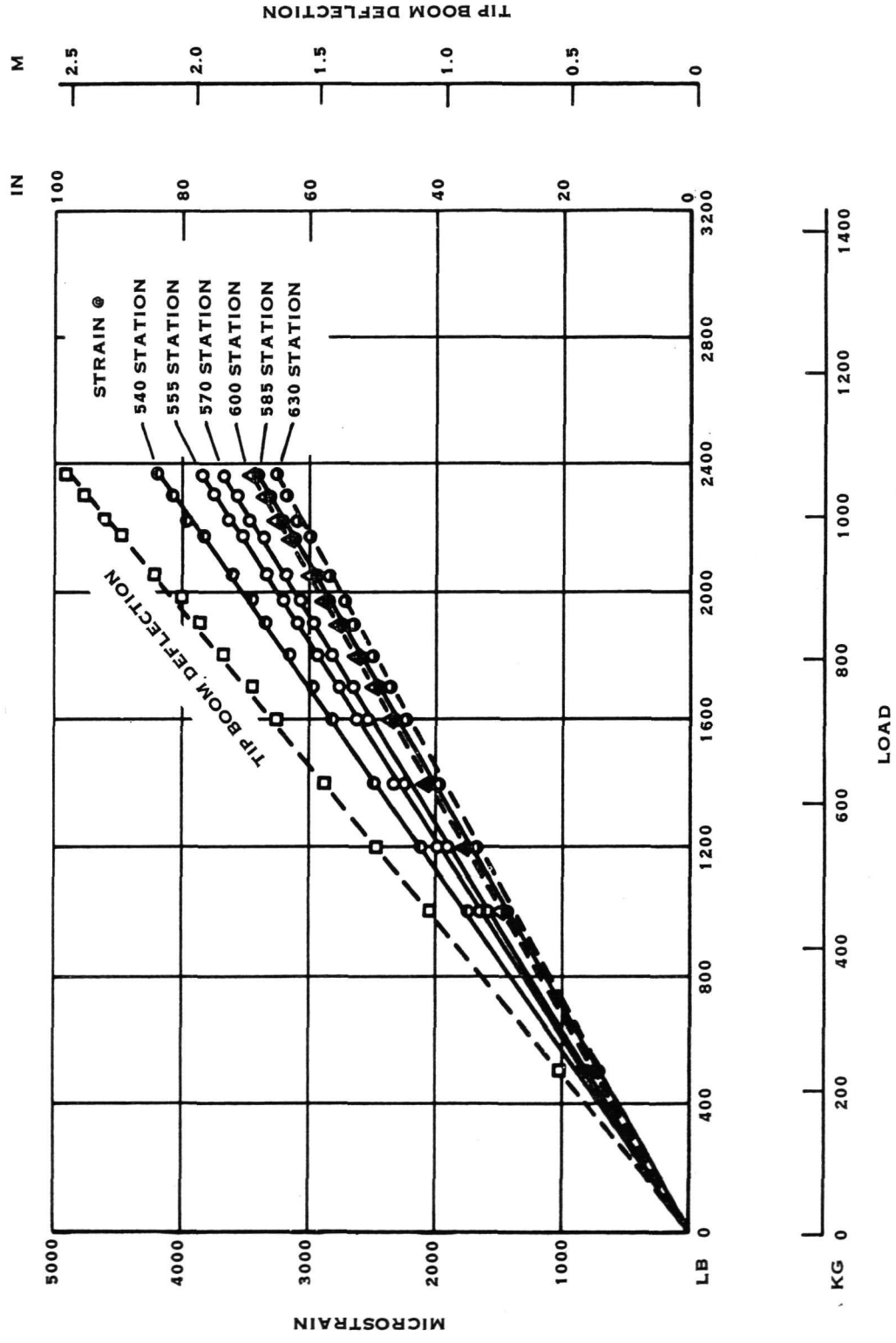
FIGURE 114. PROOF TEST STRAINS AND DEFLECTIONS

171

Page Intentionally Left Blank

APPENDIX A

TYPE II BLADE DESIGN

After completing fabrication of the manufacturing prototype blade, Hamilton Standard, using internal funding, undertook the design of a Type II blade which could operate on the Department of Energy/NASA MOD-0 100 kW experimental wind turbine, under all of the specified load conditions, without the need of an internal spar support. This was accomplished by increasing the spar wall thickness, which added 317 pounds of composite to the spar weight. This combined with the 194 pound reduction by eliminating the spar support resulted in a blade with a total weight of 2400 pounds which was acceptable for operation on the MOD-0 or MOD-0A wind turbines. Analysis of this blade design revealed that it was acceptable for operation under all loading conditions specified for the wind turbine.

The following Table traces the blade weight breakdown from the preliminary design blade through the Type II design blade

TABLE XXII
SPAR-SHELL BLADE WEIGHT BREAKDOWN

	Preliminary Design	Type I Final Design	Manufacturing Prototype	Type II Final Design
Spar and Shell	1470 lb.	1470 lb.	2145 lb.	1787 lb.
Retention Rings	260	260	267	260
Adapter and Bolts	236	236	*	236
Balance Weights	45	45	*	45
Spar Support	-	194	*	-
Paint	36	36	*	36
Tip and Root Closures	11	11	*	11
Lightning Protection	25	25	*	25
	2083 lb.	2277 lb.		2400 lb.

*Not included in manufacturing prototype hardware at completion of program.

Page Intentionally Left Blank

APPENDIX B

BLADE DRAWING

FIGURE 115. BLADE DESIGN

1. Report No. NASA CR-135389	2. Government Accession No.	3. Recipient's Catalog No.
4. Title and Subtitle DESIGN, FABRICATION, AND TEST OF A COMPOSITE MATERIAL WIND TURBINE ROTOR BLADE		5. Report Date November 1977
		6. Performing Organization Code
7. Author(s) D. G. Griffee, Jr., R. E. Gustafson, and E. R. More		8. Performing Organization Report No. HSER 7383
		10. Work Unit No.
9. Performing Organization Name and Address Hamilton Standard Division United Technologies Corporation Windsor Locks, Conn. 06096		11. Contract or Grant No. NAS 3-19773
		13. Type of Report and Period Covered Contractor Report
12. Sponsoring Agency Name and Address U.S. Department of Energy Division of Distributed Solar Technology Washington, D.C. 20545		14. Sponsoring Agency Code Report No. DOE/NASA/9773-78/1

15. Supplementary Notes

Final report. Prepared under Interagency Agreement E(49-26)-1028. Project Manager, Thomas P. Cahill, Wind Power Office, NASA Lewis Research Center, Cleveland, Ohio 44135

16. Abstract

The aerodynamic and structural design, fabrication, and test of a 60-foot (18.3-meter)- long filament wound, composite material, wind turbine turbine rotor blade are described. The blade was designed for use with the Department of Energy/NASA MOD-0 100 kilowatt experimental wind turbine located in Sandusky, Ohio.

17. Key Words (Suggested by Author(s)) Wind turbine Blade Filament wound Fiberglass	18. Distribution Statement Unclassified - unlimited STAR Category 44 DOE Category UC-60	
19. Security Classif. (of this report) Unclassified	20. Security Classif. (of this page) Unclassified	21. No. of Pages 186	22. Price* A09

☆USGPO: 1978 — 657-059/1208 Region 5-11